Fast diffusion MRI based on sparse acquisition and reconstruction for long-term population imaging

DISSERTATION

zur
Erlangung des Doktorgrades (Dr. rer. nat.)
der
Mathematisch-Naturwissenschaftlichen Fakultät
der
Rheinischen Friedrich-Wilhelms-Universität Bonn

vorgelegt von

Alexandra Koch

aus Halle

Bonn, Mai 2019

Angefertigt mit Genehmigung der Mathematisch-Naturwissenschaftlichen Fakultät der
Rheinischen Friedrich-Wilhelms-Universität Bonn

1. Gutachter: Prof. Dr. Thomas Schultz
2. Gutachter: Prof. Dr. Tony Stöcker

Tag der mündlichen Prüfung: 29. August 2019
Erscheinungsjahr: 2019

Abstract

Diffusion weighted magnetic resonance imaging (dMRI) is a unique MRI modality to probe the diffusive molecular transport in biological tissue. Due to its noninvasiveness and its ability to investigate the living human brain at submillimeter scale, dMRI is frequently performed in clinical and biomedical research to study the brain's complex microstructural architecture. Over the last decades large prospective cohort studies have been set up with the aim to gain new insights into the development and progression of brain diseases across the life span and to discover biomarkers for disease prediction and potentially prevention. To allow for diverse brain imaging using different MRI modalities, stringent scan time limits are typically imposed in population imaging. Nevertheless, population studies aim to apply advanced and thereby time consuming dMRI protocols that deliver high quality data with great potential for future analysis.

To allow for time-efficient but also versatile diffusion imaging, this thesis contributes to the investigation of accelerating diffusion spectrum imaging (DSI), an advanced dMRI technique that acquires imaging data with high intra-voxel resolution of tissue microstructure. Combining state-of-the-art parallel imaging and the theory of compressed sensing (CS) enables the acceleration of spatial encoding and diffusion encoding in dMRI. In this way, the otherwise long acquisition times in DSI can be reduced significantly.

In this thesis, first, suitable q-space sampling strategies and basis functions are explored that fulfill the requirements of CS theory for accurate sparse DSI reconstruction. Novel 3D q-space sample distributions are investigated for CS-DSI. Moreover, conventional CS-DSI based on the discrete Fourier transform is compared for the first time to CS-DSI based on the continuous SHORE (simple harmonic oscillator based reconstruction and estimation) basis functions.

Based on these findings, a CS-DSI protocol is proposed for application in a prospective cohort study, the Rhineland Study. A pilot study was designed and conducted to evaluate the CS-DSI protocol in comparison with state-of-the-art 3-shell dMRI and dedicated protocols for diffusion tensor imaging (DTI) and for the combined hindered and restricted model of diffusion (CHARMED). Population

imaging requires processing techniques preferably with low computational cost to process and analyze the acquired big data within a reasonable time frame. Therefore, a pipeline for automated processing of CS-DSI acquisitions was implemented including both in-house developed and existing state-of-the-art processing tools.
The last contribution of this thesis is a novel method for automatic detection and imputation of signal dropout due to fast bulk motion during the diffusion encoding in dMRI. Subject motion is a common source of artifacts, especially when conducting clinical or population studies with children, the elderly or patients. Related artifacts degrade image quality and adversely affect data analysis. It is, thus, highly desired to detect and then exclude or potentially impute defective measurements prior to dMRI analysis. Our proposed method applies dMRI signal modeling in the SHORE basis and determines outliers based on the weighted model residuals. Signal imputation reconstructs corrupted and therefore discarded measurements from the sparse set of inliers. This approach allows for fast and robust correction of imaging artifacts in dMRI which is essential to estimate accurate and precise model parameters that reflect the diffusive transport of water molecules and the underlying microstructural environment in brain tissue.

Zusammenfassung

Die diffusionsgewichtete Magnetresonanztomographie (dMRT) ist ein einzigartiges MRT-Bildgebungsverfahren, um die Diffusionsbewegung von Wassermolekülen in biologischem Gewebe zu messen. Aufgrund der Möglichkeit Schichtbilder nicht invasiv aufzunehmen und das lebende menschliche Gehirn im Submillimeter-Bereich zu untersuchen, ist die dMRT ein häufig verwendetes Bildgebungsverfahren in klinischen und biomedizinischen Studien zur Erforschung der komplexen mikrostrukturellen Architektur des Gehirns. In den letzten Jahrzehnten wurden große prospektive Kohortenstudien angelegt, um neue Einblicke in die Entwicklung und den Verlauf von Gehirnkrankheiten über die Lebenspanne zu erhalten und um Biomarker zur Krankheitserkennung und -vorbeugung zu bestimmen. Um durch die Verwendung unterschiedlicher MRT-Verfahren verschiedenartige Schichtbildaufnahmen des Gehirns zu ermöglich, müssen Scanzeiten typischerweise stark begrenzt werden. Dennoch streben Populationsstudien die Anwendung von fortschrittlichen und daher zeitintensiven dMRT-Protokollen an, um Bilddaten in hoher Qualität und mit großem Potential für zukünftige Analysen zu akquirieren.

Um eine zeiteffizente und gleichzeitig vielseitige Diffusionsbildgebung zu ermöglichen, leistet diese Dissertation Beiträge zur Untersuchung von Beschleunigungsverfahren für die Bildgebung mittels diffusion spectrum imaging (DSI). DSI ist ein fortschrittliches dMRT-Verfahren, das Bilddaten mit hoher intra-voxel Auflösung der Gewebestruktur erhebt. Werden modernste Verfahren zur parallelen MRT-Bildgebung mit der compressed sensing (CS) Theorie kombiniert, ermöglicht dies eine Beschleunigung der räumliche Kodierung und der Diffusionskodierung in der dMRT. Dadurch können die ansonsten langen Aufnahmezeiten für DSI erheblich reduziert werden.

In dieser Arbeit werden zuerst geeigenete Strategien zur Abtastung des q-space sowie Basisfunktionen untersucht, welche die Anforderungen der CS-Theorie für eine korrekte Signalrekonstruktion der dünnbesetzten DSI-Daten erfüllen. Neue 3D-Verteilungen von Messpunkten im q-space werden für die Verwendung in CS-DSI untersucht. Außerdem wird konventionell auf der diskreten Fourier-Transformation basierendes CS-DSI zum ersten Mal mit einem CS-DSI Verfahren verglichen, welches kontinuierliche SHORE (simple harmonic oscillator based reconstruction and

estimation) Basisfunktionen verwendet.
Aufbauend auf diesen Ergebnissen wird ein CS-DSI-Protokoll zur Anwendung in einer prospektiven Kohortenstudie, der Rheinland Studie, vorgestellt. Eine Pilotstudie wurde entworfen und durchgeführt, um das CS-DSI-Protokoll im Vergleich mit modernster 3-shell-dMRT und mit dedizierten Protokollen für diffusion tensor imaging (DTI) und für das combined hindered and restricted model of diffusion (CHARMED) zu evaluieren. Populationsbildgebung erfordert Prozessierungsverfahren mit möglichst geringem Rechenaufwand, um große akquirierte Datenmengen in einem angemessenen Zeitrahmen zu verarbeiten und zu analysieren. Dafür wurde eine Pipeline zur automatisierten Verarbeitung von CS-DSI-Daten implementiert, welche sowohl eigenentwickelte als auch bereits existierende moderene Verarbeitungsprogramme enthält.
Der letzte Beitrag dieser Arbeit ist eine neue Methode zur automatischen Detektion und Imputation von Signalabfall, welcher durch schnelle Bewegungen während der Diffusionskodierung in der dMRT entsteht. Bewegungen der Probanden während der dMRT-Aufnahme sind eine häufige Ursache für Bildfehler, vor allem in klinischen oder Populationsstudien mit Kindern, alten Menschen oder Patienten. Diese Artefakte vermindern die Datenqualität und haben einen negativen Einfluss auf die Datenanalyse. Daher ist es das Ziel, fehlerhafte Messungen vor der dMRI-Analyse zu erkennen und dann auszuschließen oder wenn möglich zu ersetzen. Die vorgestellte Methode verwendet die SHORE-Basis zur dMRT-Signalmodellierung und bestimmt Ausreißer mit Hilfe von gewichteten Modellresidualen. Die Datenimputation rekonstruiert die unbrauchbaren und daher verworfenen Messungen mit Hilfe der verbleibenden, dünnbesetzten Menge an Messungen. Dieser Ansatz ermöglicht eine schnelle und robuste Korrektur von Bildartefakten in der dMRT, welche erforderlich ist, um korrekte und präzise Modellparameter zu schätzen, die die Diffusionsbewegung von Wassermolekülen und die zugrundeliegende Mikrostruktur des Gehirngewebes reflektieren.

Contents

Part I

Introduction and background

1

Introduction

1.1 Motivation

In clinical and biomedical research, diffusion weighted magnetic resonance imaging (dMRI) provides, completely non-invasively, unique insights into the complex microstructural architecture of the living human brain. Sensitized to the diffusive molecular transport in brain tissue, diffusion MRI is the methodology of choice to investigate pathological changes of diffusion in brain tissue and the influence of disease on the structural connectivity of brain white matter (WM). As a biomarker for brain diseases, dMRI is applied in clinical applications, e.g. for the assessment of acute stoke (Jensen et al., 2011; Werring et al., 2000), and in research studies investigating e.g. the process of aging (Falangola et al., 2008; Kodiweera et al., 2016) and neurodegenerative diseases such as Alzheimer's disease (AD)(Colgan et al., 2016; Fieremans et al., 2013; Helpern et al., 2011). In the last decades, large cohort studies have been set up with the purpose to gain new insights into disease development and progression across the life span and to thereby discover biomarkers for disease prediction and potentially prevention. Diffusion MRI is one of the core MR imaging techniques applied in population studies such as the Rotterdam study (Breteler et al., 1994; De Groot et al., 2000), the Alzheimer's Disease Neuroimaging Initiative (Weiner et al., 2015) (ADNI), the Human Connectome Project (Glasser et al., 2016) (HCP), the UK Biobank study (Miller et al., 2016) and the Rhineland Study (Stöcker, 2016; Tobisch et al., 2018).

Long-term population imaging demands time efficient and versatile diffusion imaging. Thus, on the one hand, accelerated dMRI is required to collect data within a reasonable scan time. On the other hand, population imaging requires a dMRI protocol that provides reliable high quality data with maximum potential for future analysis. The acquired dMRI data should be of high spatial and high intra-voxel resolution in order to be applicable to a wide range of dMRI reconstruction techniques. Following data acquisition, quality assessment that accounts for acquisition and subject related

image artifacts is essential to minimize degradation of data quality and related adverse effects on subsequent dMRI analysis. As of today, there is no consensus in the research community on the best dMRI acquisition and reconstruction techniques to infer reliable information on the diffusion process and the underlying brain tissue microstructure. In the early days of dMRI, diffusion tensor imaging (DTI) (P Basser et al., 1994a) was proposed to quantitatively characterize the anisotropy of diffusion and to reconstruct macroscopic neuronal connections. Since DTI is possible in a few minutes of scan time, it was quickly implemented in clinical settings. Even today, DTI is widely used for clinical and research applications, despite its inherent limitations (see section 2.6.1.1). Other dMRI reconstruction techniques, e.g. diffusion spectrum imaging (DSI) (Wedeen et al., 2005) (see section 2.6.1.3), have been developed to overcome the shortcomings of DTI, however, typically at the cost of increased scan time. For dMRI in the context of population imaging, but also, in general, in studies with limited scan time, the application of advanced dMRI protocols is highly desired, thereby increasing the demand for robust acceleration techniques to speed up dMRI acquisition. Moreover, the collection of big data, e.g. in population imaging, requires processing techniques preferably with low computational cost to process and analyze the acquired data within a reasonable time frame.

This thesis contributes to the investigation and evaluation of dMRI acquisition and reconstruction strategies that match the requirements of population imaging. For fast high resolution dMRI, state-of-the-art parallel imaging is combined with compressed sensing based dMRI acquisition and reconstruction. Different approaches for accelerated dMRI are presented and compared, with a special focus on accelerated DSI. In this context, a forward-looking dMRI acquisition strategy that allows for time efficient versatile diffusion imaging at 3 Tesla (3T) MRI scanners is proposed for application in the Rhineland Study. Moreover, a novel method that corrects for signal dropout in dMRI due to fast subject motion was developed. This approach can be applied independently of the dMRI acquisition strategy and with fast performance due to lower computational effort compared to alternative methods.

1.2 Related work

Over the last decades, many dMRI reconstruction techniques have been developed and investigated to relate the acquired dMRI data quantitatively to diffusion and microstructural features of brain tissue. Each of them comes with specific requirements on the imaging protocol which itself is designed based on hardware and application constraints. Fortunately, due to advances in parallel imaging for dMRI (Cauley et al., 2014; Setsompop et al., 2012; Xu et al., 2013) and the successful translation of the compressed sensing (CS) theory (Candès and Romberg, 2007; Donoho, 2006) to MRI (Lustig et al., 2007) and dMRI (Bilgic et al., 2012; Menzel et al., 2011; Paquette et al., 2015; Setsompop et al., 2013), fast dMRI was made possible. This thesis focuses on robust compressed sensing reconstruction to accelerate DSI (CS-DSI). DSI is an advanced diffusion imaging technique that acquires dMRI data with high resolution of the intra-voxel microstructure. In addition DSI exploits the simple Fourier relationship between the dMRI signal and the diffusion propagator and thus enables model-free dMRI reconstruction. Unfortunately, those advantages come at the cost of long

acquisition times. Combining parallel imaging and CS principles to accelerate spatial encoding and diffusion encoding in dMRI, the acquisition time in DSI can be reduced significantly.

Suitable sampling schemes (Menzel et al., 2011; Paquette et al., 2015) and basis functions (J Cheng, T Jiang, et al., 2011; Fick et al., 2016; Merlet and Deriche, 2010, 2013; Ozarslan et al., 2009; Paquette et al., 2015) for compressed sensing and a sparse representation of dMRI signals have been investigated. Within the scope of this thesis, different q-space sampling strategies were compared, including a novel 3D approach (Knutsson and Westin, 2013) applied for the first time in CS-DSI. Moreover, complementing and extending the previous works, suitable basis functions were investigated for accurate sparse DSI reconstruction based on simulations (Cook et al., 2006), diffusion phantom (Moussavi-Biugui et al., 2011) and *in vivo* dMRI experiments. Based on these findings, we adapted and optimized a CS-DSI protocol for dMRI in the Rhineland Study and compared it to 3-shell dMRI (Sotiropoulos et al., 2013) and dedicated DTI and CHARMED (Assaf and Basser, 2005; De Santis, Y Assaf, et al., 2014) protocols. As in other population studies (Breteler et al., 1994; Glasser et al., 2016; Miller et al., 2016; Weiner et al., 2015), the dMRI protocol has to comply with the imposed stringent scan time limits, while delivering high quality imaging data.

In dMRI, data analysis can be severely hampered by acquisition and subject related image artifacts. Data processing methods exist to simultaneously correct for artifacts due to motion during dMRI acquisition and for geometric distortions in the image (Andersson et al., 2017, 2016, 2003; Andersson and Sotiropoulos, 2016; Raffelt et al., 2012) common to diffusion weighted MR images. In this thesis, a novel approach based on SHORE (simple harmonic oscillator based reconstruction and estimation) (J Cheng, T Jiang, et al., 2011; Ozarslan et al., 2009) signal modeling was developed for the correction of signal dropout within slices of dMRI volumes occurring due to fast macroscopic subject movements. Several works have already been proposed for outlier detection to discard affected measurements from the dMRI data set to avoid adverse effects on dMRI feature extraction (Chang et al., 2005; Scherrer and Warfield, 2012; Tax et al., 2015). However, accurate signal imputation to recover corrupted measurements facilitates and potentially improves data analysis (Chen et al., 2015; Elhabian et al., 2014). Several methods have been proposed for dropout detection and imputation in dMRI (Andersson et al., 2016; Christiaens et al., 2018; Elhabian et al., 2016) in parallel to our works on the topic presented in this thesis. In comparison, our proposed method allows for accurate performance independent of the dMRI acquisition strategy and a more rapid data processing.

1.3 Contributions and thesis outline

In this thesis, dMRI is used to investigate the human brain *in vivo*. An introduction to brain anatomy and structure is therefore given at the beginning of Chapter 2. Furthermore, Chapter 2 presents the basic principles and challenges of MRI sensitized to molecular motion in biological tissue. The last part of Chapter 2 gives an overview on dMRI methodology to extract diffusion and microstructural features of brain tissue from the acquired imaging data and a set of state-of-the-art dMRI reconstruction techniques is discussed in more detail. In Chapter 3, advances in the development of

novel acquisition strategies for fast spatial and diffusion encoding in dMRI are presented. Following a brief introduction of parallel imaging, this chapter covers the principles of CS theory and its application to dMRI for accelerated data collection.

The works published within the scope of this thesis are presented in chapters 4 - 7. For the application in CS-DSI, Chapter 4 investigates suitable q-space sampling strategies including the novel approach by Knutsson and Westin (2013) applied for the first time in CS-DSI. Further, different basis functions for CS accelerated DSI are compared with a focus on bases that allow for a sparse representation of the diffusion signal or propagator, thereby fulfilling one of the requirements for accurate CS reconstruction. In comprehensive experimental settings, the methods were investigated and evaluated based on simulations, diffusion phantom data and *in vivo* dMRI. In this work, a CS-DSI approach based on the continuous SHORE basis functions was applied for the first time and compared to conventional CS-DSI based on the Fourier transform. By doing so, this work contributes to extending and complementing previous works in this field on suitable sampling strategies and basis functions for CS-DSI.

Based on the findings presented in Chapter 4, a CS-DSI protocol was adapted and optimized for fast dMRI in a prospective cohort study, specifically the Rhineland Study. As presented in chapter 5, a pilot study was designed based on the requirements for long-term population imaging and conducted to investigate the performance of CS-DSI for high resolution dMRI. CS-DSI was further compared to state-of-the-art 3-shell HARDI dMRI and dedicated DTI and CHARMED protocols. In this work, a comprehensive evaluation framework is used to implement a reliable comparison of conceptually very different diffusion protocols. Conclusions on a suitable dMRI protocol for population imaging were based on qualitative visual inspection, quantitative statistical analysis of extracted diffusion and microstructural features of brain tissue and test-retest performance of the different acquisition strategies. The first contribution of this work is a forward-looking dMRI acquisition strategy that allows for time efficient versatile diffusion imaging at 3T which is now part of the core imaging protocol of the Rhineland Study. Second, a pipeline for automated analysis of dMRI acquisitions was designed specifically for CS-DSI and implemented including both in-house developed and existing state-of-the-art processing tools, e.g. for motion and distortion correction, CS reconstruction and diffusion and microstructural feature extraction.

The estimation of accurate and precise model parameters that reflect the diffusive transport of water molecules and the underlying microstructural environment in brain tissue is challenged by the presence of imaging artifacts in dMRI. Subject motion is a common source of artifacts because it is ever present during dMRI acquisition. Signal dropout due to fast bulk motion during the diffusion encoding leads to strong attenuation of the measured signal which can be erroneously interpreted as high diffusivity during dMRI analysis. In chapters 6 and 7, novel methods for the detection of signal dropout in dMRI and accurate signal imputation are presented. Both works incorporate signal modeling in the SHORE basis to reconstruct dMRI data. Since the SHORE model defines continuous basis functions, it was used to reconstruct the discarded corrupted measurements from a sparse set of inliers, thereby reconstructing the complete dMRI data set. In addition to studies on SHORE and our works discussed in chapter 4, we confirm its suitability to reconstruct dMRI data from sparse measurement. Chapter 6 presents a SHORE-based approach that incorporates an

iterative reweighting of model residuals to detect outliers due to signal dropout. Extending this approach with a novel outlier score, the method presented in Chapter 7 avoids reiterative processing which results in a lower computational effort to accurately detect signal dropout and to replace the affected measurements with imputed values. The contribution of these works is, thus, a fast and robust method for automatic detection of signal dropout in dMRI and accurate signal imputation.

Chapter 8 summarizes the findings and contributions of this thesis. Further, an outlook is given on future research directions in the field of accelerated dMRI by means of CS-DSI and its applications in studies with limited dMRI scan time.

1.4 Publications

The following first author journal publications and proceedings paper form the chapters 4, 5, 6 and 7 of this cumulative dissertation:

Koch A, Zhukov A, Stöcker T, Groeschel S, Schultz T (2019) SHORE-based detection and imputation of dropout in diffusion MRI. Magn. Reson. Med. (under review)

Tobisch A, Schultz T, Stirnberg R, Varela-Mattatall G, Knutsson H, Irarrázaval P and Stöcker T (2019) Comparison of basis functions and q-space sampling schemes for robust compressed sensing reconstruction accelerating diffusion spectrum imaging. NMR in Biomedicine. e4055.

Tobisch A, Stirnberg R, Harms RL, Schultz T, Roebroeck A, Breteler MMB and Stöcker T (2018) Compressed sensing diffusion spectrum imaging for accelerated diffusion microstructure MRI in long-term population imaging. Front. Neurosci. 12:650.

Tobisch A, Stöcker T, Groeschel S, Schultz T (2016) Iteratively Reweighted L1-fitting for model-independent outlier removal and regularization in diffusion MRI. In: 2016 IEEE 13th International Symposium on Biomedical Imaging (ISBI) p.911–914.

Furthermore, the following works have been published within the scope of this thesis:

Journal publications

Varela-Mattatall GE, **Koch A**, Stirnberg R, Chabert S, Uribe S, Tejos C, Stöcker T and Irarrázaval P (2019) Comparison of q-space reconstruction methods for undersampled diffusion spectrum imaging data. Magn. Reson. Med. Sci. 0015-1-11.

Harms RL, Fritz FJ, **Tobisch A**, Goebel R, Roebroeck A (2017) Robust and fast nonlinear optimization of diffusion MRI microstructure models. Neuroimage. 155:82-96.

Conference proceedings

Tobisch A, Stirnberg R, Harms RL, Schultz T, Roebroeck A, Breteler M, Stöcker T (2017) Compressed sensing diffusion spectrum imaging as a forward-looking alternative to multi-shell diffu-

sion MRI in population imaging. In proceedings of the 25th Scientific Meeting of the International Society for Magnetic Resonance in Medicine

Varela-Mattatall G, **Tobisch A**, Stirnberg R, Chabert S, Stöcker T, Tejos C, Irarrázaval P (2017) Negentropy: non-Gaussian characterization for diffusion spectrum imaging. In proceedings of the 25th Scientific Meeting of the International Society for Magnetic Resonance in Medicine

Tobisch A, Schultz T, Stirnberg R, Varela G, Knutsson H, Irarrázaval P, Stöcker T (2015) Comparing Fourier to SHORE basis functions for sparse DSI reconstruction. In proceedings of the 23rd Scientific Meeting of the International Society for Magnetic Resonance in Medicine (ISMRM Merit Award)

Varela-Mattatall G, **Tobisch A**, Stoecker T, Irarrázaval P (2015) Diffusion spectrum imaging from undersampled data using tensor fitting. In proceedings of the 23rd Scientific Meeting of the International Society for Magnetic Resonance in Medicine

Tobisch A, Varela G, Stirnberg R, Knutsson H, Schultz T, Irarrázaval P, Stöcker T (2014) Sparse isotropic q-space sampling distribution for compressed sensing in DSI. In proceedings of the 22nd Scientific Meeting of the International Society for Magnetic Resonance in Medicine

Varela G, **Tobisch A**, Stoecker T, Irarrázaval P (2014) Curvelets, a new sparse domain for diffusion spectrum imaging. In proceedings of the 22nd Scientific Meeting of the International Society for Magnetic Resonance in Medicine

2

Diffusion MRI

2.1 Introduction

In clinical studies and biomedical research, MR scans are typically collected with a spatial resolution at the scale of millimeters (Figure 2.1) depicting the brain tissue macrostructure *in vivo* and non-invasively. However, a resolution on the order of millimeters is too coarse to image tissue microstructure such as white matter axons with a much finer length scale of the order of micrometers.

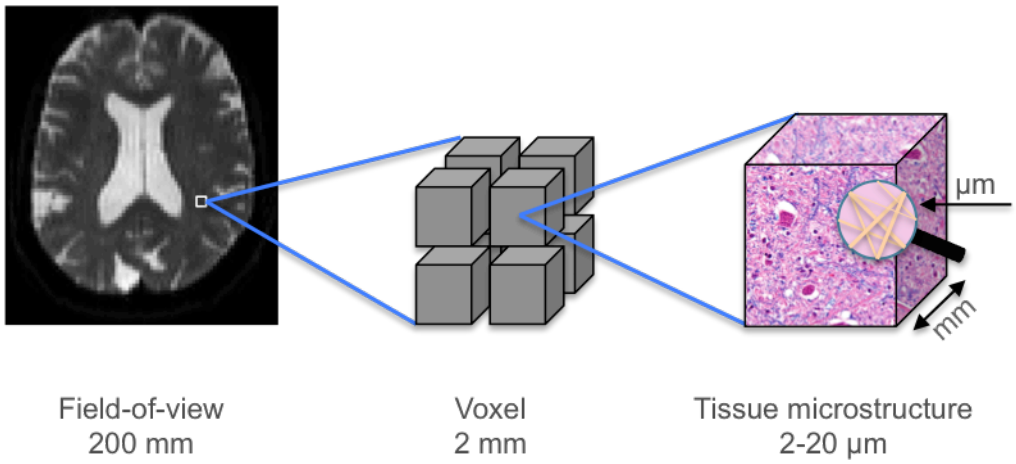

Figure 2.1: From macro to microstructure of brain tissue by means of diffusion MRI.

As an indirect approach to probe microstructural details at orders of magnitude smaller than the image resolution, diffusion magnetic resonance imaging can be applied to measure the diffusion

of water molecules in the brain. In contrast to direct biological investigations by means of histology, non-invasive dMRI provides unique insights into brain structure *in-vivo*. Water molecules in tissue randomly diffuse over a few micrometers within millisecond time scales, an effect described as Brownian motion (Einstein, 1905), and, thus, probe the underlying microstructure. Sensitized to the random motion of water molecules, dMRI offers a distinct imaging contrast to investigate *in vivo* the diffusion process at a microscopic scale (Le Bihan et al., 1986) and to reveal microstructural information from macroscopic measurements. As visualized in Figure 2.2, a dMRI experiment is performed based on the clinical or research application of interest to collect a set of diffusion weighted and non-weighted MR images. A mathematical representation of the diffusion signal, e.g. (P Basser et al., 1994a; Jensen et al., 2005; Ozarslan et al., 2009; Wedeen et al., 2005), or a biophysical model of brain tissue microstructure, e.g. (Assaf and Basser, 2005; Behrens et al., 2003; Zhang et al., 2012), is selected based on the corresponding application and fit to the data to characterize the diffusion signal as well as the underlying microstructure. Such data modeling enables the extraction of distinct features of the diffusion process and tissue properties that can be further analyzed e.g. to infer macroscopic brain connections from voxel-wise fiber orientation estimates.

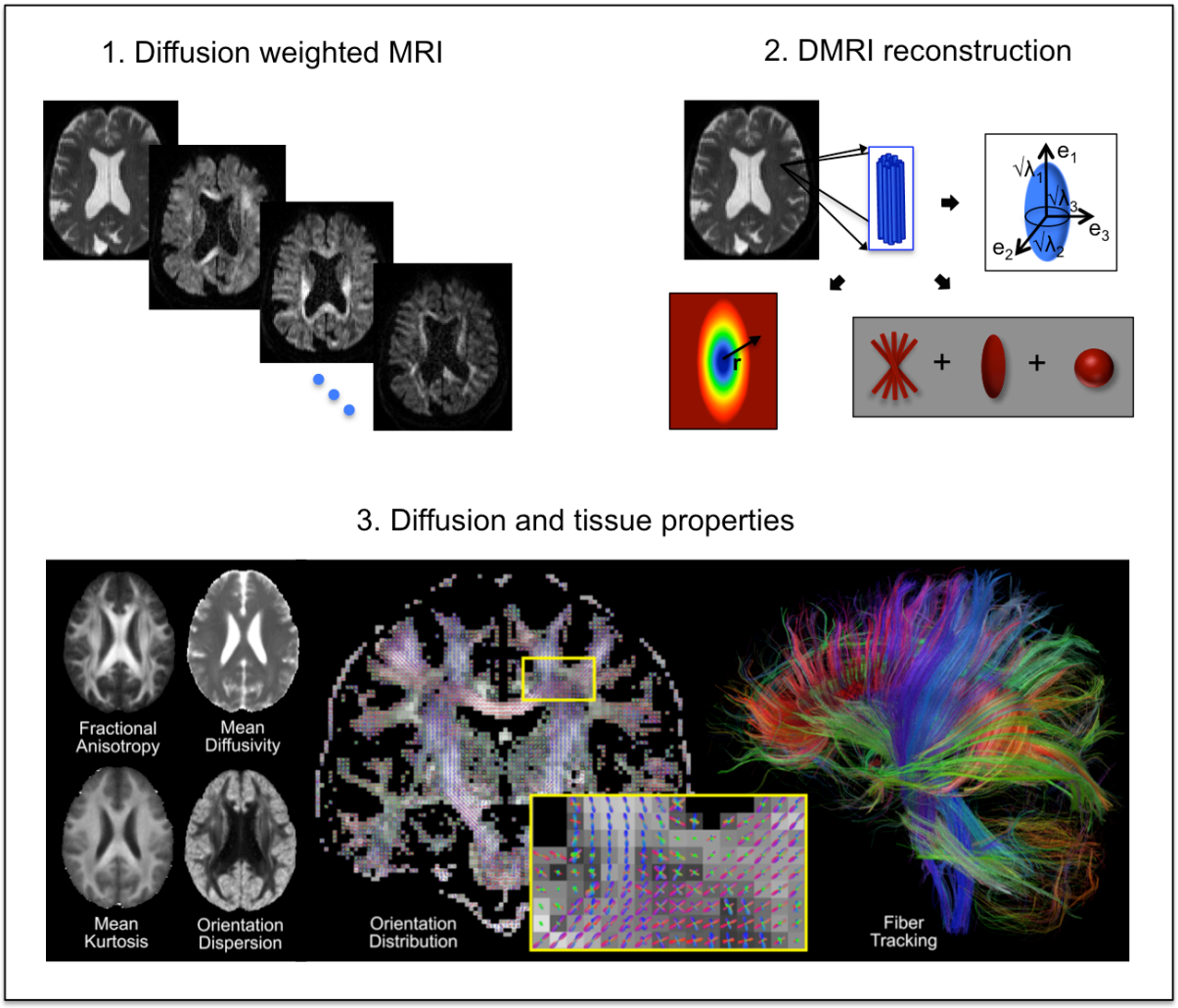

Figure 2.2: Diffusion MRI pipeline: dMRI acquisition, reconstruction and analysis.

The possibility of estimating a wide range of diffusion and microstructural parameters that are of great interest as biomarkers, makes dMRI a powerful imaging modality to study *in vivo* pathological changes of diffusion in brain tissue and the influence of disease on the structural connectivity of brain white matter (WM).

2.2 Micro and macro structure of human brain tissue

The dMRI acquisition, reconstruction and processing techniques presented in this thesis are generic and have been successfully applied for brain imaging, but also for the investigation of other organs such as the heart (Mekkaoui et al., 2017; Sosnovik et al., 2009), kidney (Caroli et al., 2018) and liver (Shenoy-Bhangle et al., 2017) or for imaging of muscle tissue structure (Oudeman et al., 2016). Here we focus on dMRI to investigate the human brain *in vivo*. This section provides basic information about the brain anatomy and structure (OpenStax College, 2013), which is required to discuss dMRI reconstruction techniques to model tissue microstructure or to track nerve fiber fascicles throughout the brain. Figures 2.3, 2.4 and 2.5 are extracted from OpenStax College (2013), an open access textbook on the human anatomy and physiology which is publicly available online. Figure 2.4 was adapted to highlight additional brain regions.

The human nervous tissue is composed of two different types of cells: neurons and neuroglia. Glia cells support and protect neurons in their function to integrate, process and convey sensory information and motor impulses throughout brain and body. The brain contains billions of neurons forming a network of neuronal connections to process and transmit signals, e.g. along sensory and motor pathways. Figure 2.3 shows a schematic of the neuronal structure.

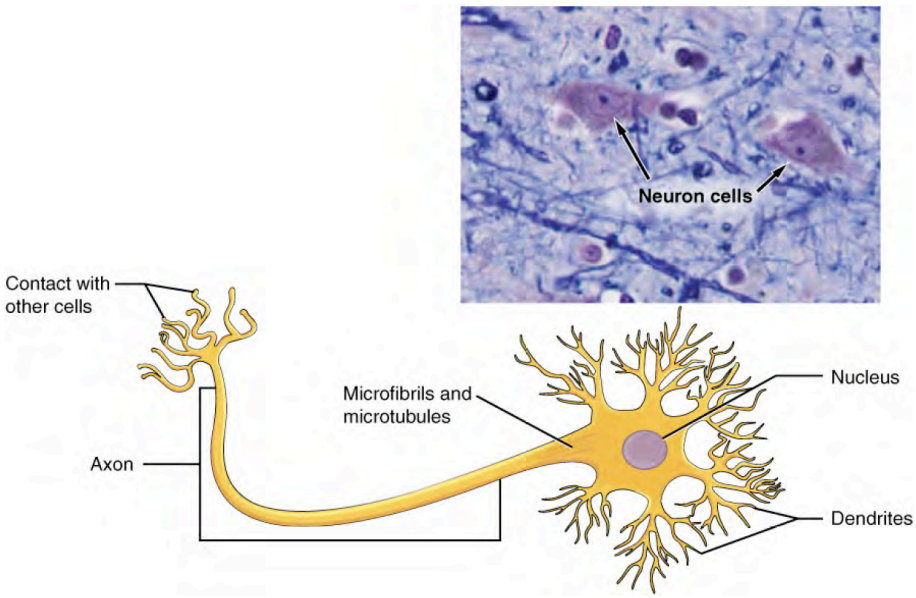

Figure 2.3: Schematic of the neuronal structure. (This illustration was downloaded for free at http://cnx.org/content/col11496/latest/).

Signals are transmitted along axons in the form of electrical impulses. Communication between neurons occurs at their junction (synapses) with the help of neurotransmitters. Dendrites receive signals from other neurons and are therefore highly branched and form a tree-like structure.

The parcellation of the human brain into different regions yields a macroscopic overview of the structural and functional organization of the central nervous system. Figure 2.4 depicts the division of the brain into four major anatomical areas: cerebrum, cerebellum, diencephalon and brain stem.

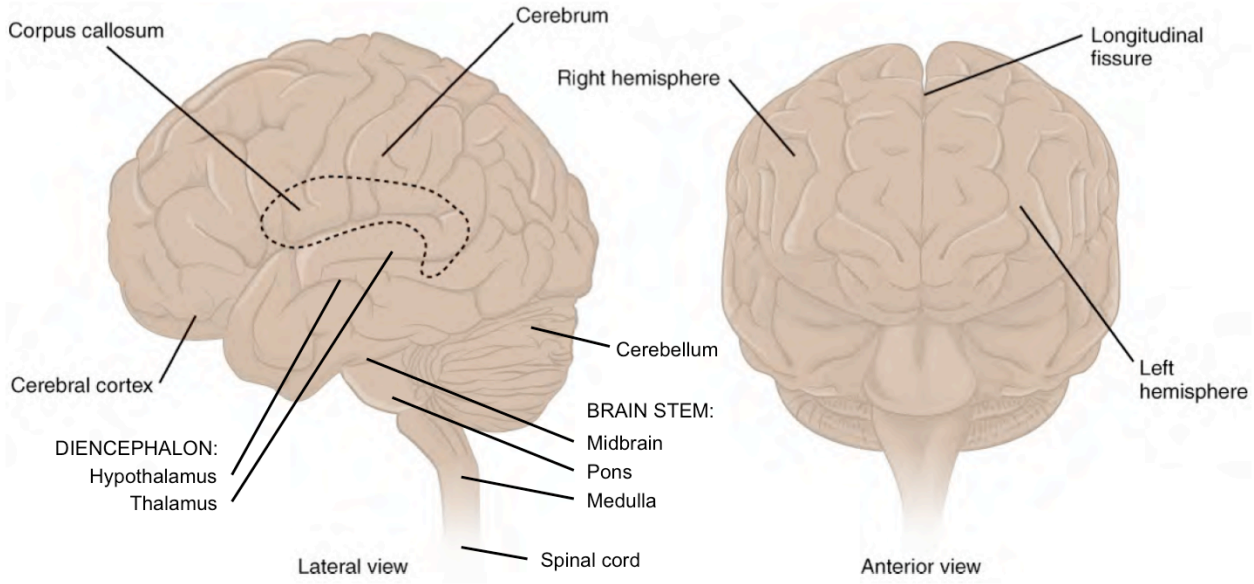

Figure 2.4: Parcellation of the human brain into cerebrum, cerebellum, diencephalon and brain stem. (This illustration was downloaded for free at http://cnx.org/content/col11496/latest/ Additional labels were included for cerebellum, spinal cord, diencephalon and brain stem.)

In the brain stem, neurons connect the spinal cord and the mid brain to transmit nerve impulses to and from the diencephalon and cerebrum. Malfunction of signal conduction via those projection fibers due to axonal loss has severe consequences. For example, loss of motor neurons and thus connectivity in this area is associated with neurodegenerative diseases such as Parkinson's (Yau et al., 2018). In the diencephalon, its two major parts, the thalamus and the hypothalamus, relay sensory and motor information to the cerebral cortex and control and regulate internal organs, respectively. The cerebrum forms the major part of the brain and, among others, is responsible for the processing of sensory information, the control of voluntary movement, emotions and consciousness. The cerebellum (Latin for "little brain") supports the cerebrum and connects to the brain stem for movement control and coordination.

The surfaces of the cerebrum and the cerebellum are the cerebral and the cerebellar cortex, respectively, and consist of gray matter (GM). Beneath the cortex, mostly myelinated nerve fibers, typically tightly packed and aligned into axonal fiber fascicles, constitute the brain white matter (WM). Within the WM, deep gray matter nuclei are located that compose the basal ganglia. Moreover, for protection of the brain and spinal cord, the cerebrospinal fluid (CSF) circulates around them and through

the ventricles, little brain cavities. The folds (gyri) as well as the shallow and deep grooves (sulci and fissures, respectively) of the cortex are a result of the more rapid enlargement of the cortex during embryonic development compared to the white matter. Fissures and sulci separate different regions throughout the brain. The longitudinal fissure separates the cerebrum into the left and right hemisphere which are connected through the corpus callosum (CC), a broad white matter tract of tightly packed and highly aligned axonal bundles. Signal transmission along axons occurs for example between gyri in one hemisphere via association fibers or from gyri in one hemispheres to the corresponding gyri in the other hemisphere via commissural fibers such as the CC.

The four lobes of each of the cerebral hemispheres are distinguished by their function and named after the cranial bones covering them: frontal, parietal, temporal and occipital lobe (see Figure 2.5). In these lobes, motor (precentral gyrus) and speech areas, somatosensory areas (postcentral gyrus), auditory areas and visual areas are located, respectively.

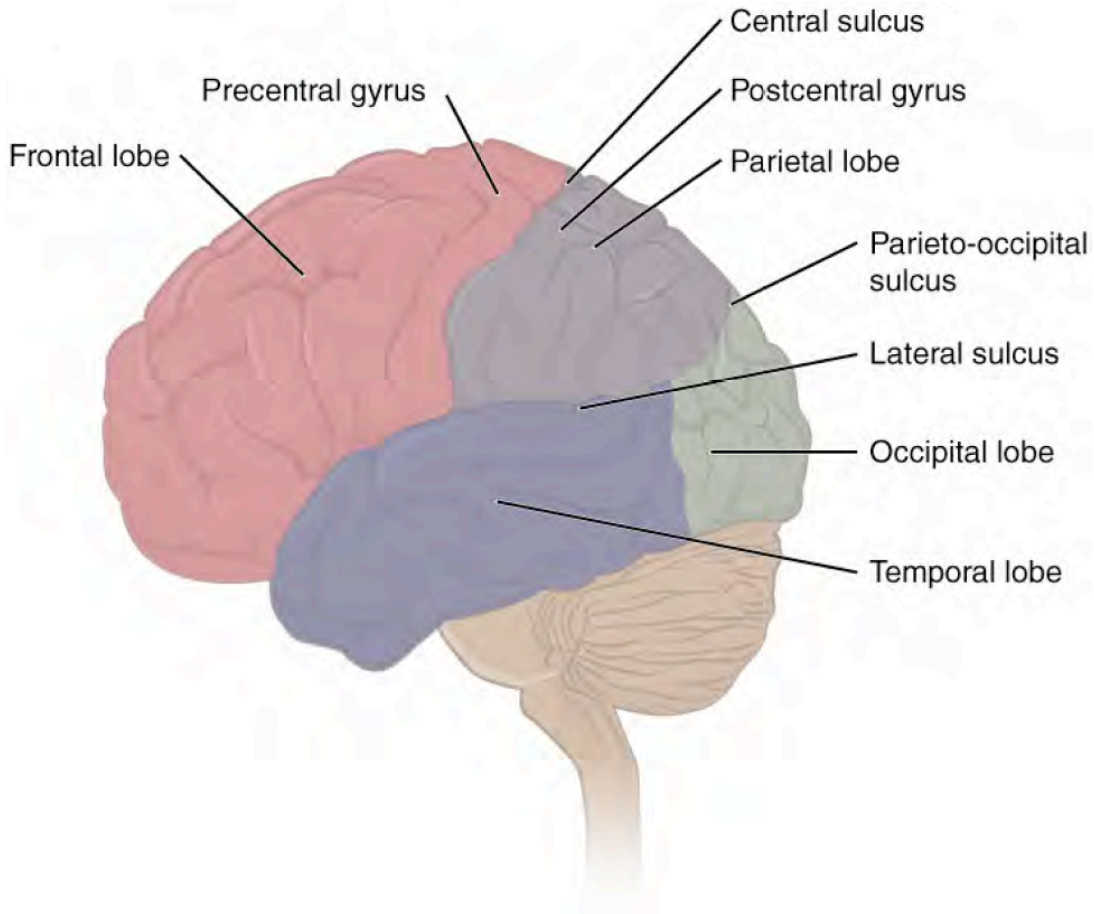

Figure 2.5: The cerebrum is divided into the frontal, parietal, temporal and occipital lobe each including regions responsible for distinct brain functions. (This illustration was downloaded for free at http://cnx.org/content/col11496/latest/)

The pathways connecting cortical areas can be determined by means of dMRI. Tractography aims to identify major fiber tracts traversing through the brain white matter. Figure 2.6 shows a collection

of projection and association white matter fiber tracts (Mori et al., 2008) reconstructed from dMRI acquisitions by means of probability fiber tracking (see section 2.6.3). Figure 5.9 in chapter 5 further visualizes the forceps major, a commissural fiber tract that connects the cortical regions in the occipital lobe of both hemispheres via the posterior part of the CC (splenium).

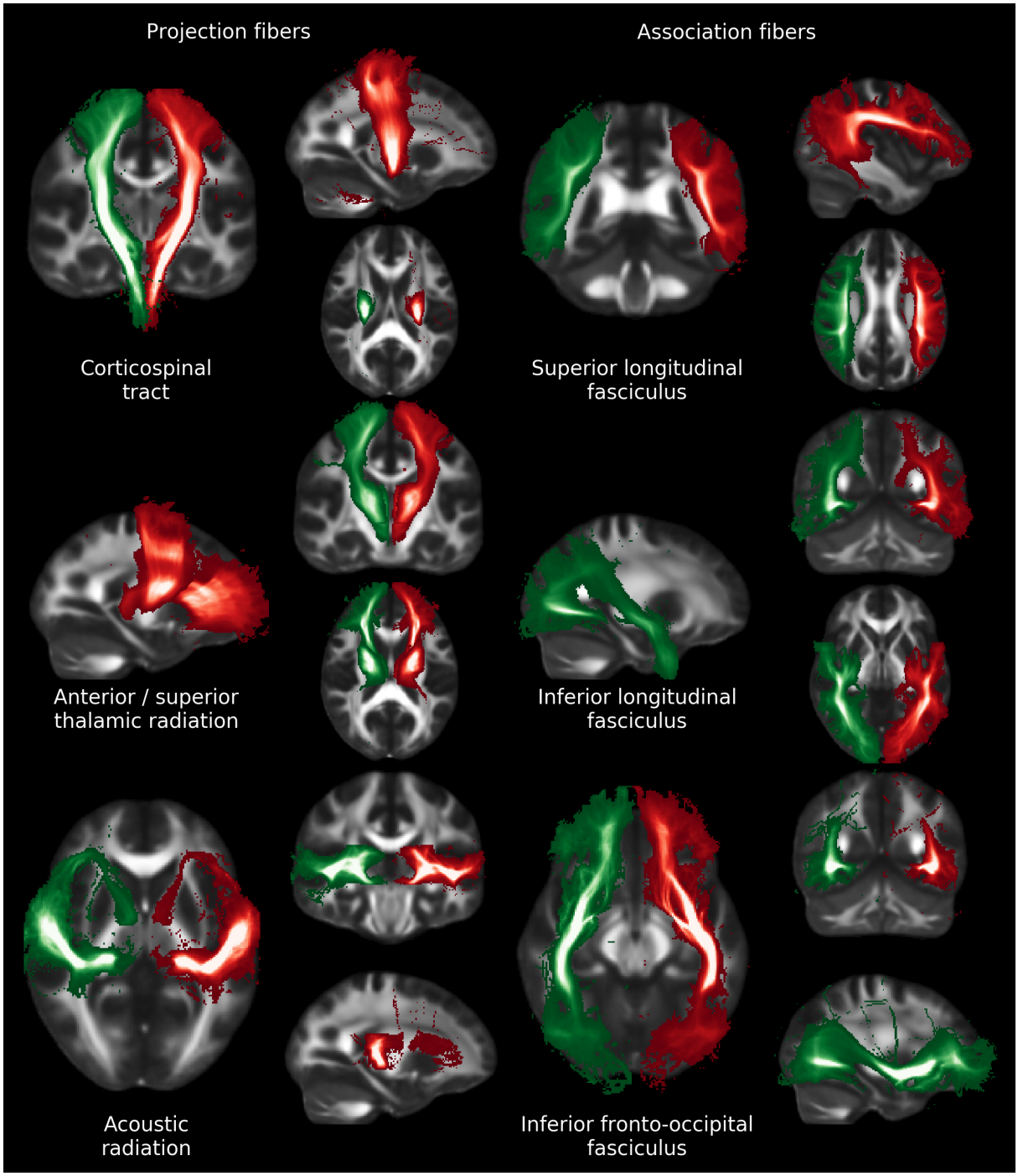

Figure 2.6: Coronal, sagittal and axial views of tractography of major fiber pathways in the brain. Projection and association fibers in the left and right hemispheres are visualized in red and green, respectively.

2.3 Molecular diffusion

Diffusion or the molecular transport process is described by Fick's first law (Fick, 1855) as the flux of molecules $\mathbf{J}$ in a volume due to a concentration gradient (see Figure 2.7 a)

$$\mathbf{J} = -D\nabla c(\mathbf{r}, t) \tag{2.1}$$

Here, $c(\mathbf{r}, t)$ is the local concentration of particles or molecules in a medium and D is an intrinsic feature of those particles, denoted the diffusion coefficient. To conserve the total number of particles, Fick's second law, the *diffusion equation*, associates the diffusion-related change of the particle concentration over time to the flux divergence

$$\frac{\partial c}{\partial t} = -\nabla \cdot \mathbf{J} = D\nabla^2 c \tag{2.2}$$

At the beginning of the 20th century, Einstein linked Fick's description of the diffusion process to observations made by Brown on the displacement of molecules over time due to random translational motion (Brown, 1866). In case of this so-called Brownian motion, "self-diffusion" of molecules is caused by random thermal collisions among the ensemble of molecules (see Figure 2.7 b), in the absence of a concentration gradient (Einstein, 1905). Einstein reformulated the expression for the molecular diffusion coefficient defined by Fick's laws based on a probabilistic description of the Brownian motion. $P(\mathbf{r}_0, t_0)$ is the probability of finding a particle at starting point $\mathbf{r}_0$ at time $t_0 = 0$ and defines the particle density $\rho(\mathbf{r}_0)$. $P(\mathbf{r}_0, \mathbf{r}_1, t)$ is the probability that a particle moves over a distance $\mathbf{R} = \mathbf{r}_1 - \mathbf{r}_0$ starting at $\mathbf{r}_0$ at time t_0. Integrating over $\mathbf{r}_0$ to account for all possible initial positions of diffusing particles, the total probability of finding a particle at location $\mathbf{r}_1$ at time t is given by

$$P(\mathbf{r}_1, t) = \int P(\mathbf{r}_0, t_0) P(\mathbf{r}_0, \mathbf{r}_1, t) d\mathbf{r}_0 \tag{2.3}$$

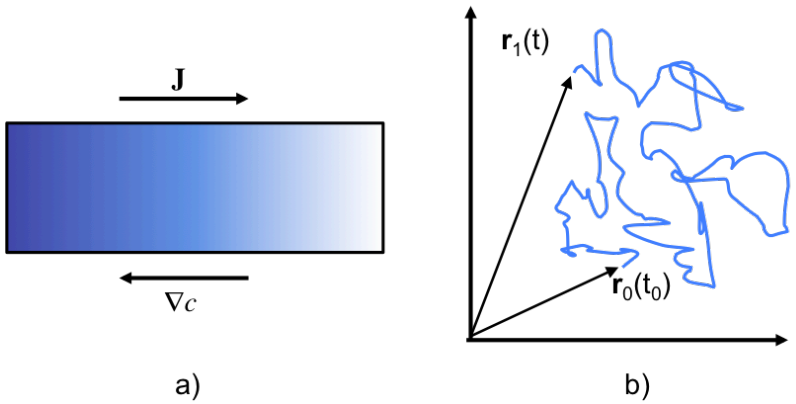

Figure 2.7: Molecular diffusion: a) Diffusion due to a concentration gradient. b) Random Brownian motion of water molecules.

Similar to a concentration function that refers to the density of particles, $P(\mathbf{r}_1, t)$ describes an ensemble-averaged probability concentration for a single particle and obeys Fick's diffusion equation (Callaghan, 1991). Considering the initial condition that all particles start at point $\mathbf{r}_0$ and time t_0 represented by the Dirac delta function, $\delta(\mathbf{R})$, and substituting $P(\mathbf{r}_0, \mathbf{r}_1, t)$ for $c(\mathbf{r}, t)$ in Eq. (2.2), the solution to the diffusion equation in the case of unrestricted self-diffusion is a Gaussian diffusion displacement probability distribution

$$P(\mathbf{r}_0, \mathbf{r}_1, t) = (4\pi Dt)^{-3/2} \exp\left(-\frac{(\mathbf{r}_1 - \mathbf{r}_0)^2}{4Dt}\right) \tag{2.4}$$

Free diffusion can be characterized by the mean-squared displacement (MSD) of molecules over the diffusion time t (Figure 2.8 a) and, for each spatial dimension, is given by

$$\left\langle (x_1 - x_0)^2 \right\rangle = 2Dt \tag{2.5}$$

Eq. (2.5) is commonly referred to as Einstein's diffusion equation and can be rewritten for the three dimensional case (Figure 2.8 b) in terms of the vectorial displacement as $\left\langle (\mathbf{r}_1 - \mathbf{r}_0)^2 \right\rangle = 6Dt$.

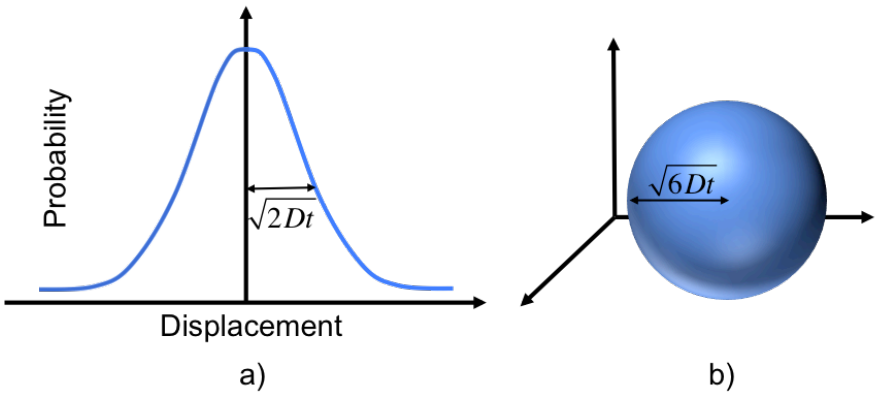

Figure 2.8: PDF for Gaussian (non-restricted) diffusion as a function of molecular displacement in one dimension (a) and in the three dimensional case (b). The diffusion coefficient relates to molecular MSD via the variance of the distribution function.

Since the displacement distribution represented by Eq. (2.4) does not depend on the starting position of a particle, but rather on the diffusion distance $\mathbf{R} = \mathbf{r}_1 - \mathbf{r}_0$, Eq. (2.3) can also be expressed in terms of the molecular displacement $\mathbf{R}$. This is most useful because the PGSE experiment (see section 2.5.1) performed in dMRI specifically measures this net displacement of water molecules in tissue microstructure. The resulting distribution $\bar{P}(\mathbf{R}, t)$ defines the average probability for any particle to move by $\mathbf{R}$ over time t. The solution to the diffusion equation is known as Green's function and often denoted the ensemble average propagator (EAP) (Callaghan, 1991; Kärger and Heink, 1983)

$$\bar{P}(\mathbf{R}, t) = \int P(\mathbf{r}_0) P(\mathbf{r}_0, \mathbf{r}_0 + \mathbf{R}, t) d\mathbf{r}_0 \tag{2.6}$$

Likewise, Eq. (2.4) for the specific case of free self-diffusion can be expressed in terms of the molecular displacement $\mathbf{R}$. In this case, all particles have a common EAP, thus the bar above can be omitted. To account for restricted, anisotropic diffusion of water molecules in biological tissue, the diffusion equation (Eq. (2.2)) takes the form

$$\frac{\partial c}{\partial t} = \nabla \mathbf{D} \nabla c \tag{2.7}$$

where $\mathbf{D}$ is the apparent diffusion tensor (Jost, 1960), a second-order tensor defined by

$$D_{ij} = \frac{\langle R_i R_j \rangle}{2t} \tag{2.8}$$

where R_i is a component of the displacement $\mathbf{R}$. The solution to Eq. (2.7) is the PDF describing anisotropy diffusion in complex tissue microstructure and will be presented in the next section.

2.4 Diffusion in biological tissue

In biological tissue, impermeable objects constitute physical barriers that restrict the diffusion of water molecules. In neuronal tissue, restrictions imposed by microstructures such as neuroglial cells, dendritic trees in gray matter or the nerve fiber fascicles constituting the brain white matter affect the water displacement and the corresponding probability distribution is no longer Gaussian. In contrast to free diffusion in pure liquids as discussed in the previous section, diffusion in complex media such as the brain tissue is denoted as restricted or hindered diffusion (Figure 2.9).

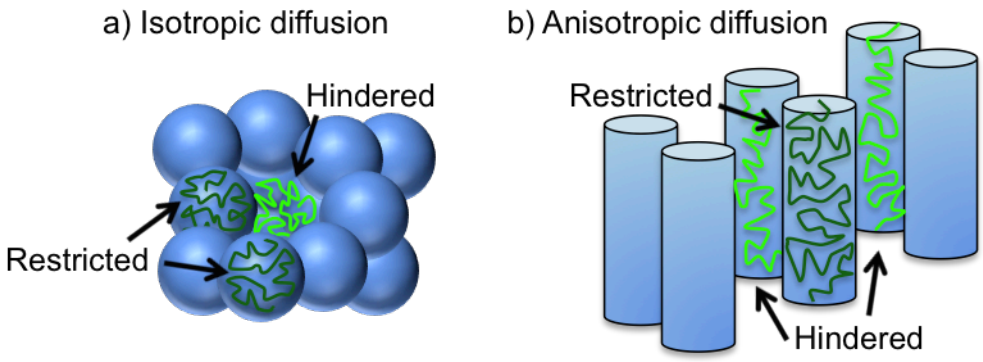

Figure 2.9: Schematic of diffusion in biological tissue: a) isotropic, restricted and hindered diffusion in glia cells depicted as spheres, b) anisotropic, restricted and hindered diffusion in axonal fiber fascicles depicted as idealized cylinders.

In the presence of microstructural obstacles, a directional dependency of water diffusion can, further, be observed with dMRI, which was first reported at the end of the 1980s and then investigated in animal and human MRI studies (Chenevert et al., 1990; Le Bihan et al., 1986; Moseley et al., 1991).

This phenomenon of diffusion anisotropy depends on the organization of the microstructure. In ordered microstructural environments such as the white matter's highly aligned axonal fascicles, the average water displacement is greater along than perpendicular to the fascicles. In this case the diffusive transport is described as anisotropic (Figure 2.9 b). If molecules encounter cells or randomly structured barriers such as the dendritic trees in gray matter, diffusion is characterized as isotropic (Figure 2.9 a). Thus, if enough time is allowed for the water molecules to diffuse and to encounter physical barriers, the molecular displacement can probe the underlying microstructure and properties of the diffusion transport can be extracted from the diffusion propagator.

Figure 2.10 schematically depicts water displacement as a function of the square root of the diffusion time. Consistent with Eq. (2.5) for free, isotropic diffusion, the diffusion coefficient is the slope of this function. In case of restricted, isotropic diffusion, the diffusion coefficient is termed the apparent diffusion coefficient (ADC) representing the reduced displacement of molecules due to microstructural obstacles.

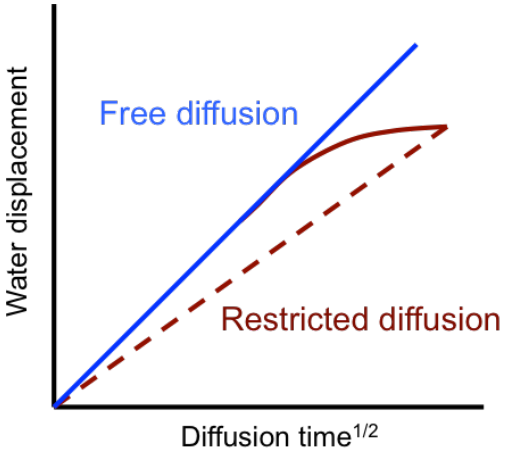

Figure 2.10: Water displacement as a function of the square root of the diffusion time. The ADC (dashed) describes the molecular displacement in the case of restricted, isotropic diffusion in complex environments (red) in comparison to free isotropic diffusion (blue).

For restricted, anisotropic diffusion the scalar ADC is insufficient to describe the directional dependency of the water displacement. In that case, the apparent diffusion tensor $\mathbf{D}$ is preferred over the ADC to model the three-dimensional hindered diffusion transport and Eq. (2.4) is rewritten as (P Basser et al., 1994a)

$$P(\mathbf{R}, t) = (4\pi t)^{-3/2} \left|\mathbf{D}\right|^{-1/2} \exp\left(-\frac{(\mathbf{R}^T \mathbf{D}^{-1} \mathbf{R})}{4t}\right) \tag{2.9}$$

where $|\mathbf{D}|$ is the determinant of the diffusion tensor.

However, Eq. (2.9) only characterizes the Gaussian (non-restricted) contribution of molecular diffusion and the tensor approach comes with further inherent limitations such as not being able to depict water displacement within microstructural environments of crossing fiber fascicles, which will

be discussed in detail in section 2.6.3.
To fully capture the diffusion process, a comprehensive description of the diffusion propagator is required. The shape of the diffusion propagator reflects the displacement of water molecules, even within complex microstructural environments. Figure 2.11 illustrates distinct displacement patterns in the case of a) isotropic diffusion transport in spherical cells or dispersed structures such as dendritic trees and of b) anisotropic spreading of water molecules in highly ordered single or crossing fiber configurations.

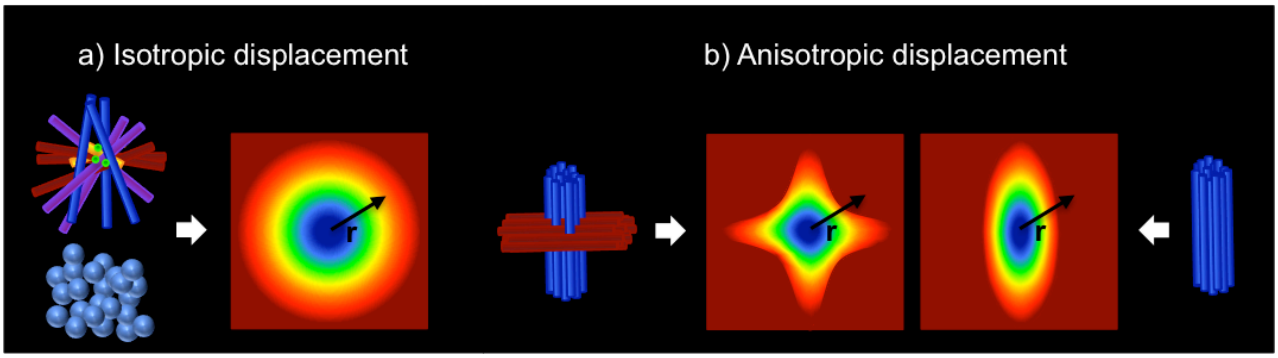

Figure 2.11: The diffusion propagator captures the distinct profiles of molecular displacement due to isotropic (a) and anisotropic (b) diffusion in biological tissue.

2.5 Diffusion MRI acquisition and preprocessing

An introduction to the basic principles of nuclear magnetic resonance (NMR) and magnetic resonance imaging (MRI) is fundamental in order to discuss dMRI. (See Brown et al. (2014), Kuperman (2000) and Callaghan (1991) for a comprehensive description of NMR and MRI theory.) Therefore, the following sections explain the excitation and relaxation of spins of hydrogen nuclei within the imaging object exposed to magnetic fields and their spatial encoding to allow MR image formation. Furthermore, different types of imaging artifacts related to dMRI acquisition are discussed as well as strategies that prevent artifacts by eliminating their source, correct for artifacts after data collection or reduce their influence on image quality.

2.5.1 Diffusion NMR

Atomic nuclei possess the intrinsic property of spin that is associated to a magnetic moment μ if the spin quantum number is odd-numberd (e.g. 1/2 in the case of hydrogen). For the investigation of brain structure and function, the hydrogen nucleus is of great interest because of its natural abundance in the human body. NMR describes the phenomenon that in the presence of a static external magnetic field $\mathbf{B}_0$, the spins precess around $\mathbf{B}_0$ at the Larmor frequency $\omega_0 = \gamma B_0$. B_0 is the magnitude of $\mathbf{B}_0$ and γ is the gyromagnetic ratio with a value of $2\pi \cdot 42.576$ MHz/T for the hydrogen nucleus in water. Although only a small excess of spins is aligned parallel to $\mathbf{B}_0$, the ensemble

average of all magnetic moments $< \mu >$ produces a measurable nuclear net magnetization $\mathbf{M}(\mathbf{R}, t)$ that is proportional to $\mathbf{B}_0$. If $\mathbf{B}_0$ is considered to be applied along the z-direction, then the equilibrium magnetization $M_0 = M_z$ and $M_x = M_y = 0$.

Exciting an ensemble of spins by a 90° radio-frequency (RF) pulse that oscillates at $\omega = \omega_0$ in the x-y-plane, rotates $\mathbf{M}$ perpendicular to $\mathbf{B}_0$ and induces a transverse magnetization. The NMR signal induced in a nearby receive coil is called free induction decay (FID), and its evolution over time is schematically depicted in Figure 2.12. After excitation, the spins aim to realign with the main field $\mathbf{B}_0$ through interactions with their surrounding environment. Thereby, the longitudinal magnetization M_z is recovered over a time defined by the T1 or spin-lattice relaxation time. Simultaneously, the T2 relaxation time, or spin-spin relaxation, characterizes the decay of the FID signal due to interactions among spins resulting in spin dephasing.

The Bloch equation (Bloch, 1946) captures the fundamental dynamics of NMR due to precession, excitation and relaxation

$$\frac{\partial \mathbf{M}}{\partial t} = \mathbf{M} \times \gamma \mathbf{B} - \begin{pmatrix} T_2^{-1} & 0 & 0 \\ 0 & T_2^{-1} & 0 \\ 0 & 0 & T_1^{-1} \end{pmatrix} \mathbf{M} + \mathbf{M}_0 \begin{pmatrix} 0 \\ 0 \\ T_1^{-1} \end{pmatrix} \tag{2.10}$$

where $\mathbf{M} = (M_x, M_y, M_z)$ is the net nuclear magnetization vector and T_1 and T_2 are the longitudinal and transverse relaxation times,respectively. Assuming excitation by means of a 90° RF pulse at $t = 0$, the solutions to the Bloch equation explain the T1 recovery of the initial longitudinal magnetization $M_z(0) = 0$ back to equilibrium state M_0 by

$$M_z(t) = M_0(1 - e^{-t/T1}) \tag{2.11}$$

and the T2 decay of the transverse magnetization $M_\perp(0) = M_0$ to zero by

$$M_\perp(t) = M_0 e^{-t/T2} \tag{2.12}$$

After complete relaxation of the longitudinal and transverse components, the nuclear net magnetization has returned to its equilibrium state. Successive RF excitations of hydrogen nuclei yield identical NMR signals that can be manipulated by magnetic field gradients and then measured by an MR receive coil to form MR images of the brain. The process of MR image formation will be described in the following section 2.5.2.

Apart from spin-spin interactions, additional dephasing arises in the presence of magnetic field inhomogeneities and leads to an even faster decay of the FID signal. In this case, the T2* relaxation time needs to be considered instead of T2. Exposing the spins to a 180° refocusing RF pulse a time τ after the 90° RF pulse, reverts the phase accrual of spins due to magnetic field inhomogeneities and results in a spin-echo formed at the echo time TE $= 2\tau$ (see Figure 2.12). In case of the spin

echo, signal attenuation is characterized by pure T2 relaxation.

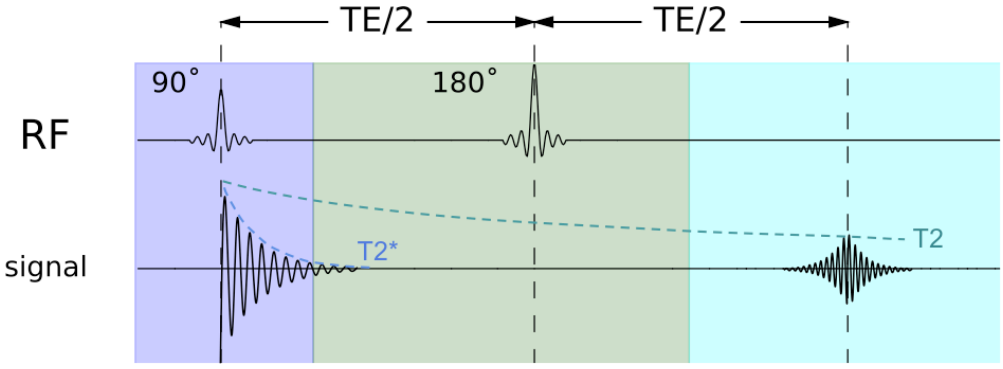

Figure 2.12: Spin-echo experiment: In the presence of magnetic field inhomogeneities, the FID signal, induced by means of a 90° RF pulse, decays rapidly according to the $T2^*$ relaxation time. A 180° refocusing pulse reverts spin dephasing due to field inhomogeneities. Following pure T2 decay, a spin echo is formed at the echo time TE.

This spin-echo experiment introduced by Hahn (1950) depends on stationary spins for an accurate refocusing. Due to the random nature of the translational Brownian motion of water molecules, however, the phase gained by individual spins is randomly distributed and not equal before and after the refocusing pulse. Thus, the net phase difference at the echo time leads to a reduced spin-echo signal. In the case of diffusing water molecules, signal attenuation is, therefore, stronger compared to the T2 decay depicted in Figure 2.12. Hahn (1950) noticed that this sensitivity on molecular diffusion could be exploited to measure the diffusion coefficient. Adding steady magnetic field gradients to the NMR spin-echo experiment, Carr and Purcell (1954) proposed a method to measure molecular diffusion. Applying the magnetic field gradient $\mathbf{G}$ parallel to $\mathbf{B}_0$ generates the total magnetic field $\mathbf{B}(\mathbf{r}) = (0, 0, \mathbf{B}_0 + \mathbf{G} \cdot \mathbf{r})^T$ and encodes the phase accrual of spins as a function of their position $\mathbf{r}$. To account for molecular diffusion, the Bloch-Torrey equation (Torrey, 1956) extends the Bloch equation by an additional diffusion term $D\nabla^2\mathbf{M}$. For the measurement of motion, we consider the complex transverse magnetization $M_+(\mathbf{R}, t) = M_x(\mathbf{R}, t) + iM_y(\mathbf{R}, t)$. Additionally accounting for time-varying field gradients $\mathbf{G}(t)$, the Bloch-Torrey equation yields

$$\frac{\partial M_+}{\partial t} = -i\omega_0 M_+ - \frac{M_+}{T_2} - i\gamma(\mathbf{G}(t) \cdot \mathbf{r})M_+ + D\nabla^2 M_+ \tag{2.13}$$

To solve the Bloch-Torrey equation, Stejskal and Tanner (1965) proposed to neglect the effects of precession and T2 relaxation by substituting the complex transverse magnetization by $M_+(\mathbf{R}, t) = \Phi(\mathbf{R}, t) \exp(-(i\omega_0 + 1/T_2)t)$. More importantly, Stejskal and Tanner (1965) adapted the spin-echo experiment by applying short duration pulsed field gradients $\mathbf{G}$ of amplitude g around the 180° refocusing pulse. This is known as the pulsed gradient spin echo (PGSE) experiment which is at the heart of today's diffusion MRI. The pulsed field gradients are switched on for a duration of δ and are separated by a time Δ (see Figure 2.13). With the application of such rectangular gradient pulses that are no longer a function of time, the solution to the Bloch-Torrey equation (2.13) that represents the spin-echo attenuation due to isotropic diffusion simplifies to

$$\frac{S(g)}{S_0} = \exp(-D(\gamma\delta g)^2(\Delta - \delta/3)) \tag{2.14}$$

where $S(g)$ is the spin echo amplitude at the echo time (TE) attenuated due to molecular diffusion and S_0 the signal amplitude at the same echo time without application of pulsed field gradients. The diffusion weighting due to the application of diffusion gradients is defined as the b-value

$$b = (\gamma\delta g)^2(\Delta - \delta/3) \tag{2.15}$$

For anisotropic diffusion, the spin-echo attenuation is rewritten in terms of the apparent diffusion tensor $\mathbf{D}$ (see section 2.6.1.1). Thus, the echo signal measured in direction $\mathbf{g}$ of $\mathbf{G}$ can be expressed as the monoexponential attenuation of the non-diffusion weighted signal S_0 by (P Basser et al., 1994a)

$$S(b, \mathbf{g}) = S_0 \exp(-b\mathbf{g}^T\mathbf{D}\mathbf{g}) \tag{2.16}$$

Under the assumption that the pulse duration of $\mathbf{G}$ is very short, i.e. $\Delta \gg \delta$, so that diffusion during this time can be neglected, the phase shift of a spin at position $\mathbf{r}$ gained due to the first gradient pulse is $\gamma\delta\mathbf{G}\cdot\mathbf{r}$ leading to a net phase difference of $\phi = \gamma\delta\mathbf{G}\cdot(\mathbf{r}' - \mathbf{r}) = \gamma\delta\mathbf{G}\cdot\mathbf{R}$ after the second diffusion gradient (Callaghan, 1991; Callaghan et al., 1988). In this context, the so-called q-space is introduced, with the gradient wave vector

$$\mathbf{q} = \frac{1}{2\pi}\gamma\delta\mathbf{G} \tag{2.17}$$

The q-value $q = \frac{1}{2\pi}\gamma\delta g$ is proportional to the square root of the diffusion weighting $\sqrt{b}$. Normalizing the signal by the echo amplitude when $\mathbf{G} = 0$ and weighting the phase term $\exp(i\phi)$ of each spin by the spin's probability of making a displacement $\mathbf{R}$ during the time Δ (see Eq. (2.6)), the normalized echo signal is given by (Callaghan, 1991)

$$\frac{S(\mathbf{q})}{S_0} = E(\mathbf{q}, \Delta) = \int \bar{P}(\mathbf{R}, \Delta)\exp(i2\pi\mathbf{q}\cdot\mathbf{R})d\mathbf{R} \tag{2.18}$$

A simple Fourier relationship exists between the normalized MR signal $|E(\mathbf{q}, \Delta)|$ and the diffusion propagator

$$\bar{P}(\mathbf{R}, \Delta) = \int |E(\mathbf{q}, \Delta)|\exp(-i2\pi\mathbf{q}\cdot\mathbf{R})d\mathbf{q} = \mathcal{F}(E(\mathbf{q}, \Delta)) \tag{2.19}$$

Although $\Delta \gg \delta$, also referred to as the narrow gradient pulse approximation, is not realizable in real MR experiments, this assumption enables a general description of water displacement by means of the ensemble average diffusion propagator. Section 2.6.1.3 will discuss an MR imaging technique,

diffusion spectrum imaging, that successfully applies this approach even if the gradient duration δ is not negligible and that was, nevertheless, found to constitute a powerful tool to unravel fine structural details of complex microenvironments.

2.5.2 Diffusion weighted MR imaging

The discovery of generating images through spatial encoding of a spin ensemble in a magnetic field (Lauterbur, 1973) lay the foundation of MRI. With the combination of MRI with the principles of diffusion NMR discussed in the previous section, whole brain *in vivo* imaging of water diffusion, i.e. diffusion MRI, was made possible. The invention of dMRI gave and continues to give rise to numerous developments in the area of diffusion MR image acquisition and the reconstruction of water diffusion-related properties of tissue microstructure from the measured diffusion signal.

The development of echo planar imaging (EPI) made rapid whole brain MR image formation possible (Mansfield, 1977; Turner et al., 1990). Even today, EPI is still the most popular acquisition technique for conducting a dMRI experiment. Figure 2.13 depicts the sequence diagram for a PGSE EPI experiment. MR image formation requires the application of imaging gradients for spatial encoding in addition to the main magnetic field and the diffusion gradients. Just as diffusion gradients, imaging gradients are pulsed field gradients that approximately produce a linear field change along one of three orthogonal directions, x, y, z, or, by superposition, along any direction. The linear phase accrual of stationary spins in the presence of imaging gradients ($\phi(\mathbf{G}(t), \mathbf{r}) \propto \mathbf{r}\dot{\int}\mathbf{G}(t)dt$) is conveniently described in k-space, where $\mathbf{k} \propto \int \mathbf{G}(t)dt$. Using an EPI sequence as depicted in Figure 2.13, a single 2D image slice is acquired over a time t = TR, the repetition time.

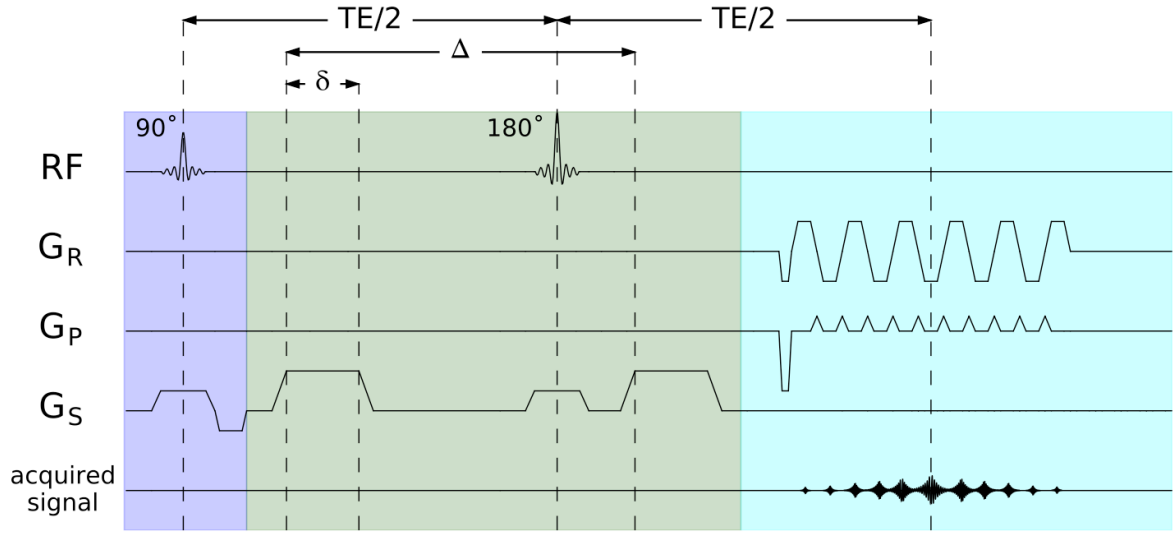

Figure 2.13: Simplified sequence diagram for single shot PGSE EPI.

Multiple slices are collected successively to form a 3D imaging volume of an object in the MR scanner. The signal acquisition of an image slice in a single shot can be schematically depicted in a k-space

diagram. The application of slice selection gradients (G_S) simultaneously with the RF pulses enables the excitation of spins within a thin slice of the imaging object. After this spatially selective excitation, a train of echo signals is acquired. So called readout (G_R) and phase encoding (G_P) gradients are inverted and incremented, respectively, to generate a zig-zag path through k-space with an echo signal formed at each readout. The corresponding sampling trajectory in k-space is depicted in Figure 2.14. In this way, the readout gradients cause a linear variation of the resonance frequency of spins, $\Delta\omega = \gamma x G_x(t)$, which separates them according to their position x, while the phase encoding gradients induce phase accrual across the spins to distinguish them along a second spatial direction.

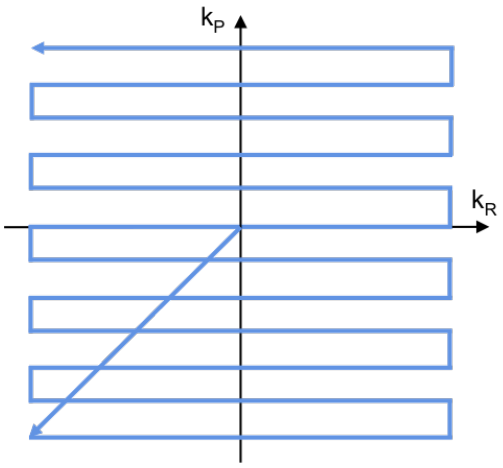

Figure 2.14: Sampling trajectory in k-space along readout and phase encoding direction for data collection using PGSE EPI.

Receiver coils in the MR scanner pick up the real and imaginary components of the complex MR signal in k-space. Those signals are digitized with the use of an analog-digital converter. Gradient encoding relates the image to the k-space via the Fourier transform. The final MR image is thus obtained by means of MR image reconstruction that performs a fast Fourier transform of the measured k-space data. Most commonly, magnitude images of the complex MR data are used for clinical diagnosis. Phase images are rarely used, for example to measure the magnetic susceptibility of tissue (Haacke et al., 2004; Shmueli et al., 2009) and thus, to establish novel MRI biomarkers (Acosta-Cabronero et al., 2013). In k-space, larger values of k represent the large spatial frequencies in an images, i.e. edges in image space, whereas low values at the center of k-space relate to low frequencies that define the overall contrast in image space. The spatial image resolution Δr per dimension $i = x, y, z$ defines the physical size of the imaged object captured by a pixel or voxel (volume elememt). The related field of view (FOV $_i$) comprising N_i voxels is given by $FOV_i = N_i \Delta r_i$. Δr_i is dictated by the sampling window $N_i \Delta k_i$ in k-space, i.e. $\Delta r_i = \frac{1}{N_i \Delta k_i}$. For an accurate image formation without aliasing, the k-space sampling rate Δk_i is defined according to the Nyquist-Shannon theorem (Shannon, 1949) as $\Delta k_i = \frac{1}{FOV_i}$. Selecting $\Delta k_i > \frac{1}{FOV_i}$ corresponds to an undersampling in k-space, which effectively reduces the FOV and leads to a fold-in of the object to incorrect locations in the image once the FOV is smaller than the object. However, the reduction in scan time due to an undersampling in k-space motivated the development of novel strategies for sparse MRI acquisition and reconstruction. By analogy with k-space, q-space (see section 2.5.3) undersampling enables

accelerated diffusion encoding. Such an approach for fast dMRI acquisition that purposefully violates the Nyquist criterion is discussed in chapter 3 and lies at the heart of the contributions of this thesis presented in chapters 4 and 5.

As discussed in the previous section, diffusion gradients are applied in direction $\mathbf{g}$ (for example in direction of G_S in Figure 2.13) and for duration δ before and after the 180° refocusing pulse to sensitize MRI for molecular diffusion. At a separation time Δ after the first diffusion gradient, the second gradient cancels out spin dephasing caused by the first one. Perfect rephasing is achieved for stationary spins. For diffusing molecules, the resulting signal attenuation depends on the molecular displacement along the direction of the applied diffusion gradient (see section 2.5.1). Imaging volumes acquired with a b-value of $b > 0$ are called diffusion weighted images (DWIs). The image intensity of a DWI represents, per voxel, the measured echo signal at the echo time TE including diffusion-related signal attenuation (see section 2.5.1) at that particular location. MR images acquired with and without diffusion weighting are shown in Figure 2.15 in comparison to T1 and T2 weighted imaging.

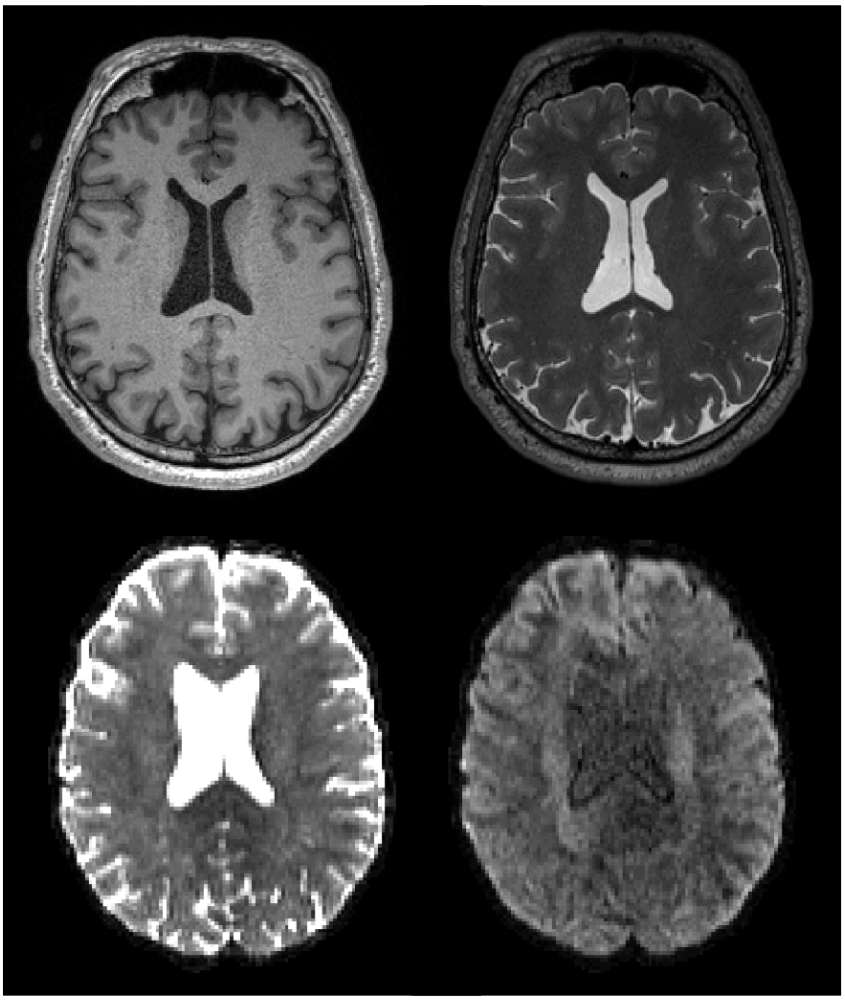

Figure 2.15: Top: T1 weighted (left) and T2 weighted (right) image. Bottom: Non-diffusion weighted (left) PGSE EPI image with $b = 0$ s/mm^2 and diffusion weighted PGSE EPI image (right) with $b = 1000$ s/mm^2.

By acquiring one image with diffusion-weighting and one without, the apparent diffusion coefficient can be calculated from Eq. (2.14). In dMRI of the highly anisotropic microstructure of the human brain, the echo signal is a function of the diffusion encoding gradient strength and direction (see Eq. (2.16) and Eq. (2.18)). Typically, a set of DWIs is acquired with different diffusion weighting gradient directions. The set of DWIs reflects the directional dependency of diffusion (see Figure 2.11). The calculated ADC can be different for each DWI depending on the underlying microstructure. Increasing the number of acquired DWIs by encoding the water diffusion along different gradient directions, therefore, allows us to better capture the anisotropic diffusion process in a three-dimensional imaging object. To reveal intrinsic features of water displacement in complex microenvironments from the measured DWIs, more advanced dMRI reconstruction techniques to determine e.g. the diffusion tensor or the propagator are preferred over the ADC calculation. Some of the most popular dMRI reconstruction approaches will be described in section 2.6.

2.5.3 Q-space sampling

A sample in q-space at location $\mathbf{q}$, given by the gradient wave vector as defined in Eq. (2.17), represents a single dMRI acquisition. In a dMRI experiment, the q-space sampling scheme, thus, refers to the set of dMRI scans each collected with a distinct diffusion weighting gradient direction and amplitude. As depicted in Figure 2.16, the center in q-space corresponds to an acquisition without diffusion weighting, whereas any other q-space sample represents a DWI.

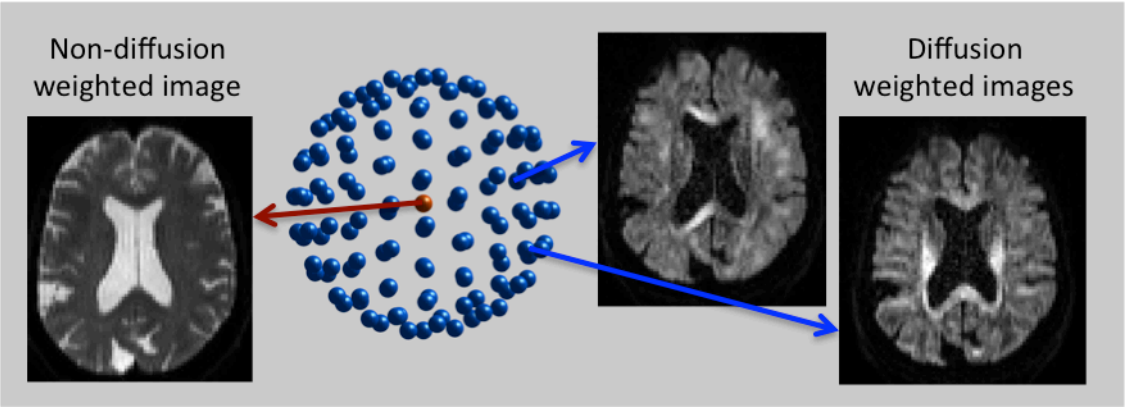

Figure 2.16: In dMRI, the set of imaging volumes acquired with and without diffusion weighting is described by the sampling in q-space. The q-space center represents non-diffusion weighted measurements. The distribution of the remaining q-space samples reflects distinct diffusion gradient directions and diffusion weightings.

The decision on the q-space sampling distribution as well as the number of imaging volumes to be acquired is normally made based on the requirements of the intended post processing technique to reconstruct microstructural information from the diffusion measurements. Due to the antipodal symmetry of the diffusion signal, sampling along the diffusion gradients $\mathbf{g}$ and $-\mathbf{g}$ is considered equal. This means, first, a set of q-space samples on one hemisphere is sufficient, and second, reversing the sign of every other sample is possible without altering the q-space encoding. In practice,

however, such a distribution of unique q-space samples on the whole sphere is recommended as it allows for efficient correction of eddy current induced distortions (Andersson and Sotiropoulos, 2015) (see section 2.5.4).

Different types of q-space sampling schemes exist: Cartesian grid schemes (Figure 2.17 a) as well as single (Figure 2.17 c) and multi-shell (Figure 2.17 b) schemes with samples on one or more shells in q-space, respectively. In analogy to k-space sampling (see section 2.5.2), the radial resolution of the diffusion propagator depends on the diffusion weighting strength. Acquiring DWIs with multiple different b-values increases the radial resolution of the imaging scheme. During a dMRI experiment, the diffusion gradient duration δ and separation Δ are fixed, but the gradient amplitude can be changed to vary the b-value (see Eq. (2.15)). Single shell schemes consider only 2 b-values: $b = 0$ for the non-diffusion weighted volumes and one specific b-value with $b > 0$ for which all samples are distributed on one spherical shell along the radial direction of q-space. Thus, single shell schemes provide a very limited radial resolution. By varying the diffusion gradient amplitude during the dMRI acquisition, more than one b-value greater than 0 can be applied. Thus, a higher radial resolution than offered by single shell schemes can be achieved by the use of multi-shell or Cartesian grid schemes that sample further out in q-space.

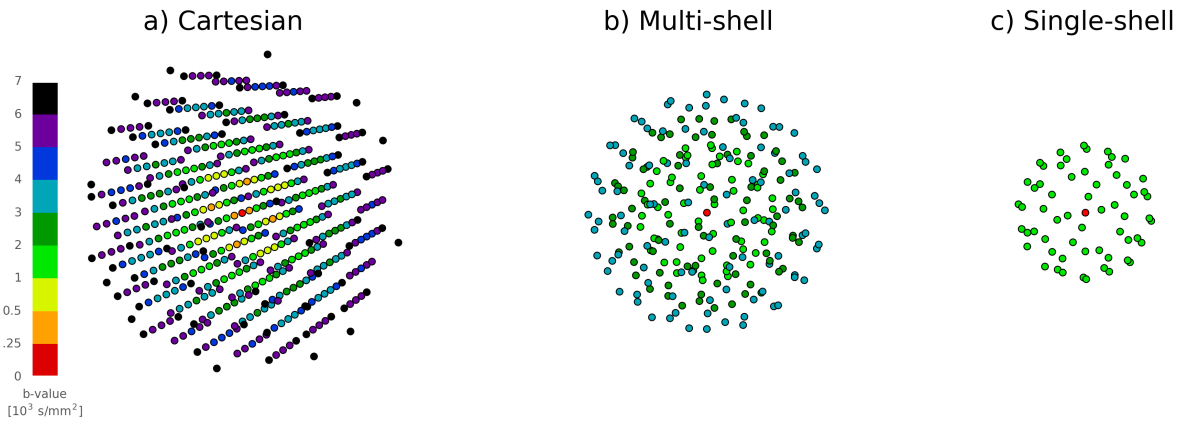

Figure 2.17: Types of q-space sampling schemes displayed in q-space: Cartesian grid scheme (a), multi-shell scheme with three shells (b) and single shell sampling scheme (c).

The angular resolution of an imaging scheme depends on the angular distribution of samples over the sphere, i.e. the different spatial directions in the three-dimensional q-space. Jones et al. (1999), Caruyer et al. (2013) and Knutsson and Westin (2013) proposed methods to optimize the generation of single and multi-shell schemes, respectively, for a uniform angular q-space coverage that is most advantageous for estimating the preferential directions of diffusion anisotropy. For an optimal coverage of the three-dimensional q-space that would allow to determine the diffusion propagator from dMRI measurements, samples should be distributed sufficiently in both the angular and the radial direction in q-space. Cartesian schemes, for example, have been specifically introduced for this purpose (Wedeen et al., 2005), since dMRI scans acquired with such sampling schemes can

be linked to the diffusion propagator by their Fourier relationship described in Eq. (2.19) in section 2.5.1. In general, dMRI with both high angular and radial resolution in q-space provides high quality data suitable for diverse dMRI analysis. As a consequence, however, increasing the number of q-space samples, i.e. the number of dMRI scans, directly results in an increase of acquisition time. Furthermore, increasing the maximum diffusion weighting strength in practice has the downside of a reduced MR signal in both weighted and non-weighted images.

2.5.4 Artifacts in dMRI

In dMRI, hardware and acquisition-related as well as subject-related artifacts degrade image quality and confound subsequent data analysis for the extraction of diffusion and microstructure measures. Visual assessment of individual images can identify corrupted dMRI data collected within the scope of a small study, but is not feasible at a large scale for example in population studies. Especially in these settings, there is a high demand for artifact prevention or automatic detection and correction methods. Therefore, methods to eliminate the source of artifacts during acquisition and processing techniques to reduce or ideally correct for image artifacts retrospectively have been proposed. The latter are commonly applied after data collection and prior to the combination of all volumes to extract diffusion and microstructural features per imaging voxel. In the following, we focus on different types of artifacts, their sources and the corresponding state-of-the-art correction methods that are common to dMRI and EPI-based data collection and relevant within the scope of this thesis.

Image artifacts that are specifically pronounced due to the application of the EPI sequence are geometric distortions and signal loss. These are typically a result of magnetic field inhomogeneities stemming from eddy currents (time-varying) and from changes of magnetic susceptibility at the intersection between tissue and air or bones in the head (static). Eddy currents arise in conducting components of the MR system due to the rapid on and off switching of the diffusion gradients. They are more prominent in dMRI because diffusion gradient are applied longer and at higher amplitude than the imaging gradients. The associated magnetic fields, so-called off-resonance fields, lead to additional spatial encoding not accounted for in image reconstruction and thus produce geometric distortions in the image. Despite advances in MR hardware and acquisition to reduce eddy currents by means of active shielding (Turner, 1993) and improved dMRI (Reese et al., 2003), additional preprocessing is usually required to correct images for the remaining geometric distortions. Specifically, eddy current induced distortions are present for diffusion weighted images and more pronounced at higher b-values. One sophisticated state-of-the-art method (Andersson and Sotiropoulos, 2016) that is fine-tuned for dMRI and widely used in large cohort studies (Glasser et al., 2016; Miller et al., 2016; Tobisch et al., 2018) performs registration-based image correction that incorporates predictions of undistorted diffusion data based on the Gaussian process model (Andersson and Sotiropoulos, 2015) to accurately estimate the eddy current fields. Simultaneously, this approach corrects for motion and static susceptibility induced distortions. The latter are caused by small local changes of $\mathbf{B}_0$ induced by tissue magnetic susceptibility differences. Despite so-called $\mathbf{B}_0$ shimming (active homogenization) such distortions cannot be prevented. Fortunately, susceptibility induced off resonance fields can be estimated and used to correct for the associated distortions if MR data

is acquired twice, once with reversed phase encoding polarity (Andersson et al., 2003). In dMRI, the scan time is, thus, typically prolonged only by the acquisition of a few additional $b = 0$ scans with reversed phase encoding, which is acceptable for most imaging experiments. Figure 2.18 shows susceptibility induced geometric distortions for anterior-posterior (AP) and posterior-anterior (PA) phase encoding as well as the correction using an implementation of the method by Andersson et al. (2003) called *topup*. Other EPI-related imaging artifacts are the Nyquist ghosting due to the misalignment of echo signals and fat shifting both of which can fortunately be corrected substantially at the acquisition stage (Wu and Miller, 2017).

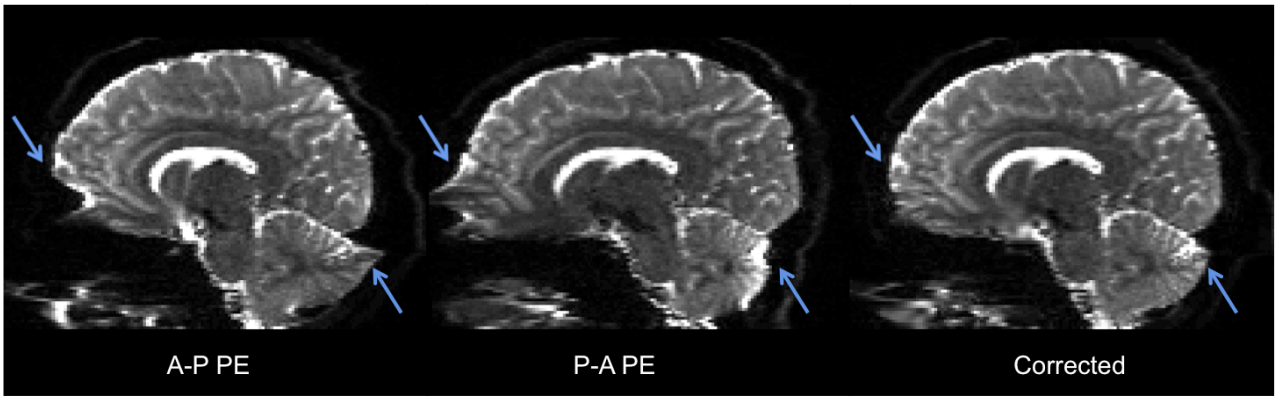

Figure 2.18: Susceptibility induced geometric distortions in dMRI data collected with AP (left) and PA (middle) phase encoding. The distortion artifact as well as related signal pile-up can be corrected by means of *topup* (right).

Another source of image artifacts is subject motion. There are different types of motion that can occur during image acquisition: (1) fast motion during the collection of image slices (between / across slices), (2) slow movements during the acquisition of dMRI volumes (between / across volumes) and (3) physiological motion e.g. due to respiration or cardiac movement. To avoid motion artifacts, fast imaging sequences are required to reduce the scan time and thereby the amount of motion. Single shot EPI is most commonly applied in dMRI. It allows for rapid spatial encoding of the complete k-space in one shot (see section 2.5.2). After MR reconstruction, only the magnitude images are of interest for subsequent dMRI analysis, while phase data is typically discarded. In addition to the application of fast imaging sequences (see section 3), increasing the subject's comfort in the MR scanner reduces voluntary movements. However, in general, it is impossible to completely avoid subject motion, especially when conducting studies with children, the elderly or patients. To correct for motion-related image artifacts, processing techniques specifically tailored for each type of motion have been proposed. Fast macroscopic motion typically leads to signal dropout within slices of dMRI volumes (see Figures 7.7 and 7.8 in chapter 7). Several approaches for the detection of corrupted measurements (Chang et al., 2005; Scherrer and Warfield, 2012; Tax et al., 2015) and subsequent imputation of those signals (Andersson et al., 2016; Christiaens et al., 2018; Elhabian et al., 2016; Koch et al., 2019; Tobisch et al., 2016) have been developed. Signal imputation recovers the complete data set after the exclusion of detected faulty measurements and thereby facilitates accurate dMRI analysis (Chen et al., 2015; Elhabian et al., 2014). Chapter 6 and 7 will present a novel SHORE-based approach for the detection and imputation of signal dropout in dMRI. Those

methods detect faulty signals based on increased residuals which present the difference between measurement and signal prediction obtained from dMRI models. Furthermore, fast motion between slices can lead to image artifacts especially when acquiring slices in an interleaved way. Recently, an approach specifically tailored to mitigate artifacts due to intra-volume movements was proposed (Andersson et al., 2017). Slow subject movement throughout the acquisition of several imaging volumes results in their misalignment. Processing techniques for spatial realignment of imaging volumes have been proposed (Andersson and Sotiropoulos, 2016, 2015; Raffelt et al., 2012) which further account for geometric distortions. Physiological motion for example due to respiration can lead to diffuse noise-like artifacts in single-shot PGSE EPI. Cardiac and respiratory gating (Hamaguchi et al., 2016) and motion navigators (Kober et al., 2011; Stirnberg et al., 2016; Wallace et al., 2018) have also been investigated to track the degree of motion during the acquisition and guide subsequent correction methods.

2.6 Diffusion MRI reconstruction and feature extraction

Due to its sensitivity to molecular motion in brain tissue, diffusion MRI allows inferences on the diffusive process itself and on the underlying brain microstructure. For the purpose of obtaining quantitative diffusion and microstructural measures, such as the mean diffusivity (MD) in brain tissue or fiber orientation estimates, dMRI reconstruction techniques are applied to the acquired data. Two categories of reconstruction methods can be distinguished: (1) signal representations that describe the dMRI signal per voxel by means of mathematical formulae and (2) biophysical models that link the diffusion signal per voxel to a collection of compartments representing the tissue microstructure. Those categories of models for quantitative dMRI reconstruction are referred to as diffusion and microstructure modeling, respectively. The focus of the former is an accurate description of the diffusion signal, e.g. by means of a combination of suitable basis functions, from which diffusion measures can be extracted. In contrast microstructure models directly estimate a set of model parameters from the measurements that can be related to or already represent meaningful microstructural features. This distinction of dMRI models arose once the limitations of the early simple dMRI signal models became clear. Biophysical models with high specificity for tissue microstructure were thus developed. A wide range of models of either category has been proposed over the last decades to extract quantitative information on the diffusive process of water molecules and the brain microstructure from dMRI acquisitions. The most commonly used diffusion and microstructure models will be presented in the following sections 2.6.1 and 2.6.2, respectively. For a comprehensive overview, recent works review the advantages and limitations of state-of-the-art models and the applications and research questions for which they are tailored (Alexander et al., 2017; Novikov et al., 2018). Typically, a specific dMRI model is chosen application-oriented. As of today, there is no consensus in the dMRI community on which model provides the most accurate and meaningful diffusion or microstructural measures. However, this is an active field of research with the aim to investigate, validate and improve those models in simulations, diffusion phantom experiments, animal studies and human clinical and population studies. Fast and robust model fitting is essential for whole brain dMRI analysis and state-of-the-art processing tools enable diffusion

and microstructural modeling highly accelerated through the parallelization of calculations on the CPU and GPU (CPU: central processing unit, GPU: graphics processing unit) (Daducci et al., 2015; Harms et al., 2017). As a measure for the goodness of fit, the log likelihood (LL) can be computed, which, however, favors more complex models with a higher number of parameters. Thus, for model comparison (Ferizi et al., 2014; Harms et al., 2017; Panagiotaki et al., 2012), the more sophisticated Bayesian information criterion (BIC) (Schwarz, 1978) is usually considered which incorporates the LL, but also accounts for model complexity.

2.6.1 Diffusion signal representations

Reconstruction techniques that aim for an accurate description of the dMRI signal and the related diffusion propagator as defined in Eq. (2.18) and Eq. (2.19) formulate mathematical representations of signal attenuation due to molecular displacement. To capture a most comprehensive view of the diffusive transport, discrete (see section 2.6.1.3) and continuous (see section 2.6.1.4) representations are based on a linear combination of suitable basis functions. For an accurate reconstruction, those methods, however, require high quality dMRI data with sufficient angular and radial resolution in q-space at the cost of long acquisition times. To overcome this limitation, less complex models were developed that can deal with fewer q-space samples. In the early days of dMRI, the first one was the diffusion tensor model (see section 2.6.1.1). The DT model and others approximate the dMRI signal by mathematical formulae derived from a Taylor series expansion of the logarithm of the signal in powers of b (Jensen et al., 2005)

$$\ln(S(b,\mathbf{g})) = \ln(S_0) - b\mathbf{g}^T\mathbf{D}\mathbf{g} + \frac{1}{6}b^2MD^2K(\mathbf{g}) + O(b^3) \tag{2.20}$$

Models such as the DT model are based on the first two terms of Eq. (2.20) that characterize only the Gaussian (non-restricted) contribution of molecular diffusion. To avoid such a strong assumption about the dMRI signal, more complex models account for restricted anisotropic diffusion. The inclusion of the second order term allows us to describe the diffusional kurtosis K (Jensen et al., 2005) to capture the deviation of the diffusive transport of water molecules from the Gaussian behavior (see section 2.6.1.2). In practice, the choice of the diffusion model is often driven by the need to balance between the degree of signal approximation and the available scan time. Therefore, methods that accelerate dMRI acquisition without imposing limitations on dMRI reconstruction methods are of great interest to obtain comprehensive descriptions of the dMRI signal and propagator within acceptable scan times. Acceleration methods of this kind are the focus of chapters 3, 4 and 5.

2.6.1.1 Diffusion tensor imaging

For restricted and anisotropic diffusion as described in section 2.4, the diffusion tensor $\mathbf{D}$ is preferred over the ADC for an improved description of the directional dependency of the diffusive transport of water molecules. Figure 2.19 depicts the anisotropic displacement profile expected for a tightly

packed and aligned bundle of fiber fascicles. This displacement profile can be approximated in 3D by means of the symmetric and positive definite 3×3 diffusion tensor (DT)

$$\mathbf{D} = \begin{bmatrix} D_{xx} & D_{xy} & D_{xz} \\ D_{xy} & D_{yy} & D_{yz} \\ D_{xz} & D_{yz} & D_{zz} \end{bmatrix} \tag{2.21}$$

where the diagonal and off-diagonal components represent the diffusivities along the three orthogonal direction x, y and z and their correlations, respectively.

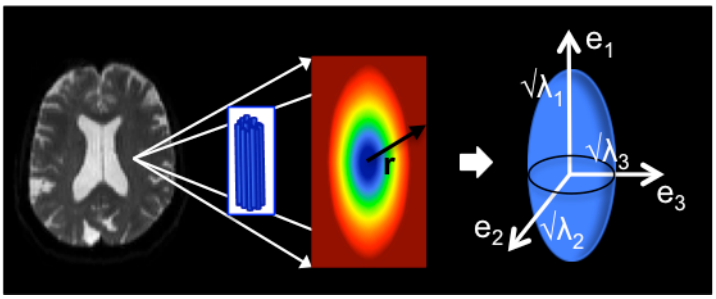

Figure 2.19: The diffusion tensor models the displacement of water molecules per voxel.

Based on the DT, one of the most simplistic approaches for the estimation of diffusion measures characterizing the tissue microstructure was introduced by P Basser et al. (1994a) as diffusion tensor imaging (DTI). Considering Eq. (2.16), the vector $\mathbf{x} = (\ln(S_0), D_{xx}, D_{xy}, D_{xz}, D_{yy}, D_{yz}, D_{zz})^T$ of the unique elements of $\mathbf{D}$, can be related to the n acquired diffusion signals $(S(b_1, \mathbf{g}_1), \cdots, S(b_n, \mathbf{g}_n))^T$ by

$$\mathbf{y} = \mathbf{B}_D \mathbf{x} \tag{2.22}$$

where $\mathbf{y} = (\ln(\frac{S(b_1,\mathbf{g}_1)}{S_0}), \cdots, \ln(\frac{S(b_n,\mathbf{g}_n)}{S_0}))^T$ and the b-matrix $\mathbf{B}_D$ is defined by

$$\mathbf{B}_D = \begin{bmatrix} 1 & -b_1 g_{1x}^2 & -2b_1 g_{1x} g_{1y} & -2b_1 g_{1x} g_{1z} & -b_1 g_{1y}^2 & -2b_1 g_{1y} g_{1z} & -b_1 g_{1z}^2 \\ \vdots & \vdots & \vdots & \vdots & \vdots & \vdots & \vdots \\ 1 & -b_n g_{nx}^2 & -2b_n g_{nx} g_{ny} & -2b_n g_{nx} g_{nz} & -b_n g_{ny}^2 & -2b_n g_{ny} g_{nz} & -b_n g_{nz}^2 \end{bmatrix} \tag{2.23}$$

In DTI, typically, one single b-value of 1000 s/mm^2 is applied for all DWIs, i.e. single-shell imaging is performed. A minimum number of six non-collinear DWIs is required to estimate $\mathbf{x}$, but for an accurate model fitting robust against acquisition noise, 30 to 60 DWIs are usually acquired depending on the available scan time (Figure 2.20).

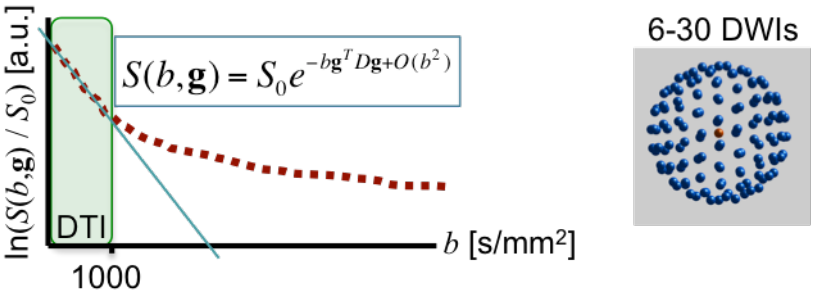

Figure 2.20: Diffusion tensor imaging: signal representation and q-space sampling.

Due to the linearization of the tensor model by the natural log-transformation of the diffusion weighted signals, Eq. (2.22) can be solved for $\mathbf{x}$ via the simple and fast linear least squares (LLS) approach $\mathbf{x} = (\mathbf{B}_D^T\mathbf{B}_D)^{-1}\mathbf{B}_D^T\mathbf{y}$. This linearization, however, leads to heteroscedastic log-transformed signals because their variance depends on the signal intensity (P Basser et al., 1994b). For an improved modeling precision compared to the LLS approach, a weighted linear least squares (WLLS) approach $\mathbf{x} = (\mathbf{B}_D^T\mathbf{W}_D\mathbf{B}_D)^{-1}\mathbf{B}_D^T\mathbf{W}_D\mathbf{y}$ accounts for signal heteroscedasticity in linearized models by employing the matrix $\mathbf{W}_D$ of iteratively updated weights defined as the inverse variances of the log-transformed signals (Veraart et al., 2013). Further, non-linear least squares (NLLS) optimization methods have been introduced including constraints to ensure positive definiteness of the resulting DT elements (Koay et al., 2006). While typically more time consuming than linear approaches, non-linear optimization has been improved and accelerated through implementation on the GPU (Harms et al., 2016).

Following the estimation of $\mathbf{x}$, an eigen decomposition of $\mathbf{D}$ is required to relate the elements of the DT with the principal axis of diffusion. From the resulting eigenvalues $\{\lambda_1, \lambda_2, \lambda_3\}$ with $\lambda_1 \geq \lambda_2 \geq \lambda_3$ and eigenvectors $\{\mathbf{e}_1, \mathbf{e}_2, \mathbf{e}_3\}$ (Figure 2.21), the following scalar diffusion measures can be derived (Basser and Pierpaoli, 1996):

1. Fractional anisotropy: $\text{FA}_\text{D} = \sqrt{\frac{3}{2}\frac{(\lambda_1-\bar{\lambda})^2+(\lambda_2-\bar{\lambda})^2+(\lambda_3-\bar{\lambda})^2}{\lambda_1^2+\lambda_2^2+\lambda_3^2}}$
2. Mean diffusivity: $\text{MD}_\text{D} = \bar{\lambda} = \frac{\lambda_1+\lambda_2+\lambda_3}{3}$
3. Axial diffusivity: $\text{AD}_\text{D} = \lambda_1$
4. Radial diffusivity: $\text{RD}_\text{D} = \frac{\lambda_2+\lambda_3}{2}$

As depicted in Figure 6.3, the orientation of the eigenvector corresponding to the principal eigenvalue per voxel can be used to generate a color encoded FA map. Colors red, green and blue indicate left-right, anterior-posterior and inferior-superior orientation, respectively, which is the same color coding as used in fiber tractography (see section 2.6.3).

Due to its relatively short acquisition time and inexpensive computation to derive a set of useful diffusion measures, DTI is of great interest in clinical applications, e.g. for the assessment of acute stoke (Horsfield and Jones, 2002; Werring et al., 2000). However, DTI comes with some limitations

due to its underlying assumption of Gaussian diffusion and thus monoexponential signal decay which is often violated in complex brain microstructure. Indices derived from the DT model such as FA are strongly dependent on the underlying microstructural configuration (De Santis, Drakesmith, et al., 2014). Additionally, the DT model is incapable to represent multiple crossing (kissing) or bending fiber fascicles per voxel, which may bias DT indices. Therefore, DT-derived parameters require careful interpretation and higher order models should be considered for an accurate description of the complex microstructural architecture which will be discussed in section 2.6.3.

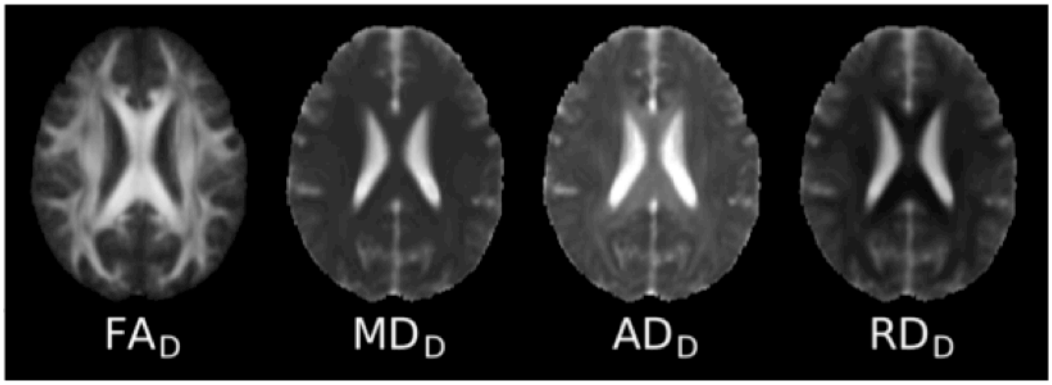

Figure 2.21: Maps of FA_D, MD_D, AD_D and RD_D derived from the diffusion tensor model and averaged across 16 subjects.

2.6.1.2 Diffusion kurtosis imaging

Diffusion kurtosis imaging (DKI) (Jensen et al., 2005) extends the description of the monoexponential diffusion signal decay assumed in diffusion tensor imaging (Eg. 2.16) by including higher order terms to model and quantify diffusional non-Gaussianity in complex tissue structure

$$S(b,\mathbf{g}) = S_0 \exp\left(-b\mathbf{g}^T\mathbf{D}\mathbf{g} + \frac{1}{6}b^2\left(\frac{1}{3}\sum_{i=1}^{3}D_{ii}\right)^2\sum_{i=1}^{3}\sum_{j=1}^{3}\sum_{k=1}^{3}\sum_{l=1}^{3}g_i g_j g_k g_l W_{ijkl}\right) \tag{2.24}$$

In addition to the second-order diffusion tensor $\mathbf{D}$, a fourth-order kurtosis tensor $\mathbf{W}$ is incorporated. In order to estimate all unknown parameters via kurtosis model fitting, the vector of unknowns including the elements of the diffusion and the kurtosis tensor can be written as

$$\begin{aligned}\mathbf{x} = \Big(\ & \ln(S_0) \quad D_{xx} \quad D_{xy} \quad D_{xz} \quad D_{yy} \quad D_{yz} \quad D_{zz} \quad tr(\mathbf{D})^2W_{1111} \quad tr(\mathbf{D})^2W_{2222} \\ & tr(\mathbf{D})^2W_{3333} \quad tr(\mathbf{D})^2W_{1112} \quad tr(\mathbf{D})^2W_{1113} \quad tr(\mathbf{D})^2W_{2221} \quad tr(\mathbf{D})^2W_{2223} \\ & tr(\mathbf{D})^2W_{3331} \quad tr(\mathbf{D})^2W_{3332} \quad tr(\mathbf{D})^2W_{1122} \quad tr(\mathbf{D})^2W_{1133} \quad tr(\mathbf{D})^2W_{2233} \\ & tr(\mathbf{D})^2W_{2311} \quad tr(\mathbf{D})^2W_{1322} \quad tr(\mathbf{D})^2W_{1233}\ \Big)^T\end{aligned} \tag{2.25}$$

where the matrix trace $tr(\mathbf{D}) = (D_{xx} + D_{yy} + D_{zz})$. In analogy to equation 2.22 in DTI, the measurements $\mathbf{y}$ are related to the vector $\mathbf{x}$ by

$$\mathbf{y} = \mathbf{B}\mathbf{x} \tag{2.26}$$

where the matrix $\mathbf{B} = \begin{pmatrix} \mathbf{B}_D & \mathbf{B}_K \end{pmatrix}$ is composed of the DTI b-matrix $\mathbf{B}_D$ and the DKI b-matrix

$$\mathbf{B}_K = \frac{1}{54}\begin{bmatrix} b_1^2 g_{1x}^4 & b_1^2 g_{1y}^4 & b_1^2 g_{1z}^4 & 4b_1^2 g_{1x}^3 g_{1y} & 4b_1^2 g_{1x}^3 g_{1z} & 4b_1^2 g_{1y}^3 g_{1x} \\ \vdots & \vdots & \vdots & \vdots & \vdots & \vdots \\ b_n^2 g_{nx}^4 & b_n^2 g_{ny}^4 & b_n^2 g_{nz}^4 & 4b_n^2 g_{nx}^3 g_{ny} & 4b_n^2 g_{nx}^3 g_{nz} & 4b_n^2 g_{ny}^3 g_{nx} \\ 4b_1^2 g_{1y}^3 g_{1z} & 4b_1^2 g_{1z}^3 g_{1x} & 4b_1^2 g_{1z}^3 g_{1y} & 6b_1^2 g_{1x}^2 g_{1y}^2 & 6b_1^2 g_{1x}^2 g_{1z}^2 & 6b_1^2 g_{1y}^2 g_{1z}^2 \\ \vdots & \vdots & \vdots & \vdots & \vdots & \vdots \\ 4b_n^2 g_{ny}^3 g_{nz} & 4b_n^2 g_{nz}^3 g_{nx} & 4b_n^2 g_{nz}^3 g_{ny} & 6b_n^2 g_{nx}^2 g_{ny}^2 & 6b_n^2 g_{nx}^2 g_{nz}^2 & 6b_n^2 g_{ny}^2 g_{nz}^2 \\ 12b_1^2 g_{1y} g_{1z} g_{1x}^2 & 12b_1^2 g_{1x} g_{1z} g_{1y}^2 & 12b_1^2 g_{1x} g_{1y} g_{1z}^2 \\ \vdots & \vdots & \vdots \\ 12b_n^2 g_{ny} g_{nz} g_{nx}^2 & 12b_n^2 g_{nx} g_{nz} g_{ny}^2 & 12b_n^2 g_{nx} g_{ny} g_{nz}^2 \end{bmatrix} \tag{2.27}$$

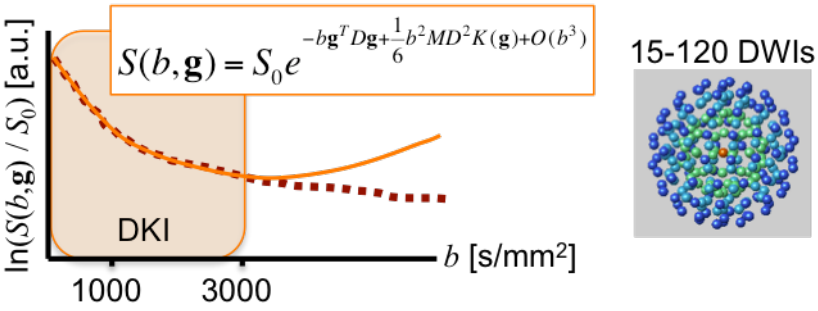

Figure 2.22: Diffusion kurtosis imaging: signal representation and q-space sampling.

As for DTI, it is necessary to include a constraint on the maximum b-value used for DKI. Since, in contrast to DTI, DKI includes a higher order term which is quadratic in b, higher b-values are required. As depicted in Figure 2.22, the kurtosis model accurately fits dMRI signals with diffusion weightings up to b = 3000 s/mm^2. To achieve short scan times in clinical settings, DKI is typically performed using 2-shell imaging protocols collecting at least a minimum of 15 DWIs at b = 1000 s/mm^2 and b = 2000 s/mm^2 (Tabesh et al., 2011). Recent research and population studies perform multi-shell dMRI or DSI (see section 2.6.1.3) which allows fitting the kurtosis model to all DWIs with b-values up to b = 3000 s/mm^2 (Sotiropoulos et al., 2013; Sprenger et al., 2016; Tobisch et al., 2018). Similar to DTI, $\mathbf{x}$ can be estimated via the linear least squares approach or its weighted variant as well as non-linear optimization strategies (Harms et al., 2016; Tabesh et al., 2011). Furthermore, constraints to increase the robustness to noise (Groeschel et al., 2016) should be integrated to improve the fit

and the derived parameter maps. Quantitative parameter maps can be obtained for mean, axial and radial kurtosis (Figure 2.23) derived from the kurtosis tensor and denoted MK, AK and RK, respectively (Jensen and Helpern, 2010). Furthermore, FA_K, MD_K, AD_K and RD_K can be derived from the diffusion tensor estimated via DKI.

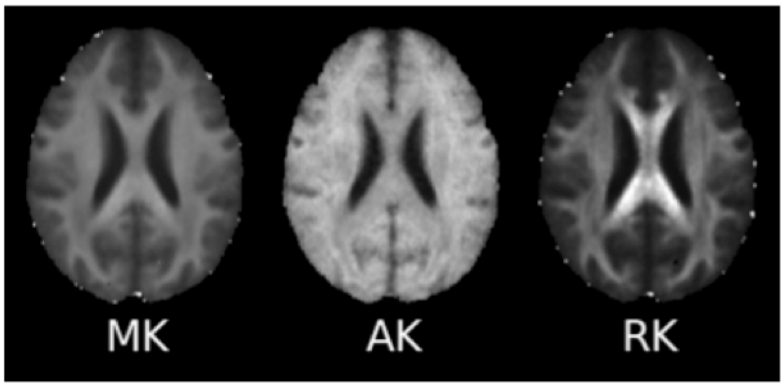

Figure 2.23: Maps of MK, AK and RK derived from the kurtosis model and averaged across 16 subjects.

Those measures have been found to represent potential biomarkers to investigate WM and GM integrity in normal aging (Falangola et al., 2008), but also stroke (Hui et al., 2012; Jensen et al., 2011) and neurodegenerative diseases such as AD (Fieremans et al., 2013; Helpern et al., 2011). DKI measures have also been successfully related to tissue microstructure (Fieremans et al., 2013, 2011) to provide more specificity compared to DTI, similar to biophysical models.

2.6.1.3 Diffusion spectrum imaging

Diffusion spectrum imaging (DSI) (Wedeen et al., 2005) aims for a complete description of the diffusion propagator to capture both the angular and the radial characteristics of the diffusion process. In contrast to DTI and DKI, DSI does not introduce assumptions to neglect higher order terms, but reconstructs the propagator in a model-free way. DSI exploits the Fourier relationship between the normalized dMRI q-space signal and the displacement space of diffusive water molecules as described by Eq. (2.19) in section 2.5.1. The ensemble average diffusion propagator is therefore linked to the dMRI measurements via $\bar{P}(\mathbf{R}, \Delta) = \mathcal{F}(E(\mathbf{q}, \Delta))$. Due the application of the discrete Fourier transform, conventional DSI requires a dMRI acquisition strategy to sample q-space on a Cartesian grid. A typical DSI protocol considers a q-space grid of radius 5, i.e. a grid of size 11x11x11. This grid is, however, truncated to a sphere to reduce the number of dMRI acquisitions (Figure 2.24). Due to the antipodal symmetry of the diffusion signal, considering samples of one hemisphere is sufficient. Therefore, at least $n = 258$ unique imaging volumes are acquired to fully sample the q-space for DSI. In the early days of DSI, the acquisition of this high number of required dMRI volumes resulted in scanning times of about or over an hour, depending on the scanner hardware as well as dMRI sequence parameters such as the imaging resolution. Nowadays, conventional DSI is possible even at high spatial resolution in less than an hour (Tobisch et al., 2019) due to a new

generation of MRI systems with high gradient strength up to 80 mT/m (Glasser et al., 2016). Recent advances in DSI acquisition strategies combining parallel imaging suitable for dMRI (Cauley et al., 2014; Setsompop et al., 2012; Xu et al., 2013) and the compressed sensing (CS) theory (Bilgic et al., 2012; Menzel et al., 2011; Paquette et al., 2015; Setsompop et al., 2013) enable accelerated high resolution DSI performed in about 12 minutes of scan time (Tobisch et al., 2018). These CS-DSI approaches will be discussed in more detail in chapters 3 - 5. Compared to DTI and DKI models, there is no restriction on the maximum diffusion weighting imposed by DSI and thus, the b-value can be selected specifically for each application. However, the available scanner system imposes a technical limit on the maximum b-value. For clinical MR systems using 80 mT/m gradients, maximum b-values in the range of 6000-8000 s/mm^2 are typically applied (Bilgic et al., 2012; Paquette et al., 2015; Yeh and Verstynen, 2016).

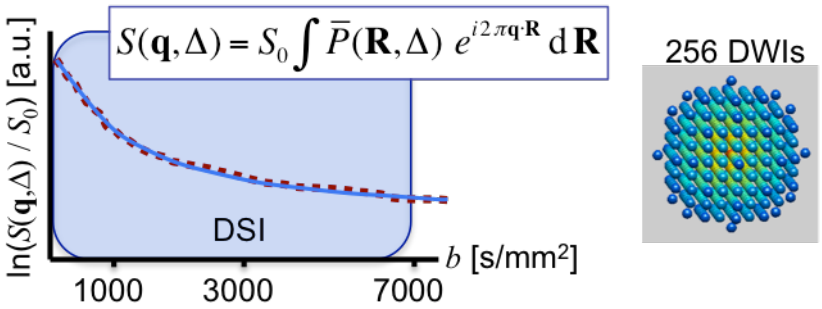

Figure 2.24: Diffusion spectrum imaging: signal representation and q-space sampling.

Due to the high intra-voxel resolution in q-space, DSI provides rich data with great potential for dMRI analysis. Diffusion measures can be extracted from the diffusion propagator describing the mean squared displacement (MSD) of water molecules and the zero displacement or so called return-to-origin probability (RTOP) (Assaf et al., 2000; Wu and Alexander, 2007; Wu et al., 2008), maps of which are presented in Figure 2.25. The latter characterizes the degree of restriction which water molecules are exposed to during the diffusion time. For example, in white matter, where diffusion is typically restricted due to the complex fiber architecture, RTOP is consistently high.

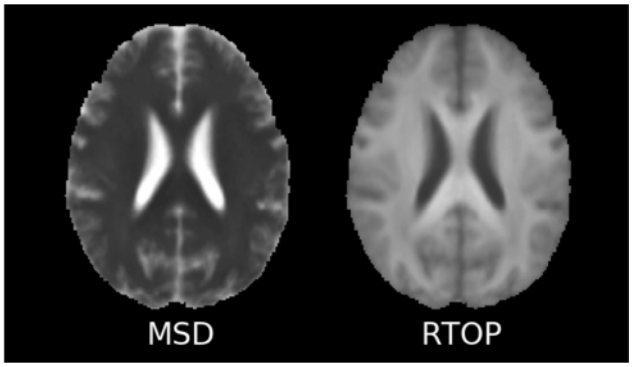

Figure 2.25: Maps of MSD and RTOP derived from the diffusion propagator by means of DSI and averaged across 16 subjects.

Furthermore, diffusion models such as the DTI and DKI model and microstructure models such as NODDI and CHARMED (see section 2.6.2) can be fitted to DSI data to obtain the model-related diffusion features (Sprenger et al., 2016; Tobisch et al., 2018; Zerbato et al., 2014). One of the reasons for which DSI became famous is its ability to reconstruct the diffusion orientation distribution function (dODF) in a model-free way. The dODF is constructed by a weighted sum of the propagator $\bar{P}(\mathbf{R}, \Delta)$ along a unique radial direction $\mathbf{u}$ (Wedeen et al., 2005), expressed as a continuous integral

$$\text{dODF}(\mathbf{u}) = \int \bar{P}(\rho\mathbf{u}, \Delta)\rho^2 d\rho \tag{2.28}$$

where $\rho = |\mathbf{R}|$. The maxima of the dODF are then linked to the orientation of nerve fiber fascicles. In this way macroscopic brain connections can be inferred from those estimates of the underlying microstructure via DSI tractography (Wedeen et al., 2008) which is described in section 2.6.3.

2.6.1.4 SHORE

In contrast to the discrete description of the diffusion propagator as discussed in the previous section, continuous signal representations have been proposed to recover the propagator by fitting continuous basis functions (J Cheng, T Jiang, et al., 2011; Fick et al., 2016; Merlet and Deriche, 2013; Ozarslan et al., 2009) to the acquired dMRI data. A popular basis among these is the simple harmonic oscillator based reconstruction and estimation (SHORE) basis (J Cheng, T Jiang, et al., 2011; Ozarslan et al., 2009). A linear combination of the SHORE basis Φ yields a continuous representation of the diffusion signal

$$\begin{aligned} E(q\mathbf{u}) &= \sum_{l=0,even}^{N_{max}} \sum_{n=l}^{(N_{max}+l)/2} \sum_{m=-l}^{l} c_{nlm}\Phi_{nlm}(q\mathbf{u}) \\ \text{with } \Phi_{nlm}(q\mathbf{u}) &= X_{nl}(q,\zeta)Y_l^m(\mathbf{u}) \end{aligned} \tag{2.29}$$

The SHORE basis is composed of a radial basis X and an angular basis Y. Indices n, l and m represent the radial order and the angular order and degree, respectively. c_{nlm} are the SHORE coefficients. Because the dMRI signals are real and symmetric, a real and symmetric spherical harmonic (SH) basis Y_l^m is applied. ζ is the SHORE scale factor that is typically calculated based on the mean diffusivity for brain white matter.

Different l_2-norm regularization approaches have been proposed for a robust estimation of the SHORE coefficients $\mathbf{c}$ from the dMRI signals by solving a penalized least squares problem using separated (Assemlal et al., 2009; Merlet and Deriche, 2013) or Laplacian regularization (Fick et al., 2014). For the reconstruction of the EAP using SHORE, analytical formulae exists to obtain the diffusion propagator (J Cheng, T Jiang, et al., 2011) and its related features such as the ODF (Merlet and Deriche, 2013), MSD and RTOP from the estimated SHORE coefficients. Due to the

availability of such analytical formulae and the common goal to describe the diffusion propagator, the SHORE model has been applied in multi-shell q-ball imaging (QBI) (Tuch, 2004) and DSI. Those imaging techniques can be accelerated using CS theory similar to Fourier-based CS-DSI (Merlet and Deriche, 2013; Tobisch et al., 2018). In this case, l_1-norm regularization is introduced to promote sparsity in the SHORE coefficients. Those approaches will be discussed in more detail in chapters 3 and 4.

Compared to the dMRI reconstruction approaches presented in the previous section, any kind of diffusion signal can be modeled in the SHORE basis, since the SHORE model can be applied independently of the dMRI acquisition strategy. Therefore, this model has not only been found advantageous for EAP reconstruction in DSI (Brusini et al., 2015) and QBI (Merlet and Deriche, 2013), but for a wide range of dMRI applications such as multi-tissue deconvolution and ODF estimation (Ankele et al., 2017) or the detection and imputation of signal dropout in dMRI (Elhabian et al., 2014; Koch et al., 2019).

To model dMRI signals in the SHORE basis, several model parameters have to be determined: the SHORE order, the scale factor and the regularization parameter. Further, the SHORE order is composed of a radial and an angular order, where the latter is restricted by the former. This means the angular and radial order cannot be chosen independently. These model limitations highlight the advantages of model-free DSI. In contrast to SHORE, however, DSI is typically restricted to q-space sampling on the Cartesian grid. Moreover, SHORE modeling of signals representing isotropic diffusion was found to be more challenging than for single or crossing fiber voxels (Fick et al., 2016). Studies conducted within this thesis are in agreement with those findings (Tobisch et al., 2019) (see chapter 4). Improving upon this modeling inaccuracy is the mean apparent propagator (MAP) model (Özarslan et al., 2013) that is highly related to the SHORE model. This approach generalizes the SHORE model by incorporating an anisotropic scale factor. In the case of isotropic scaling, the MAP basis corresponds to the SHORE basis. This model has likewise been investigated for EAP reconstruction and the extraction of propagator-based indices with and without the application of CS-acceleration (Avram et al., 2016; Fick et al., 2016; Özarslan et al., 2013; Varela-Mattatall et al., 2019). Further, MAP improved upon the modeling of isotropic diffusion as well as the accuracy of signal estimation when using lower radial orders (Fick et al., 2016).

2.6.2 Tissue microstructure models

With the aim to provide higher specificity of the brain tissue microstructure compared to mathematical representations of the dMRI signal as discussed in the previous section, biophysical models have been developed. Inferences on tissue microstructure are made directly based on the estimated model parameters or their related microstructural features. This approach is also referred to as multi-compartment modeling because a biophysical model expresses the diffusion signal $S(b, \mathbf{g})$ as a weighted sum of signals each derived from a single compartment i out of the set Ω of multiple compartments

$$S(b, \mathbf{g}) = S_0 \sum_{i \in \Omega} w_i S_i(b, \mathbf{g}) \tag{2.30}$$

Each individual compartment i is a model itself. Those single compartment models represent a specific microstructural environment for which a distinct behavior of the diffusive transport is expected. The performance of individual and composite compartment models has been investigated in detail in fixed animal tissue (Panagiotaki et al., 2012) and *in vivo* dMRI (Ferizi et al., 2014; Harms et al., 2017). In the following, some of the most popular state-of-the-art composite multi-compartment models and their constituent compartments are presented. These models define intra-cellular (IC) and extra-cellular (EC) compartments to describe restricted and hindered diffusion, respectively. Additionally, another compartment for isotropic diffusion is often included. For isotropic, restricted and hindered diffusion, the *ball*, *stick* and *tensor* model are defined, respectively. Simple geometric objects, often highly idealized, are used to model the inherent type of diffusion in each compartment. Sticks and cylinders are for example commonly used to depict axonal fascicles; the *ball* represents isotropic diffusion.

2.6.2.1 Ball-and-Stick

The *ball-and-stick* model is a simple two-compartment model that assumes a single main fiber direction of all axonal fascicles passing through one voxel (Behrens et al., 2003). Intra-axonal anisotropic diffusion along the assumed fibre direction and extra-cellular isotropic diffusion of water molecules are modeled by the *stick* and *ball* compartment, respectively. The signal function of the *ball* model is given by Eq. (2.14). The *stick* model expresses restricted diffusion by means of cylinders with zero radius, thus, without considering radial diffusion. This means, diffusion is impossible along any direction perpendicular to the main fibre direction. The composite signal function of the *ball-and-stick* model evaluated along fibre direction $\mathbf{n}$ is given by

$$E(b, \mathbf{g}) = w_r E_r + w_{iso} E_{iso} = w_r \exp(-bD(\mathbf{g} \cdot \mathbf{n})^2) + w_{iso} \exp(-bD) \tag{2.31}$$

where w_r and w_{iso} are the weights of the *stick* and *ball* compartment, respectively. The *ball-and-stick* model became famous as one of the first models that accounted for restricted diffusion and thus, addressed the limitations inherent in the diffusion tensor model. Including several *stick* compartments allows the modeling of multiple distinct axonal fascicles. Due to its specificity to orientational information on the tissue microstructure, the *ball-and-stick* model and its estimates of fiber orientation were incorporated into the reconstruction of fiber tracks across the brain by means of probabilistic tractography (Behrens et al., 2007, 2003) which will be discussed in section 2.6.3.

2.6.2.2 CHARMED

The composite hindered and restricted model of diffusion (CHARMED) describes the dMRI signal attenuation due to the diffusive transport in white matter by means of a restricted and a hindered diffusion compartment for the intra- and extra-axonal space, respectively (Assaf and Basser, 2005; Assaf et al., 2004). This model is, therefore, able to distinguish between the Gaussian and non-Gaussian signal components. Gaussian hindered diffusion is modeled by means of an anisotropic diffusion tensor as defined by Eq. (2.16). A single hindered compartment E_h is sufficient in CHARMED; however, as for the *ball-and-stick* model several restricted compartments E_r can be applied to model distinct populations of axonal fascicles in the form of idealized parallel cylinders

$$E(b, \mathbf{g}) = w_h E_h(b, \mathbf{g}) + \sum_{i \in \Omega} w_r^i E_r^i(b, \mathbf{g}) \tag{2.32}$$

Estimates of the microstructural fiber configuration and measures of the intra-axonal diffusivities (IAD) and the restricted volume fraction (FR), also interpreted as axonal density, can be extracted by CHARMED modeling (Assaf and Basser, 2005; De Santis et al., 2012; De Santis, Drakesmith, et al., 2014). To model Gaussian diffusion, on the one hand, by means of the diffusion tensor, low b-value acquisitions need to be collected. On the other hand, the estimation of fiber orientation and axonal density requires high angular and high radial resolution in q-space, respectively. For CHARMED modeling, a suitable dMRI imaging protocol thus collects a high number of DWIs at low as well as high b-values. A 10-shell q-space sampling scheme was proposed originally to acquire around 200 DWIs with diffusion weightings up to 10.000 s/mm^2 (Assaf and Basser, 2005). Similar to DSI, such schemes are, however, not applicable in clinical settings due to the long acquisition time. Thus, 8-shell sampling schemes optimized for CHARMED have been proposed that collect less than 50 DWIs to reduce the scanning time while maintaining accuracy and precision in the estimated CHARMED indices (De Santis, Y Assaf, et al., 2014). CHARMED parameters have also been investigated in comparison to the diffusion parameters obtained by DTI and DKI (De Santis et al., 2012; De Santis, Drakesmith, et al., 2014). As discussed earlier, a strong dependency exists between DTI measures and the underlying microstructural arrangement, which hampers their interpretation. In contrast, FR and IAD are not influenced in that way by specific fiber configurations and thus, CHARMED modeling provides higher specificity to dMRI than DTI. Correlations between CHARMED parameters and DKI kurtosis measures have been reported (De Santis et al., 2012) with the aim to further explain DKI by using a biophysical model of the tissue microstructure. An extension of the CHARMED model, the AxCaliber model, applies a distribution of cylinders with varying diameter for the restricted compartment (Assaf et al., 2008; Barazany et al., 2009). In this way, an axon diameter distribution can be estimated per brain voxel non-invasively from dMRI, which only invasive histology had been able to provide before. However, AxCaliber requires the acquisitions of dMRI scans for different diffusion times and is, thus, not feasible for studies with limited scan time. Moreover, recent works suggest that the mapping of axonal diameter is challenging, in general, due to limitations of dMRI sequences and the dependency of estimates on imaging related parameters (Huang et al., 2015; Novikov et al., 2018).

2.6.2.3 NODDI

The application of idealized parallel cylinders to represent axonal fascicles inhibits the modeling of more complex fiber arrangements such as fanning or bending nerve fiber bundles. Therefore, the orientation dispersion inherent in these fiber configuration cannot be captured by the microstructural models described in the previous sections. To overcome this limitation, neurite orientation dispersion and density imaging (NODDI) was proposed to model how dispersed and how densely packed axonal fascicles are within the brain tissue microstructure (Zhang et al., 2012). NODDI incorporates restricted intra-cellular, hindered extra-cellular and isotropic diffusion compartments to describe the composite normalized signal by

$$E(b,\mathbf{g}) = (1-w_{iso})(w_r E_r(b,\mathbf{g}) + (1-w_r)E_h(b,\mathbf{g})) + w_{iso}E_{iso}(b,\mathbf{g}) \tag{2.33}$$

The restricted intra-cellular compartment is defined as

$$E_h(b,\mathbf{g}) = \int_{\mathbb{S}^2} f(\mathbf{n}) \exp(-b d_{||}(\mathbf{g}\cdot\mathbf{n})^2) d\mathbf{n} \tag{2.34}$$

Similar to the restricted compartment of the *ball-and-stick* model, diffusive transport along fibers of orientation $\mathbf{n}$ and with diffusivity $d_{||}$ leads to signal attenuation. The ODF $f(\mathbf{n})$ defines the probability of finding axonal fascicles along direction $\mathbf{n}$. In conventional NODDI, a Watson distribution is used to model the ODF. A recent extension of NODDI applies the Bingham distribution instead to account for anisotropic orientation dispersion (Tariq et al., 2016). As for the *ball-and-stick* and the CHARMED model, isotropic and hindered (Gaussian) diffusion are modeled by means of an isotropic and an anisotropic diffusion tensor, respectively. In NODDI, the latter, however, is a cylindrically symmetric tensor $\mathbf{D}_r(\mathbf{n})$ and Eq. (2.16) is adapted to

$$E_h(b,\mathbf{g}) = \exp\left(-b\mathbf{g}^T\left(\int_{\mathbb{S}^2} f(\mathbf{n})\mathbf{D}(\mathbf{n})d\mathbf{n}\right)\mathbf{g}\right) \tag{2.35}$$

As for the CHARMED model, the estimated restricted volume fraction is linked to axonal density. NODDI therefore provides a map of the neurite density index (NDI). Additionally, the orientation dispersion index (ODI) can be calculated based on the degree of dispersion κ about the mean orientation modeled by the ODF. (Harms et al., 2017; Zhang et al., 2012)

NODDI was specifically tailored for its application in clinical settings to overcome the common drawback of more sophisticated biophysical models: the long acquisitions time which prevents their widespread use. A clinical imaging protocol suitable for NODDI performs q-space sampling for at least two shells, typically at b-values of about 700-1000 s/mm^2 and 2500-3000 s/mm^2 collecting, respectively, 30 and 60 DWIs for a high angular resolution (Zhang et al., 2012). Clinical studies have been conducted to investigate the NODDI parameters with their specificity to tissue microstructure as biomarkers for human development and aging in health (Chang et al., 2015; Kodiweera et al., 2016; Kunz et al., 2014) and disease (Broad et al., 2018; Colgan et al., 2016; Schneider et al.,

2017). However, careful interpretation of the estimated microstructural indices is required due to the simplifying assumptions underlying the NODDI model (Jelescu et al., 2015, 2016).

2.6.3 From local fiber orientations to macroscopic brain connections

Many dMRI reconstruction methods, some of which have been discussed in the previous sections, allow estimation of one or more dominant fiber orientations per imaging voxel. Connecting those local estimates of the fiber orientation across voxels, tractography techniques reconstruct fiber tracts. These so called streamlines determine macroscopic neuronal connections that transverse the white matter throughout the brain (Jeurissen et al., 2017; Mori et al., 1999). A single fiber population can be distinguished per voxel by means of the diffusion tensor obtained by fitting the simple DT model (see section 2.6.1.1) to the dMRI measurements. As depicted in Figure 2.26, tightly packed and highly aligned fiber bundles in the corpus callosum (CC) can be accurately reconstructed. However, DTI fails in resolving crossing fibers. In this case, fiber tracking is adversely affected by an inaccurate description of the local microstructure by means of the diffusion tensor.

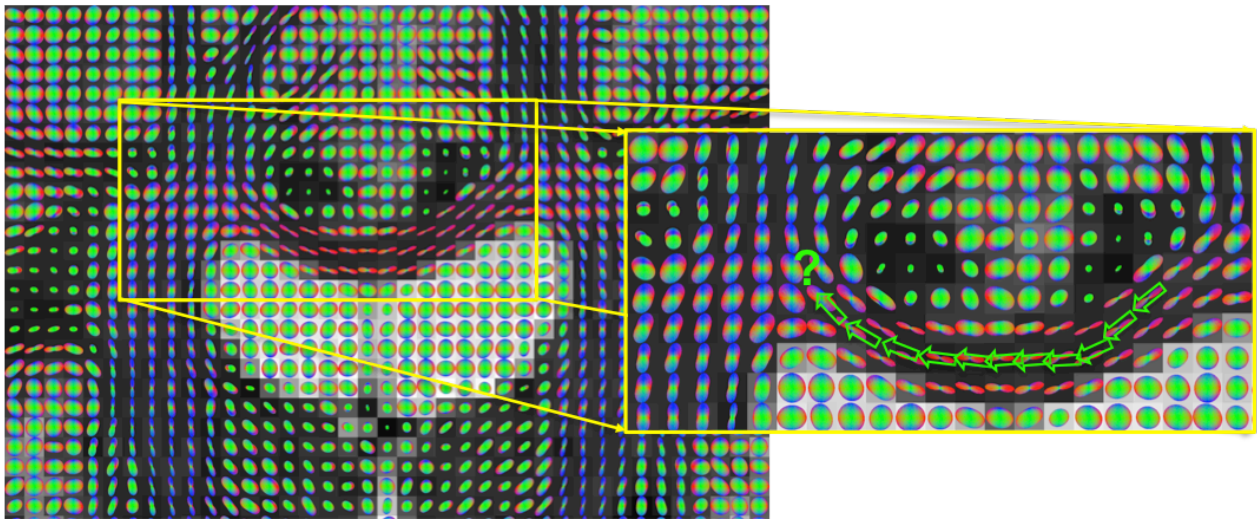

Figure 2.26: Diffusion tensors in a coronal slice obtained by means of the DT model. The inset highlights the accurate tracking of single fiber populations in the CC. The DT model, however, fails to resolve the crossing of multiple nerve fiber fascicles from the CC, corticospinal tract and superior longitudinal fasciculus (see Fig. 2.6). Color coding represents left-right, anterior-posterior and inferior-superior orientation in red, green and blue, respectively.

Since crossing fibers are ever-present in the complex brain architecture, more advanced approaches for the estimation of local fiber orientations have been proposed. For the comprehensive description of dMRI reconstruction by means of DSI and SHORE (see sections 2.6.1.3 and 2.6.1.4, respectively), the estimation of orientation distribution functions was already introduced briefly. In DSI, the diffusion ODF defines a probability distribution for the quantification of the average diffusive transport considering a set of directions of displacement (see Eq. (2.28)). In SHORE, analytical formulae exist to reconstruct the dODF from the diffusion propagator (Merlet and Deriche, 2013). The high

dimensional dODF is usually reduced to its peak maxima that represent the principal fiber orientations. In this way, multiple fiber populations can be distinguished per imaging voxel as depicted in Figure 2.27 and neuronal connections can be constructed despite complex fiber configurations. Figure 2.28 visualizes whole brain tractography performed on DSI data using the TrackVis software (Wang et al., 2007).

For fibers crossing at relatively low angles, the dODF can be suboptimal for fiber tracking, because its broad lobes tend to merge in this case (Dell'Acqua and Tournier, 2018; Tuch et al., 2003) as can be seen in the crossing fiber area in Figure 2.27. Strategies for optimal dODF reconstruction (Paquette et al., 2016) have been proposed to minimize this effect (see dODFs in Figure 5.9). Alternatively, the fiber ODF (fODF) is usually preferred for the estimation of orientational information, as it is free of diffusion-related contributions along directions other than the main fiber orientations (Dell'Acqua and Tournier, 2018), thus leading to a sharper profile of molecular displacement. State-of-the-art approaches reconstruct the fODF as a continuous distribution function on the sphere via constraint spherical deconvolution (CSD) from single shell dMRI data (Dell'Acqua et al., 2007; Descoteaux et al., 2007; Tournier et al., 2007, 2004). High angular resolution diffusion imaging (HARDI) data (Tuch et al. (2002)) with a maximum b-value of about 3000 s/mm^2 is optimal for fODF estimation (Tournier et al., 2013).

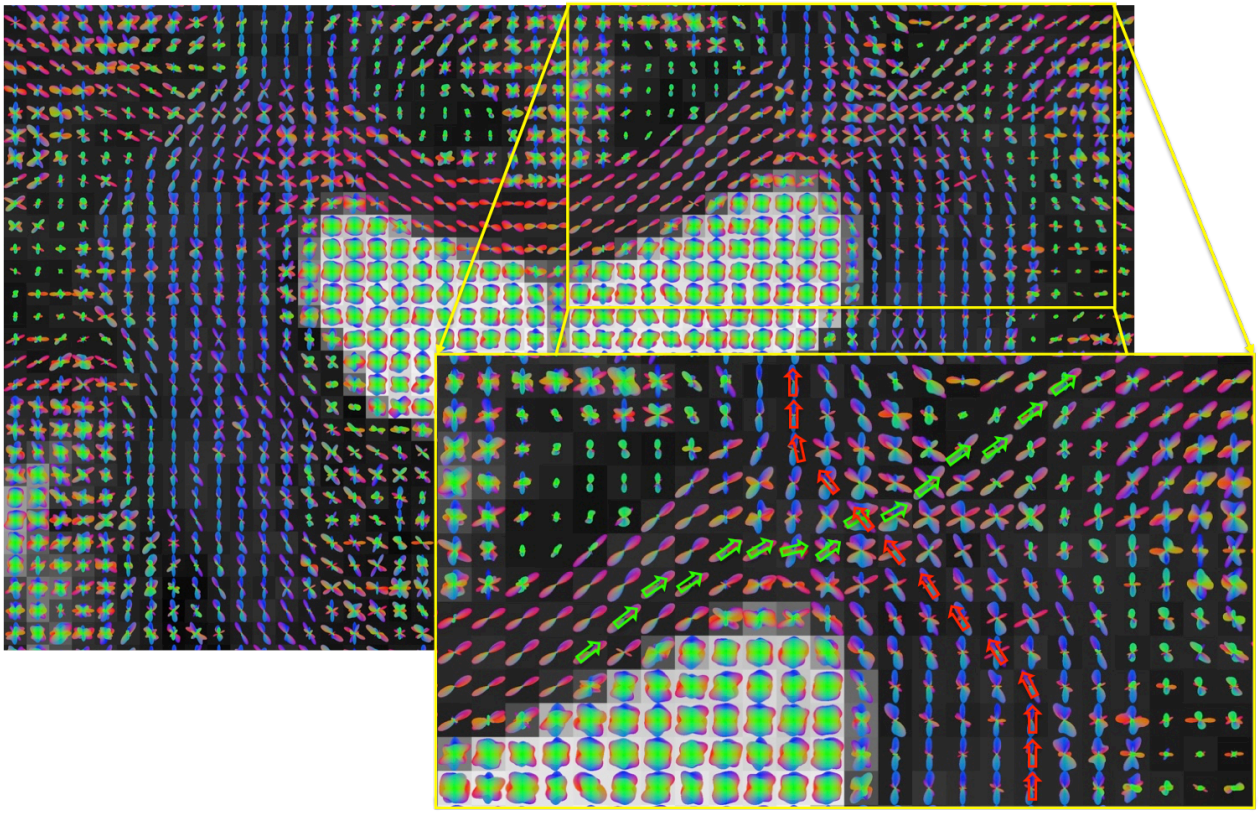

Figure 2.27: Diffusion ODFs in a coronal slice calculated from the DSI propagator resolve crossing fibers. The inset highlights the accurate tracking of multiple crossing nerve fiber fascicles from the CC, corticospinal tract and superior longitudinal fasciculus (see Fig. 2.6). Color coding represents left-right, anterior-posterior and inferior-superior orientation in red, green and blue, respectively.

Spherical deconvolution (SD) was adapted for multi-shell dMRI data and robust and accurate fODF estimation for different types of brain tissue (Jeurissen et al., 2014). Recently, SHORE-based multi tissue CSD has been proposed to obtain the fODF from the dMRI data independently of the acquisition strategy (Ankele et al., 2017). In chapter 5, Figure 5.9 compares diffusion and fiber ODFs reconstructed by means of DSI, conventional CSD and SHORE-based multi-tissue CSD. Moreover, orientational information of multiple fiber populations can also be obtained from parametric diffusion and microstructure models (see section 2.6) such as the kurtosis (Jensen et al., 2014; Lazar et al., 2008) or CHARMED model. However, parametric models fix a discrete number of fiber populations prior to model fitting and are thus less generic than the non-parametric SD approach.

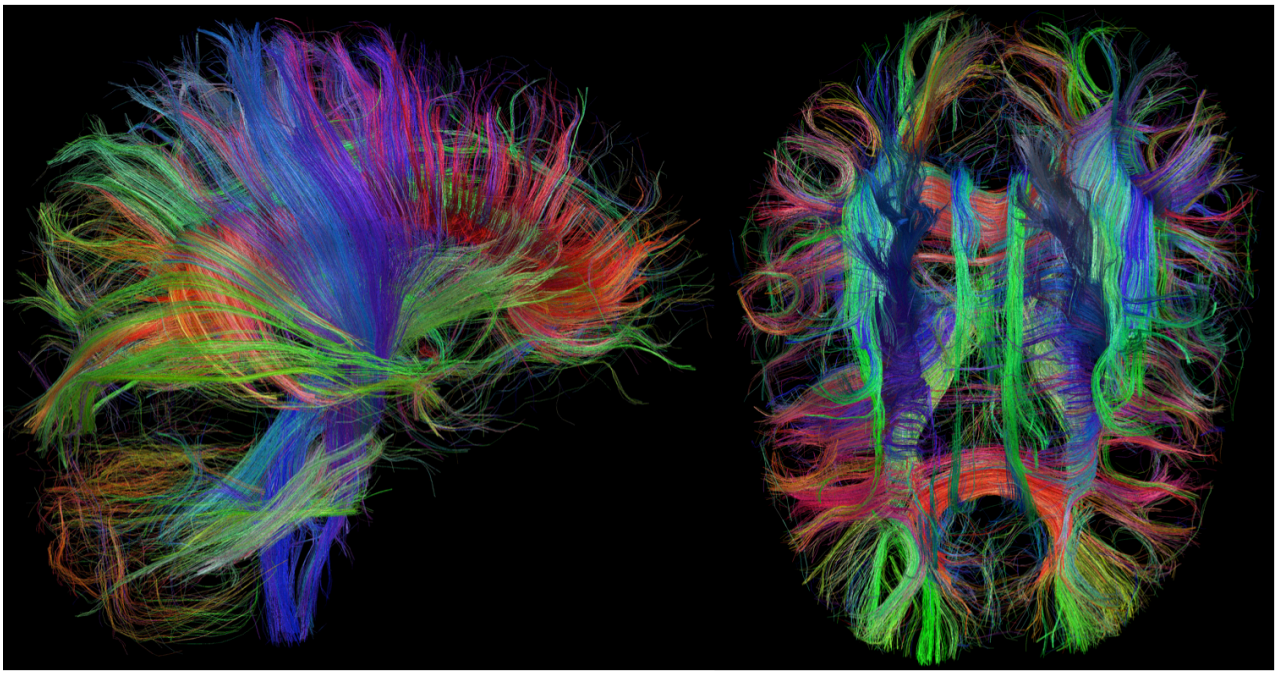

Figure 2.28: Visualization in sagittal (left) and axial (right) views of whole brain tractography performed on DSI data using TrackVis. Color coding represents left-right, anterior-posterior and inferior-superior orientation in red, green and blue, respectively.

Once a local estimate of the fiber orientation is obtained, whole brain neuronal connections can be inferred by means of tractography. Deterministic and probabilistic fiber tracking methods reconstruct streamlines, respectively, based on unique ODF estimates per imaging voxel and on a collection of fODFs per voxel and their uncertainty due to errors occurring in the estimation of local ODFs (Jeurissen et al., 2017). For region or tract-specific dMRI analysis, brain connectivity can be investigated using probabilistic local fiber tracking (Behrens et al., 2007; De Groot et al., 2013). Individual WM tracts can thus be reconstructed as depicted in Figure 2.6. These can then be used for tractometry (Bells et al., 2011; De Santis, Drakesmith, et al., 2014), the tract-based analysis of diffusion and microstructural parameters. The combination of tractography with strategies for the parcellation of the human brain cortex (Fischl and Sereno, 2018) is called connectomics (Behrens and Sporns, 2012). This approach generates the so-called human connectome describing a comprehensive network of neuronal connections (Jbabdi et al., 2015; Sotiropoulos and Zalesky, 2017). It should be

noted, however, that, together with tractography in general, this area of research still faces many challenges due to inherent methodological limitation and careful interpretation of fiber tracking and connectivity outcomes is required (Jones, 2010; Maier-Hein et al., 2017). Linking those results to functional connectivity which can be investigated by means of functional MRI (fMRI) might improve interpretability and provide further insights into brain connectivity.

3

Accelerated diffusion MRI

The acceleration of data collection in MRI is an active field of research because acquisition time is usually limited, especially in clinical and big cohort studies. Various approaches have been developed to accelerate MR image acquisition. In general, fast MR sequences such as single shot EPI already provide a more rapid k-space sampling compared to conventional multi shot imaging. While the latter is typically used to acquire a single image volume at submillimeter resolution, dMRI requires the acquisition of several ten to hundred image volumes (DWIs) using EPI to amply capture the diffusive transport of water molecules. For multi-slice sequences such as single shot EPI the acquisition time increases with the number of slices per imaging volume to achieve high isotropic spatial resolution. Therefore, additional improvements on singe shot EPI have been proposed to acquire multiple image slices simultaneously, i.e. performing parallel imaging, thereby accelerating data collection. To further reduce the scan time, the sampling of specific q-space data points can be omitted following the compressed sensing (CS) theory which allows the accurate data reconstruction from undersampled measurements. While parallel imaging specifically focuses on rapid spatial undersampling in k-space, CS theory has been investigated to accelerate dMRI through undersampling of either k-space or q-space, or even both. Since the application of parallel imaging and CS acceleration of the diffusion encoding in dMRI (CS-dMRI) is central to the works in this thesis (see chapters 4 and 5), this chapter is dedicated to the introduction of parallel imaging as well as CS theory and its application to various dMRI techniques for accelerated image acquisition and the full recovery of the diffusion propagator from sparse measurements. Compared to parallel imaging, which is a premise for fast dMRI in general, CS-dMRI is pivotal to this work, and is thus explained in more detail.

3.1 Parallel imaging in MRI

In dMRI, parallel imaging was introduced in the late 90s, early 2000s when the spatial information inherent to multi-channel receive coils was first used to compensate for k-space undersampling either in image space (Pruessmann et al., 1999) or k-space (Griswold et al., 2002). The application of parallel imaging across multiple simultaneously excited slices was first reported by Larkman et al. (2001) for MR imaging of the knee. The slices at different positions across the leg were distinguished by the spatial information given by the positions of multiple MR receive coils. For accelerated slice parallel imaging, Breuer et al. (2005) proposed to acquire multiple slices simultaneously with additional shifts along the phase (and/or readout) direction with respect to each other. Thus, they could be separated more efficiently and distinctly. Nunes et al. (2006) introduced simultaneous multi-slice (SMS) acquisition to single shot EPI as presented in section 2.5.2. All of such introduced simultaneous multi-slice methods have in common that a multi-band RF pulse is used for excitation of several slices repeated by a certain distance. The number of excited slices is often denoted as the multi-band factor. More recently, advances in SMS EPI by Setsompop et al. (2012), Xu et al. (2013) and Cauley et al. (2014) further improved simultaneous multi-slice imaging for dMRI. Yielding a significant reduction in scan time, especially in combination with compressive sampling approaches, SMS imaging with slice acceleration up to a multi-band factor 3 was successfully applied in long-term population studies (Setsompop et al., 2013; Tobisch et al., 2018).

3.2 Compressed sensing theory

In signal processing, the established Nyquist-Shannon theorem (Shannon, 1949) states that signal sampling should be performed at least at the Nyquist rate to avoid aliasing. This Nyquist criterion also dictates the acquisition of MR signals as discussed in section 2.5.2. With the introduction of CS as a novel compressive sampling approach (E.J. Candès et al., 2006; Donoho, 2006), however, a research field successfully investigating Sub-Nyquist signal sampling opened up. Combining the data acquisition with CS, the signal of interest is sampled below the Nyquist rate, but a full recovery of the complete signal is possible if two main premises are accounted for: sparsity and incoherence (Candès and Romberg, 2007; Candès and Wakin, 2008; Donoho, 2006). Compared to parallel imaging, no spatial coil information would thus be needed if CS was used for undersampled k-space reconstruction. In the following sections, the CS theory is explained in the context of its application to MRI proposed by Lustig et al. (2007).

3.2.1 Sparsity and incoherence

Sensing an object of interest, e.g. to generate an image of this object, means, in a discrete description, that a subset $\mathbf{\Omega} \subset \{1, \ldots, n\}$ of $|\mathbf{\Omega}| = m$ samples of the discrete signal $\mathbf{f} \in \mathbb{R}^n$ representing the object in time (e.g. sound wave) or space (e.g. image) domain are acquired by means of a sensing

basis $\mathbf{\Phi}$ of size $n \times n$

$$\mathbf{y} = \mathbf{\Phi f} \tag{3.1}$$

where $\mathbf{y} \in \mathbb{R}^m$ is the vector of m measurements, with $m = n$ in this case. Signal sampling often captures redundant information. This is because the signal itself is usually compressible and $\mathbf{f}_s$ defines a sparse representation of the signal $\mathbf{f}$ in a suitable basis $\mathbf{\Psi}$ of size $n \times n$

$$\mathbf{f}_s = \mathbf{\Psi c} \tag{3.2}$$

where $\mathbf{c}$ is the vector of coefficients of the sparsifying transform. Signal sparsity describes the amount of non-zero coefficients that suffice to represent the object of interest without significant loss of quality compared to the representation with the complete set of coefficients. The exploitation of such signal sparsity is ever-present in today's signal processing, for example, to condense the acquired signal by means of compression algorithms or to correct for noise in audio and image processing. Common choices for a sparsifying transform are the discrete cosine transform (DCT) used e.g. in MPEG video compression and the wavelet transform applied in JPEG-2000 image compression (Sandilya and Nirmala, 2017). In MRI, the wavelet transform as well as the total variation (TV) (Rudin et al., 1992) are frequently applied, with the latter also being beneficial in combination with other sparsifying transforms (Lustig et al., 2007). These processing techniques for retrospective compression or denoising, however, require the complete signal to be collected.

In contrast, if a sparse representation of an object of interest exists, the knowledge of this signal sparsity can already be exploited at the sampling stage to improve the efficiency of the acquisition process. The CS acquisition approach aims at collecting only the information content during signal sampling that allows an accurate reconstruction of the sparse signal representation $\mathbf{f}_s$, i.e. CS already acquires the compressed signal itself. This is achieved by incorporating an undersampling matrix $\mathbf{R_\Omega} \in \mathbb{R}^{m \times n}$ (now $m \ll n$) in Eq. (3.1) (Candès and Romberg, 2007; Candès and Wakin, 2008)

$$\mathbf{y} = \mathbf{R_\Omega \Phi f} \tag{3.3}$$

To enable an accurate reconstruction of the signal from undersampled measurements, the second CS condition, incoherence, needs to be accounted for. Specifically, incoherence of the sensing and the sparsity basis is required. For this purpose the restricted isometry property (RIP) (E.J. Candès et al., 2006; E Candès et al., 2006) has been introduced as a measure of the robustness of CS and is linked to the coherence of sensing and sparsity domain. For the assessment of incoherence, it is beneficial to rewrite Eq. (3.3) using a sparse representation of the signal as described in Eq. (3.2)

$$\mathbf{y} = \mathbf{R_\Omega \Phi \Psi c} = \mathbf{Ac} \tag{3.4}$$

where the matrix $\mathbf{A}$ is the CS matrix composed of the undersampling, sensing and sparsity bases.

For an accurate CS reconstruction, $\mathbf{A}$ must obey the RIP which demands that column vectors taken from arbitrary subsets of $\mathbf{A}$ are nearly orthogonal (Candès and Wakin, 2008). It is, however, a difficult task to prove that the RIP is obeyed for a specific combination of sensing and sparsity bases. Fortunately, Baraniuk et al. (2008) showed that with high probability the RIP is obeyed when choosing Cartesian random matrices as the sensing basis $\mathbf{\Phi}$.

With the accurate translation of CS theory into MR imaging, an undersampled MRI acquisition is possible and thus, the imaging process can be significantly accelerated, which is of great interest for experiments with limited scan time. The raw MR signal in MRI is acquired in time domain, which imaging gradients transform into the domain of spatial frequencies, the k-space, and thus, $\mathbf{y}$ is a vector of Fourier coefficients collected by means of the sensing basis Φ. The MR image represents the desired signal $\mathbf{f}$ which is formed via the Fourier transform and has a sparse representation in the image or another sparsifying domain of $\mathbf{\Psi}$. To take advantage of the sparse representation of the MR image for an efficient sampling process, the incoherence requirement in CS demands that the undersampling in the domain of the sensing basis $\mathbf{\Phi}$, e.g. k-space, leads to incoherent, noise-like artifacts in the space in which a sparse representation of the MR image is given via $\mathbf{\Psi}$ (Lustig et al., 2007). This constraint is fulfilled by an incoherent random sampling in the sensing domain (Baraniuk et al., 2008; Candès and Romberg, 2007).
The importance of incoherence can be illustrated by a simple 1D example. Figure 3.1 depicts the effect of random versus equispaced undersampling in the sensing domain on the reconstructed signal with (right column) and without added noise (left column). Assuming a signal $\mathbf{f}$ that is already sparse in its natural domain (Figure 3.1 a-b), i.e. $\mathbf{\Psi} = \mathbf{I}$, a 2-fold undersampling in the sensing domain can be achieved by random or equidistant undersampling (Figure 3.1 c-d). However, while equispaced sampling results in coherent aliasing upon transformation (here FT) back to the sparse domain (Figure 3.1 e-f) and the signal cannot be recovered correctly, acquiring random measurements in the frequency domain will introduce noise-like artifacts in the signal domain from which the strong signal components are already distinguishable (Figure 3.1 g-h). For a full recovery of the signal, the solution of an l_1-norm minimization needs to be found (Figure 3.1 i-j). The details of the reconstruction procedure will be discussed in the next section. As shown by the 1D example, random undersampling is at the core of the CS acquisition process. Thus, a suitable and efficient undersampling scheme needs to be established to allow for accelerated MRI acquisitions and subsequent CS reconstruction by means of an l_1-norm minimization approach.

3.2.2 CS reconstruction

Following an undersampled image acquisition that meets the CS requirements discussed in the previous section, the CS reconstruction aims at the recovery of the coefficients vector $\mathbf{c}$ from m undersampled measurements. Since $m \ll n$, this problem is ill-posed, but a solution can be found by solving the convex optimization problem via l_1-norm minimization known as the LASSO method (Tibshirani, 1996). From the reconstructed vector $\mathbf{c}$, an estimate of the desired representation of the signal $\mathbf{f}$, which, given the sparsity constraint in CS, is accurately approximated by $\mathbf{f}_s$, can be obtained via Eq. (3.2). In MRI, the outcome of the CS reconstruction is the MR image of the object

of interest obtained from a reduced number of measurements compared to conventional MRI. In this context, the sensing basis Φ is the Fourier transform $\mathcal{F}$ and $\mathbf{y}$ the vector of acquired k-space measurements.

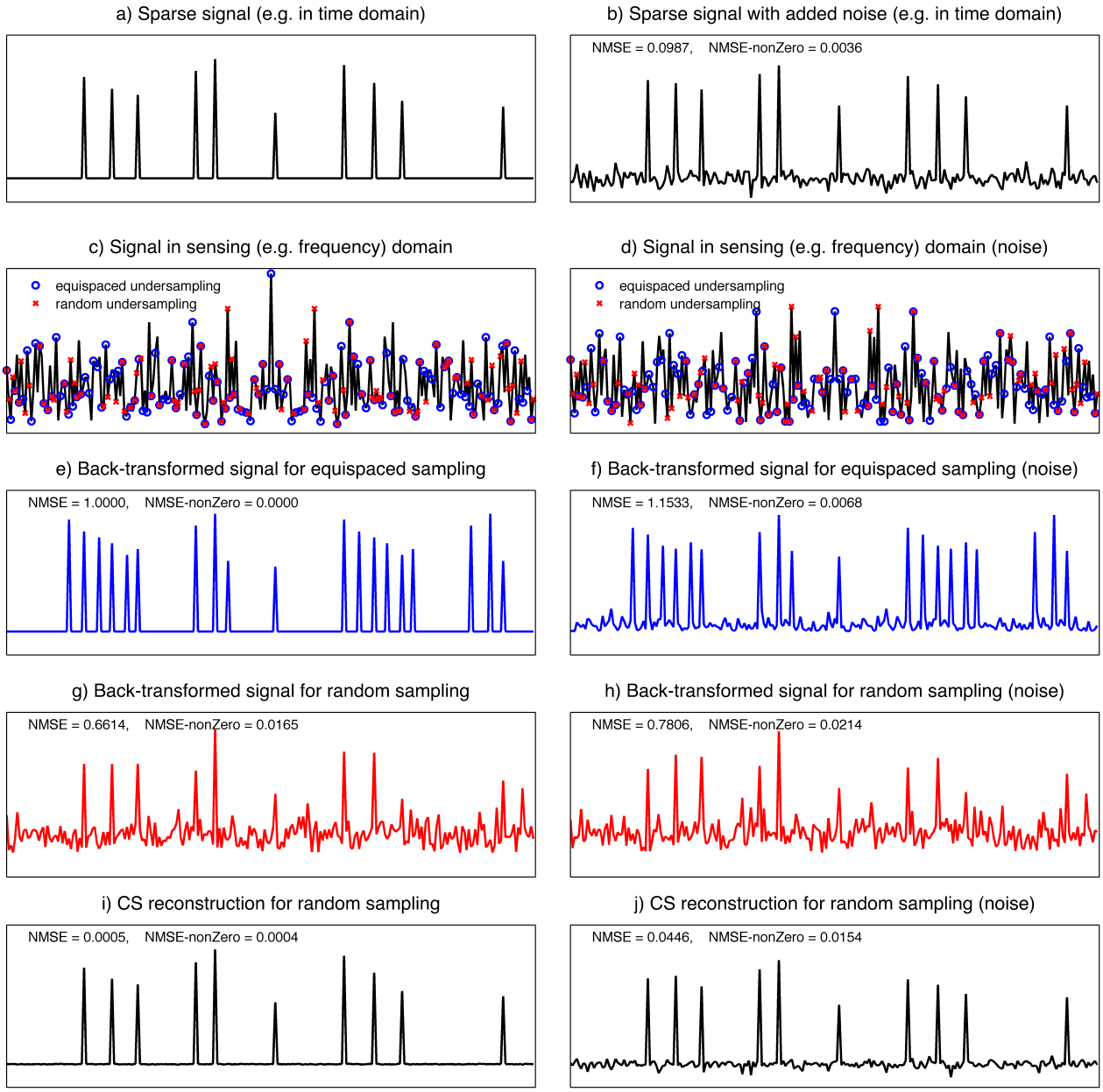

Figure 3.1: Sparsity and incoherence in CS: For a sparse signal (e.g. in time domain) (a-b), signal sensing can be performed (e.g. in frequency domain) by means of equispaced or random undersampling (c-d). While equispaced sampling results in aliasing artifacts in the back-transformed signal (e-f), random undersampling leads to noise-like artifacts in the back-transformed signal (g-h). Only in case of random sampling, accurate CS signal reconstruction is possible (i-j).

In order to recover the coefficients $\mathbf{c}$, a convex optimization problem needs to be solved by means of

$$\underset{\mathbf{c}}{\operatorname{argmin}} \left\| \mathbf{R}_{\mathbf{\Omega}} \mathbf{\Phi} \mathbf{\Psi} \mathbf{c} - \mathbf{y} \right\|_{l_2} + \lambda \left\| \mathbf{c} \right\|_{l_1} \tag{3.5}$$

where the regularization parameter λ balances the data consistency term $\left\| \mathbf{A}\mathbf{c} - \mathbf{y} \right\|_{l_2}$ that ensures a solution close to the original measurements and the term $\left\| \mathbf{c} \right\|_{l_1}$ that promotes sparsity of $\mathbf{c}$. Various optimization techniques have been proposed to solve this minimization problem. For instance, a nonlinear conjugate gradient descent (NLCG) algorithm can be applied to find a solution to Eq. (3.5) (Khare et al., 2012). Alternatively, several variates of the iterative soft thresholding algorithm (ISTA) have been proposed to solve Eq. (3.5) (Beck and Teboulle, 2009; Gong et al., 2013).

3.3 CS accelerated dMRI

Although compressive sampling can be applied in k-space, q-space or both to accelerate dMRI, within the scope of this thesis dMRI methods that accelerate q-space sampling are of main interest (see chapters 4 and 5). Acceleration of the diffusion encoding in dMRI by means of CS theory corresponds to undersampling of q-space which linearly translates to reduced scan time. However, sufficient data must be collected to fully recover the diffusion signal and the propagator through post hoc non-linear reconstruction. To fulfill the requirements of CS (see section 3.2), dMRI measurements are collected based on random sampling in q-space. Due to this randomness, the sampling scheme is, however, prone to miss important features of the diffusion process. In order to provide enough samples equally along all three directions of the q-space, it is essential to design an undersampling scheme that enables a robust and accurate reconstruction of the diffusion propagator. Different strategies for accelerated diffusion encoding that aim for an optimal distribution of q-space samples have been proposed and are based on either multi-shell (Jones et al., 1999; Merlet and Deriche, 2013) or Cartesian grid (Knutsson and Westin, 2013; Menzel et al., 2011; Paquette et al., 2015; Tobisch et al., 2014) sampling schemes. Furthermore, a wide range of sparsity bases has been proposed for CS-dMRI. In general, it has been shown, that sparse representations of the dMRI signal exist in suitable transformation domains, such as the total variation (Mani et al., 2014; Rathi et al., 2014), wavelet (Candès and Romberg, 2007) or curvelet (Varela et al., 2014) domain, which have also been combined successfully (Menzel et al., 2011; Sprenger et al., 2016). It has further been shown that the diffusion propagator itself is naturally sparse due to its Gaussian-like signal attenuation (Merlet and Deriche, 2010; Tobisch et al., 2019). Moreover, CS approaches based on dictionaries that learn the white matter structure in a data-driven way have been proposed for accelerated dMRI (Bilgic et al., 2012; Gramfort et al., 2014), but are considered less generalizable, especially for the application in population studies that investigate healthy as well as diseased individuals across the lifespan. CS accelerated dMRI has been investigated for different acquisition strategies that are typically tailored for specific dMRI reconstruction methods, such as single shell DTI/HARDI (Kuhnt et al., 2013; Landman et al., 2012; Michailovich et al., 2011), multi-shell HARDI

methods (J Cheng, S Merlet, et al., 2011; Rathi et al., 2014, 2011) such as SHORE (Merlet and Deriche, 2013), or DSI (Bilgic et al., 2012; Gramfort et al., 2014; Lee and Singh, 2010; Menzel et al., 2011; Paquette et al., 2015; Setsompop et al., 2013; Tobisch et al., 2019).

The works of this thesis focus on CS approaches to accelerate DSI. Conventional CS-DSI methods (Menzel et al., 2011; Paquette et al., 2015) reconstruct the diffusion propagator from sparse DSI measurements. Due to the Fourier relationship between propagator and dMRI signal (see section 2.6.1.3), the latter can also be recovered which means that the recovered dMRI signal can be used in addition to the propagator for subsequent dMRI analysis. This is in contrast to CS applications for single and multi-shell dMRI that recover the dMRI signal from sparse q-space samples by fitting e.g. tensor models (Landman et al., 2012) or continuous basis functions such as SHORE (Merlet and Deriche, 2013). Depending on the dMRI acquisition scheme, those CS methods extract diffusion features such as the diffusion tensor, the fODF or the propagator from the reconstructed dMRI signal. Various continuous basis functions (J Cheng, T Jiang, et al., 2011; Fick et al., 2016; Merlet and Deriche, 2013; Ozarslan et al., 2009) have been proposed for this purpose. SHORE signal modeling has been found to perform particularly well when combined with CS principles (Merlet and Deriche, 2013). Because they can be applied independently of the dMRI acquisition strategy, continuous basis functions can be used to model the dMRI signal from multi-shell as well as DSI acquisitions. In this thesis, we take advantage of this fact and investigate continuous signal modeling for the first time in CS-DSI. With the aim to compare Fourier to SHORE basis functions for sparse DSI reconstruction, chapter 4 evaluates conventional Fourier-based CS-DSI and a CS-DSI approach based on the SHORE basis in simulations, diffusion phantom data and *in vivo* DSI. Moreover, multiple approaches to generate q-space undersampling schemes are investigated in this work to determine an efficient sparse sampling strategy for accurate and robust CS-DSI. The findings on optimal CS-DSI presented in chapter 4 are then translated into the context of population imaging with particularly limited total scan time, which is an area of application appropriate to exploit the beneficial impact of CS-DSI. Chapter 5 proposes a Fourier-based CS-DSI protocol for population imaging. In a pilot study, this dMRI approach was compared to state-of-the-art multi-shell imaging conventionally applied in large cohort studies (Glasser et al., 2016; Miller et al., 2016).

Part II

Accelerated sparse dMRI acquisition and reconstruction

4

Comparison of basis functions and q-space sampling schemes for robust compressed sensing reconstruction accelerating diffusion spectrum imaging

Based on:

Tobisch A, Schultz T, Stirnberg R, Varela-Mattatall G, Knutsson H, Irarrázaval P and Stöcker T (2019) Comparison of basis functions and q-space sampling schemes for robust compressed sensing reconstruction accelerating diffusion spectrum imaging. NMR in Biomedicine. e4055.

Abstract

Time constraints placed on magnetic resonance imaging often restrict the application of advanced diffusion MRI (dMRI) protocols in clinical practice and in high throughput research studies. Therefore, acquisition strategies for accelerated dMRI have been investigated to allow for the collection of versatile and high quality imaging data, even if stringent scan time limits are imposed. Diffusion spectrum imaging (DSI), an advanced acquisition strategy that allows for a high resolution of intra-voxel microstructure, can be sufficiently accelerated by means of compressed sensing (CS) theory. CS theory describes a framework for the efficient collection of fewer samples of a data set than conventionally required followed by robust reconstruction to recover the full data set from sparse measurements. For an accurate recovery of DSI data, a suitable acquisition scheme for sparse q-space sampling and the sensing and sparsifying bases for CS reconstruction need to be selected. In this work we explore three different types of q-space undersampling schemes and two frameworks for CS reconstruction based on either Fourier or SHORE basis functions. After CS recovery, diffusion and microstructural parameters and orientational information are estimated from the reconstructed data by means of state-of-the-art processing techniques for dMRI analysis. By means of simulation, diffusion phantom and *in vivo* DSI data, an isotropic distribution of q-space samples was found to be optimal for sparse DSI. The CS reconstruction results indicate superior performance of Fourier-based CS-DSI compared to the SHORE-based approach. Based on these findings we outline an experimental design for accelerated DSI and robust CS reconstruction of the sparse measurements that is suitable for the application within time-limited studies.

Keywords: Diffusion MRI, Diffusion Spectrum Imaging, Compressed Sensing, sparse acquisition, q-space undersampling, basis functions, microstructure

4.1 Introduction

An accurate description of the diffusive transport of water molecules in tissue such as the brain's white matter is of great interest for the investigation of the complex microstructural architecture of the living human brain. Advanced diffusion magnetic resonance imaging (dMRI) techniques such as diffusion spectrum imaging (DSI) (Wedeen et al., 2005), multi-shell q-ball imaging (Aganj et al., 2010; Descoteaux et al., 2007; Tuch, 2004; Yeh et al., 2010) and diffusion propagator imaging (Descoteaux et al., 2011) sample q-space at both high angular and high radial resolution. Thus, they enable the reconstruction of the displacement of water molecules described by the diffusion propagator from the acquired diffusion weighted measurements.

The acquisition of dMRI data with such high resolution of the intra-voxel microstructure, however, is very time consuming and often not feasible for clinical applications or in time-limited research studies. Fortunately, the recent advance of simultaneous multi-slice (SMS) acquisitions (Cauley et al., 2014; Setsompop et al., 2012; Xu et al., 2013) and successful application of compressed sensing theory (Candès and Romberg, 2007; Donoho, 2006) to MRI (Lustig et al., 2007) and dMRI (Bilgic et al., 2012; Menzel et al., 2011; Paquette et al., 2015; Setsompop et al., 2013; Tobisch et al., 2015) can reduce the acquisition time significantly. Instead of sampling q-space as dictated by the Nyquist criterion, an efficient sampling strategy that selects fewer randomly distributed q-space samples can be applied to collect enough data to fully recover the diffusion signal and propagator through post hoc nonlinear reconstruction.

In dMRI, CS theory has been successfully applied to accelerate data collection and to reconstruct the desired signals from a set of undersampled measurements. For an accurate CS reconstruction, both an efficient q-space undersampling scheme and suitable sparsifying transforms for a sparse representation of the desired outcome of the dMRI experiment are required. Throughout the last decade, multiple works have investigated accelerated dMRI using compressed sensing to determine suitable q-space undersampling schemes, sparsity inducing bases and signal representations for robust and accurate CS reconstruction (Menzel et al., 2011; Merlet and Deriche, 2013; Paquette et al., 2015; Tobisch et al., 2015). With the common goal to recover the diffusion propagator and associated diffusion measures, two categories of CS reconstruction can be distinguished: first, accelerated DSI via CS incorporating the discrete Fourier transform, and second, CS reconstruction based on continuous signal modeling in a suitable orthonormal basis function. The former approach exploits the advantageous Fourier relationship between the diffusion weighted measurements and the displacement space to recover a discrete version of the diffusion propagator. Conventional DSI requires a high number of diffusion weighted measurements. But the successful application of CS theory to accelerate Fourier-based DSI first reported by Menzel et al. (2011) made fast DSI possible even in time-limited studies. With regard to the second category, several works have proposed to recover the propagator from sparse q-space samples by fitting continuous basis functions (J Cheng, T Jiang, et al., 2011; Fick et al., 2016; Merlet and Deriche, 2013; Ozarslan et al., 2009). Among these, the SHORE basis has been found to perform best, in particular when combined with CS principles (Merlet and Deriche, 2013).

To the best of our knowledge, the CS approach based on continuous signal modeling has never

been compared to Fourier-based CS reconstruction used to accelerate DSI. Therefore, our work presents a comparison of Fourier- to SHORE-based CS-DSI to investigate the performance of the Fourier and the SHORE basis in the reconstruction of sparse DSI acquisitions. We further examine the influence of q-space undersampling schemes and regularization strategies on CS reconstruction as well as the suitability of several sparsifying transforms based on simulation, diffusion phantom and *in vivo* dMRI experiments.

4.2 Material and methods

4.2.1 Fast dMRI via compressed sensing

Instead of acquiring a high number of n dMRI scans typically required for DSI and multi-shell q-ball imaging, the acquisition time can be significantly reduced by only collecting a subset of m acquisitions via an efficient sampling strategy suitable for CS. This means, an undersampling of q-space is performed compared to the conventional q-space sampling to acquire sufficient data for an accurate reconstruction of the diffusion signal and the molecular displacement space. The collection of a subset $\mathbf{\Omega} \subset \{1, \dots, n\}$ of $|\mathbf{\Omega}| = m$ random sparse acquisitions can be described by an undersampling matrix $\mathbf{R}_{\mathbf{\Omega}} \in \mathbb{R}^{m \times n}$ (Candès and Romberg, 2007; Candès and Wakin, 2008). In the case of DSI, conventional image acquisition requires the collection of at least $n = 258$ unique imaging volumes when considering a spherically truncated q-space grid of radius 5 (Wedeen et al., 2005) and utilizing the antipodal symmetry of the diffusion signal. Besides an efficient undersampling scheme, CS theory further requires that a sparse representation of the desired outcome $\mathbf{f} \in \mathbb{R}^n$ of the dMRI experiment, representing e.g. the fully sampled diffusion signal or the corresponding diffusion propagator, exists in a suitable orthonormal sparsifying basis $\mathbf{\Psi} \in \mathbb{R}^{n \times n}$, i.e. $\mathbf{f} = \mathbf{\Psi}\boldsymbol{x}$. If both conditions are met, CS reconstruction aims to recover the S-sparse coefficients vector $\mathbf{x} \in \mathbb{R}^n$ from the measurements vector $\mathbf{y} \in \mathbb{R}^m$. Since $m \ll n$, this problem is ill-posed, but a solution can be found by solving the convex optimization problem via l_1-norm minimization well known as the LASSO method (Tibshirani, 1996)

$$\underset{\mathbf{x} \in R^n}{\operatorname{argmin}} \left\| \mathbf{R}_{\mathbf{\Omega}} \mathbf{\Phi} \mathbf{\Psi} \mathbf{x} - \mathbf{y} \right\|_{l_2} + \lambda \left\| \mathbf{x} \right\|_{l_1} \tag{4.1}$$

The CS matrix $\mathbf{A} = \mathbf{R}_{\mathbf{\Omega}} \mathbf{\Phi} \mathbf{\Psi}$ is composed of the undersampling matrix $\mathbf{R}_{\mathbf{\Omega}}$ that restricts the q-space signals to the sparse measurements, the sparsity inducing basis $\mathbf{\Psi}$ and the sensing basis $\mathbf{\Phi}$ that describes an orthogonal measurement system for sensing $\mathbf{f}$, i.e. $\mathbf{y} = \mathbf{\Phi}\boldsymbol{f}$ (Candès and Romberg, 2007; Donoho, 2006). The regularization parameter λ balances the influence of the data consistency term $\|\mathbf{R}_{\mathbf{\Omega}} \mathbf{\Phi} \mathbf{\Psi} \boldsymbol{x} - \mathbf{y}\|_{l_2}$ and the sparsity constraint $\|\mathbf{x}\|_{l_1}$. From the reconstructed vector $\mathbf{x}$, the desired vector $\mathbf{f}$ representing the fully sampled diffusion weighted measurements or the corresponding diffusion propagator can be obtained via its sparse representation.

4.2.2 Basis functions for sparse DSI reconstruction

In recent literature several types of basis functions have been proposed and evaluated as sensing and sparsifying bases for sparse dMRI reconstruction. Our work aims to answer the question which of these bases performs best for sparse DSI reconstruction under otherwise similar conditions. We, therefore, investigate two different bases that have been introduced for CS recovery. First, we consider the discrete Fourier transform traditionally used in CS-DSI. Secondly, the 3D SHORE basis, a specific basis among those that enable a continuous signal representation, has been found to be well suited and to perform better than other continuous basis functions (Merlet and Deriche, 2013) when combining analytical signal modeling with CS principles. In this work, both basis functions are applied for the use of CS recovery from sparse DSI acquisitions. We investigate the ability of Fourier- and SHORE-based CS-DSI to fulfill the requirements of CS theory such as the required sparsity property and assess their performance in sparse signal reconstruction. For both approaches, the measurements vector $\mathbf{y}$ represents the m sparse q-space signals obtained through normalization of the undersampled DSI acquisitions by the non-diffusion weighted measurements.

4.2.2.1 Fourier-based CS-DSI

In traditional, fully sampled DSI, the Fourier transform relates the normalized dMRI q-space signal $E(\mathbf{q}, \Delta)$ to the displacement space of diffusive water molecules, the ensemble average diffusion propagator $P(\mathbf{R}, \Delta)$

$$P(\mathbf{R}, \Delta) = \int |E(\mathbf{q}, \Delta)| \exp(-i2\pi\mathbf{q} \cdot \mathbf{R}) d\mathbf{q} = \mathcal{F}^{-1}(E(\mathbf{q}, \Delta)) \tag{4.2}$$

where the diffusion gradient vector $\mathbf{q} = q\mathbf{g} = \frac{1}{2\pi}\gamma\delta\mathbf{g}$ describes the measurement of diffusion along the direction $\mathbf{g}$ in q-space with the diffusion gradient separation time Δ and the gradient duration δ as well as the gyromagnetic ratio γ. $\mathbf{R} = R\mathbf{r}$ represents the molecular displacement along the direction $\mathbf{r}$. To recover a complete DSI data set from undersampled DSI measurements, the simple Fourier relationship is incorporated into the CS formalism. The desired vector $\mathbf{f}$ that Fourier-based CS-DSI aims to reconstruct from sparse DSI acquisitions is the diffusion propagator $\mathbf{p}$ where $\mathbf{p}$ is comprised of the entries $P(\mathbf{R}, \Delta)$. Thus, the sensing basis is given by the discrete Fourier transform, i.e. $\mathbf{\Phi} = \mathcal{F}$. The sparsifying transform $\mathbf{\Psi}$ describes a suitable basis that provides a sparse representation of the diffusion propagator by means of the coefficients vector $\mathbf{x}$. Acknowledging their successful implementation in CS-DSI as reported in previous works (Menzel et al., 2011; Merlet and Deriche, 2010; Paquette et al., 2015), we investigate two different sparsifying transforms: total variation (TV) and the canonical basis, i.e. $\mathbf{\Psi} = \mathbf{I}$. The latter exploits sparsity directly in the propagator space (Merlet and Deriche, 2010) which means that $\mathbf{x} = \mathbf{p}$ and the CS matrix in this case is given by $\mathbf{A} = \mathbf{R}_{\mathbf{\Omega}}\mathcal{F}$. The canonical basis was found to outperform TV as the sparsifing transform (see also supplementary material). It was, thus, selected for the comparison of Fourier- to SHORE-based CS-DSI. For Fourier-based CS-DSI applying $\mathbf{I}$ as the sparsity transform, equation (4.1) can, thus, be rewritten as

$$\underset{\mathbf{p}\in R^n}{\operatorname{argmin}} \left\|\mathbf{R}_{\mathbf{\Omega}}\mathcal{F}\mathbf{p}-\mathbf{y}\right\|_{l_2} + \lambda_F \left\|\mathbf{p}\right\|_{l_1} \tag{4.3}$$

The regularization parameter λ_F is determined empirically (see Supplementary Figure 4.1) and set to a value of 10^{-6} and 10^{-3} for the canonical basis and the TV transform, respectively.

4.2.2.2 SHORE-based CS-DSI

The SHORE basis belongs to the category of basis functions that allow for a continuous representation of the diffusion signal and provide analytical expressions for several diffusion measures such as the diffusion propagator and the orientation distribution function (ODF) (Assemlal et al., 2009; J Cheng, T Jiang, et al., 2011; Merlet and Deriche, 2013). dMRI measurements are modeled in the SHORE basis as a linear combination of the basis Θ that is comprised of the radial basis X and the angular basis Y with k, i and j respectively representing the radial order and the angular order and degree

$$E(q\mathbf{u}) = \sum_{i=0,even}^{K} \sum_{k=i}^{(K+i)/2} \sum_{j=-i}^{i} c_{kij}\Theta_{kij}(q\mathbf{u}) \text{ with } \Theta_{kij}(q\mathbf{u}) = X_{ki}(q,\zeta)Y_i^j(\mathbf{u}) \tag{4.4}$$

where q is the norm of the diffusion gradient vector $\mathbf{q}$ and c_{kij} form the SHORE coefficients $\mathbf{c}\in\mathbb{R}^{n_c}$. n_c is the number of atoms of the SHORE basis and K is the radial SHORE order that bounds the angular order by $i \leq k$. Due to the symmetry property of the real diffusion signal, only the real and symmetric spherical harmonic basis Y_i^j is considered. ζ is the SHORE scale factor that is defined in units of mm^{-2} as $\zeta = 1/(8\pi^2\tau MD)$. It is calculated based on the diffusion sequence parameters applied for the image acquisition and the mean diffusivity (MD) obtained from the data (Merlet and Deriche, 2013). Note that in this work, the formation of the SHORE basis is identical to the one implemented in the Dipy library (Garyfallidis et al., 2014) which differs from the SHORE basis defined by Merlet and Deriche (2013). Selecting a SHORE order of $\{6,8,10,12\}$ results in $\{50,95,161,252\}$ basis atoms.

SHORE-based CS-DSI aims to reconstruct the fully sampled DSI data $\mathbf{y}_n \in \mathbb{R}^n$ directly from the acquired sparse q-space signals, i.e. the desired outcome of CS reconstruction is $\mathbf{f} = \mathbf{y}_n$. Previous work (Merlet and Deriche, 2013) reports that the SHORE basis $\mathbf{\Theta} \in \mathbb{R}^{n\times n_c}$ is a suitable sparsity inducing basis because modeling the signal in the SHORE basis, a sparse representation of the diffusion signal is given by means of the SHORE coefficients, i.e. $\mathbf{x} = \mathbf{c}$. For SHORE-based CS-DSI, $\mathbf{\Theta}_\Omega \in \mathbb{R}^{m\times n_c}$ forms the CS matrix $\mathbf{A}$ and equation (4.1) can, thus, be expressed as

$$\arg\min_{\mathbf{c}\in R^{n_c}} \left\|\mathbf{\Theta}_\Omega\mathbf{c}-\mathbf{y}\right\|_{l_2} + \lambda_{SH}\left\|\mathbf{c}\right\|_{l_1} \tag{4.5}$$

SHORE-based CS-DSI with l_1-norm regularization promotes the sparsity of the SHORE coefficients. We apply the iterative shrinkage and thresholding algorithm by Gong et al. (2013) to solve the

convex optimization problem expressed by equation (7.2). The regularization parameter λ_{SH} is determined empirically (see Supplementary Figure 4.1) and set to 10^{-6}. For SHORE order 8, λ_{SH} was adjusted to 10^{-7} for simulation data. To improve the robustness of SHORE modeling, Cheng (2012) recommends to apply a constraint for $E(0) = 1$ and Özarslan et al. (2013) have proposed to incorporate a non-negativity constraint on the diffusion propagator. We adopt the former constraint and implement the latter as an iteratively refined soft constraint, similar to Tournier et al. (2007).

4.2.2.3 Sparsity inducing bases

Besides the CS reconstruction framework based on the sparsity promoting l_1-norm minimization, according to CS theory, an accurate signal recovery requires a suitable sparsity inducing basis. For the evaluation of the required sparsity property, we determined the number of basis atoms that are associated with the sparse entries of the reconstructed vector $\mathbf{x}$ that suffice for an accurate representation of the signal of interest. In this case, we did not consider undersampled measurements, but rather the representation of the fully sampled signal of interest in a suitable sparsifying domain $\mathbf{\Psi}$, i.e. $\mathbf{f} = \mathbf{\Psi}\boldsymbol{x}$. For Fourier-based CS-DSI, the evaluation of the sparsity property of the canonical basis effectively means the evaluation of the sparsity of the diffusion propagator. That is because the propagator itself is assumed to naturally be sparse due to its Gaussian-like signal attenuation (Merlet and Deriche, 2010). A single Fourier transformation of $\mathbf{y}_n$ yields the propagator $\mathbf{p}$ and sparsity is determined in the displacement space. For the SHORE-based approach, we applied a least squares approach to compute the SHORE coefficients $\mathbf{c}$ from the signals $\mathbf{y}_n$ (Merlet and Deriche, 2013): $\mathbf{c} = (\mathbf{A}^T\mathbf{A})^{-1}\mathbf{A}^T\mathbf{y}_n$. We considered SHORE orders $\{6, 8, 10, 12\}$ to analyze the effect of the SHORE order on sparsity and reconstruction quality. To assess the sparsity property of the canonical and the SHORE basis used as sparsity inducing bases in Fourier- and SHORE-based CS-DSI, respectively, we quantified the minimum number of basis atoms required for an accurate representation of the signals $\mathbf{y}_n$. We consider the signal representation to be accurate if an NMSE of 0.015 and 0.05 or less is reached for noise-free simulations and *in vivo* data, respectively. The minimum number of atoms was determined by successively increasing the number of atoms (starting at 1) until NMSE≤ 0.015 and NMSE≤ 0.05 for simulation and *in vivo* data, respectively. If the NMSE threshold is never reached, all basis atoms have to be used. For simulations, we additionally assessed the sparsity at NMSE thresholds 0.03 and 0.05.

4.2.3 Sampling schemes for compressed sensing

The accurate recovery of the diffusion signal and propagator by means of CS reconstruction relies on a suitable q-space sampling scheme to collect the undersampled dMRI data. To reduce the risk of missing subtle details of the diffusive transport of the water molecules in brain tissue, recommendations are made in general for dMRI acquisitions schemes for an optimal sampling distribution that allows uniform angular q-space coverage (De Santis, Y Assaf, et al., 2014; Sprenger et al., 2016). They should likewise be considered for the generation of CS undersampling schemes. In state-of-the-art DSI accelerated using CS, dMRI scans are acquired by applying diffusion weighting gradients

distributed on a three-dimensional Cartesian q-space grid (Menzel et al., 2011) due to the Fourier relationship between the diffusion signal and the propagator. The samples are typically restricted by a spherical q-space truncation. Multiple Cartesian q-space sampling strategies have been investigated in recent literature on CS-DSI. Menzel et al. (2011) introduced CS-DSI and recommend to generate the undersampling scheme with a densely sampled q-space center based on a random Gaussian sampling distribution. Paquette et al. (2015) extended the approach for scheme generation commonly applied in single shell high angular resolution diffusion imaging (HARDI) (Tuch et al., 2002). They propose to introduce a random radius to each of the q-space samples that have been uniformly distributed on a sphere based on the electrostatic repulsion algorithm (Jones et al., 1999) and to subsequently match them to the Cartesian grid. Knutsson and Westin (2013) introduced a method to generate 3D non-Cartesian sample distributions that aim for isotropic sampling of q-space. Similar to the uniform angular and random radial sampling scheme by Paquette et al. (2015), this approach extends the electrostatic repulsion algorithm used for q-ball imaging (Jones et al., 1999). We generated an isotropic undersampling scheme with the metric T-21112 and a charge density of r^{-2} to sample more densely in the center of q-space (Knutsson and Westin, 2013) which was found to be optimal for sparse DSI acquisition (Tobisch et al., 2015, 2014). The generation of these 3D q-space sample distributions naturally tends to promote the formation of shells and thus, combines aspects of both multi-shell and Cartesian sampling. It was, further, suggested to be potentially advantageous for compressed sensing applications. In this work, we investigate the suitability of this approach for q-space undersampling in CS-DSI. Fourier-based CS-DSI investigated in this work requires Cartesian q-space sampling. Thus, all samples have to be matched to the Cartesian grid. To investigate the influence of q-space sampling strategies on CS reconstruction, we compare three approaches for the generation of undersampling schemes: random Gaussian (rG) (Menzel et al., 2011), uniform angular and random radial (ua-rr) (Paquette et al., 2015) and isotropic (iso) (Knutsson and Westin, 2013; Tobisch et al., 2015, 2014) q-space sampling.

4.2.4 Evaluation metrics for CS reconstruction

CS reconstruction was performed by means of Fourier- and SHORE-based CS-DSI to recover the diffusion propagator and the fully sampled diffusion signals, respectively. In this work, CS undersampling was performed retrospectively for simulations, diffusion phantom and *in vivo* DSI data. This allows the quantification of the CS reconstruction error with respect to the fully sampled data sets. A q-space grid of size 11x11x11 truncated to a sphere is fully covered by 515 samples forming the q-space signal vector $\mathbf{s} \in \mathbb{R}^{2n-1}$. The resulting data set of 515 imaging volumes containing one b=0 image and 514 DWIs provides the ground truth signals for CS evaluation. In case of simulation data, we take the noise-free signals as the ground truth.

First, we computed the normalized mean square error (NMSE) between the ground truth and the reconstructed signals. CS recovery reconstructs the signal vector $\mathbf{y}_n$, but also the signals corresponding to the antipodal symmetric q-space samples of the diffusion gradient directions applied during data acquisition. For the vector $\hat{\mathbf{s}}_i$ representing the reconstructed diffusion signals at voxel location i, the NMSE was determined with respect to the fully sampled q-space signals $\mathbf{s}_i$ according

to

$$\frac{1}{|\Omega|}\sum_{i\in\Omega}\frac{\|\hat{\mathbf{s}}_i-\mathbf{s}_i\|^2}{\|\mathbf{s}_i\|^2} \tag{4.6}$$

where $|\Omega|$ is the sum of all voxels of the set of voxels Ω.

We further computed different parameters related to tissue microstructure from the reconstructed and the ground truth data and determine the CS reconstruction quality. The mean apparent propagator (MAP) MRI model (Fick et al., 2016; Özarslan et al., 2013) implemented in the Dipy library was applied to generate parameter maps for three different q-space indices: mean squared displacement (MSD), return-to-origin probability (RTOP) and non-Gaussianity (NG). For the evaluation of the diffusion parameter $\hat{p}_i$ estimated from the reconstructed signals $\hat{\mathbf{s}}_i$, the NMSE was calculated by

$$\frac{1}{|\Omega|}\sum_{i\in\Omega}\frac{\|\hat{p}_i-p_i\|^2}{\|p_i\|^2} \tag{4.7}$$

where the microstructural parameter p_i is estimated from the fully sampled measurements $\mathbf{s}_i$.

Moreover, the estimation of fiber orientation distribution functions (fODFs) provides orientational information of the diffusive transport of water molecules in brain microstructure. We determined the orientation of dominant fODF peaks and the crossing angle between crossing fibers using the multi-tissue deconvolution approach by Ankele et al. (2017) which can be applied independently of the acquisition scheme. For a quantitative assessment of the orientational information obtained via CS-DSI, the angular deviation in fiber orientation between CS reconstruction and ground truth was computed. Further, the mean absolute error in the crossing angle was evaluated for all $i \in \Omega_{cross}$ with Ω_{cross} the subset of multi-fiber voxels in Ω with a crossing angle between the two dominating fiber fascicles greater than 30°. Additionally, we computed the angular cross correlation (acc) (Anderson, 2005) between fODFs of CS reconstructed and ground truth diffusion signals for distinct regions of interest within the imaging volumes of the diffusion phantom and *in vivo* data.

4.2.5 CS-DSI experiments

4.2.5.1 Simulations

By means of the Camino Monte-Carlo simulator (Hall and Alexander, 2009) we generated pulsed gradient spin echo diffusion signals within a substrate of crossing cylinders (TE = 135.5 ms, b_{max} = 8350 s/mm^2, Δ = 65.9 ms, δ = 57.4 ms). For fully sampled DSI, we sampled q-space at 258 points distributed on a spherically truncated Cartesian 11x11x11 grid. Diffusion signals were simulated for voxels containing two fiber bundles with crossing angles of 35°, 55° and 90°. Across the Monte-Carlo repetitions, the gradient directions used for the simulation were randomly rotated in 3D to vary

the orientation of the simulated crossing structures with respect to the sampling scheme. In this way, the simulation data approximates brain microstructure with well-defined but unknown orientations. In total, 600 different crossing structures were thus generated per crossing angle. Subsequently, Rician noise corresponding to SNR of 20 in the b=0 signal was added to simulate realistic dMRI acquisitions. Retrospective undersampling of the ground truth data was performed for a range of CS acceleration factors to simulate accelerated DSI acquisition. We investigate acceleration factors of {8.0,5.4,4.0,3.2,2.7,2.3,2.0} which correspond to N={32,48,64,80,96,112,128} DWI samples drawn from the ground truth data set. We applied 100 random instances of each of the three different Cartesian sampling schemes for CS reconstruction of each of the 1800 crossing structure signals. We further evaluated the influence of Cartesian compared to non-Cartesian q-space sampling, such as multi-shell sampling, on CS reconstruction. The SHORE basis can be applied to dMRI data for a continuous representation of q-space signals, independently of the sampling strategy. Thus, we applied the isotropic q-space sampling scheme without matching the samples to the Cartesian grid for SHORE-based CS-DSI with 4-fold CS acceleration. By design this scheme resembles a multi-shell sampling scheme for optimal q-space coverage. For each evaluation metric, we report the mean and standard deviation of the error values across all instances of the sampling patterns.

4.2.5.2 Diffusion phantom

We acquired fully sampled DSI data (258 q-space samples) from two physical diffusion phantoms (Moussavi-Biugui et al., 2011) respectively containing microstructure crossing at 60° and 90° (TE/TR = 139ms/2000ms, b_{max} = 8350 s/mm^2, Δ = 66.1ms, δ = 55.9ms). All phantom scans were collected on a 3T Siemens MAGNETOM Prisma MRI scanner (Siemens Healthcare, Erlangen, Germany) at 2.0mm isotropic spatial resolution using a 64-channel head-neck coil. Per phantom data set, a single slice representing the region of the two fiber bundles crossing within each of the phantoms was selected for the evaluation of CS reconstruction. Following CS recovery according to various undersampling schemes, we quantified the reconstruction quality based on the NMSE of the reconstructed signal with respect to the acquired data and on the angular error in the crossing angle and orientation of the phantom fiber bundles. Instead of determining microstructural parameters by means of the MAP MRI model which is tailored for brain tissue data, for the phantom data we focused on the extraction of orientational information. We visualized fODFs within the crossing fiber region of each of the diffusion phantoms and determined the corresponding angular cross correlation of reconstructed and ground truth fODFs. We masked the phantom data to only process single and crossing fiber voxels.

4.2.5.3 *In vivo* dMRI

DSI acquisitions were collected from one healthy female (34 years) on the 3T Prisma scanner at 1.5mm isotropic resolution (TE/TR = 105ms/6100ms, b_{max} = 6800 s/mm^2, Δ = 51.3ms, δ = 20.1ms) using a 64-channel head-neck coil. Approval to undertake the MRI acquisition was obtained from the ethics committee of the University of Bonn, Medical Faculty. The study was carried out in accor-

dance with the recommendations of the International Council for Harmonisation (ICH) Good Clinical Practice (GCP) standards (ICH-GCP). We obtained written informed consent from the participant in accordance with the Declaration of Helsinki. The imaging protocol applied monopolar diffusion weighting and a partial Fourier factor of 6/8 to minimize TE. Image acquisition of 96 axial slices was accelerated by an SMS dMRI sequence employing threefold slice-acceleration. The readout bandwidth was 1785 Hz/pixel. No in-plane acceleration was applied (GRAPPA R=1). Sequence parameters were optimized to allow for 2.3-fold accelerated CS-DSI within about 12 minutes (Tobisch et al., 2018). 257 diffusion weighted and 8 interleaved, non-weighted images were acquired with both anterior-to-posterior and posterior-to-anterior phase encoding (PE). The total scan time was 55 minutes. The acquisition of DSI data with reversed PE polarity enables the accurate correction of image distortions. We applied FSL's topup (Andersson et al., 2003) and eddy (Andersson and Sotiropoulos, 2015) to estimate and correct for susceptibility-induced geometric distortions as well as eddy-current-induced artifacts and subject motion. Retrospective undersampling of the fully sampled *in vivo* DSI data was performed for a CS acceleration factor of 2.3 and 4. Selected at random, only one distinct instance of each of the three sampling scheme types was applied in contrast to simulation and phantom data. After CS reconstruction, we estimated fODFs and diffusion parameter maps as for simulation and phantom data. The angular error and cross correlation as well as the NMSE of the diffusion signal, MSD, NG and RTOP were computed. For the calculation of the CS reconstruction error metrics, we considered the voxels within well-known white matter tracts in the brain defined in standard space by the JHU ICBM DTI 81 atlas (Mori et al., 2008) available in FSL which we transformed into diffusion native space. This mask was further adjusted to contain mainly pure WM voxels based on recommendations by Jeurissen et al. (2013).

4.3 Results

4.3.1 Basis functions for sparse DSI reconstruction

We assessed Fourier- and SHORE-based CS-DSI in terms of the sparsity property of the applied basis functions to ensure both approaches comply with the requirements of CS theory. Figure 4.1 depicts the number of basis atoms (top row) required for an accurate representation of the diffusion signal (bottom row) representing the degree of sparsity of the selected sparsity inducing bases in Fourier- and SHORE-based CS-DSI. For simulations that represent WM microstructure (Figure 4.1A), the number of atoms as well as the corresponding NMSE is plotted for the three different NMSE thresholds $\{0.015, 0.03, 0.05\}$ for each CS-DSI approach. NMSE values as low as the selected threshold for correct reconstruction are obtained for the canonical basis and for the SHORE basis applying different SHORE orders. The higher the SHORE order the lower the sparsity. The sparsity of the canonical basis representation of the diffusion propagator is lower than for the SHORE basis. For an axial slice of the *in vivo* data, Figure 4.1B depicts the minimum number of atoms required for an accurate signal representation and the corresponding NMSE. Further, the mean and standard deviation were computed across WM, GM and CSF voxels of the whole brain. The sparsity induced by the SHORE basis decreases for increasing SHORE order in WM and GM. The same trend is

observed in CSF except for SHORE order 6, for which an increase in the average number of required atoms is observed compared to order 8 and 10. This coincides with the NMSE values obtained for CSF at SHORE order 6 which are above the selected threshold, whereas a mean NMSE at or below the NMSE threshold is reached for any other combination of SHORE order and brain tissue type. For the diffusion propagator, the NMSE threshold is reached throughout the brain with a high sparsity for GM and WM and a lower sparsity for CSF.

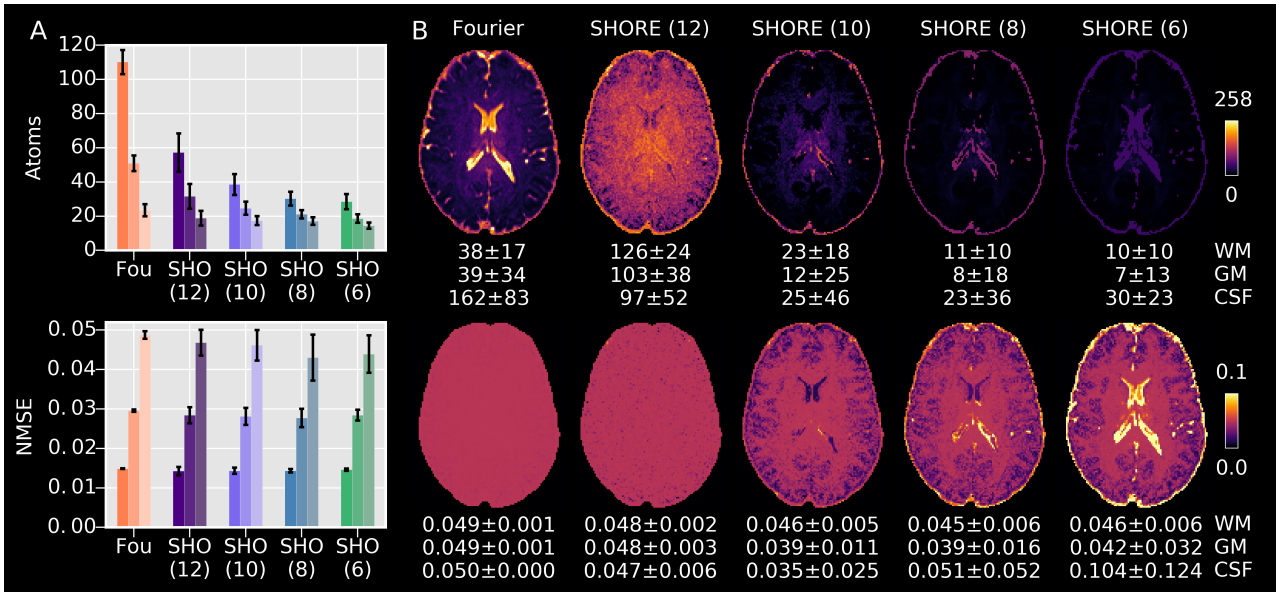

Figure 4.1: Degree of sparsity induced by the canonical and SHORE (order 6, 8, 10 and 12) basis used as sparsifying transforms in Fourier- and SHORE-based CS-DSI, respectively. (A) For simulations, the number of required atoms for sparse representation of the diffusion signal and the propagator as well as the corresponding NMSE are depicted for three NMSE thresholds. From left to right per CS-DSI approach, atom and NMSE values refer to: NMSE $\leq$ 0.015, NMSE $\leq$ 0.03, NMSE $\leq$ 0.05. (B) The number of atoms required to reach an NMSE as close as possible to the NMSE threshold for accurate representation (NMSE $\leq$ 0.05) are depicted for an axial slice of *in vivo* dMRI data as well as the mean and standard deviation across WM, GM and CSF voxels of the whole brain.

4.3.2 CS-DSI experiments

For simulations, diffusion phantom and *in vivo* DSI data, we analyzed the performance of different reconstruction methods in terms of CS recovery differing in their selected sensing and sparsifying bases. For Fourier-based CS-DSI, exploiting the sparsity directly in the propagator space leads to comparable or even lower NMSE and angular error compared to Fourier-based CS-DSI using TV (see Supplementary Figures 4.2, 4.3 and 4.4). Due to the superior reconstruction obtained using the canonical basis as the sparsifying basis, only the results for this approach are presented here. In the following we compare the reconstruction results obtained from sparse simulation, diffusion phantom and *in vivo* DSI data by applying Fourier-based and SHORE-based CS-DSI (SHORE orders 6 and 8).

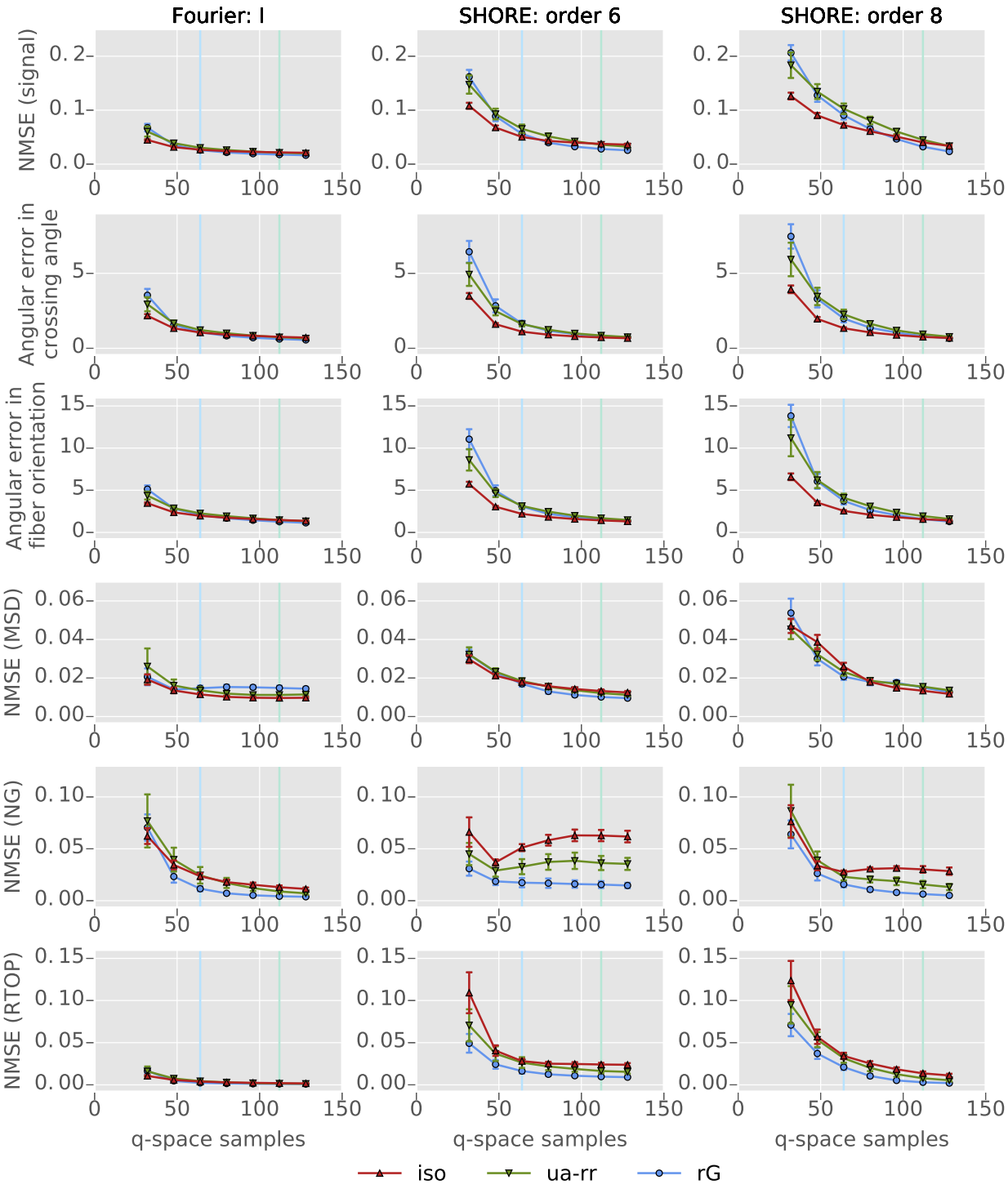

Figure 4.2: CS reconstruction of simulations obtained from Fourier-based CS-DSI applying the canonical basis as sparsity basis and from SHORE-based CS-DSI using SHORE order 6 and 8. CS reconstruction quality is quantified by computing the angular error in crossing angle and in fiber orientation and the NMSE of the diffusion signal, MSD, NG and RTOP. For each metric, the three different q-space sampling schemes under investigation, iso, ua-rr and rG, are compared. The number of q-space samples corresponding to CS acceleration factors 4 and 2.3 are marked by the light blue and light green vertical lines, respectively. Overall, lower reconstruction errors are obtained using Fourier-based CS-DSI.

Table 4.1: The NMSE of the diffusion signal quantifies the quality of CS reconstruction of simulations obtained from Fourier-based CS-DSI applying the canonical basis as sparsity basis and from SHORE-based CS-DSI using SHORE order 6 and 8. For an CS acceleration factor of 4, the iso q-space sampling scheme was compared against its non-Cartesian variant in the case of SHORE-based CS-DSI. Overall, Fourier-based CS-DSI yielded lower reconstruction errors than SHORE-based CS-DSI. For the latter, comparable CS reconstruction is observed with and without Cartesian sampling.

		Fourier: I	SHORE: order 6	SHORE: order 8
NMSE (noise-free)	Cartesian	0.0115 ± 0.0005	0.0409 ± 0.0024	0.0415 ± 0.0031
	non-Cartesian		0.0440 ± 0.0029	0.0452 ± 0.0028
NMSE (SNR 20)	Cartesian	0.0263 ± 0.0008	0.0514 ± 0.0024	0.0745 ± 0.0034
	non-Cartesian		0.0547 ± 0.0019	0.0701 ± 0.0036

4.3.2.1 Simulations

For simulations, CS reconstruction quality was quantified across the simulated crossing structures by computing the angular error in crossing angle and in fiber orientation and the NMSE for four different diffusion measures: the diffusion signal, MSD, NG and RTOP. For each metric, the three different q-space sampling schemes under investigation, iso, ua-rr and rG, were compared. For simulation data, Figure 4.2 compares CS reconstruction results obtained from Fourier- and SHORE-based CS-DSI, with the latter applying SHORE orders 6 and 8. Overall, using a SHORE order of 6 in SHORE-based CS-DSI improves CS reconstruction compared to order 8, except for the reconstruction of NG and RTOP at low acceleration factors, in which case the SHORE order of 8 further reduces the NMSE. Fourier-based CS-DSI, however, provides lower reconstruction errors than SHORE-based CS-DSI across all metrics. The isotropic CS sampling scheme performs similar or even superior to the schemes ua-rr and rG for both Fourier- and SHORE-based CS-DSI, apart from the following exceptions: the Gaussian undersampling scheme is more performant in the Fourier-based CS reconstruction of NG in the range of 3- to 5-fold CS acceleration; furthermore, the Gaussian scheme outperforms the other schemes in SHORE-based CS reconstruction of the diffusion signal at very low CS factors and of NG and RTOP across all CS factors. For acceleration factors below 8, only small standard deviations across the 100 instances of each undersampling scheme are observed for both CS-DSI methods. A similar trend was observed in noise free simulations (see Supplementary Figure 4.5), albeit with reduced reconstruction errors.

For 4-fold CS acceleration, Table 4.1 reports NMSE values obtained from Fourier-based CS-DSI applying the canonical basis as sparsity basis and from SHORE-based CS-DSI using SHORE order 6 and 8. For the latter CS approach, Cartesian and non-Cartesian q-space sampling were considered. Comparable performance was observed for both sampling strategies. Fourier-based CS-DSI yielded the lowest reconstruction errors for simulations with and without noise.

4.3.2.2 Diffusion phantom

The CS reconstruction of undersampled dMRI acquisitions of the 90° and the 60° diffusion phantoms was assessed. We computed the NMSE of the diffusion signal as well as the angular error in crossing angle and in fiber orientation and investigate Fourier- and SHORE-based CS-DSI with respect to the three different q-space sampling schemes of interest. Figure 4.3 depicts the reconstruction errors of Fourier- and SHORE-based CS-DSI with regard to these metrics. Comparable results are obtained using either SHORE order 6 or 8 in SHORE-based CS-DSI. The reconstruction errors for Fourier-based CS-DSI are again lower than those for the SHORE-based CS recovery. For both CS approaches, the isotropic sampling schemes outperforms the schemes ua-rr and rG in all of the metrics at high CS factors greater than 3 and comparable results across schemes are obtained otherwise. Extending the assessment of the reconstruction of the orientational information obtained via CS-DSI, Figure 4.4 visualizes fODFs within the crossing fiber region of both the 90° and the 60° diffusion phantom for both Fourier- and SHORE-based CS-DSI with acceleration factors of 4 and 2.3. For 4-fold CS acceleration, Fourier-based CS-DSI in combination with an isotropic undersampling of q-space provides the highest correlation between ground truth and reconstruction. Overall, for all schemes, SHORE-based CS-DSI using order 8 performs worst and the correlation values for SHORE-based CS-DSI using order 6 are comparable to or further exceeded by Fourier-based CS-DSI. For a CS acceleration factor of 2.3, Fourier-based CS-DSI provides the highest correlation factors up to 0.98. Using SHORE order 6 again leads to better fODF reconstruction compared to order 8.

4.3.2.3 *In vivo* dMRI

Based on the results of the simulation and phantom experiments, we applied SHORE-based CS-DSI with an SHORE order of 6 for the reconstruction of *in vivo* dMRI acquisitions. Figure 4.5 shows NMSE and angular error values of the CS reconstruction of the retrospectively undersampled DSI acquisitions for both Fourier- and SHORE-based CS-DSI with respect to the three different types of q-space sampling schemes of interest. Since only one instance of each sampling scheme type was selected, no standard deviation is provided for the NMSE of MSD, NG and RTOP. Overall, Fourier-based CS-DSI outperforms the SHORE-based approach in the reconstruction of the diffusion signal itself and MSD and RTOP obtained from the propagator for both 4-fold and 2.3-fold CS acceleration. NG reconstruction is superior for SHORE-based CS-DSI for an acceleration factor of 4, but comparable for both CS approaches for lower acceleration. With respect to the angular errors both CS-DSI approaches perform comparably. Comparable NMSE of the signal and angular errors are obtained across undersampling schemes for both Fourier- and SHORE-based CS-DSI. For a CS factor of 2.3, the Gaussian scheme provides the best reconstruction of NG. For MSD and RTOP, CS reconstruction errors are very low for Fourier-based CS-DSI across all schemes, for SHORE-based CS-DSI the Gaussian scheme yields the best reconstruction results.

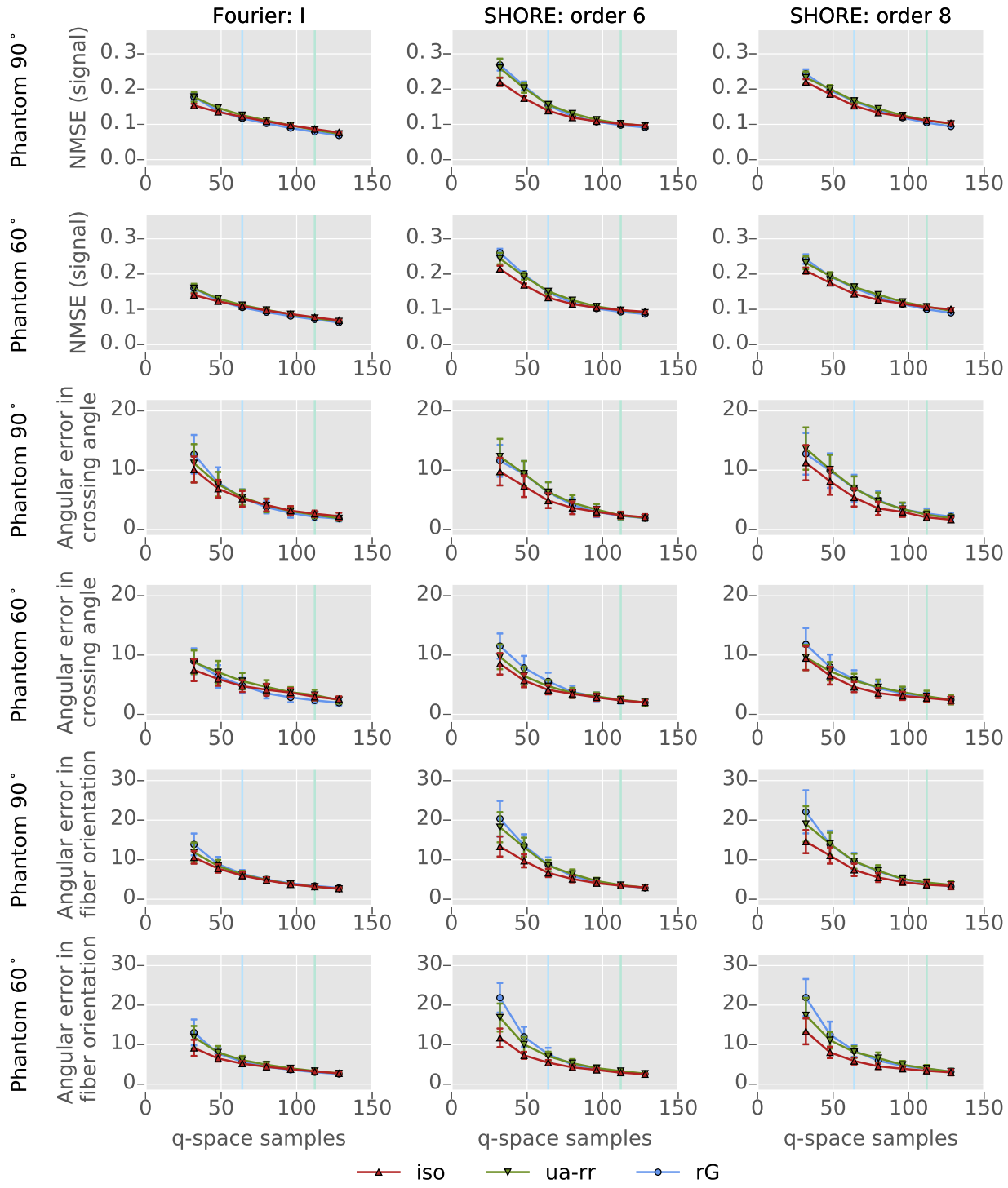

Figure 4.3: CS reconstruction of diffusion phantom data obtained from Fourier-based CS-DSI applying the canonical basis as sparsity basis and from SHORE-based CS-DSI using SHORE order 6 and 8. CS reconstruction quality is quantified by computing the angular error in crossing angle and in fiber orientation and the NMSE of the diffusion signal. For each metric, the three different q-space sampling schemes under investigation, iso, ua-rr and rG, are compared. The number of q-space samples corresponding to CS acceleration factors 4 and 2.3 are marked by the light blue and light green vertical lines, respectively. Comparable or even lower reconstruction errors are obtained using Fourier-based CS-DSI.

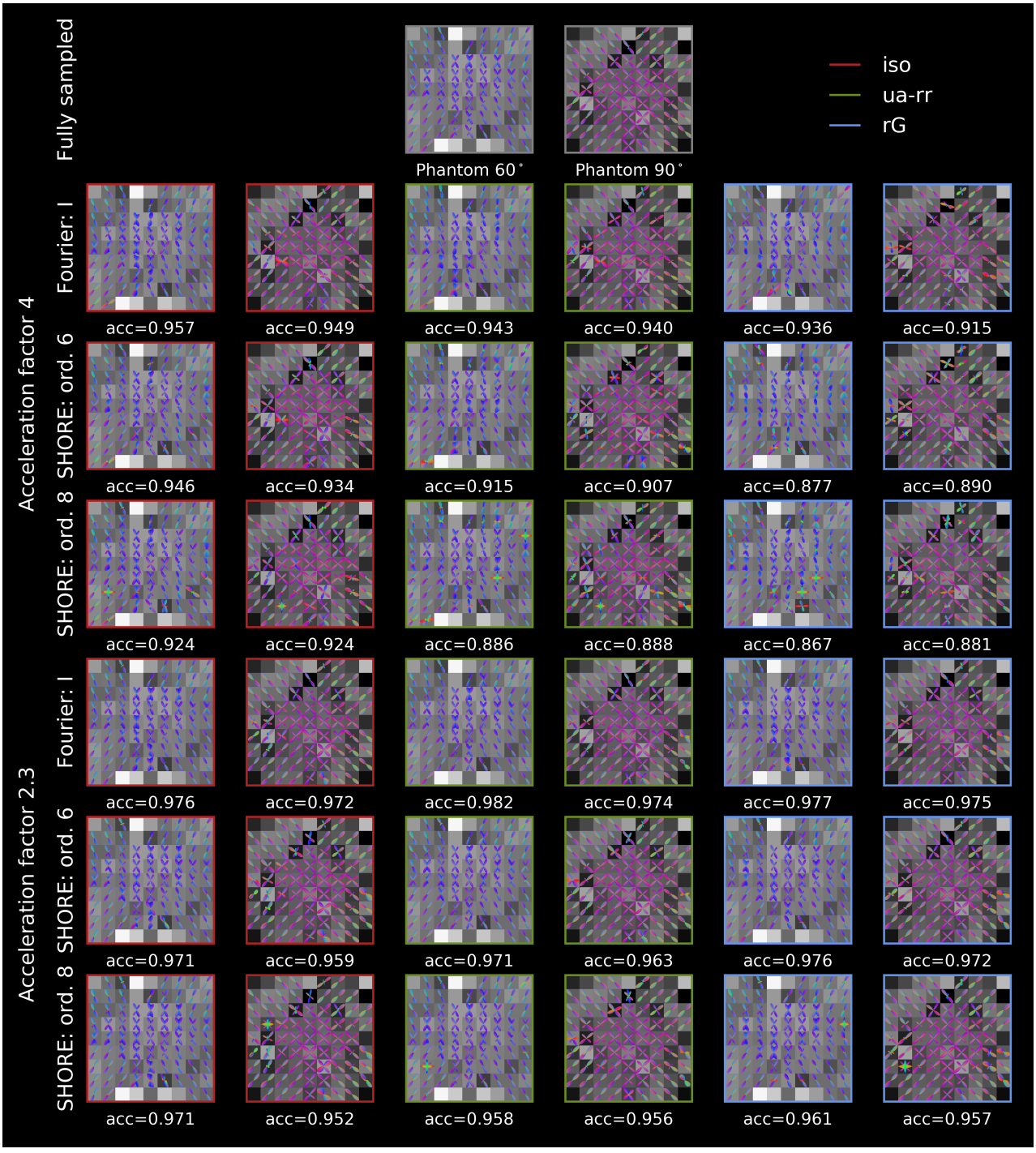

Figure 4.4: FODFs obtained from diffusion phantom data are depicted for ROIs within the crossing region of the 90° and the 60° diffusion phantoms. FODFs are estimated from fully sampled DSI and from CS-DSI using CS acceleration factor 4 and 2.3. For Fourier-based CS-DSI applying the canonical basis as sparsity basis and for SHORE-based CS-DSI using SHORE order 6 and 8, the angular cross correlation of fODFs from the fully sampled signal and the reconstruction was computed. One instance per q-space sampling schemes iso, ua-rr and rG was used.

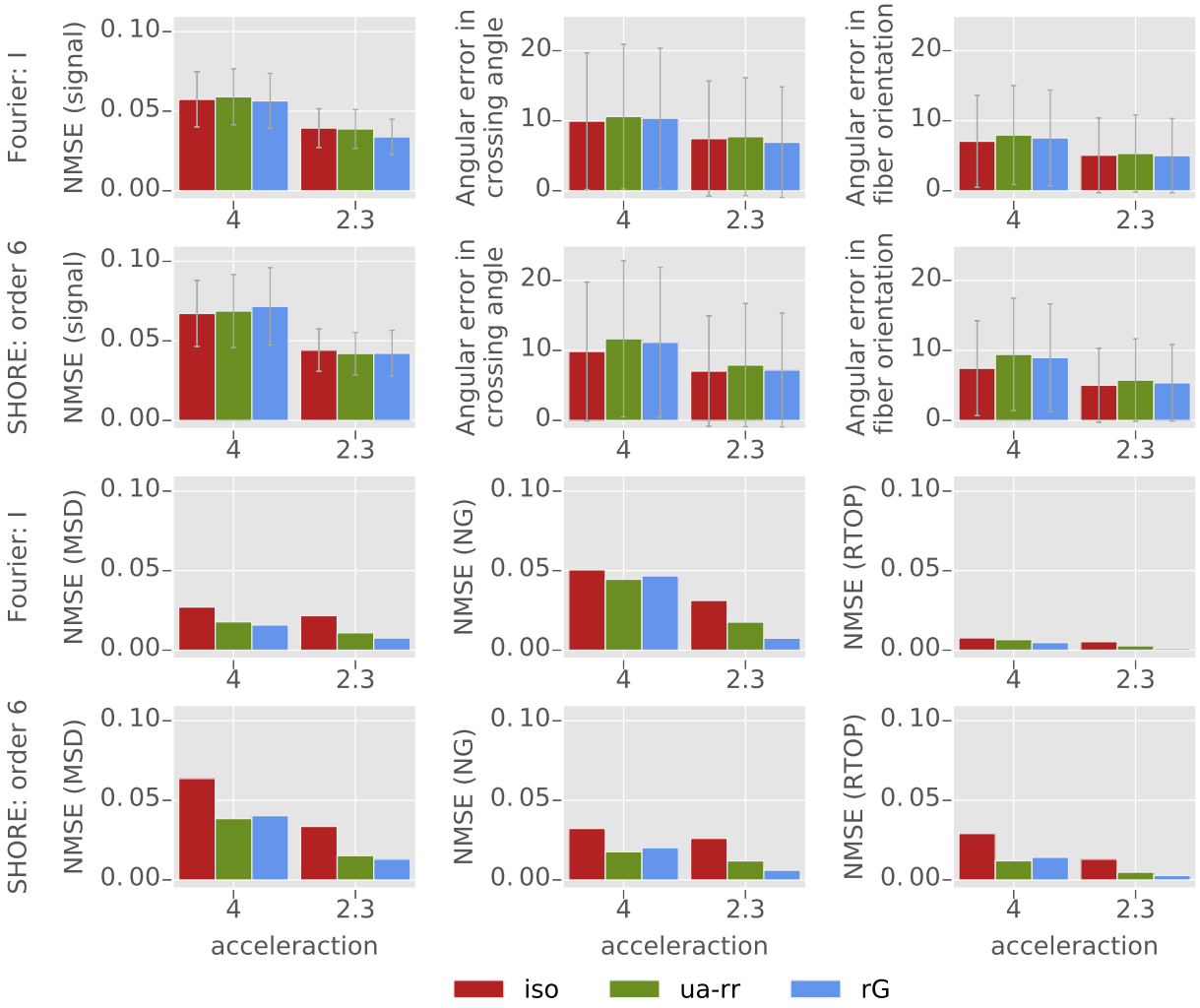

Figure 4.5: CS reconstruction of *in vivo* dMRI data obtained from Fourier- and SHORE-based CS-DSI applying the sparsity transform l and SHORE order 6, respectively. CS reconstruction quality is quantified by computing the angular error in crossing angle and in fiber orientation and the NMSE of the diffusion signal, MSD, NG and RTOP. One instance of each of the q-space sampling schemes under investigation, iso, ua-rr and rG, was used.

Figure 4.6 depicts axial slices showing the relative error in MSD, NG and RTOP between the ground truth and the CS reconstruction obtained from Fourier- and SHORE-based CS-DSI using the iso, ua-rr and rG sampling scheme. The degree of the reconstruction errors presented in Figure 4.5 is well captured by those difference maps. The parameter maps used to generate the difference maps are shown in Supplementary Figure 4.6. The difference maps for SHORE-based CS-DSI show more tissue contrast compared to Fourier-based CS-DSI. For both acceleration factors, difference magnitudes in the diffusion parameter maps are higher for SHORE-based CS-DSI than for Fourier-based CS-DSI.

For CS acceleration factors of 4 and 2.3, Figure 4.7 compares fODFs estimated from Fourier- and SHORE-based CS-DSI acquisitions with respect to fODFs estimated from fully sampled DSI acquisi-

tions. The mean angular cross correlation was computed for all fODFs within the depicted region of interest of a coronal slice of the imaging volume showing crossing fibers from the corpus callosum, the corticospinal tract and the superior longitudinal fasciculus. For 4-fold CS acceleration, the highest correlation values are obtained for the isotropic undersampling scheme and Fourier-based CS-DSI outperforms the SHORE-based approach. For moderate 2.3-fold acceleration, angular cross correlation is high for all schemes and CS-DSI methods.

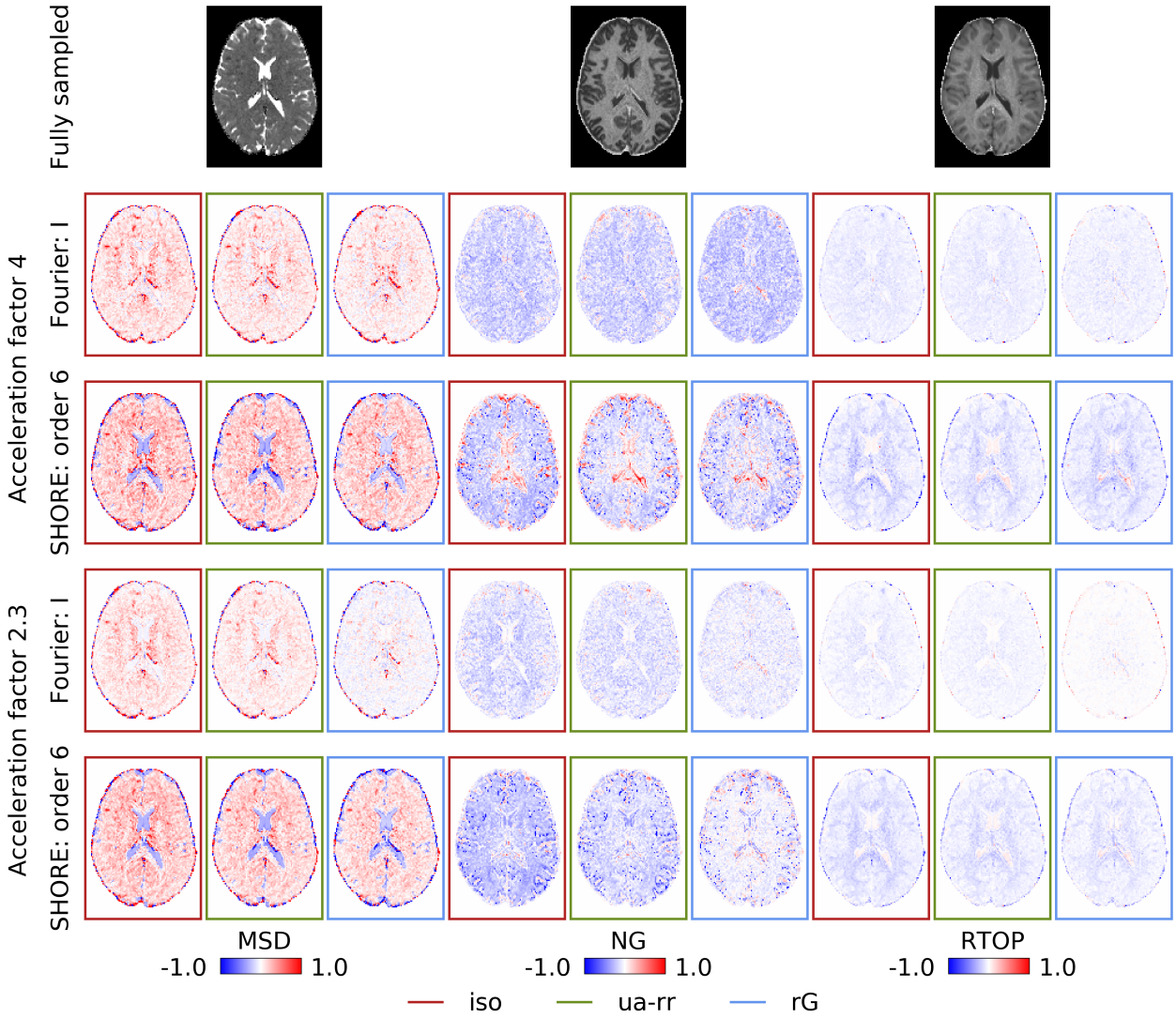

Figure 4.6: For 2.3- and 4-fold CS acceleration, axial slices of difference maps depict the relative error in MSD, NG and RTOP between the fully sampled *in vivo* DSI acquisitions and the CS reconstruction obtained from Fourier- and SHORE-based CS-DSI. One instance of each of the q-space sampling schemes under investigation, iso, ua-rr and rG, was used.

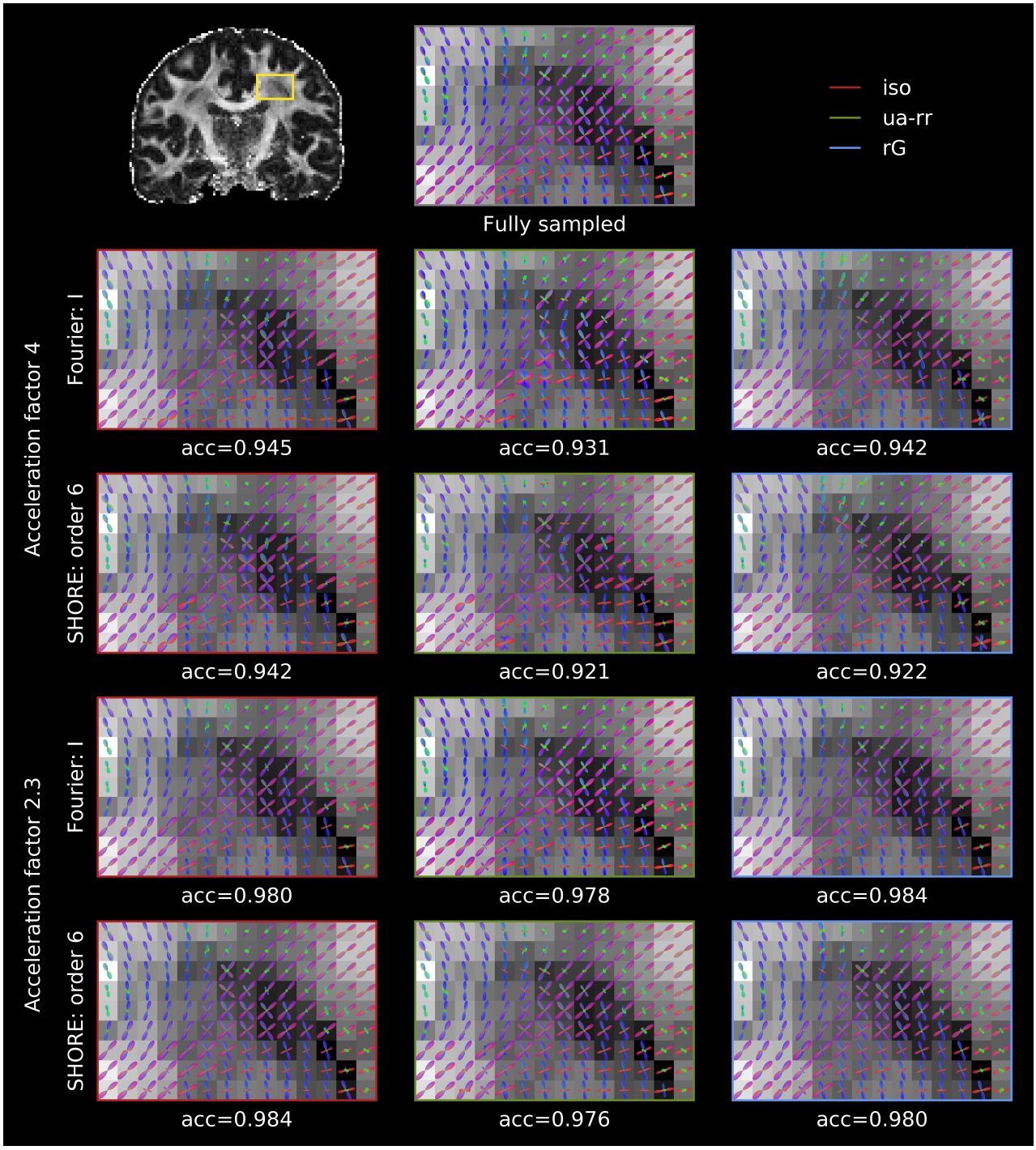

Figure 4.7: For 2.3- and 4-fold CS acceleration, fODFs obtained from Fourier- and SHORE-based CS-DSI are compared with respect to fODFs estimated from fully sampled *in vivo* DSI acquisitions. One instance of each of the q-space sampling schemes under investigation, iso, ua-rr and rG, was used. The angular cross correlation was computed between fODFs from fully sampled DSI and both CS approaches.

4.4 Discussion

4.4.1 Sampling schemes for CS-DSI

In our work, we investigate the three types of undersampling schemes, iso, ua-rr and rG for their suitability in CS applications. Further, a non-Cartesian variant of the iso scheme was considered. According to our simulations, no loss in reconstruction quality was observed for Cartesian q-space sampling when compared to multi-shell sampling in SHORE-based CS-DSI. Small shifts of sample positions in q-space have thus no adverse effects on CS reconstruction, as long as angular and radial resolution are kept sufficiently high. This finding is also supported by the low variation across different instances of Cartesian sampling schemes for CS acceleration factors below 8. This indicates that for the range of parameters tested here the number and optimal distribution of samples in q-space are more relevant than their specific q-space location on a grid or shell. In this work, we thus decided to use Cartesian sampling for all experiments. In this way, the same sampling strategy was applied for both SHORE- and Fourier-based CS-DSI, since the latter requires Cartesian q-space sampling.

Our CS-experiments overall indicate better reconstruction quality for Fourier-based CS-DSI compared to SHORE-based approach. Thus, we draw our main conclusions on the performance of the undersampling schemes based on Fourier-based CS-DSI. In this case, our simulation and phantom results suggest that the isotropic sampling performs comparable to or even better than ua-rr or rG schemes, especially at high CS acceleration factors. For *in vivo* data, the reconstruction results for the diffusion signal and orientational information indicate robust performance of the isotropic scheme comparable to the other schemes. For the reconstruction of MSD, NG and RTOP, the *in vivo* results suggest that the rG scheme outperforms the other schemes. However, this might be related to the specific scheme instances used as the simulations and phantom results with 100 instances per scheme do not support this conclusion. Furthermore, for an acceleration factor of 2.3, reconstruction errors are overall very low. Especially for reconstruction errors of MSD and RTOP below 3%, we believe that differences between sampling scheme types have a minor effect. For an accurate reconstruction close to the fully sampled data, we recommend using a modest CS acceleration factor to reduce the risk of reconstruction artifacts and retain high quality data. Our results overall indicate that applying an CS acceleration factor of 2.3 yields robust reconstruction results. This finding holds independently of the type of undersampling scheme. The respective number of 112 unique q-space samples for 2.3-fold acceleration is thus sufficient to optimally undersample q-space despite the randomness in the selection of samples during scheme generation. Therefore, we conclude that any of the three types of undersampling scheme under investigation in this work is suitable for CS-DSI with modest acceleration factors. For a straight-forward generation of an undersampling scheme, the ua-rr scheme can be easily generated as described in the methods section following the optimal distribution of samples on the sphere based on the design proposed by Caruyer et al. (2013).

4.4.2 Basis functions for sparse DSI reconstruction

4.4.2.1 Sparsity inducing bases

To ensure that both Fourier- and SHORE-based CS-DSI fulfill the requirements for an accurate CS reconstruction, we validated the sparsity properties of the selected sparsifying bases. For simulations, both the diffusion propagator and the SHORE basis provide a sparse representation of the respective signals of interest for CS recovery and NMSE values as low as 0.015 are always achieved. The SHORE basis at order 6 contains only 50 atoms, which is already a sparse representation of the fully sampled signal. Additional sparsity promotion yields an even sparser representation of less than 10 atoms for WM and GM *in vivo* data, confirming the findings by Merlet and Deriche (2013) that the SHORE basis is highly suitable for sparse representation of dMRI signals. Our results show that the diffusion propagator provides a less sparse representation compared to the SHORE basis, but is nevertheless as suitable for the purpose of CS reconstruction as originally proposed by Merlet and Deriche (2010). One advantage of exploiting the sparsity of the diffusion propagator is that low NMSE values and thus correct signal representation are obtained throughout the brain, which, for the SHORE basis, is only possible at orders above 8. However, a SHORE order of 12 is not suitable for CS reconstruction due to the low sparsity induced by the respective SHORE basis. Further, such high SHORE orders imply high computational cost, especially when selected for CS-DSI, and are not favorable in practice. For this reason, we only considered SHORE order 6 and 8 in the CS-DSI experiments conducted in this work although the NMSE for CSF brain tissue can be higher than the required NMSE for an accurate representation of the true signal. However, these regions are typically not of main interest in dMRI analysis and thus, were neglected for the decision of an appropriate SHORE order. Overall, the determined degree of sparsity of the diffusion propagator and the SHORE basis at the selected NMSE threshold confirms the suitability of both the Fourier- and the SHORE-based CS-DSI framework for CS reconstruction.

4.4.2.2 Fourier- versus SHORE-based CS-DSI

Based on the results obtained from simulation and phantom experiments, we conclude that Fourier-based CS-DSI performs optimally when exploiting the sparsity directly in the propagator space. Nevertheless, using TV as a sparsity transform also leads to adequate reconstruction results, especially for modest acceleration factors. Future work could also explore a combination of different regularizers as suggested by Sprenger et al. (2016). The results obtained from simulation and phantom data suggest that using a SHORE order of 6 is preferred over order 8. This finding is in agreement with related works likewise showing the suitability of SHORE order 6 for accurate signal modeling in the SHORE basis (Fick et al., 2016; Merlet and Deriche, 2013). Adding to this, SHORE order 6 enables a high level of sparsity in the representation of the diffusion signal, as discussed in the previous section, and benefits the computational time required for CS reconstruction.

For an adequate CS acceleration up to a factor of 4, SHORE-based CS-DSI using a SHORE order of 6 leads to average NMSE and angular error values, respectively, of about 5% and 3° for

simulations, 13% and 5° for phantom data and 5% and 5° for *in vivo* dMRI. This confirms the suitability and robust performance of the SHORE basis as a sparsity inducing basis in CS recovery as previously suggested by Ozarslan et al. (2009); J Cheng, T Jiang, et al. (2011); Merlet and Deriche (2013); Fick et al. (2016). However, if CS acceleration is too strong, SHORE-based CS-DSI is prone to introduce more reconstruction artifacts than Fourier-based CS-DSI. Further, for *in vivo* dMRI, we observe more tissue contrast in the difference maps for propagator-based parameters, especially in brain voxels with complete or partial CSF volume. This indicates a greater degree of tissue-dependent under- or overestimation for SHORE-based CS-DSI than for Fourier-based CS-DSI. The recovery of signals representing isotropic diffusion was found to be more challenging than for single or crossing fiber voxels when applying continuous signal modeling for sparse reconstruction as previously reported by Fick et al. (2016). Our results are in agreement with those findings and suggest that, in contrast, Fourier-based CS-DSI performs equally well across different tissue types of the human brain. Across the range of investigated CS factors and especially for high acceleration, Fourier-based CS-DSI using the canonical basis as sparsity inducing basis yields NMSE and angular error values comparable to or in many cases below those for SHORE-based CS-DSI. This finding holds for all of the three datasets used for CS evaluation in this work and our results indicate that for a modest CS acceleration of 2.3, Fourier-based CS-DSI provides reconstructed signals comparable to the fully sampled data. Overall, comparing CS reconstruction results obtained from Fourier- and SHORE-based CS-DSI applied to sparse simulations, phantom and *in vivo* dMRI data, we observe better quality of the reconstruction of the diffusion signal and of propagator-derived parameters for the Fourier-based CS-DSI approach. Additionally, for Fourier-based CS-DSI requires only the selection of the regularization parameter and no additional model parameters have to be determined as for the SHORE-based method. In terms of the recovery of orientational information from sparse DSI measurements, fODFs estimated from CS reconstructed phantom and *in vivo* data are comparable to those of the fully sampled data for both CS-DSI approaches. This is indicated by similar angular error values and an angular cross correlation of respectively up to 0.982 and 0.984 for Fourier-based and 0.976 and 0.984 for SHORE-based CS-DSI for an acceleration factor of 2.3.

We took special care to avoid introducing bias in favor of the Fourier-based approach into our analysis. In particular, we did not use the traditional DSI approach to determine properties of the diffusion propagator, such as MSD, NG, RTOP, or ODFs. This would have involved taking the Fourier transform on a regular grid, and might have biased results in favor of using the same Fourier basis for CS reconstruction. Instead, we use the MAP MRI model and the deconvolution approach by Ankele et al. (2017), which apply SHORE for signal modeling. If this introduces any bias at all, it should be in favor of SHORE-based CS-DSI. Despite this, we found that Fourier-based CS-DSI performs comparable to or even better than the SHORE-based approach.

4.4.3 CS-DSI in time-limited dMRI studies

To perform a CS-DSI experiment within time-limited dMRI studies aiming to extract diffusion parameters as well as orientational information from the acquired data, we recommend the following acquisition and analysis strategy. A modest CS acceleration factor of about 2.3 should be chosen

since combined with state-of-the-art MRI hardware and parallel imaging the scan time can already be reduced to about 12 minutes to collect undersampled DSI acquisitions. Thus, higher CS acceleration might not be required and potential reconstruction artifacts can be avoided. For dMRI acquisition, we recommend using any of the three types of undersampling schemes presented in this work. If 4-fold CS acceleration or higher is required to further reduce the scan time or to acquire higher quality or resolution dMRI data depending on the respective research question, an isotropic distribution of q-space samples forming the sparse DSI q-space sampling scheme is optimal for robust CS reconstruction. CS reconstruction of the undersampled DSI acquisitions should be performed using Fourier-based CS-DSI using the canonical basis as the sparsity inducing basis. Subsequently, conventional DSI analysis tools can be applied to the reconstructed data to extract the diffusion measures of interest.

4.4.4 Limitations and future directions

This work focuses on the comparison of Fourier- to SHORE-based CS-DSI. Previously, the SHORE basis was found to provide superior sparsity properties and more accurate CS reconstruction compared to other bases for analytical signal modeling (Merlet and Deriche, 2013). Thus, we aimed to explore its performance in CS-DSI and compared SHORE to Fourier basis functions conventionally used in this context. Future work will investigate continuous basis functions other than SHORE and dictionary-based approaches for sparse DSI reconstruction.

Suitable processing techniques (Andersson et al., 2003; Andersson and Sotiropoulos, 2015) were applied on the *in vivo* DSI data to account for acquisition-related artifacts and subject motion. Results in Merlet and Deriche (2013) suggest that the regularization inherent in CS-DSI can have a denoising effect on dMRI data. However, experiments that specifically investigate the impact of different types of image degradations and artifacts on CS reconstructions are left for future work.

For the *in vivo* experiments conducted in this work, all sequence parameters were fixed. Thus, the conclusions drawn on CS acceleration and the derived recommendations apply to CS-DSI acquired with a high spatial resolution of 1.5 mm isotropic at 3T. They might vary for dMRI data of, for instance, different spatial resolution. In this case, even higher CS acceleration factors might be applicable while still maintaining good reconstruction quality. This work, however, focuses on high-resolution dMRI at 3T. According to the normalized mean square error, ODF accuracy and MAP analysis, we conclude that accurate CS reconstruction was achieved.

Previous work (Tobisch et al., 2018) furthermore demonstrated, based on a comparable imaging protocol, the suitability of CS-DSI for various established diffusion and microstructure models such as DTI (P Basser et al., 1994a), DKI (Jensen et al., 2005), NODDI (Zhang et al., 2012) and CHARMED (Assaf and Basser, 2005) compared to state-of-the-art 3-shell HARDI imaging. Also, test-retest analysis has been conducted and the performance of distortion and motion correction has been investigated. While only one instance of a ua-rr sampling scheme has been utilized for Fourier-based CS-DSI, the present work presented results for various sampling schemes and undersampling factors for Fourier- and SHORE-based CS-DSI in simulations and *in vivo*. However, future work could

investigate a wider range of SNR to represent a broader variation of realistic low-, medium- or high-resolution dMRI protocols.

4.5 Conclusion

In this work, we evaluate the suitability of pairs of basis functions, previously proposed for CS recovery, in the context of sparse DSI reconstruction and investigate the performance of two different CS-DSI approaches based on either Fourier or SHORE basis functions. We further explore the influence of three different types of undersampling schemes among which the approach by Knutsson and Westin (2013) for optimal isotropic distribution of q-space samples is introduced for the first time to sparse DSI reconstruction. A quantitative assessment of CS-DSI applied to simulation, phantom and *in vivo* DSI data was made. The NMSE and angular error values were derived from the reconstructed diffusion signal as well as the corresponding propagator-derived diffusion parameters and orientational information provided by the fODF. Overall, our results indicate that better reconstruction quality of the diffusion signal and of propagator-derived parameters is obtained for Fourier-based CS-DSI, but the reconstruction of orientational information is comparable for both CS-DSI approaches. Using an isotropic distribution of q-space samples for the generation of sparse DSI q-space sampling schemes is found to be optimal for robust CS reconstruction of orientational information at high CS acceleration factors. For modest CS acceleration, the reconstructed signal and extracted diffusion measures are comparable to those from fully sampled ground truth data. Based on our findings, we have formulated recommendations for performing CS-DSI experiments within time-limited dMRI studies since this is an area of application appropriate to exploit the beneficial impact of CS-DSI.

4.6 Supplementary material

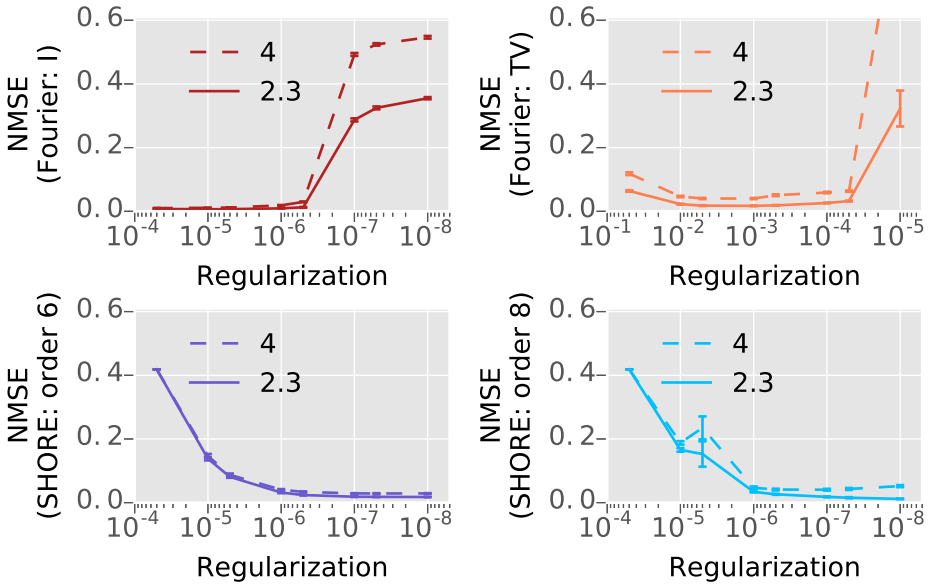

Supplementary Figure 4.1: NMSE of signal reconstruction for acceleration factor 4 and 2.3 as a function of the regularization parameter for Fourier-based CS-DSI using the canonical basis and TV for sparse representation and for SHORE-based CS-DSI with SHORE order 6 and 8.

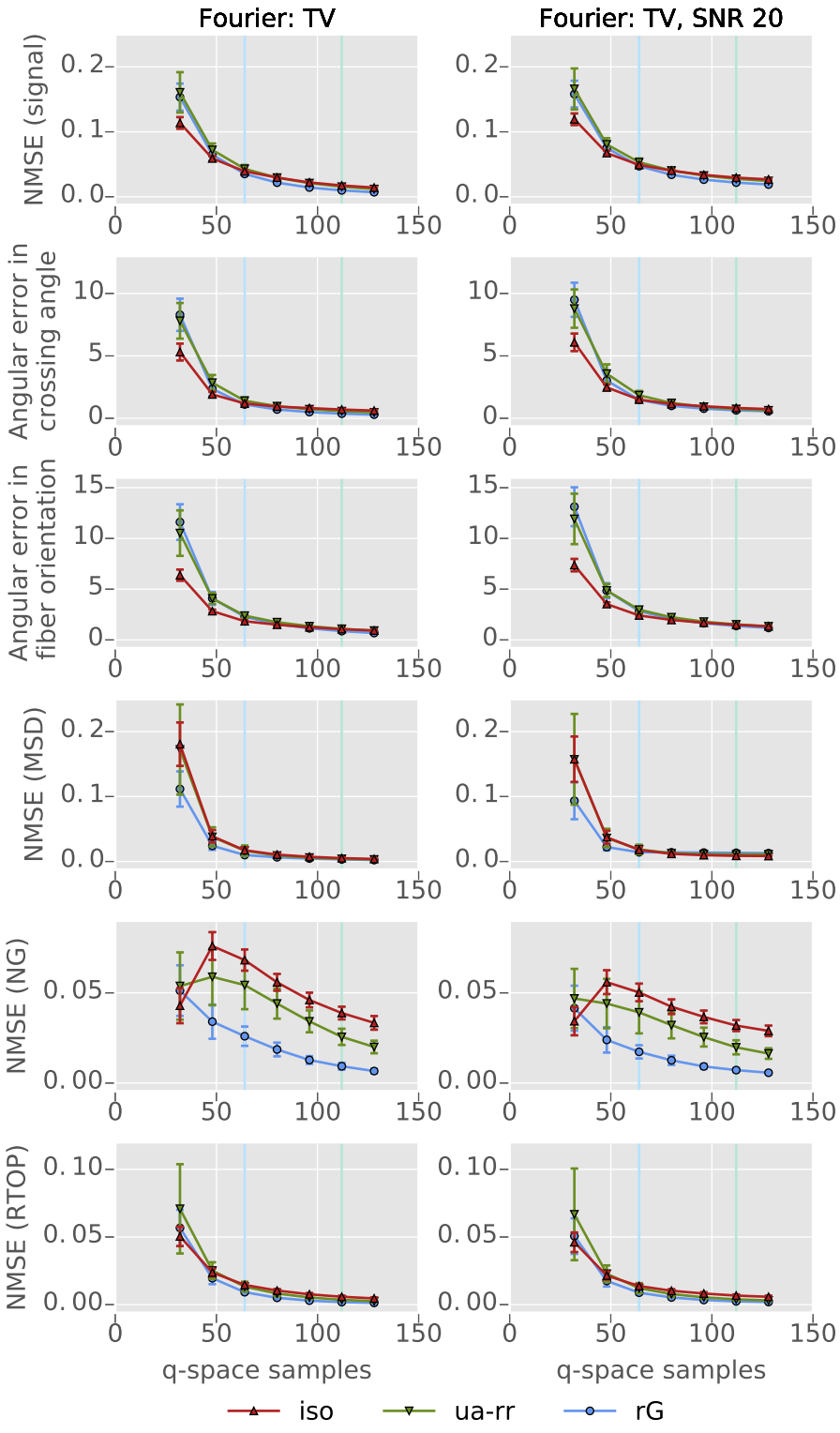

Supplementary Figure 4.2: CS reconstruction of simulations with and without noise obtained from Fourier-based CS-DSI applying the sparsity transform TV. CS reconstruction quality is quantified by computing the angular error in crossing angle and in fiber orientation and the NMSE of the diffusion signal, MSD, NG and RTOP. For each metric, the three different q-space sampling schemes under investigation, iso, ua-rr and rG, are compared. The number of q-space samples corresponding to CS acceleration factors 4 and 2.3 are marked by the light blue and light green vertical lines, respectively.

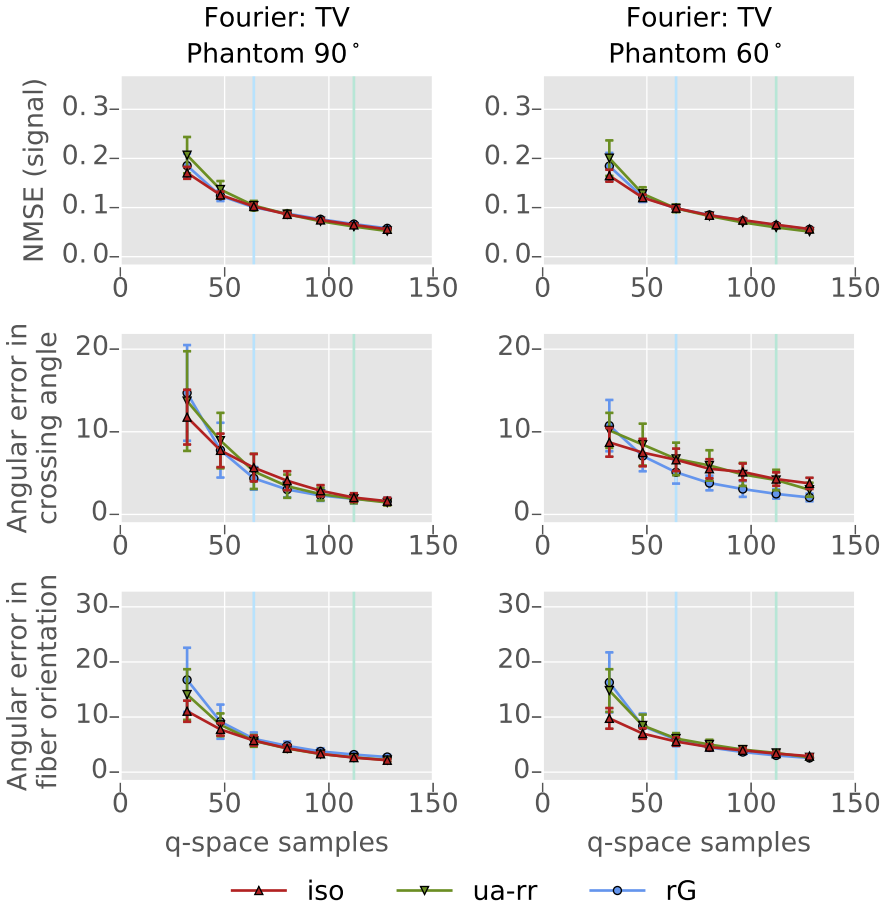

Supplementary Figure 4.3: CS reconstruction of diffusion phantom data obtained from Fourier-based CS-DSI applying the sparsity transform TV. CS reconstruction quality is quantified by computing the angular error in crossing angle and in fiber orientation and the NMSE of the diffusion signal. For each metric, the three different q-space sampling schemes under investigation, iso, ua-rr and rG, are compared. The number of q-space samples corresponding to CS acceleration factors 4 and 2.3 are marked by the light blue and light green vertical lines, respectively.

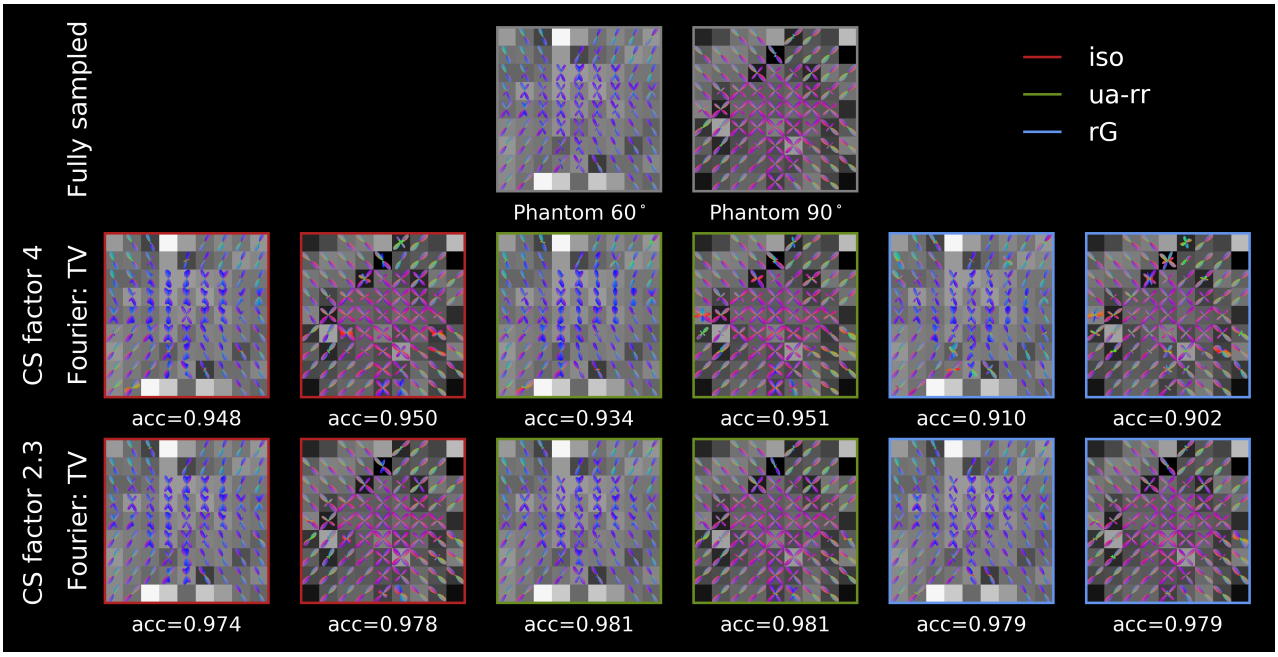

Supplementary Figure 4.4: FODFs obtained from diffusion phantom data are depicted for ROIs within the crossing region of the 90° and the 60° diffusion phantoms. FODFs are estimated from fully sampled DSI and from CS-DSI using CS acceleration factor 4 and 2.3. For Fourier-based CS-DSI applying the sparsity transform TV, the angular cross correlation of fODFs from the fully sampled signal and the reconstruction was computed. One instance per q-space sampling schemes iso, ua-rr and rG was used.

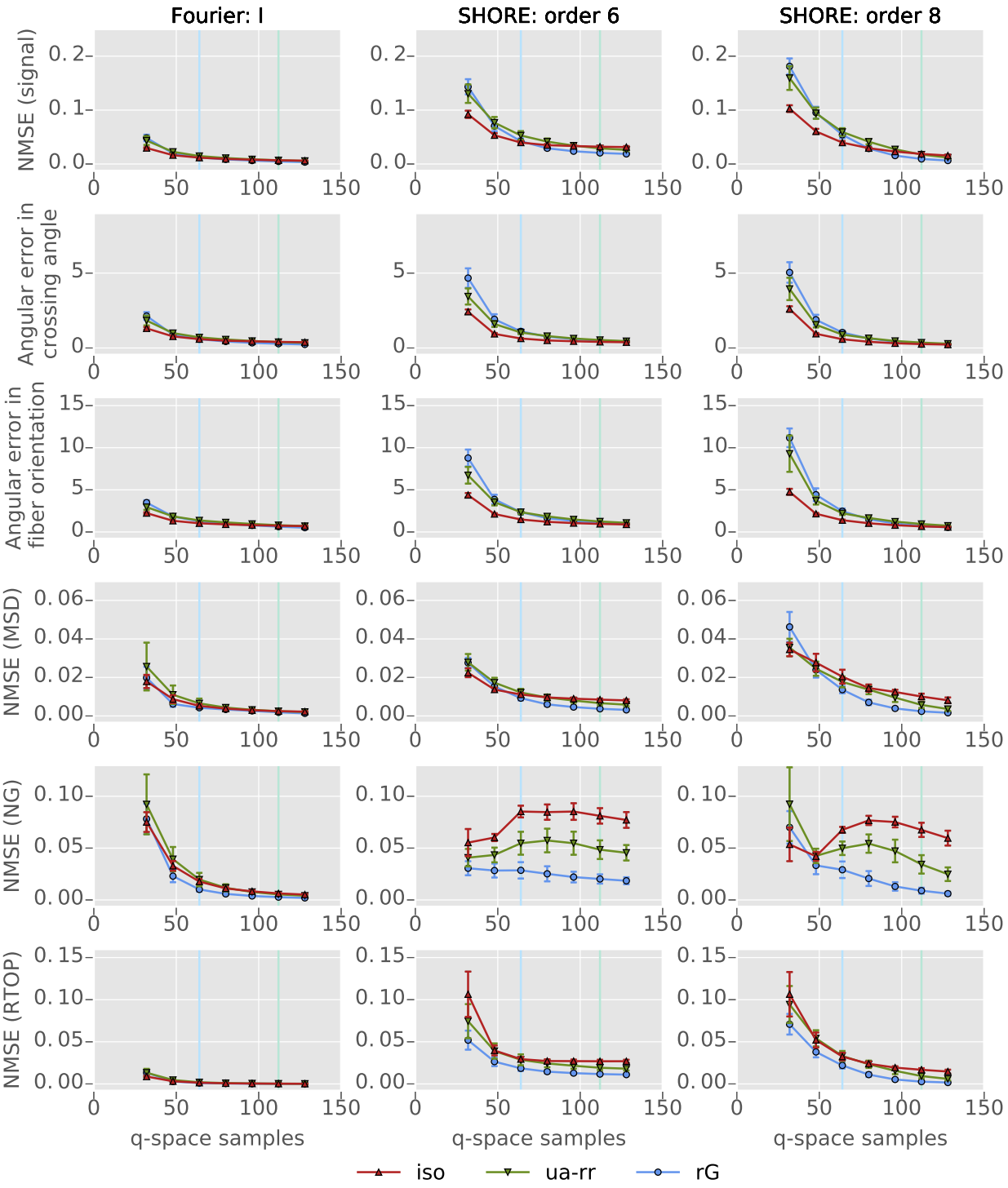

Supplementary Figure 4.5: CS reconstruction of noise free simulations obtained from Fourier-based CS-DSI applying the sparsity transform I and from SHORE-based CS-DSI using SHORE order 6 and 8. CS reconstruction quality is quantified by computing the angular error in crossing angle and in fiber orientation and the NMSE of the diffusion signal, MSD, NG and RTOP. For each metric, the three different q-space sampling schemes under investigation, iso, ua-rr and rG, are compared. The number of q-space samples corresponding to CS acceleration factors 4 and 2.3 are marked by the light blue and light green vertical lines, respectively.

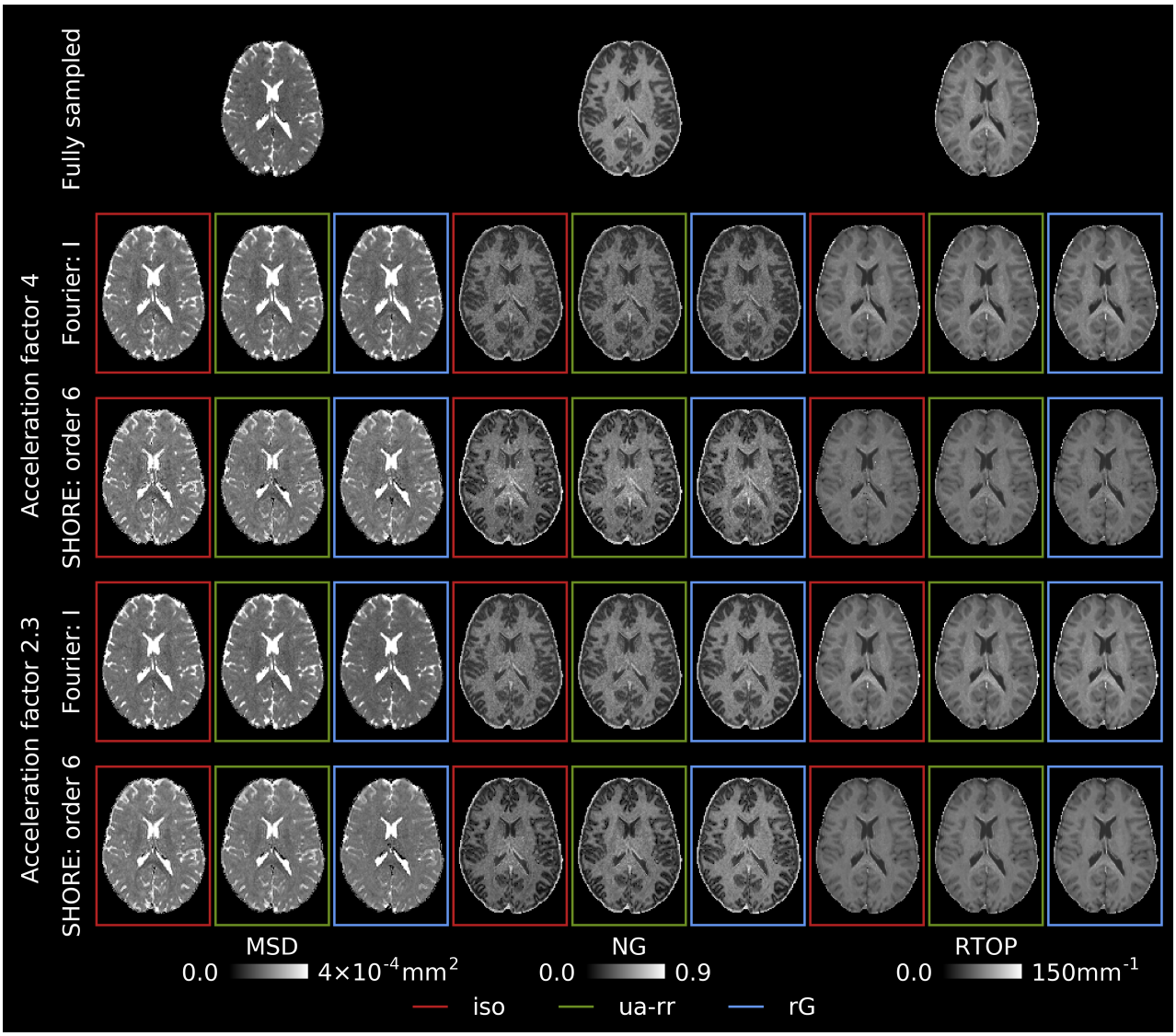

Supplementary Figure 4.6: For 2.3- and 4-fold CS acceleration, axial slices of parameter maps of MSD, NG and RTOP for the fully sampled *in vivo* DSI acquisitions and the CS reconstruction obtained from Fourier- and SHORE-based CS-DSI. One instance of each of the q-space sampling schemes under investigation, iso, ua-rr and rG, was used.

5

Compressed sensing diffusion spectrum imaging for accelerated diffusion microstructure MRI in long-term population imaging

Based on:

Tobisch A, Stirnberg R, Harms RL, Schultz T, Roebroeck A, Breteler MMB and Stöcker T (2018) Compressed sensing diffusion spectrum imaging for accelerated diffusion microstructure MRI in long-term population imaging. Front. Neurosci. 12:650.

Abstract

Mapping non-invasively the complex microstructural architecture of the living human brain, diffusion magnetic resonance imaging (dMRI) is one of the core imaging modalities in current population studies. For the application in longitudinal population imaging, the dMRI protocol should deliver reliable data with maximum potential for future analysis. With the recent introduction of novel MRI hardware, advanced dMRI acquisition strategies can be applied within reasonable scan time. In this work we conducted a pilot study based on the requirements for high resolution dMRI in a long-term and high throughput population study. The key question was: can diffusion spectrum imaging accelerated by compressed sensing theory (CS-DSI) be used as an advanced imaging protocol for microstructure dMRI in a long-term population imaging study? As a minimum requirement we expected a high level of agreement of several diffusion metrics derived from both CS-DSI and a 3-shell high angular resolution diffusion imaging (HARDI) acquisition, an established imaging strategy used in other population studies. A wide spectrum of state-of-the-art diffusion processing and analysis techniques was applied to the pilot study data including quantitative diffusion and microstructural parameter mapping, fiber orientation estimation and white matter fiber tracking. When considering diffusion weighted images up to the same maximum diffusion weighting for both protocols, group analysis across 20 subjects indicates that CS-DSI performs comparable to 3-shell HARDI in the estimation of diffusion and microstructural parameters. Further, both protocols provide similar results in the estimation of fiber orientations and for local fiber tracking. CS-DSI provides high radial resolution while maintaining high angular resolution and it is well-suited for analysis strategies that require high b-value acquisitions, such as CHARMED modeling and biomarkers from the diffusion propagator.

Keywords: Diffusion MRI, Diffusion Spectrum Imaging, Compressed Sensing, Multi-shell HARDI, Microstructure, Population Imaging

5.1 Introduction

Diffusion magnetic resonance imaging (dMRI) provides, completely non-invasively, unique insights into the complex microstructural architecture of the living human brain. Sensitized for the random motion of water molecules, dMRI offers a distinct imaging contrast to investigate the diffusion process at a microscopic scale (Le Bihan et al., 1986). A whole range of mathematical representations, e.g. (P Basser et al., 1994a; Jensen et al., 2005; Ozarslan et al., 2009; Wedeen et al., 2005), and biophysical models, e.g. (Assaf and Basser, 2005; Behrens et al., 2003; Zhang et al., 2012), exists to characterize the diffusion signal as well as the underlying microstructure and to infer macroscopic brain connections from voxel-wise fiber orientation estimates. This makes dMRI a powerful imaging modality to study in vivo pathological changes of diffusion in brain tissue and the influence of disease on the structural connectivity of brain white matter (WM).

The increasing life expectancy in modern society and its consequences for the public health sector give rise to a growing number of population studies that have been set up in the last decades [e.g. Rotterdam study (Breteler et al., 1994; De Groot et al., 2000), Alzheimer's Disease Neuroimaging Initiative (Weiner et al., 2015) (ADNI), Human Connectome Project (Glasser et al., 2016) (HCP), UK Biobank study (Miller et al., 2016), Rhineland Study (Stöcker, 2016)] to acquire rich data from their participants with the aim to provide new insights into disease development and progression and to discover biomarkers for disease prediction at an early state and potentially its prevention, but also for health promotion in general. As a potential biomarker for brain diseases dMRI is, thus, a natural fit for being one of the core imaging protocols in population imaging. Long-term population studies require the dMRI protocol to deliver reliable data with maximum potential for future analysis. Therefore, an extensive pilot phase is the starting point of such studies to define the acquisition strategies based on suggestions from state-of-the-art research. For dMRI, decisions with respect to the diffusion protocol must be made on e.g. spatial resolution, q-space sampling, acceleration strategies, phase encoding directions and many more. DMRI analysis techniques further influence the choice of the imaging protocol by imposing special requirements on the dMRI acquisitions for accurate data processing.

Since the 1990s population studies have been investigating brain changes due to disease by means of neuroimaging aiming for large sample sizes and using standard MR scanners with the purpose of acquiring imaging data comparable to that of other clinical studies (Ikram et al., 2015; Miller et al., 2016; Weiner et al., 2015). Due to common MR hardware and scan time limitations, diffusion tensor imaging (P Basser et al., 1994a) (DTI) or 2-shell HARDI is performed in these studies for the collection of dMRI acquisitions. With the aim to provide very high quality diffusion data, the two consortia of the Human Connectome (Behrens and Sporns, 2012; Jbabdi et al., 2015) Project use highly customized MR scanners to improve diffusion imaging by very strong magnetic field gradients with a maximum amplitude of 100mT/m (Sotiropoulos et al., 2013; Van Essen et al., 2012) or even 300mT/m (Setsompop et al., 2013). In this context, advanced dMRI protocols such as multi-shell high angular resolution diffusion imaging (Tuch et al., 2002) (HARDI), high b-value q-Ball imaging (Tuch, 2004; Wu and Alexander, 2007) and diffusion spectrum imaging (Wedeen et al., 2005) (DSI) are employed to collect high resolution dMRI acquisitions in about one hour of acquisition time (Fan

et al., 2016; McNab et al., 2013; Sotiropoulos et al., 2013). The bespoke systems developed in this context have paved the way for a new generation of clinical MRI systems with higher maximum gradient strength up to 80mT/m (Glasser et al., 2016). With these scanners' introduction the advantages of the aforementioned studies can now be combined, meeting both the aim for high quality diffusion data as well as the scan time limitation in high throughput population studies. Thus, MRI scanners with a powerful gradient system allow for high resolution diffusion imaging by means of advanced dMRI protocols within a reasonable scan time. Following the well-established HCP dMRI protocol (Sotiropoulos et al., 2013), a 3-shell HARDI protocol is a natural candidate for being the dMRI protocol of choice in this setting. However, advances in the development of novel acquisition strategies for fast collection of dMRI scans that provide high resolution of intra-voxel microstructure indicate that diffusion spectrum imaging (Wedeen et al., 2005) (DSI) accelerated by the application of the compressed sensing (Bilgic et al., 2012; Menzel et al., 2011; Paquette et al., 2015; Setsompop et al., 2013; Tobisch et al., 2015) (CS) theory also has high potential to fit the task of time efficient versatile diffusion imaging.

In this work we conducted a pilot study specifically designed based on the requirements for a long-term population study, the Rhineland Study, to investigate the performance of CS-DSI for the acquisition of high resolution dMRI data at 3T. The CS-DSI protocol was time-matched with a state-of-the-art 3-shell HARDI protocol that runs 12 minutes in total. As part of the one-hour MR protocol in the Rhineland Study (Stöcker, 2016), the dMRI scheme should deliver data with maximum potential for future analysis to enable both microstructure imaging and fiber tracking and thereby tractometry (Bells et al., 2011; De Santis, Drakesmith, et al., 2014), as well as connectomics analysis. Thus, a wide spectrum of state-of-the-art diffusion processing and analysis techniques was applied to the pilot study acquisitions. The results of this work validate the applicability of DSI accelerated with compressed sensing for population imaging and highlight the potentials of this imaging protocol in the context of a long-term population study.

5.2 Material and methods

5.2.1 DMRI acquisition

5.2.1.1 Diffusion MR imaging protocols

Based on previous works (Paquette et al., 2015; Sotiropoulos et al., 2013; Tobisch et al., 2015), we adapted and optimized a CS-DSI and a 3-shell HARDI protocol for dMRI at 3T. Figure 5.1 depicts the three-dimensional q-space sampling and the corresponding b-value distribution of both advanced protocols in comparison to dedicated sampling schemes for DTI and CHARMED (Assaf and Basser, 2005).

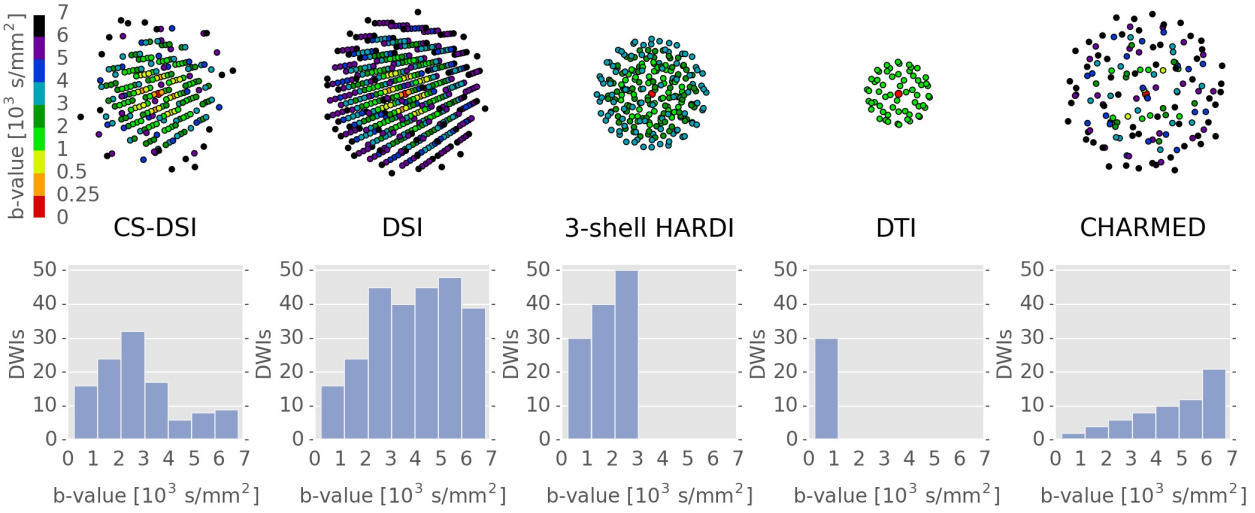

Figure 5.1: DMRI sampling distributions and diffusion weighting of the advanced imaging protocols CS-DSI and 3-shell HARDI and of DTI and CHARMED schemes. Top row: The color coding of the q-space samples highlights the range of b-values specific to each protocol. The number of depicted q-space samples per protocol corresponds to the sum of acquired DWIs and their antipodal counterparts. Bottom row: The number of DWIs acquired per protocol is depicted as a function of the b-value. In contrast to the single (DTI) and the multi-shell (3-shell HARDI) scheme, CS-DSI, DSI and CHARMED contain high b-value acquisitions.

3-shell HARDI samples the q-space with high angular resolution and provides adequate radial resolution by incorporating three different diffusion-weightings at b-values of 1000, 2000 and 3000 s/mm^2. In addition to 14 interleaved b = 0 scans, these three q-space shells respectively contain 30, 40, and 50 samples that are optimally distributed for an advantageous uniform angular q-space coverage (De Santis, Y Assaf, et al., 2014; Sprenger et al., 2016) following the design proposed by Caruyer et al. (2013). In total, 120 diffusion weighted images (DWIs) are acquired using 3-shell HARDI. Our choice of a HARDI scheme with three shells at b-values of 1000, 2000 and 3000 s/mm^2 is based on recent literature on comparable variants of multi-shell schemes. Several works report the suitability of those schemes for population imaging (Sotiropoulos et al., 2013) and their advantages for optimal diffusion parameter extraction by means of microstructure models (Alexander and Barker, 2005; Kamath et al., 2012; Poot et al., 2010; Sprenger et al., 2016; Zhang et al., 2012) and for the estimation of orientational information (Kamath et al., 2012; Sotiropoulos et al., 2013; Tournier et al., 2013). In our work, we, therefore, consider 3-shell HARDI as a gold standard protocol for multi-shell imaging in population studies to which we aim to compare CS-DSI. In contrast to the multi-shell protocol, DSI requires a uniform Cartesian grid sampling scheme, typically of size 11x11x11 truncated to a sphere, which leads to a total number of 258 unique samples in q-space covering the latter at both high angular and high radial resolution. One drawback of traditional DSI is the long acquisition time. However, recent advances in combining DSI with CS theory allow for accelerated imaging by reducing the MR acquisition to fewer q-space samples sufficient for subsequent recovery of the full data by means of non-linear reconstruction. Exploiting the antipodal symmetry of the diffusion signal and applying an acceleration factor of 2.3, the CS-DSI protocol, thus, acquires 112 DWIs with diffusion weightings in the range of b = 270 - 6800 s/mm^2 plus 8 interleaved b = 0 scans.

The b-vectors and b-values applied for CS-DSI and 3-shell HARDI data acquisition are provided as supplementary material. We select the maximum b-value of the CS-DSI scheme in accordance with recent literature on conventional and CS-accelerated DSI (Bilgic et al., 2012; Gigandet et al., 2013; Paquette et al., 2015; Yeh and Verstynen, 2016) and recommendations for microstructure imaging requiring high b-values such as CHARMED modeling (De Santis, Y Assaf, et al., 2014). The CS-DSI acquisition scheme was generated based on the design proposed by Paquette et al. (2015). All samples follow a uniform angular distribution and cover q-space randomly in the radial direction (Jones et al., 1999; Paquette et al., 2015) subject to Cartesian discretization within the 11x11x11 truncated sphere. Based on simulation experiments, no significant difference in CS reconstruction was observed across 100 randomly generated instances of this sampling scheme for 2.3-fold CS acceleration (Tobisch et al., 2015). By means of CS reconstruction of the undersampled DSI acquisitions, all 515 samples on the q-space grid are recovered forming the basis for the following DSI data analysis. As state-of-the-art reference protocols, we further consider a dedicated CHARMED protocol containing 72 q-space samples in the range of b = 850 - 6800 s/mm^2 (De Santis, Y Assaf, et al., 2014) as well as a DTI scheme with 30 DWIs at b-value 1000 s/mm^2. The latter is represented by the inner shell of the 3-shell HARDI sampling scheme similarly to other works that utilize a suitable subset of the acquired multi-shell data for fitting the tensor model (Miller et al., 2016; Sotiropoulos et al., 2013).

The selection of a suitable q-space sampling scheme only covers one aspect in the process of designing a diffusion protocol. The following section will summarize the key decisions made during a first sequence development stage with respect to the dMRI acquisition in the context of scan time-limited population imaging. All dMRI scans are collected on a 3T Siemens MAGNETOM Prisma MRI scanner (Siemens Healthcare, Erlangen, Germany) equipped with a powerful gradient system with maximum amplitudes of 80mT/m and slew rates of 200 mT/m/ms as well as a 64-channel head-neck coil. We perform accelerated diffusion imaging by means of a simultaneous-multi-slice (SMS) dMRI sequence employing threefold slice-acceleration (Cauley et al., 2014; Setsompop et al., 2012; Xu et al., 2013). No in-plane acceleration is applied (GRAPPA R = 1) in combination with multiband excitation. Facilitated by the performant gradient system, a relatively large readout bandwidth of 1785 Hz/pixel is selected to counteract increased geometric distortions along the phase encode direction at 1.5 mm resolution. All imaging protocols apply monopolar diffusion weighting and a partial Fourier factor of 6/8 to minimize TE. All sequence parameters are matched across protocols with identical spatial resolution, except for the gradient pulse separation (Δ), the gradient pulse duration (δ), the echo time (TE) and the repetition time (TR). Allowing for small differences, the latter parameters are optimized separately for each protocol to match the time requirement of the population study while still providing comparable diffusion contrast among the imaging protocols of interest. Slightly higher values for TE and TR due to higher b-value acquisitions result in a reduced number of CS-DSI scans and a slightly reduced signal-to-noise ratio (SNR) in comparison to the 3-shell HARDI protocol. For all dMRI acquisitions, TR and TE are kept constant across q-space samples to avoid effects through noise levels varying with the diffusion weighting and T2 relaxation, which would prevent data processing with state-of-the-art diffusion analysis tools. Running straightforward data analysis outweighs the increase in SNR achievable by optimizing TE and TR separately for different b-values. Due to powerful MRI hardware and advanced diffusion sequences acquiring

dMRI scans at a higher resolution than 2.0mm isotropic is feasible and likewise preferred for diffusion imaging in renowned population studies (Sotiropoulos et al., 2013).

5.2.1.2 Diffusion pilot study

Diffusion MRI scans were acquired from 20 healthy subjects (age range 20-77, mean age 47.5, 5 males, 15 females) at 1.5mm isotropic resolution using the two advanced imaging protocols: CS-DSI (TE/TR = 101.4ms/5300ms, Δ = 49.5ms, δ = 19.7ms) and 3-shell HARDI (TE/TR = 90ms/4800ms, Δ = 43.9ms, δ = 14ms). In addition, reference scans were acquired with a dedicated 1.5mm isotropic CHARMED protocol (TE/TR = 101.4ms/5300ms, Δ = 49.5ms, δ = 19.7ms) in 4 of the subjects. Approval to undertake the study was obtained from the ethics committee of the University of Bonn, Medical Faculty. The study was carried out in accordance with the recommendations of the International Council for Harmonisation (ICH) Good Clinical Practice (GCP) standards (ICH-GCP). We obtained written informed consent from all participants in accordance with the Declaration of Helsinki. The scan time per subject was 11 min for the 3-shell and the CS-DSI protocol, supporting the applicability in population imaging. One minute of additional b = 0 scans, including an autocalibration scan, with reversed phase encoding (PE) polarity were collected per protocol. Further, rescans are collected on the same day, but only for one specific imaging protocol per subject. In total, 5 rescans were acquired for each imaging protocol of interest. In addition to dMRI, a rapid, 1mm isotropic T1-weighted MP-RAGE scan (Brenner et al., 2014) was acquired per subject within 3 minutes at the end of the first scanning session (TI = 1100ms, TE/TR = 2.83ms/2530ms). For dMRI analysis, the acquisitions of all 20 subjects are divided into two distinct subsets: the scans of 16 subjects for the investigation of CS-DSI and 3-shell HARDI (Group A) and the scans of the remaining 4 subjects for the comparison of these protocol to the CHARMED reference protocol (Group B).

5.2.2 DMRI preprocessing

5.2.2.1 Motion and distortion correction

All images are corrected for subject motion and distortions prior to the estimation of diffusion and microstructural parameters. FSL's topup is used to estimate susceptibility-induced geometric distortions (Andersson et al., 2003) whereas FSL's eddy is applied to simultaneously correct for those distortions as well as eddy-current-induced artifacts and subject motion (Andersson and Sotiropoulos, 2015). However, eddy is not designed for DSI data as it requires the dMRI samples to be acquired on shells in q-space. For a fair comparison of both protocols of interest, independently of differences between processing algorithms, we aim to use the same motion and distortion correction. Thus, we apply a post hoc adjustment of the nominal DSI b-values according to the requirements of eddy such that the DSI q-space samples acquired on a Cartesian grid shift by maximal 50 s/mm^2 to b-values corresponding to samples on 20 shells in q-space. This enables the Gaussian process modeling in eddy. Note that the adjustments only affect the nominal b-values not the actual b-values

nor the CS-DSI acquisitions. After motion and distortion correction, the original, unshifted b-values are used for all subsequent processing steps. To validate this approach, we additionally acquired dMRI data from one healthy subject using the 3-shell HARDI and the CS-DSI imaging protocol. We have extended the 3-shell HARDI scheme by 6 uniformly distributed DWIs at b = 700 s/mm^2 to allow for an adequate comparison to corresponding CS-DSI DWIs with b < 1000 s/mm^2. Instead of just collecting a few b = 0 images with reversed phase encoding polarity as in the pilot study, the complete protocols are run twice, once with anterior-to-posterior (AP) and once with posterior-to-anterior (PA) PE direction. In this way, eddy becomes applicable for DSI data without the nominal b-value shifts. To assess the performance of eddy, the mean squared error (MSE) between corresponding images of the AP and PA data sets is calculated before and after eddy correction and for CS-DSI, additionally with and without the shift of nominal b-values. In the pilot study, DWIs are only acquired with AP PE direction and thus motion and distortion correction is performed with the help of a few b = 0 scans with reversed phase encoding polarity. To simulate a scenario similar to the pilot study, the quality of those corrected AP PE DWIs is evaluated by calculating the MSE with respect to the PA PE DWIs that were corrected using both AP and PA PE data.

5.2.2.2 Compressed sensing in dMRI

Compressed sensing (CS) reconstruction was applied to recover the diffusion propagator $\mathbf{p}$ from the undersampled DSI acquisitions $\mathbf{y}$ by means of the discrete Fourier transform $\mathcal{F}$ combined with a sparsity term (Paquette et al., 2015; Tobisch et al., 2015):

$$\underset{\mathbf{p}\in R^n}{\operatorname{argmin}} \left\|\mathbf{R}_{\mathbf{\Omega}}\mathcal{F}\mathbf{p}-\mathbf{y}\right\|_{l_2} + \lambda \left\|\mathbf{p}\right\|_{l_1} \tag{5.1}$$

The CS matrix $\mathbf{R}_{\mathbf{\Omega}}\mathcal{F}$ incorporates the undersampling matrix $\mathbf{R}_{\mathbf{\Omega}}$. λ is the empirically determined regularization parameter set to 5×10^{-6}. The l_2-norm and l_1-norm are applied to the data consistency and the sparsity term, respectively. In this setting, the diffusion propagator itself defines a natural sparsity domain well-suited for CS reconstruction (Merlet and Deriche, 2010). For the complete DSI data recovery, an iterative shrinkage and thresholding algorithm (Gong et al., 2013) solves the convex optimization problem. Here, we do not validate or describe in more detail the CS theory as this exceeds the scope of the paper. For the interested reader, we refer to the corresponding literature on applications of CS in dMRI, specifically CS-DSI (Bilgic et al., 2012; Menzel et al., 2011; Paquette et al., 2015; Setsompop et al., 2013; Tobisch et al., 2015). We choose the degree of CS acceleration to be relatively small to ensure good CS reconstruction quality and thus, selected a modest acceleration factor of 2.3. CS reconstruction generates 257 unique DWIs from the 112 measurements fully describing the diffusion propagator in DSI. For brevity, we will refer to this set of 257 reconstructed DWIs as the CS-DSI data from now on. We also considered sparse reconstruction for the multi-shell scheme. Several recent works on CS for spherical sampling strategies exist (Fick et al., 2016; Michailovich et al., 2011; Rathi et al., 2014). Having run an extensive evaluation study of CS methods for sparse reconstruction, Ning et al. (2015) report that signal reconstruction with the MAPL MRI model proposed by Fick et al. (2016) allows signal extrapolation at higher b-values and

performs similar to the CS approach by Rathi et al. (2014). We considered the former CS method which is implemented as part of the Dipy library (Garyfallidis et al., 2014). The 3-shell HARDI, CS-DSI and CHARMED data of Group B were used to reconstruct the respective signals for the diffusion directions of the CHARMED reference protocol with b-values up b = 6800 s/mm^2. To compare the reconstruction quality, we computed the normalized mean square error (NMSE) as defined in Ning et al. (2015) with respect to the CHARMED reference signal of both 3-shell HARDI and CS-DSI. For the analysis of CS-DSI and 3-shell HARDI acquisitions in the context of population imaging, we decided against sparse reconstruction for the multi-shell scheme, the reasons for which will be discussed later on. Thus, in this work, all dMRI analysis is performed on 3-shell HARDI and CS-DSI acquisitions with CS reconstruction only done for the latter.

5.2.3 DMRI analysis

5.2.3.1 Diffusion and microstructural parameter estimation

Using the Maastricht Diffusion Toolbox (Harms et al., 2017) and in-house implementations, several mathematical and biophysical diffusion models were fitted to the data to estimate the following diffusion and microstructure parameters: fractional anisotropy (FA) and mean, axial and radial diffusivity (MD, AD, RD) from the tensor model (P Basser et al., 1994a), mean, axial and radial kurtosis (MK, AK, RK) as well as FA, MD, AD and RD from the kurtosis model (Jensen et al., 2005), the weight (volume fraction) of the intra-cellular compartment (wIC) and orientation dispersion (ODI) from the NODDI model (Zhang et al., 2012), and intra-axonal restricted volume fraction (FR) from the CHARMED model (Assaf and Basser, 2005). Each diffusion model comes with specific requirements or recommendations for the maximum or optimal b-values of the dMRI data. Considering these specifications, we fit the tensor, kurtosis and NODDI model to DWIs acquired with b-values of approx. 1000 s/mm^2, up to 3000 s/mm^2 and on two shells of approx. 1000 s/mm^2 and 3000 s/mm^2, respectively. The CHARMED model specifically requires acquisitions of b-values greater than 3000 s/mm^2. Table 5.1 lists the selection and the resulting total number of unique DWIs based on the b-value requirements of specific diffusion models and highlights the differences in the model fitting process between 3-shell HARDI and CS-DSI acquisitions. For CS-DSI, additional maps of mean squared displacement (MSD), return-to-origin-probability (RTOP) (Wu et al., 2008) and non-Gaussianity (NG) (Özarslan et al., 2013) are derived from the diffusion propagator by means of the MAPL MRI model.

As the basis for statistical group analysis, the standard tract-based spatial statistics (TBSS) routine was applied to project all estimated diffusion parameters to a mean FA skeleton (Smith et al., 2006). The TBSS framework is well established and likewise preferred in other works (Giezendanner et al., 2016; Zhu et al., 2015) also in combination with atlas-based identification of WM tracts (De Santis et al., 2012). We acknowledge, however, the reported limitations of TBSS (Bach et al., 2014; Edden and Jones, 2011). Thus, for population-based analysis, alternative analysis techniques should be investigated. Regions of interest (ROIs) were automatically defined by mapping the labels of well-known white matter tracts in the brain provided in standard space by the JHU ICBM DTI 81

atlas (Mori et al., 2008) available in FSL to the TBSS mean FA skeleton. We selected nine ROIs of well-known WM tracts for statistical analysis: the splenium, body and genu of the corpus callosum (SCC, BCC, GCC), the anterior limb of internal capsule (ALIC), the sagittal stratum (SS), the superior corona radiata (SCR), the corticospinal tracts (CST), the superior longitudinal fasciculus (SLF) and the superior fronto-occipital fasciculus (SFO). Left (L) and right (R) regions are considered for all tracts, except the CC. For each diffusion parameter, the group mean and standard error (SEM) were subsequently calculated from the mean across all voxels within the tract ROIs. To provide further statistical information, we performed voxel-wise analysis of paired two-group differences using FSL's randomise (5000 permutations, TFCE, variance smoothing) (Winkler et al., 2014). Additional statistical analysis was performed to investigate effects across WM structures. For each diffusion parameter, we used a linear fixed effects model with random intercept for each model in order to account for the clustering of the measurements within each subject. As fixed effects we included acquisition scheme and WM ROI. This statistical analysis was performed using R Statistical Software (version 3.4.1) and the lme4 package.

To quantify the test-retest (TRT) reliability of a diffusion imaging protocol, we assessed the differences between diffusion parameters estimated from the scans and rescans of a subgroup of subjects from the pilot study. Per subject, diffusion parameter maps of both scan and rescan were, first, linearly registered to a mid-space to account for the influence of resampling effects on the data that could mask TRT variability in the case of registering one scan to the other. Second, the difference between the registered parameter maps as well as their mean was calculated and warped into MNI space. Finally, the parameter specific mean and differences for each subject were projected onto the WM skeleton and subsequent ROI based analysis was performed as for the group analysis described before. To asses the reliability and repeatability of the 3-shell HARDI and the CS-DSI diffusion protocol, the intraclass correlation coefficient (ICC) and the within-subject coefficient of variation (wsCV) were calculated, respectively (Bartko, 1966; Bland and Altman, 1996).

Table 5.1: Selection and resulting total number of unique DWIs for the CS-DSI and the 3-shell HARDI protocol based on the b-value requirements of the tensor, kurtosis, NODDI and CHARMED model.

		3-shell HARDI	CS-DSI
DT	b [s/mm^2]	1000	270 - 1300
	DWIs	30	28
Kurtosis	b [s/mm^2]	1000 - 3000	270 - 3000
	DWIs	120	85
NODDI	b [s/mm^2]	1000, 3000	270 - 1300, 3000 - 3800
	DWIs	30, 50	28, 52
CHARMED	b [s/mm^2]	n/a	270 - 6800
	DWIs	n/a	257

5.2.3.2 Fiber orientation and macroscopic brain connections

Fiber orientation distribution functions (fODFs) were obtained by means of the recently proposed method by Ankele et al. (2017) which incorporates the SHORE (Ozarslan et al., 2009) model that continuously describes the diffusion signal. The novel SHORE-based multi tissue constrained spherical deconvolution (CSD) approach by Ankele et al. (2017), here denoted as the SHORE/MT-CSD model, can be applied independently of the dMRI sampling scheme. It allows the generation of brain tissue volume fraction maps for white matter, gray matter (GM) and cerebrospinal fluid (CSF) and the estimation of fODFs for both CS-DSI and 3-shell HARDI. fODF estimation as proposed by Ankele et al. (2017) requires T1 imaging data for tissue segmentation similar to Jeurissen et al. (2014). In contrast, state-of-the-art methods for optimal fiber orientation estimation that depend on specific q-space sampling exist for both CS-DSI and 3-shell HARDI: for CS-DSI, diffusion ODFs (dODFs) can be directly calculated from the DSI diffusion propagator (Paquette et al., 2016; Wedeen et al., 2005); the high angular resolution of HARDI data is most advantageous for estimating fiber orientation by means of CSD providing the fiber ODF instead of the diffusion ODF (Tournier et al., 2007). All ODFs were reconstructed using either the approach by Ankele et al. (2017) or the Dipy library (Garyfallidis et al., 2014) and visualized using MATLAB. For a voxel-wise qualitative as well as quantitative comparison of the orientational information provided by both advanced dMRI protocols, CS-DSI and 3-shell HARDI acquisitions are registered to a mid-space prior to ODF estimation. To avoid any influence of methodological differences in the ODF estimation on the quantitative analysis, we consider the fODFs estimated via (Ankele et al., 2017) for a quantitative comparison of CS-DSI and 3-shell HARDI. Ankele et al. (2017) recommend a SHORE order of 4 for fODF estimation. For an optimal visualization, we additionally compute the fODFs with SHORE order 8. Complementing the visual fODF comparison, we performed voxel-wise analysis for fODFs with SHORE order 8 by means of the angular cross-correlation (Anderson, 2005). Further analysis was conducted on fODFs with SHORE order 4. We compare the CS-DSI and the 3-shell HARDI scheme with respect to the angular difference between corresponding fODF peak directions as well as the deviation between crossing angles of the two most dominant fiber directions in voxels with at least two fibers. To restrict the analysis mainly to pure WM voxels, we followed the recommendations by Jeurissen et al. (2013). The minimum crossing angle that occurs in at least 1% of the WM voxels was determined for each scheme. We also compute the percentages of voxels containing one, two or three dominant fiber fascicles (1/2/3 fiber voxels) within the applied WM mask. For this purpose, we define the number of detected fibers per voxel as the minimum number of fibers that are detected by both schemes with a corresponding partial WM volume fraction greater than 0.1. To extend the investigation of 3-shell HARDI and CS-DSI from voxel-wise ODFs to macroscopic brain connections, we used FSL's bedpostx and probtrackx in combination with the autoPtx plugin (Behrens et al., 2007; De Groot et al., 2013). Those tools provide a standard pipeline for probabilistic tractography to generate path probability maps for distinct WM tracts in the brain. For both 3-shell HARDI and CS-DSI, tract-specific probability maps were averaged across all subjects and thresholded for visualization based on the recommendations in De Groot et al. (2015).

5.3 Results

5.3.1 DMRI preprocessing

5.3.1.1 Motion and distortion correction

Figure 5.2A demonstrates that for both CS-DSI and 3-shell HARDI, susceptibility-induced distortions are corrected successfully using FSL's topup. Eddy-current-induced artifacts as well as subject motion were corrected using FSL's eddy. The applicability of this approach for DSI acquisitions as introduced above is validated by calculating the MSE between corresponding images acquired with AP and PA PE directions before and after eddy correction. Figure 5.2B depicts comparable MSE for dMRI data with and without the small post hoc shift of nominal b-values ("shells"). Further, for the calculated deviations in AP and PA PE measurements as well as the simulated pilot study scenario, which utilizes only AP PE DWIs ("AP"), both diffusion protocols, overall, yield similar differences between the MSE before and after eddy correction. However, Figure 5.2B shows that in the lower b-value regime the reduction in MSE due to eddy correction is higher for CS-DSI than for 3-shell HARDI, whereas in the higher b-value regime the opposite trend is observed. Specifically, considering the simulated pilot study scenario, where only AP sampling of $b > 0$ is used: up to $b = 2000$ s/mm^2 the MSE curves of both CS-DSI and 3-shell HARDI largely overlap, and for instance at b-values of approx. 1000 s/mm^2, the MSE reduction is 25% and 12% for CS-DSI and 3-shell HARDI, respectively. However, at $b = 3000$ s/mm^2 considerably higher MSE values are observed for CS-DSI. Accordingly, the MSE reduction is only 14% for CS-DSI compared to 28% for 3-shell HARDI. The same holds for eddy correction based on AP and PA PE measurements. At low b-values, the MSE reduction is 31% for CS-DSI and 25% for 3-shell HARDI. For higher b-values the MSE is reduced by 24% and 32%, respectively. The AP and PA PE eddy-current correction approach leads to smallest MSE values for 3-shell HARDI for all b-values up to 3000 s/mm^2.

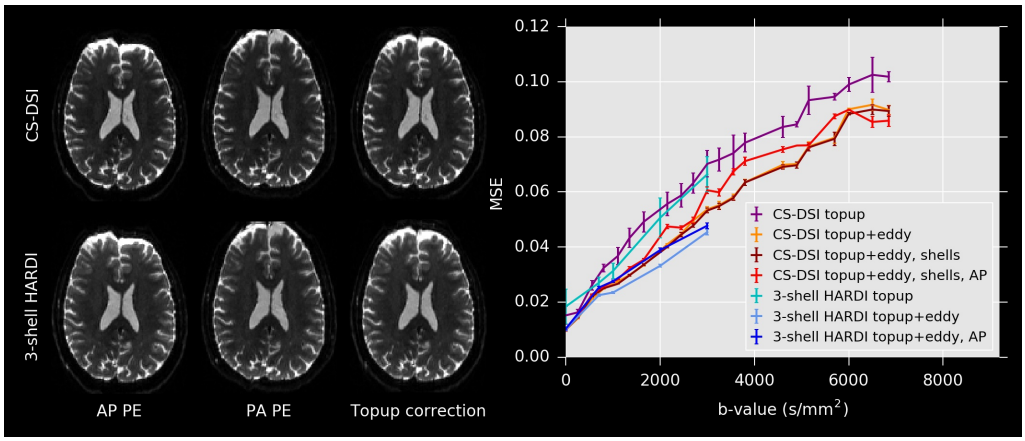

Figure 5.2: **(A)** Example b = 0 images with opposite PE directions and following topup correction for CS-DSI and 3-shell HARDI. **(B)** MSE calculated for the simulated pilot study scenario ("AP") and between corresponding images acquired with both AP and PA PE directions before and after eddy correction as well as with ("shells") and without a nominal b-value shift for CS-DSI acquisitions.

5.3.1.2 Compressed sensing in dMRI

Figure 5.3 depicts the NMSE with respect to the CHARMED reference signal of both 3-shell HARDI and CS-DSI. In general, the reconstruction error increases with increasing b-value. In the b-value regime below 4000 s/mm^2, a low NMSE of about 5% is observed for both 3-shell HARDI and CS-DSI. However, for 3-shell HARDI, signal extrapolation at higher b-values leads to an NMSE of up to 30% and is, thus, inferior compared to the signal interpolation for CS-DSI.

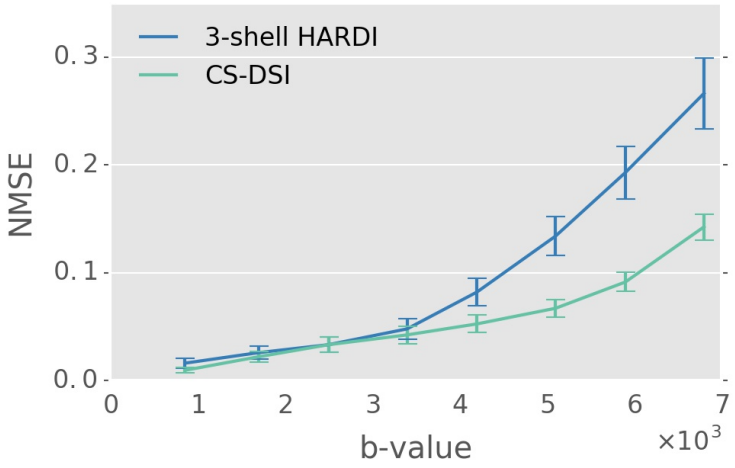

Figure 5.3: For 3-shell HARDI, CS-DSI and CHARMED data of Group B the respective signals for the diffusion directions of the CHARMED reference protocol were reconstructed using the MAPL MRI model. The NMSE with respect to the CHARMED reference signal was computed as a function of the b-value for both 3-shell HARDI and CS-DSI. Superior reconstruction quality is observed for CS-DSI in the b-value regime above 4000 s/mm^2.

5.3.1.3 DMRI analysis

5.3.1.4 Diffusion and microstructural parameter estimation

Group averaged whole brain diffusion parameter maps obtained by means of the tensor (FA_D, MD_D, AD_D, RD_D), kurtosis (MK, AK, RK) and NODDI (wIC, ODI) model are visualized in Figure 5.4. We denote FA and diffusivities derived from the tensor model by the subscript D, those from the kurtosis model by the subscript K. Figure 5.4 further presents tissue volume fraction maps for WM, GM and CSF obtained for both CS-DSI and 3-shell HARDI using the approach by Ankele et al. (2017). To generate the parameter maps, MR scans from the subset of 16 subjects (Group A) were used. SNR is slightly lower for CS-DSI due to higher b-value acquisitions. However, no significant difference between the group averaged parameter maps is noticeable by visual comparison of CS-DSI and 3-shell HARDI.

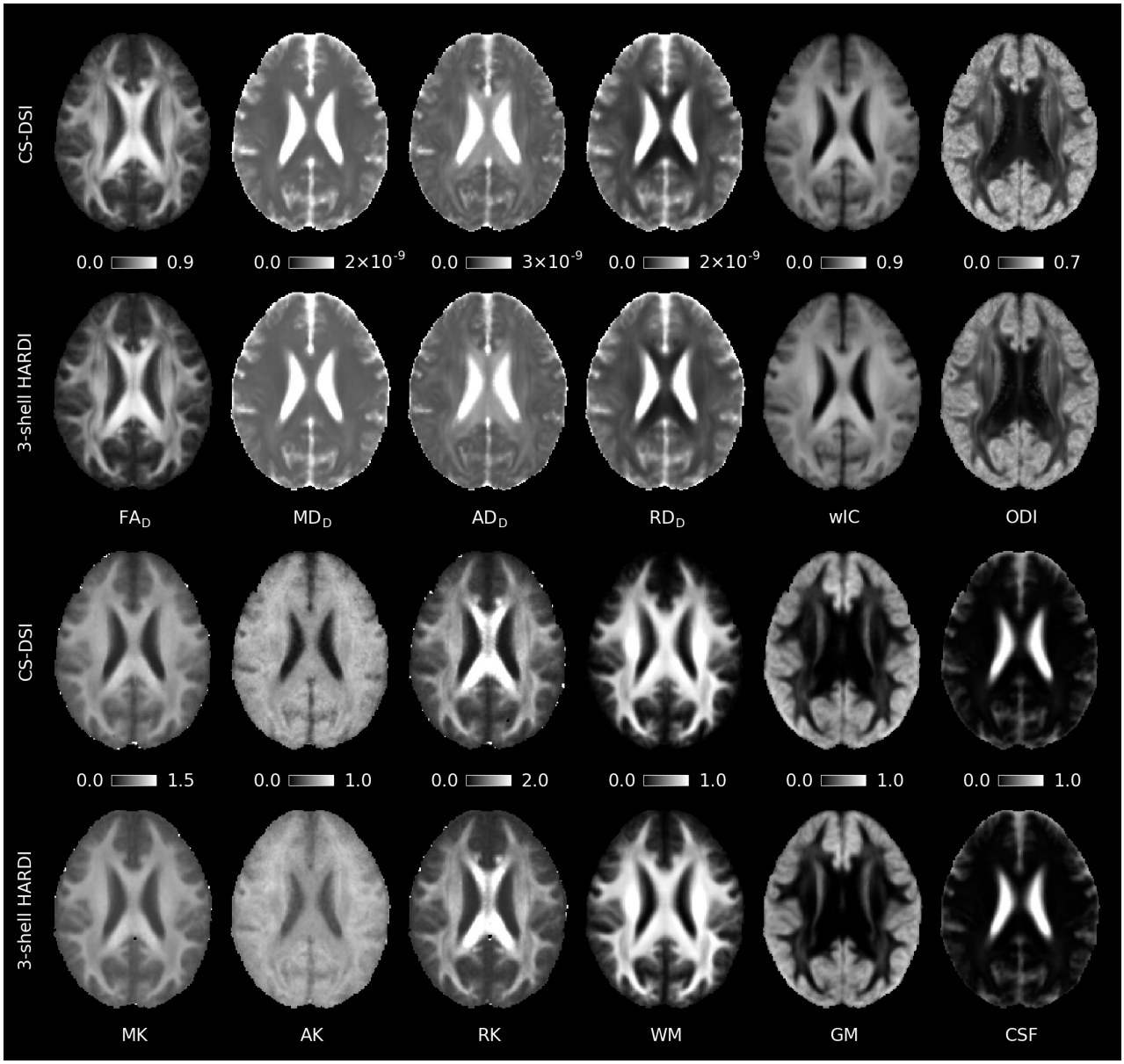

Figure 5.4: Group averaged whole brain diffusion parameter maps estimated from CS-DSI and 3-shell HARDI acquisitions by means of the tensor (FA_D, MD_D, AD_D, RD_D), kurtosis (MK, AK, RK) and NODDI (wIC, ODI) model. Brain tissue volume fraction maps for WM, GM and CSF were estimated using multi-tissue deconvolution. Comparable parameter maps are obtained for both CS-DSI and 3-shell HARDI. Diffusivities are given in units of m^2/s.

For parameters derived from the tensor (FA_D, MD_D, AD_D), kurtosis (FA_K, MD_K, AD_K, MK, AK, RK) and NODDI (wIC) model, the group mean and standard error calculated across all voxels on the TBSS white matter skeleton within each of the nine WM tract ROIs are shown in Figure 5.5. For each WM ROI, Figure 5.5, further, indicates the statistical significance ($p < 0.025$) of the differences between CS-DSI and 3-shell HARDI in the estimated diffusion parameters obtained from FSL's randomise. To this end, the mean p-value was extracted from the respective skeleton within each

WM ROI (Vovk and Wang, 2012). A linear fixed effects model was run for each diffusion parameter depicted in Figure 5.5 and the resulting p-value and the effect size with confidence intervals are reported in Table 5.2. The significance level of these 1-tailed tests was Bonferroni corrected for multiple comparisons and set to 0.025/N, where N $=$ 10 is the number of the independent linear fixed effects models. Significant differences in CS-DSI and 3-shell HARDI are observed for FA using both FSL's randomise and the fixed effects model. For the latter, significant differences are also observed in AD_D and ODI. To further explore differences in estimated diffusion parameters between the two imaging protocols, we determined residual errors of the MDT model fitting by computing the NMSE for the tensor and the NODDI model fitted to CS-DSI and 3-shell HARDI acquisitions. For the tensor model, the average NMSE across voxels within the WM ROIs was 0.027 ± 0.013 and 0.022 ± 0.010 for CS-DSI and 3-shell HARDI, respectively. For the NODDI model, the average NMSE was 0.060 ± 0.016 and 0.053 ± 0.015 for CS-DSI and 3-shell HARDI, respectively. Figure 5.6 provides more details on the analysis of the three subregions of the CC by depicting the group mean across CC voxels on the skeleton calculated for parameters estimated from the tensor (FA_D, MD_D), kurtosis (FA_K, MD_K, MK, AK, RK) and NODDI (wIC, ODI) model. The results presented in Figure 5.5 and 5.6 indicate similar performance of both the CS-DSI and the 3-shell HARDI imaging protocol in the estimation of FA, MD and AD from both the tensor and the kurtosis model as well as MK, AK, RK, wIC and ODI. For the tensor model, a slight upward FA bias is noticeable for CS-DSI compared to 3-shell HARDI, which is reduced through the application of the kurtosis model. Differences in mean diffusivity between the protocols are less significant for MD_K in comparison with MD_D. Comparable kurtosis and NODDI metrics are derived for both acquisition schemes, except for ODI estimated in the CC regions. Overall, differences in mean and standard error between CS-DSI and 3-shell HARDI are smaller than differences in the diffusion parameter values between different WM tracts.

FR was estimated by fitting the CHARMED model to CS-DSI (Group A and B) and dedicated CHARMED (Group B) acquisitions. Figure 5.7 compares the resulting group averaged FR maps and shows additional maps of MSD, RTOP and NG derived from the diffusion propagator by means for the MAPL MRI model. Here, RTOP is visualized as the return-to-origin-probability to the power of $1/3$ (Özarslan et al., 2013). Similar to Figure 5.5 and 5.6, Figure 5.7 further depicts the group mean and standard error of the group-specific FR calculated across all voxels on the skeleton within each WM ROI and provides a detailed visualization for the three subregions of the CC. Overall, FR obtained from CS-DSI is close to the CHARMED reference.

The test-retest reliability and repeatability of both diffusion imaging protocols of interest is validated by means of ICC and wsCV, respectively. Figure 5.8 depicts the TRT results for FA, MD and AD from both the tensor and the kurtosis model as well as MK, AK, wIC and FR as the average across the nine WM tracts and its standard error. For both protocols, diffusion parameter specific ICC and wsCV values greater than 0.85 and less than 4%, respectively, lie within acceptable ranges (Vollmar et al., 2010; Willats et al., 2014). The ICC values present similar reliability for both imaging protocols. For 3-shell HARDI acquisitions, wsCV increases for diffusion metrics of more advanced diffusion models. For CS-DSI, slightly lower repeatability is indicated by higher wsCV compared to 3-shell HARDI, however, repeatability of diffusivities improves with the use of the kurtosis model.

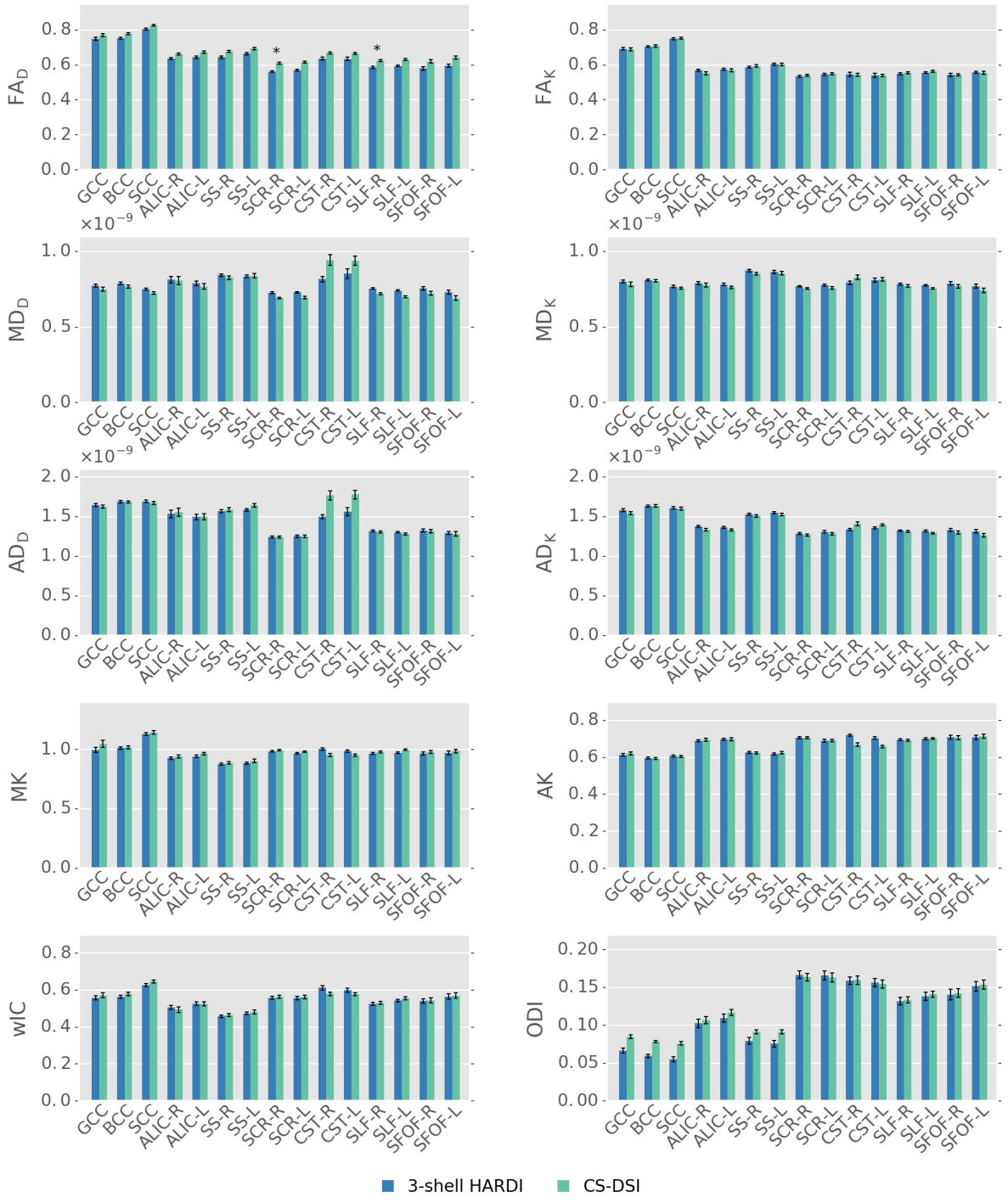

Figure 5.5: Parameter specific group mean and standard error for the tensor (FA_D, MD_D, AD_D), kurtosis (FA_K, MD_K, AD_K, MK, AK) and NODDI (wIC, ODI) model. For each WM ROI, mean p-values were extracted from the respective skeleton and are, if significant ($p < 0.025$), indicated as: $^{*}p < 0.025$ and $^{**}p < 0.005$. Except for FA derived from the tensor model, the analysis of significant differences in diffusion parameters estimated from CS-DSI and 3-shell HARDI acquisitions indicates comparable performance of both schemes. Diffusivities are given in units of m^2/s.

Table 5.2: The effect size and the corresponding confidence interval obtained from a linear mixed effects model for each of the diffusion parameter depicted in Figure 5.5 is provided together with the degree of significance. The significance level of these 1-tailed tests was Bonferroni corrected for multiple comparisons and set to 0.025/N, where N is the number of the independent linear fixed effects models. If significant (p < 0.025/N), p-values are indicated as: *p < 0.025/N, **p < 0.005/N, ***p < 0.0005/N and ****p < 0.00005/N.

FA_D	3.38×10^{-2}	$(2.95 \times 10^{-2}$ to $3.80 \times 10^{-2})^{****}$
MD_D	-7.94×10^{-12}	$(-1.80 \times 10^{-11}$ to $2.11 \times 10^{-12})$
AD_D	3.21×10^{-11}	$(1.38 \times 10^{-11}$ to $5.05 \times 10^{-11})^{**}$
FA_K	2.66×10^{-4}	$(-3.97 \times 10^{-3}$ to $4.50 \times 10^{-3})$
MD_K	-1.12×10^{-11}	$(-1.66 \times 10^{-11}$ to $-5.79 \times 10^{-12})$
AD_K	-1.51×10^{-11}	$(-2.41 \times 10^{-11}$ to $-6.15 \times 10^{-12})$
MK	9.08×10^{-3}	$(1.96 \times 10^{-3}$ to $1.62 \times 10^{-2})$
AK	-5.67×10^{-3}	$(-9.95 \times 10^{-3}$ to $-1.39 \times 10^{-3})$
wIC	2.08×10^{-3}	$(-2.97 \times 10^{-3}$ to $7.13 \times 10^{-3})$
ODI	6.59×10^{-3}	$(3.87 \times 10^{-3}$ to $9.31 \times 10^{-3})^{****}$

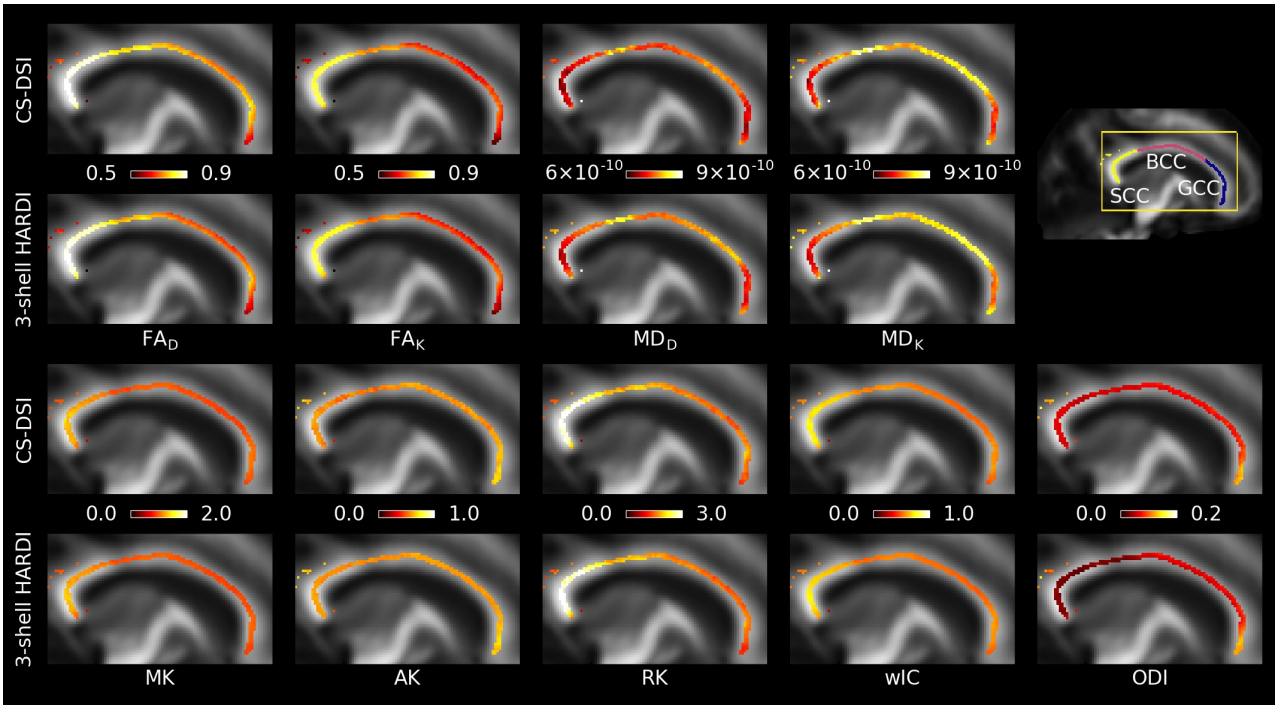

Figure 5.6: Sagittal view of group mean values across CC voxels on the TBSS white matter skeleton for parameters estimated from the tensor (FA_D, MD_D), kurtosis (FA_K, MD_K, MK, AK, RK) and NODDI (wIC, ODI) model overlaid on the FA map in WM atlas space. Top two rows: Kurtosis model fitting reduces the differences in FA and MD between CS-DSI and 3-shell HARDI compared to the tensor model. Bottom two rows: Comparable kurtosis and NODDI metrics are derived for both acquisition schemes. Diffusivities are given in units of m^2/s.

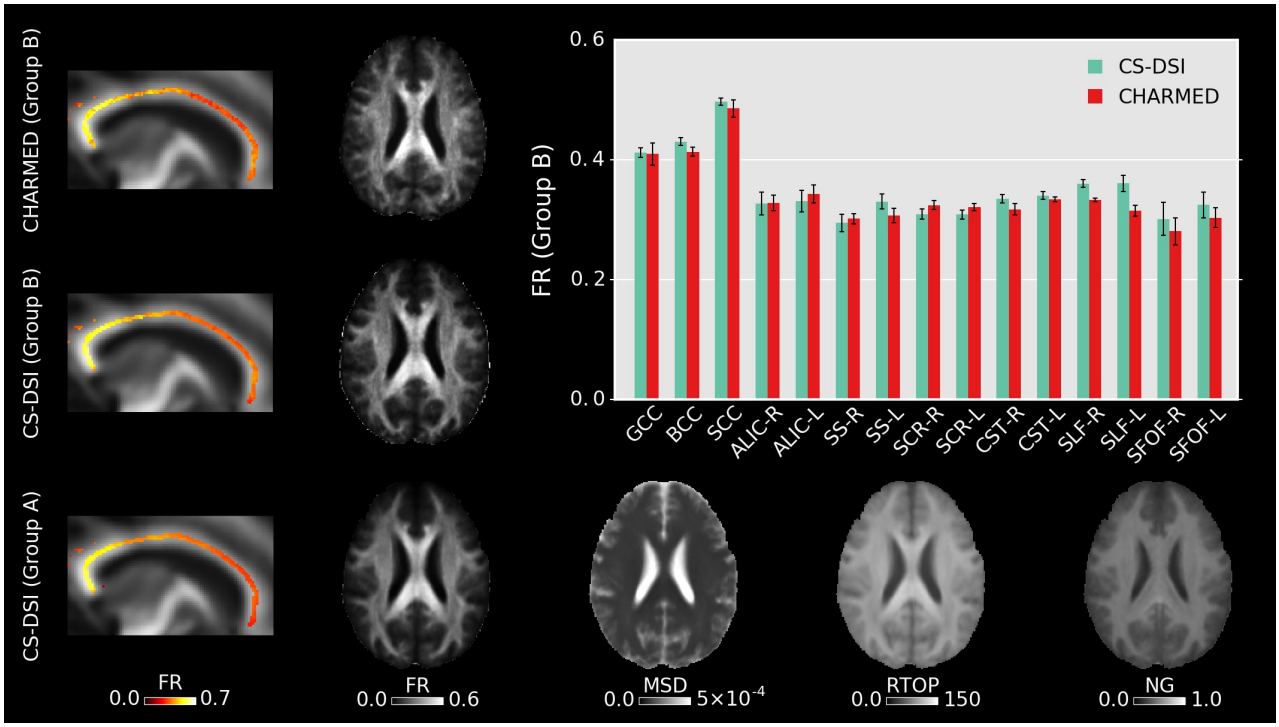

Figure 5.7: Group averaged whole brain FR maps, FR across the CC skeleton and the FR group mean and standard error across the skeleton within well-known WM ROIs are obtained by fitting the CHARMED model to CS-DSI (Group A and B) and CHARMED (Group B) acquisitions. Both CS-DSI and CHARMED schemes incorporate high b-value acquisitions that allow for accurate CHARMED modeling. For CS-DSI, additional maps of MSD, RTOP and NG are obtained from the diffusion propagator by means of the MAPL MRI model. MSD and RTOP are given in units of mm^2 and mm^{-1}, respectively.

5.3.1.5 Fiber orientation and macroscopic brain connections

Figure 5.9 visualizes group averaged tract probability maps overlaid on the WM atlas. Representative of sensorimotor, association and commissural tracts, the left (red) and right (green) corticospinal tract (CST), the left (red) and right (green) anterior thalamic radiation (ATR) and in blue the forceps major (FMA) are selected, respectively. The tracking results for CS-DSI and 3-shell HARDI show similar visitation counts for streamlines of the CST, ATR and FMA. Note that for the CST no lateral projections are shown due to the pre-defined target mask of the autoPtx plugin. Additionally, Figure 5.9 depicts single-subject diffusion and fiber ODFs in a coronal ROI of crossing fibers from the CC, CST and SLF. By visual comparison, diffusion ODFs calculated from the diffusion propagator indicate similar orientational information to that of fODFs obtained from CS-DSI and 3-shell HARDI. Comparable fODFs estimated via (Ankele et al., 2017) are obtained for both CS-DSI and 3-shell HARDI. This finding is supported by the quantitative analysis results presented in Table 5.3. Across all subjects, a high angular cross-correlation of 0.93 is observed with low standard error, as well as a small angular deviation of 9.7° and 7.8° in the estimated fiber directions and in the crossing angle in multi-fiber voxels, respectively.

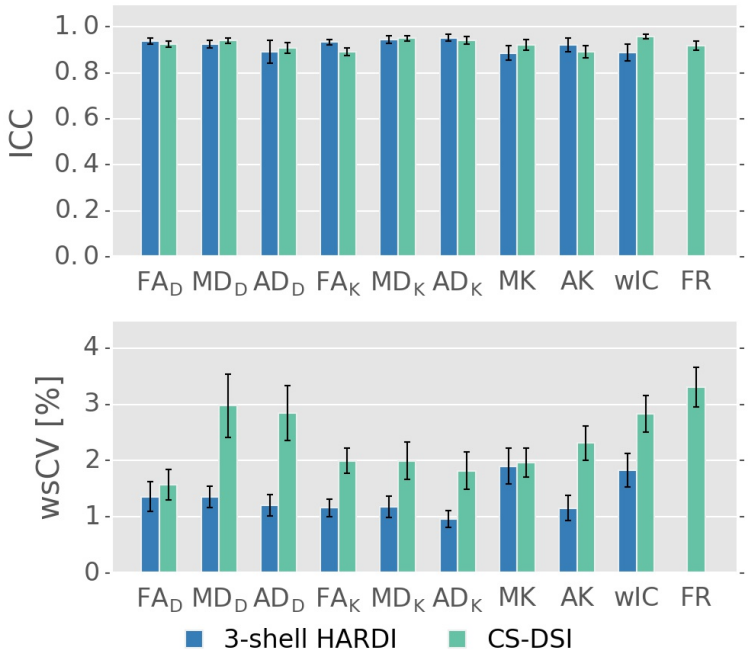

Figure 5.8: Parameter specific ICC and wsCV averaged over nine WM tracts for the tensor (FA_D, MD_D, AD_D), kurtosis (FA_K, MD_K, AD_K, MK, AK), NODDI (wIC) and CHARMED (FR) model. The latter is only reported for CS-DSI. ICC values present similar reliability for both imaging protocols. For CS-DSI, slightly lower repeatability is indicated by higher wsCV compared to 3-shell HARDI.

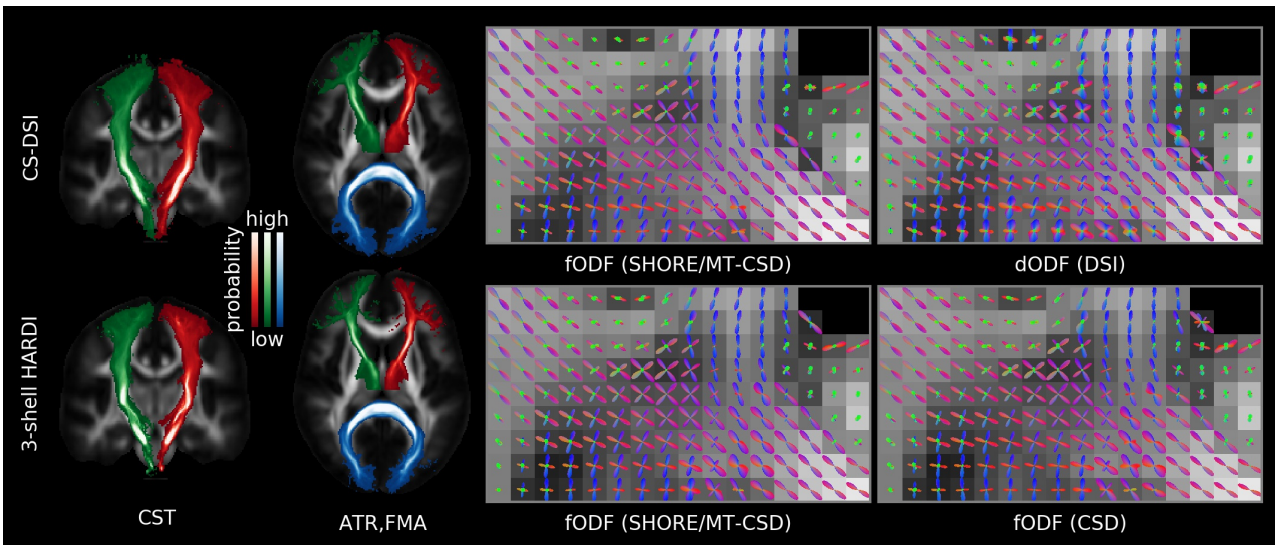

Figure 5.9: Comparable orientational information can be extracted from both CS-DSI and 3-shell HARDI acquisitions. Left: Group averaged tract probability maps are superimposed on the JHU ICBM FA white matter atlas for the left (red) and right (green) corticospinal tract (CST), the left (red) and right (green) anterior thalamic radiation (ATR) and in blue the forceps major (FMA). Right: Single-subject fODFs obtained by means of the SHORE/MT-CSD model (SHORE order 8) for both CS-DSI and 3-shell HARDI and, only for the latter, by means of the CSD model. Single-subject dODFs are derived from the DSI propagator.

Table 5.3: Quantitative analysis of the orientational information obtained from CS-DSI and 3-shell HARDI acquisitions: Group mean and standard error are reported for the angular cross correlation of both schemes, the angular deviation in the estimated fiber directions and in the crossing angle in multi-fiber voxels, the minimum crossing angle resolved by each scheme and the percentages of 1/2/3 fiber voxels within the WM mask. All metrics are computed for fODFs estimated with SHORE order 4, except for the angular cross correlation (SHORE order 8).

	Mean	SEM
Angular cross-correlation	0.931	0.006
Angular peak difference	9.7	0.4
Deviation in crossing angle	7.8	0.3
Min. crossing angle (CS-DSI / 3-shell)	28.7 / 29.1	0.2 / 0.4
Percentage of 1/2/3 fiber voxels	15.6 / 32.9 / 51.6	0.6 / 0.9 / 1.3

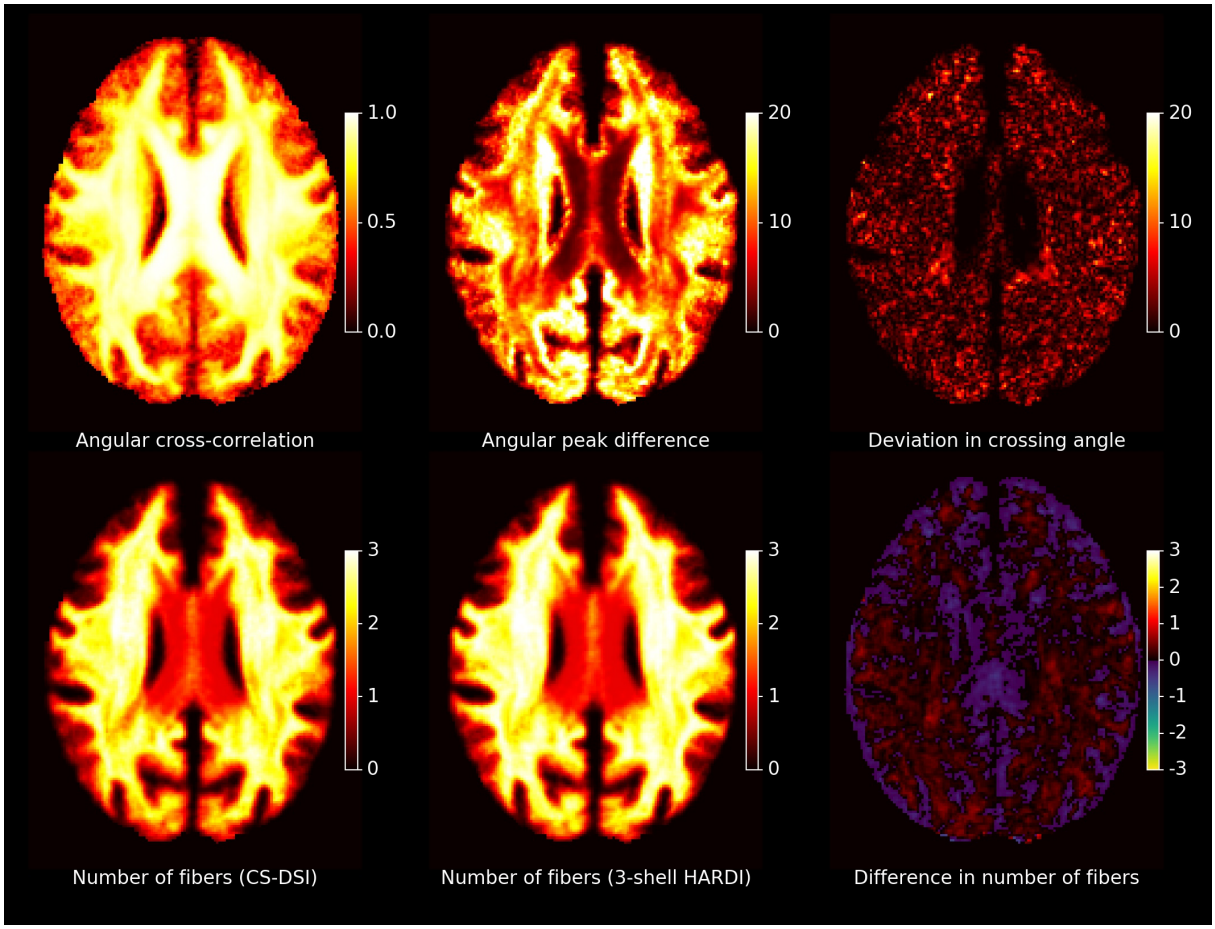

Figure 5.10: Spatial maps of the orientational information obtained from CS-DSI and 3-shell HARDI acquisitions: An axial slice of group-averaged whole brain maps of the angular cross correlation, the angular peak difference, the deviation in crossing angle and the number of fibers per imaging scheme and the corresponding difference (3-shell HARDI – CS-DSI) is shown. All metrics are computed for fODFs estimated with SHORE order 4, except for the angular cross correlation (SHORE order 8). The angular peak difference and the deviation in crossing angle are reported in degrees.

The minimum crossing angle that occurs in at least 1% of the WM voxels, is, on average, as low as 28.7° for CS-DSI and 29.1° for 3-shell HARDI. Percentages of 15.6 / 32.9 / 51.6 are determined for 1/2/3 fiber voxels within the applied WM mask. To support the quantitative analysis of the orientational information obtained from CS-DSI and 3-shell HARDI acquisitions (Table 5.3), Figure 5.10 provides maps of the group-averaged angular cross correlation, angular peak difference, deviation in crossing angle and number of fibers for an axial slice. For the latter, the number of fibers estimated in both CS-DSI and 3-shell HARDI and the difference of both maps (3-shell HARDI − CS-DSI) are shown.

5.4 Discussion

This work investigates CS-DSI for accelerated diffusion microstructure MRI in population imaging. For this purpose, we consider a 3-shell HARDI acquisition scheme as a gold standard protocol for multi-shell imaging in population studies, to which CS-DSI is compared to. We aimed to implement the comparison of these two conceptually very different diffusion protocols as even as possible, but we do not expect perfect agreement of diffusion parameters estimated from 3-shell HARDI and CS-DSI acquisitions due to differences in: the dMRI sequence parameters, even though the differences were kept minimal, subject motion during acquisitions and the selection of specific DWIs based on the b-value requirements for diffusion model fitting. Keeping these effects in mind, qualitative as well as quantitative dMRI analysis, overall, indicates comparable performance of CS-DSI and 3-shell HARDI on both single-subject and group level.

5.4.1 DMRI preprocessing

5.4.1.1 Motion and distortion correction

Considering 3-shell HARDI data to be the reference for FSL's eddy, the validation results of our approach to apply FSL's eddy to DSI data, overall, indicate adequate and similar correction of susceptibility-induced and eddy-current-induced distortions and motion artifacts in CS-DSI acquisitions. However, our validation experiment still captured differences in eddy correction between CS-DSI and 3-shell HARDI. They suggest that, in the low b-value regime, eddy correction leads to more reduction in MSE for CS-DSI compared to 3-shell HARDI. At higher b-values, on the other hand, the reduction in MSE due to eddy correction is lower for CS-DSI than for 3-shell HARDI and the final MSE level is considerably lower for 3-shell HARDI at b $=$ 3000 s/mm^2. The latter effect might be caused due to the sparse sampling distribution for CS-DSI at high b-values. Note, however, that this experiment was only performed with a single subject and for two different acquisitions for CS-DSI and 3-shell HARDI. Thus, the graphs presented in Figure 5.2 do not allow us to draw conclusions at a significant level. Within the scope of this work, using the same and preferably state-of-the-art processing tools for all data is a requirement for a reasonable comparison between the 3-shell HARDI and CS-DSI imaging protocol. Nevertheless, we notice that this approach might

perform in favor of 3-shell HARDI acquisitions and improved corrections could be achieved with tools specifically tailored for CS-DSI acquisitions. This work's overall comparable results for 3-shell HARDI and CS-DSI, however, show no preference of this processing step towards multi-shell data or any negative effect on subsequent dMRI analysis. Note, that we have tried to support motion estimation across low and high b-values by interleaving b = 0 measurements every 14 and 10 DWIs for CS-DSI and 3-shell HARDI, respectively. Nevertheless, we acknowledge that motion estimation becomes increasingly difficult the higher the b-value gets. We currently investigate the use of integrated free induction decay navigators (FIDnav) (Kober et al., 2011) as an independent means to estimate rigid-body head motion parameters. Such a navigator signal can be acquired within less than 3 ms before each excitation and diffusion weighting (Kober et al., 2012). Ongoing improvements (Stirnberg et al., 2016; Wallace et al., 2018) may potentially make purely FIDnav-informed prospective motion correction possible.

5.4.1.2 Compressed sensing in dMRI

In the context of population imaging, it has been shown before that CS-DSI provides comparable results to conventional DSI (Setsompop et al., 2013). A general concern with CS-DSI is the risk of missing subtle details about the diffusion process due to insufficient angular q-space sampling. However, the results of this work support that the risk of a dMRI protocol to not fully capture all diffusion information is not increased for CS-DSI accelerated by moderate undersampling because comparable diffusion parameters are estimated for both CS-DSI and 3-shell HARDI. Prior experiments based on full DSI simulations, phantom and in vivo measurements also confirmed the accurate CS reconstruction at such modest acceleration factors. For a single subject and 2.3-fold CS acceleration, for instance, the angular cross-correlation and peak difference both calculated between full and CS reconstructed DSI data over the brain WM are 0.964 and 5.3°, respectively. Fortunately, about 2-fold q-space undersampling already enables CS-DSI acquisitions within a similar time frame as 3-shell HARDI. Combining CS with an undersampling factor of 2.3 and SMS acquisition with an MB factor of 3 results in about 7-fold accelerated dMRI acquisitions compared to traditional DSI. CS-DSI scans, thus, can be acquired within the scan time limits of high throughput population studies.

In our work, we did consider sparse reconstruction for the 3-shell HARDI scheme, but decided against it for the following reasons. Ning et al. (2015) thoroughly investigated CS reconstruction methods as well as the degree of CS acceleration for multi-shell imaging. They recommend the CS approaches by Rathi et al. (2014) and Fick et al. (2016) for accurate signal reconstruction and suggest a CS factor similar to the one applied for CS-DSI in this work. Thus, our choice on the degree of undersampling for CS-DSI complies with other works in this research field. However, we do not apply the CS approach by Rathi et al. (2014) since (1) staggered q-space sampling is preferred over collinear acquisition schemes for diffusion and microstructure modeling (De Santis, Y Assaf, et al., 2014; Sprenger et al., 2016) and (2) more thorough investigations are recommended to ensure incorporating CS reconstruction based on dictionaries is suitable for population imaging (Bilgic et al., 2012). And (3), realizing a target angular resolution corresponding to 120 directions per shell (the resolution of the staggered 3-shell scheme) with an undersampling factor of 2.3 would

require a collinear sampling with 50 directions per shell. I.e. only two shells would be feasible in our scan time limit, or barely three shells, if we sacrificed target angular resolution (e.g. 92 = 2.3 $\times$ 40 directions per shell). Note, however, that this case would not allow for additional sparse radial reconstruction without exceeding a total undersampling factor of 2.3.

Subsampling the established HCP protocol containing 90 directions per shell was investigated using the CS approach by Fick et al. (2016). Applying a CS factor of 2.3 results in about 120 DWIs which is the number of diffusion weighted acquisitions we chose for the time-matched 3-shell HARDI protocol in this work. We use the approach by Fick et al. (2016) for signal interpolation of the 3-shell HARDI as well as CS-DSI data to obtain information of the diffusive transport along different gradient directions than those applied during image acquisition. As depicted in Figure 5.3, the reference signal can be adequately reconstructed for both 3-shell HARDI and CS-DSI as indicated by an NMSE of about 5% which is similar to the results reported by Ning et al. (2015). Thus, both the 3-shell HARDI as well as the CS-DSI data can be further enriched by reconstructing additional DWIs across the chosen b-value regime via the approach by Fick et al. (2016). Such investigations of increasing the angular as well as radial resolution are highly interesting but beyond the scope of this work.

A limitation of this work is the choice of different maximum b-values for CS-DSI and 3-shell HARDI. We selected the well-established 3-shell HARDI scheme as a gold standard protocol for multi-shell imaging in population studies, as investigating a novel design of the 3-shell HARDI scheme as outlined above exceeds the scope of this work. We decided against including shells at higher b-values for the 3-shell HARDI scheme since, to comply with the scan time limits of our study, this adaptation would come at the cost of a reduced number of samples at lower b-value shells, which would increase the CS factor, or the exclusion of shells, which we do not consider for the reasons discussed before. We aimed to address this limitation of our work by applying the CS approach by Fick et al. (2016) to extrapolate high b-value acquisitions for 3-shell HARDI. Overall, we observe an increase in the reconstruction error with increasing b-value (see Figure 5.3). Compared to signal interpolation, of course, higher NMSE was expected for signal extrapolation, yet not to this extent, since Ning et al. (2015) report lower NMSE for signal extrapolation using this method. We argue that an NMSE of up to 30% due to signal extrapolation and reduced SNR at higher b-values for 3-shell HARDI is not favorable for subsequent diffusion and microstructural parameter estimation. Thus, we did not include results from sparse reconstruction for the 3-shell HARDI scheme in our dMRI analysis. We acknowledge, however, that 3-shell HARDI variants specifically tailored for high b-values (e.g. including b = 6800 s/mm^2) would avoid signal extrapolation and may thus reduce the NMSE at high b-values compared to Figure 5.3.

5.4.2 DMRI analysis

5.4.2.1 Diffusion and microstructural parameter estimation

Diffusion parameter maps and the quantitative statistical analysis across all subjects show good agreement between CS-DSI and 3-shell HARDI for diffusion models processing DWIs with b-values

up to approx. 3000 s/mm^2. Overall, diffusion parameters stemming from distinct WM tracts can be well distinguished for both CS-DSI and 3-shell HARDI and are not masked by differences in the dMRI protocols. For the DT model, a slight upward FA bias of CS-DSI compared to 3-shell HARDI is explained by reduced SNR due to longer TE for higher b-value acquisitions (Farrell et al., 2007). Slightly lower residual errors from the tensor and NODDI model fitting for 3-shell HARDI compared to CS-DSI support this finding. Additionally, the 3-shell HARDI protocol allows us to fit the DT model to the 30 DWIs of the inner shell at b = 1000 s/mm^2 (Table 5.1). In contrast, a subset of 28 CS-DSI DWIs is used to fit the DT model to measurements with multiple b-values in the range of 230 - 1300 s/mm^2 (Table 5.1). This may lead to a different fit to the mono-exponential signal decay. The resulting difference between CS-DSI and 3-shell HARDI in FA_D is confirmed by statistical analysis as depicted in Figure 5.5 and Table 5.2. For ODI estimated for both acquisition schemes in the CC WM regions, our results show an anterior-posterior gradient indicated by a decrease in ODI from the genu over the body to the splenium of the CC (Figure 5.5 and Figure 5.6). In these WM ROIs, an overall increase in ODI is observed for CS-DSI compared to 3-shell HARDI which is supported by the statistical analysis using the linear fixed effects model. This difference might stem from differences in the acquisition scheme, but further investigations are needed. To investigate the significant differences observed for AD_D and ODI with fixed effects models, we performed further statistical analyses. As depicted in Figure 5, the biggest differences in AD_D and ODI between acquisition schemes occur in the WM regions of the CST and CC, respectively. Running a linear fixed effects model with CST and CC regions excluded for AD_D and ODI, respectively, we observe p-values above the significance level. This finding confirms that mainly these WM regions affect the overall significance obtained for AD_D and ODI by the fixed effects model across all WM ROIs. Fitting the kurtosis model results in more similar DT derived parameters of both protocols. This can be explained by the reduced b-value dependency of the kurtosis model compared to the DT model (Veraart et al., 2011). The kurtosis model accounts for the diffusional non-Gaussianity and incorporates the non-monoexponential behavior of the multiple b-value CS-DSI acquisitions in the estimation of the diffusion tensor. The similarity between protocols in parameters derived from the kurtosis model is supported by p-values above the significance levels across all WM ROIs. An in-house implementation of the kurtosis model that integrates important constraints for robustness to noise (Groeschel et al., 2016) was found to improve the fit and the derived parameter maps. Since DT derived metrics from the DT model and the kurtosis model, however, are not directly comparable (Lanzafame et al., 2016), those parameters should be reported for both models. To further extend the comparison of DT model parameters obtained from CS-DSI and 3-shell HARDI, future work could convert CS-DSI and 3-shell HARDI data to corresponding single-shell HARDI data (Yeh and Verstynen, 2016). In this way, FA and diffusivities can be obtained for CS-DSI and 3-shell HARDI without fitting the tensor model to measurements with multiple b-values. Despite the slight SNR reduction and the effects of multi b-value data on the DT model fitting, the CS-DSI imaging protocol delivers reliable data. Our results on kurtosis metrics agree with recent findings by Sprenger et al. (2016) who investigate acquisition schemes for diffusion kurtosis imaging (DKI) and report that both 3-shell and CS-DSI schemes are suitable choices. The comparable performance of both schemes with respect to kurtosis model fitting indicates a low dependency of kurtosis parameter estimation on the acquisition scheme as similarly suggested by Sprenger et al. (2016) with respect to the bias on DKI metrics. Further, in contrast to the 3-shell HARDI scheme, CS-DSI provides high b-value acquisitions increasing its potential for future image

analysis. In this work, we selected the CHARMED model as an example of a state-of-the-art diffusion model that requires DWIs at high b-values (> 3000 s/mm^2). Our results show that compared to the dedicated CHARMED reference, CS-DSI allows for accurate FR parameter estimation that the standard 3-shell HARDI scheme applied in population imaging cannot provide. Together with the diffusion parameter maps derived from the diffusion propagator, this experiment highlights the advantages of the higher b-value CS-DSI acquisitions. Future developments of novel mathematical or biophysical diffusion models might have similar requirements which would be fulfilled by dMRI data collected with the CS-DSI imaging protocol. In the context of a long-term population study, this benefit gained from including scans with higher diffusion weighting in the imaging protocol makes up for the compromise of a slightly reduced SNR (~4% in brain tissue) that, in any case, with the emergence of novel denoising techniques (Veraart, D S Novikov, et al., 2016) could potentially be overcome.

Measures for test-retest reliability and repeatability, the ICC and the wsCV, were obtained on a subset of 5 subjects for each of the diffusion protocols of interest. Due to the wide range of questions we aimed to answer, rescans could be collected for just a small sample size. Differences between the subjects, e.g. through subject motion during acquisition, will not be smoothed out across just 5 subjects and will, therefore, influence the TRT evaluation and comparison between CS-DSI and 3-shell HARDI. Despite this limitation of our pilot study data, we report ICC and wsCV values above 0.85 and smaller than 4%, respectively, for both imaging protocols. TRT indices of this scale are in agreement with related work on TRT analysis of diffusion models (Vollmar et al., 2010; Willats et al., 2014) and lie within acceptable ranges for reliability and repeatability. Both CS-DSI and 3-shell HARDI provide similar ICC confirming the validity of both diffusion protocols. Our results, further, show that for both protocols, repeatability decreases with the use of more advanced methods. This may simply be explained by the models' requirements of higher b-value acquisitions with lower SNR and increased eddy-current-induced distortions contributing to more differences between scan and rescan. The same effects occurs for high b-value CS-DSI data that provides adequate repeatability indices but higher within-subject variability than 3-shell HARDI. Our results on test-retest repeatability point towards a similar direction as the findings by Sprenger et al. (2016) on the superior performance of multi-shell schemes in terms of bias and precision. However, due to the limitations of our pilot study, which influence TRT analysis, further investigation in this regard is necessary. Additionally, for CS-DSI, the TRT results show improved repeatability of diffusivities when using the kurtosis rather than the DT model. This supports our earlier findings from the group averaged diffusion parameters indicating that, for multiple b-value CS-DSI acquisitions, the kurtosis model is better suited for the estimation of DT derived parameters than the tensor model.

5.4.2.2 Fiber orientation and macroscopic brain connections

Three state-of-the-art methods for the estimation of fiber orientations which form the basis for tractography were evaluated and compared for both CS-DSI and 3-shell HARDI. Visual comparison suggests that comparable orientational information is provided by CS-DSI and 3-shell HARDI. Specifically, for 3-shell HARDI, fODFs estimated via (Ankele et al., 2017) are in good agreement with fODFs

obtained by means of the state-of-the-art CSD approach. Thus, we based the quantitative comparison of the orientational information obtained for CS-DSI and 3-shell HARDI on the fODFs estimated using the former method. In this regard, the similarity of the orientational information obtained from both advanced dMRI acquisitions and their robustness across subjects is quantified by a high angular cross-correlation with low standard error. Additionally, the high angular cross-correlation coincides with the small angular deviation in the estimated fiber directions and in the crossing angle in multi-fiber voxels. An adequate minimum crossing angle can be resolved by each of the advanced acquisition schemes. The reported percentages of 1/2/3 fiber voxels within the applied WM mask agree with previous works (Jeurissen et al., 2013; Schultz, 2012). We do not compute this metric per acquisitions scheme due to the lack of a protocol-specific criterium for choosing the threshold used for fiber selection. Due to this limitation, Figure 5.10 shows small variations in the estimated number of fibers between CS-DSI and 3-shell, which are, however, on average below 1 fiber in WM. Additionally, comparable tissue volume fraction maps for WM, GM and CSF are obtained for CS-DSI and 3-shell HARDI, which can provide guidance for fiber tracking equally well for both acquisition schemes. Thus, despite acquiring dMRI data with different diffusion protocols and employing different methods for ODF reconstruction, comparable fiber orientations of the brain microstructure can be estimated from both CS-DSI and 3-shell HARDI. Supporting these results, probabilistic fiber tracking based on the standard FSL pipeline further indicates good agreement of fiber orientation estimates from both dMRI protocols. Recent investigations by Gigandet et al. (2013) on the dependency of brain network connectivity measures on different acquisitions schemes agree with our finding that DSI acquisitions are at least as suitable as 3-shell HARDI scans for the extraction of orientational information, although both schemes are conceptually very different. Gigandet et al. (2013) further report the highest connectivity for a DSI acquisitions scheme similar to the one applied in this work.

5.4.3 CS-DSI in population imaging

This work primarily focuses on showing that for a wide range of state-of-the-art diffusion analysis techniques, CS-DSI is able to provide diffusion information similar to that captured by 3-shell HARDI, despite the small SNR loss due to higher b-value acquisitions. This is the starting point for validating the applicability of CS-DSI for population imaging. Note that in this work we do not aim to decide whether CS-DSI or a multi-shell scheme is more suitable for population imaging. We rather chose the latter as a gold standard protocol. The CS-DSI protocol proposed in this work for population imaging should at least deliver dMRI data comparable to that obtained by conventional and well-established dMRI protocols such as 3-shell HARDI. Our pilot study affirms the above for CS-DSI and 3-shell HARDI acquisitions collected at both 1.5mm and 2.0mm isotropic resolution. Here, we only present the results for 1.5mm isotropic resolution as we observed the same trends for both resolutions. Furthermore, the collection of CS-DSI acquisitions allows for high flexibility in dMRI analysis as already noted in previous works such as Sprenger et al. (2016). First, CS-DSI contains high b-value acquisitions and thus provides dMRI data applicable to diffusion models that specifically require high diffusion weightings and with a great potential to be well-suited for future methods developed for dMRI analysis (Veraart, Els Fieremans, et al., 2016). Second, complimentary biomarkers can be extracted directly from the diffusion propagator which is obtained in a model-free manner by CS-DSI

without any prior assumptions. Diffusion measures such as the return-to-origin probability and the return-to-axis probability as well as the propagator anisotropy and non-Gaussianity have already been proposed to map the microstructure of brain tissue (Özarslan et al., 2013). Also, the clinical feasibility of estimating those parameters from subsampled MR data has recently been reported (Avram et al., 2016). Future developments might further exploit the diffusion information content provided by the diffusion propagator. In this work, we additionally determined propagator-based diffusion parameters and CHARMED parameters to highlight and quantify the potentials of CS-DSI to provide dMRI data well-suited for such analysis which further extends this protocol's scope of application for population imaging.

5.5 Conclusion

The contributions of this work are three-fold: 1) defining an imaging protocol for compressed sensing DSI complying with stringent scan time limits of long-term population studies, 2) conducting a pilot study delivering dMRI data for an in depth investigation of this protocol based on a wide spectrum of state-of-the-art diffusion processing and analysis techniques and 3) validating the applicability and potentials of accelerated DSI using CS for population imaging. The results of this work indicate comparable performance of CS-DSI and the 3-shell HARDI scheme well-established in population imaging in the estimation and reliability of diffusion and microstructural parameters when considering DWIs up to the same maximum diffusion weighting for both protocols. Further, both schemes perform comparable in the inference of fiber orientation and macroscopic brain connections. These findings hold despite the slightly smaller SNR of CS-DSI scans due to higher b-value acquisitions. Providing such high b-value data, CS-DSI enables the accurate fitting of specific microstructure models such as the CHARMED model. Additionally, the diffusion propagator obtained by means of the model-free DSI approach allows for high quality fiber orientation estimation and the extraction of further complimentary biomarkers. Even if stringent scan time limits are imposed, CS-DSI provides high radial resolution while maintaining high angular resolution and it is a forward-looking acquisition strategy with a great potential for future developments. Thus, CS-DSI presents a well-suited imaging protocol for dMRI within the scope of a scan time-limited, high throughput, long-term population study.

5.6 Supplementary Material

Table 5.4: B-values and b-vectors of the CS-DSI imaging protocol.

b-values	b-vectors		
0	0	0	0
270	0	0	-1
270	0	1	0
270	1	0	0
540	0	0.70710678118655	-0.70710678118655
540	0	0.70710678118655	0.70710678118655
540	-0.70710678118655	0.70710678118655	0
540	0.70710678118655	0	-0.70710678118655
540	-0.70710678118655	0	-0.70710678118655
540	0.70710678118655	0.70710678118655	0
820	0.57735026918963	-0.57735026918963	-0.57735026918963
820	0.57735026918963	-0.57735026918963	0.57735026918963
820	0.57735026918963	0.57735026918963	-0.57735026918963
820	0.57735026918963	0.57735026918963	0.57735026918963
1090	0	0	1
1090	0	1	0
1090	-1	0	0
0	0	0	0
1360	0	-0.44721359549996	0.89442719099992
1360	0	-0.44721359549996	-0.89442719099992
1360	0	-0.89442719099992	0.44721359549996
1360	0	-0.89442719099992	-0.44721359549996
1360	-0.44721359549996	0.89442719099992	0
1360	0.44721359549996	0	-0.89442719099992
1360	0.44721359549996	0	0.89442719099992
1360	0.44721359549996	0.89442719099992	0
1360	-0.89442719099992	0.44721359549996	0
1360	-0.89442719099992	0	0.44721359549996
1360	-0.89442719099992	0	-0.44721359549996
1360	-0.89442719099992	-0.44721359549996	0
1630	0.40824829046386	-0.81649658092773	-0.40824829046386
1630	-0.40824829046386	0.81649658092773	-0.40824829046386
1630	-0.40824829046386	0.40824829046386	0.81649658092773
1630	0.40824829046386	-0.40824829046386	0.81649658092773
0	0	0	0
1630	0.40824829046386	0.40824829046386	-0.81649658092773
1630	0.40824829046386	0.40824829046386	0.81649658092773
1630	-0.40824829046386	-0.81649658092773	0.40824829046386
1630	-0.40824829046386	-0.81649658092773	-0.40824829046386
1630	0.81649658092773	-0.40824829046386	-0.40824829046386
1630	-0.81649658092773	0.40824829046386	-0.40824829046386
1630	-0.81649658092773	-0.40824829046386	0.40824829046386
1630	-0.81649658092773	-0.40824829046386	-0.40824829046386
2180	0	-0.70710678118655	0.70710678118655
2180	0	-0.70710678118655	-0.70710678118655
2180	0.70710678118655	-0.70710678118655	0
2180	-0.70710678118655	0	-0.70710678118655
2180	-0.70710678118655	-0.70710678118655	0
2450	0	0	1
2450	0	1	0
2450	0.33333333333333	0.66666666666667	-0.66666666666667
0	0	0	0
2450	-0.33333333333333	-0.66666666666667	-0.66666666666667
2450	0.66666666666667	-0.66666666666667	0.33333333333333
2450	0.66666666666667	-0.33333333333333	-0.66666666666667
2450	0.66666666666667	-0.33333333333333	0.66666666666667
2450	-0.66666666666667	-0.66666666666667	0.33333333333333

b-values	b-vectors		
2450	0.66666666666667	0.66666666666667	0.33333333333333
2450	1	0	0
2720	0	0.31622776601684	-0.94868329805051
2720	0	-0.31622776601684	-0.94868329805051
2720	0	0.94868329805051	-0.31622776601684
2720	0	-0.94868329805051	-0.31622776601684
2720	0.31622776601684	-0.94868329805051	0
2720	0.31622776601684	0	-0.94868329805051
2720	0.31622776601684	0	0.94868329805051
2720	-0.31622776601684	-0.94868329805051	0
2720	0.94868329805051	-0.31622776601684	0
0	0	0	0
2720	0.94868329805051	0	-0.31622776601684
2720	-0.94868329805051	0	-0.31622776601684
2990	0.30151134457776	-0.90453403373329	-0.30151134457776
2990	-0.30151134457776	0.30151134457776	0.90453403373329
2990	0.30151134457776	-0.30151134457776	0.90453403373329
2990	-0.30151134457776	-0.90453403373329	0.30151134457776
2990	0.30151134457776	0.90453403373329	0.30151134457776
2990	-0.90453403373329	-0.30151134457776	-0.30151134457776
3260	0.57735026918963	-0.57735026918963	-0.57735026918963
3260	-0.57735026918963	0.57735026918963	-0.57735026918963
3260	-0.57735026918963	-0.57735026918963	0.57735026918963
3260	-0.57735026918963	-0.57735026918963	-0.57735026918963
3540	0	0.83205029433784	-0.55470019622523
3540	0.55470019622523	-0.83205029433784	0
3540	-0.83205029433784	0	0.55470019622523
3540	0.83205029433784	0	0.55470019622523
0	0	0	0
3540	0.83205029433784	0.55470019622523	0
3810	0.53452248382485	-0.26726124191242	-0.80178372573727
3810	0.53452248382485	0.26726124191242	0.80178372573727
3810	-0.53452248382485	-0.80178372573727	-0.26726124191242
3810	-0.80178372573727	0.53452248382485	0.26726124191242
3810	0.80178372573727	-0.26726124191242	0.53452248382485
3810	-0.80178372573727	-0.26726124191242	0.53452248382485
3810	-0.80178372573727	-0.26726124191242	-0.53452248382485
3810	0.80178372573727	0.53452248382485	0.26726124191242
4620	0.24253562503633	0	0.97014250014533
4620	-0.24253562503633	-0.97014250014533	0
4620	0.727606875109	-0.48507125007267	0.48507125007267
4620	0.97014250014533	-0.24253562503633	0
4900	-0.94280904158206	0.23570226039552	-0.23570226039552
4900	0.94280904158206	0.23570226039552	-0.23570226039552
5170	-0.22941573387056	0.68824720161169	-0.68824720161169
0	0	0	0
5170	0.22941573387056	0.68824720161169	0.68824720161169
5170	0.68824720161169	0.22941573387056	-0.68824720161169
5170	-0.68824720161169	-0.22941573387056	-0.68824720161169
5170	-0.68824720161169	-0.68824720161169	0.22941573387056
5440	-0.44721359549996	0	0.89442719099992
5710	-0.21821789023599	0.43643578047198	-0.87287156094397
5710	-0.87287156094397	-0.21821789023599	0.43643578047198
5980	-0.42640143271122	0.63960214906683	0.63960214906683
5980	0.63960214906683	-0.63960214906683	-0.42640143271122
6530	-0.40824829046386	0.81649658092773	-0.40824829046386
6530	-0.40824829046386	0.40824829046386	0.81649658092773
6530	-0.40824829046386	0.40824829046386	-0.81649658092773
6530	-0.40824829046386	-0.40824829046386	-0.81649658092773
6530	-0.40824829046386	-0.81649658092773	0.40824829046386
6800	0	0.6	0.8
6800	-0.6	0	0.8

b-values	b-vectors		
0	0	0	0

Table 5.5: B-values and b-vectors of the 3-shell HARDI imaging protocol.

b-values	b-vectors		
0	0	0	0
0	0	0	0
1000	-0.084899954968383	-0.060642824977416	-0.99454232962963
1000	-0.3050901500203	0.31722441735066	-0.89793578244612
1000	-0.51088934316965	-0.064077646431447	-0.85725499955585
1000	-0.28241382100923	-0.43661523248052	-0.85417186354325
1000	0.15069369463011	-0.42609941240237	-0.89203738775294
1000	0.35817920054867	-0.043258357554187	-0.93265018886828
1000	0.12997935052105	0.32754796331305	-0.93585132375159
1000	-0.31524428072045	0.70150513017464	-0.63914911860356
1000	-0.69812050315587	0.40709260109585	-0.58898503988336
1000	-0.83421847508829	-0.055383799175986	-0.54864576058711
0	0	0	0
1000	-0.67172578338753	-0.51245059763585	-0.53495687388337
1000	-0.27386635263343	-0.78693243098466	-0.5529326993042
1000	0.20968490450875	-0.77635402661091	-0.59439605162398
1000	0.5924896640895	-0.48334683123091	-0.64446244164121
1000	0.72913469700569	-0.019051025337441	-0.68410500075355
1000	0.56636900362945	0.43819987130964	-0.69800216655251
1000	0.16794126163783	0.7133175236576	-0.68042181261514
1000	-0.38793128039871	0.89016374162917	-0.23899337810277
1000	-0.76385312076859	0.61662519499687	-0.19053025688105
1000	-0.96913460688006	0.19764104684137	-0.14736393843436
0	0	0	0
1000	-0.95586744331653	-0.26840480745301	-0.11948343041457
1000	-0.72798276157231	-0.67598399288857	-0.11439729110422
1000	-0.33771715050097	-0.93175295881806	-0.13335497737731
1000	0.12479179617966	-0.9775357367407	-0.16985550035565
1000	0.55623728113285	-0.80229863291124	-0.21660330262183
1000	0.8551577633292	-0.44662085615169	-0.26312546563975
1000	0.95404282845016	0.0086573759387492	-0.29954520748072
1000	0.82987435791553	0.45911629404513	-0.31705012003871
1000	0.51087708541693	0.80181725609505	-0.30998982471061
1000	0.071054524643738	0.95663652691081	-0.28248506138852
0	0	0	0
2000	-0.99572330586683	-0.023270286360971	0.08940688970268
2000	-0.92738763005052	-0.36384957215985	-0.086980874152691
2000	-0.95370485908667	-0.044073652024544	-0.29749715116568
2000	-0.94635854119975	0.29749692821674	-0.12609952101368
2000	-0.91253668269993	0.32091894076159	0.25355046083072
2000	-0.88645116378918	0.0024487601209646	0.46281566286231
2000	-0.89363603022878	-0.34031618685425	0.29257398797901
2000	-0.69288019314824	-0.72103610205709	0.0048966798102349
2000	-0.72987277032525	-0.57802004629785	-0.36493638516263
2000	-0.75796057269037	-0.25591883633649	-0.60000109954488
0	0	0	0
2000	-0.76899310778606	0.14204331290316	-0.62327626092851
2000	-0.76012468107259	0.48961332114177	-0.42718762269619
2000	-0.73268030229315	0.67632027903983	-0.0759635096023
2000	-0.69671298903797	0.64283711642344	0.31835742908589
2000	-0.66247154981088	0.40042180552339	0.63308279344219
2000	-0.64163671508078	0.02693894605301	0.76653546496291
2000	-0.64068750093617	-0.36138205119727	0.67743821800708
2000	-0.66012642865499	-0.63930611457867	0.39436124309259
2000	-0.37335169400571	-0.92052614390915	-0.11506576798864

b-values	b-vectors		
2000	-0.41047449234671	-0.76581062004983	-0.49501998480021
0	0	0	0
2000	-0.44191045264613	-0.46027238281148	-0.76997693826707
2000	-0.46045492070374	-0.063679935842007	-0.88539603103406
2000	-0.46428127204709	0.3417796171534	-0.81708603814092
2000	-0.45090827762793	0.67881300490727	-0.57956417205981
2000	-0.42390852924954	0.8784462874911	-0.22053044874254
2000	-0.3895070426633	0.90150057673016	0.18862919676147
2000	-0.35157157197415	0.74479273784072	0.56716946977015
2000	-0.32086310298731	0.43965593119253	0.83889780742864
2000	-0.30262200633336	0.046557231743594	0.95197287012559
2000	-0.2975292610463	-0.35752487335605	0.88524138163158
0	0	0	0
2000	-0.31104639671551	-0.69311913598811	0.65025841203125
2000	-0.33802721832183	-0.89405749773528	0.2939367115842
2000	-0.0073451958367	-0.94630606362818	-0.3231886168148
2000	-0.040432129899767	-0.74983222723204	-0.66039145502952
2000	-0.068562199995085	-0.43830834996858	-0.89620589993575
2000	-0.084517581108225	-0.060019731511638	-0.99461269362143
2000	-0.089385573539904	0.32815525628348	-0.94038521203625
2000	-0.078340948431306	0.66467398434686	-0.74301493277817
2000	-0.057577203485755	0.9004094587666	-0.43121650270183
2000	-0.028168639095136	0.99814960271894	-0.053887831312433
0	0	0	0
3000	0.027992876719197	-0.99774610591995	0.060984481423965
3000	0.3068992001664	-0.94169070539657	-0.13795468932561
3000	-0.0030003315549562	-0.95910598706768	-0.28303127668421
3000	-0.28304486616721	-0.95515140349713	-0.08701379277932
3000	-0.25412531467782	-0.9334603094268	0.25312482131295
3000	0.054986667349556	-0.91577795076714	0.39790352009315
3000	0.3350278084622	-0.92007636950814	0.20301685109799
3000	0.64766200862423	-0.75560567672827	-0.097948884020332
3000	0.47003078802496	-0.78005109502014	-0.4130270541581
3000	0.15002813291263	-0.79914985464794	-0.582109155701
0	0	0	0
3000	-0.21202183937424	-0.8070831338444	-0.55105676176984
3000	-0.49888876020833	-0.80182121380176	-0.32892665753214
3000	-0.62024814889927	-0.78431378828553	0.012004802881921
3000	-0.53791017650016	-0.76087294482644	0.36293939418134
3000	-0.27907242869409	-0.73819158557791	0.61415939504721
3000	0.074985116931287	-0.72385632877669	0.68586386953151
3000	0.41302519530539	-0.72204404603025	0.55503385809805
3000	0.62606229629788	-0.73407304390198	0.2630261724063
3000	0.86462224260195	-0.48478819382884	-0.13194235378434
3000	0.72499927500109	-0.50899949100076	-0.4639995360007
0	0	0	0
3000	0.46290048709176	-0.53088587180502	-0.70984739921199
3000	0.12201970777434	-0.54708836190625	-0.82813375440288
3000	-0.23788239622541	-0.55572526177029	-0.79660617559519
3000	-0.55310814321403	-0.55410833877138	-0.62212163667112
3000	-0.7702677145543	-0.54318879091296	-0.33411612553394
3000	-0.85139769560747	-0.52424487955148	0.017007944565602
3000	-0.7829017519948	-0.50093713633384	0.36895369921594
3000	-0.576716901485	-0.47776547471375	0.66267470655902
3000	-0.26906269891412	-0.45810675131103	0.84719742000097
3000	0.086984083368982	-0.44591840439731	0.8908369917444
0	0	0	0
3000	0.43089358242609	-0.44189086643232	0.78680568299149
3000	0.70281939861885	-0.44888465146496	0.55185819066516
3000	0.85618795388608	-0.46410188154573	0.22704984291138
3000	0.92633863866996	-0.16806143768526	-0.33712324107103
3000	0.73888880560151	-0.19197111052164	-0.64590279894259
3000	0.45178838669964	-0.21190074774408	-0.86659409572697

b-values	b-vectors		
3000	0.10400915320824	-0.22802006664884	-0.96808519524594
3000	-0.2579704640727	-0.23597298264014	-0.93689273192294
3000	-0.58385959864776	-0.23594326246724	-0.7768131988858
3000	-0.82946878233046	-0.22712836379857	-0.51028839443731
0	0	0	0
3000	-0.96205099005375	-0.21101118388913	-0.173009169729
3000	-0.96364351783541	-0.18992973899246	0.18793047858201
3000	-0.8346916383989	-0.16693832767978	0.5248061199514
3000	-0.59310409890484	-0.1440252786548	0.7921390326014
3000	-0.27107686118676	-0.12603573619754	0.95427057406706
3000	0.087963063268513	-0.1139521501433	0.98958446177077
3000	0.43607741061119	-0.11001953020007	0.89315854971511
3000	0.72512255606884	-0.11401927088531	0.67911478009757
3000	0.91874003335064	-0.12696407424976	0.37389420290875
3000	0.98924387867785	-0.14503575572122	0.019004685232436
0	0	0	0

6

Iteratively reweighted L1-fitting for model-independent outlier removal and regularization in diffusion MRI

Based on:

Tobisch A, Stöcker T, Groeschel S, Schultz T (2016) Iteratively reweighted L1-fitting for model-independent outlier removal and regularization in diffusion MRI. In: 2016 IEEE 13th International Symposium on Biomedical Imaging (ISBI) p.911–914.

Abstract

Diffusion magnetic resonance imaging is negatively affected by subject motion occurring during the image acquisition. The induced data artifacts adversely influence the estimation of microstructural diffusion measures. State-of-the-art procedures for outlier removal detect and reject defective images during model fitting. These methods, however, are tailored only for specific diffusion models and excluding a varying number of diffusion-weighted images might be disadvantageous for the parameter estimation. Therefore, this work proposes a novel method based on an iteratively reweighted L1-Fitting for model-independent outlier removal with subsequent reconstruction of faulty images by modeling the signal in the continuous SHORE basis. We validate the proposed method on simulation data and clinical *in vivo* human brain scans and demonstrate its effect on diffusion parameters determined by the kurtosis and NODDI model.

Keywords: Diffusion MRI, SHORE Basis, Sparsity, Robust Estimation, Outlier Correction, Clinical Applications

6.1 Introduction

Diffusion magnetic resonance imaging (dMRI) provides the possibility to investigate the structural connectivity of brain white matter non-invasively and to examine pathological conditions of the central nervous system. However, the technique is sensitive to artifacts occurring during the image acquisition. Spatially and temporally varying artifacts, e.g. induced by subject motion, potentially degrade the signal quality and complicate subsequent analysis of the complex white matter architecture. Especially in clinical applications, when data is collected from diseased patients, children in particular, measures need to be taken against the image degradation due to frequently occurring motion artifacts.

Robust estimation procedures have been introduced to reduce the influence of defective images on diffusion model parameters. Widely used in clinical applications is the RESTORE method (Chang et al., 2005) that improves the estimation of the model parameters in diffusion tensor imaging (DTI) through outlier rejection based on iteratively reweighted least squares (IRLS) regression. Consequently, microstructural features are more accurately extracted from the DT model. To this end, the RANSAC paradigm has also been investigated for robust tensor estimation and artifact detection in diffusion-weighted images (Scherrer and Warfield, 2012). Extending DTI to the popular diffusion kurtosis imaging (DKI) model (Jensen and Helpern, 2010) complements the information derived from the diffusion tensor and provides further insights on the non-Gaussianity of water diffusion in brain tissue. Recent literature shows that the dedicated outlier removal method REKINDLE (Tax et al., 2015) limits the impact of faulty DKI scans on the estimation of diffusion parameters. However, the robust estimation methods proposed in the literature so far are mainly tailored for specific diffusion models as well as limited to models than can be linearized.

The present work explores a novel approach to reduce the influence of artifacts on diffusion-weighted images (DWIs) and to provide a robust estimation of the dMRI measurements independently of the diffusion model that, specific for each application, is used to extract structural measures from the data. We use the Simple Harmonic Oscillator based Reconstruction and Estimation (SHORE) basis to capture both the angular and the radial characteristics of the diffusion process (Ozarslan et al., 2009). Modeling the signal in the SHORE basis not only provides a continuous signal representation but also analytical formulae for the diffusion ensemble average propagator and commonly derived diffusion parameters (Merlet and Deriche, 2013). Promoting the sparsity of the SHORE basis coefficients by means of an L1-norm regularizer has been found to outperform linear least squares estimation of the diffusion signal modeled in the SHORE basis (Merlet and Deriche, 2013). Nevertheless, the SHORE basis is not immune from artifacts challenging the inference of structural parameters. Therefore, we propose a novel robust estimation procedure, IRL1 SHORE, that iteratively reweights the diffusion signal to detect and reject erroneous signals based on the model residuals. State-of-the-art methods for outlier removal proceed similarly and discard faulty DWIs from the data before extracting the diffusion measures of interest. Recent literature, however, indicates that excluding DWIs due to outlier removal might negatively affect the extracted diffusion parameters (Chen et al., 2015; Elhabian et al., 2014). To account for this potential problem, the proposed method recovers excluded DWIs by means of sparse signal reconstruction in the SHORE

basis and subsequent image analysis is performed on the full data set. To evaluate the proposed method we use simulations and *in vivo* dMRI data. We demonstrate the advantages of IRL1 SHORE to correct for motion artifacts and to improve diffusion parameter estimation independently of the required diffusion model.

6.2 Materials and Methods

6.2.1 SHORE - an analytical model for sparse signal reconstruction

For a continuous representation, the signal is expressed as a linear combination of basis Φ that separates a radial basis X and an angular basis Y with the radial order n and, respectively, the angular order and degree l and m

$$s(q\mathbf{u}) = \sum_{l=0,even}^{N_{max}} \sum_{n=l}^{(N_{max}+l)/2} \sum_{m=-l}^{l} c_{nlm}\Phi_{nlm}(q\mathbf{u}) \quad \text{with} \quad \Phi_{nlm}(q\mathbf{u}) = X_{nl}(q,\zeta)Y_l^m(\mathbf{u}) \tag{6.1}$$

where q is the norm of the diffusion gradient vector $\mathbf{q}$, $\mathbf{u}$ a unit vector and c_{nlm} are the SHORE coefficients. A real and symmetric spherical harmonic (SH) basis Y_l^m is considered, as the diffusion signal is real and symmetric. ζ is a scale factor based on a typical diffusivity for brain tissue.

When combining analytical signal modeling with compressed sensing principles to recover the signal of sparse measurements, the SHORE basis is well suited and outperforms other continuous basis functions (Merlet and Deriche, 2013). For sparse signal reconstruction, we use an iterative shrinkage and thresholding algorithm (Gong et al., 2013) to solve the convex optimization problem

$$\arg\min_{\mathbf{c}\in R^{n_c}} \|\mathbf{\Phi c} - \mathbf{s}\|_{l_2} + \lambda \|\mathbf{c}\|_{l_1} \tag{6.2}$$

where the signal vector $\mathbf{s}$ with entries $s(q\mathbf{u})$ is obtained from all the measurements through normalization by the non-diffusion weighted signal $S(0)$. The terms $\|\mathbf{\Phi c} - \mathbf{s}\|_{l_2}$ and $\|\mathbf{c}\|_{l_1}$ promote data consistency and sparsity, respectively.

6.2.2 Outlier detection by iteratively reweighted L1 SHORE

Similar to state-of-the-art approaches for robust signal estimation, the proposed method contains an iterative reweighting of the model residuals. Specifically, we adapt equation (7.2) to include an iterative reweighting of the SHORE residuals during the L1-norm fitting routine for each voxel

$$\arg\min_{\mathbf{c}\in R^{n_c}} \|\mathbf{\Omega}(\mathbf{\Phi c}-\mathbf{s})\|_{l_2} + \lambda \|\mathbf{c}\|_{l_1} \tag{6.3}$$

where $\mathbf{\Omega}$ is the diagonal weight matrix containing the weights $\sqrt{w_i}$ for each normalized measurement s_i. We use the Geman-McClure M-estimator and the weight function $w(\hat{r}_i) = \frac{1}{(\hat{r}_i^2+1)^2}$ that have been found suitable as a robust estimator for dMRI (Chang et al., 2005; Tax et al., 2015). When assessing the residual magnitudes, it needs to be considered that the elements of $\mathbf{s}$ have been normalized by the signal magnitude at b = 0, which itself is a random variable estimated as part of the iterative fit, i.e. the estimate $\hat{s}(0)$. Approximating the raw signals to be Gaussian distributed with standard deviation σ, this can be corrected by normalizing the residuals according to Geary (1930)

$$\hat{r}_i = (\hat{s}(0)s_i - \hat{s}_i)/(\sigma_n\sqrt{s_i^2+1}) \tag{6.4}$$

where $\hat{s}$ are the SHORE estimates of the normalized signals and σ_n is the standard deviation normalized, as the measurements, by $S(0)$. In each iteration, the weights are updated from the previous residuals and a new estimate of the SHORE coefficients is determined. If convergence or the maximum number of iterations has been reached, signals are accepted if $|\hat{r}_i| <= t$. The threshold t is a critical parameter that balances sensitivity and specificity of detecting faulty data points. Signals with $|\hat{r}_i| > t$ are detected as outliers and discarded from the data set. Next, L1 SHORE is applied to the retained DWIs and rejected measurements are reconstructed.

6.2.3 Simulations and experiments

Synthetic data is generated using the Camino Monte-Carlo simulator (Cook et al., 2006) to validate the proposed method. For 600 instances of a 55° crossing microstructure of well-defined, but random orientation, we simulate diffusion signals for two b = 0 scans and for two shells in q-Space with 30 and 64 uniformly distributed diffusion-weighting directions with b-values 700 and 2000 s/mm^2, respectively. We reduce the signal intensities by 70% to simulate signal dropouts due to subject motion in a well-defined amount of data. Rician noise is added with SNR of 20 defined on the non-diffusion weighted image, i.e. $\text{SNR}_{\text{DWI}} < 20$. We calculate sensitivity and specificity of the outlier detection and the normalized mean square error (NMSE) between the signal reconstructed with IRL1 SHORE and the ground truth simulation data.

Furthermore, we investigate the impact of IRL1 SHORE on *in vivo* clinical dMRI scans that are affected by strong motion artifacts because they were acquired from children suffering from metachromatic leukodystrophy, a rare neurodegenerative disease. Parents gave informed written consent for the scientific use of the data. The images were collected on a 3.0T SIEMENS MAGNETOM Skyra scanner using a twice-refocused echo planar imaging sequence. The imaging protocol has the same parameters as used for simulations with a spatial resolution of 2x2x2mm^3, TR/TE = 9100/89 and FOV = 96x96mm^2 for 50 contiguous slices. To validate the performance of IRL1 SHORE, we extract common diffusion features such as fractional anisotropy (FA), kurtosis anisotropy (KA) and

mean and radial kurtosis (MK, RK) using ExploreDTI (Leemans et al., 2009). This toolbox also enables the comparison of our method with the REKINDLE approach for outlier removal (Tax et al., 2015). We apply REKINDLE with the default settings for outlier removal and a constraint that promotes positive diagonal elements of the kurtosis tensor. In addition, a measure for the fiber density is obtained from the NODDI model (Zhang et al., 2012).

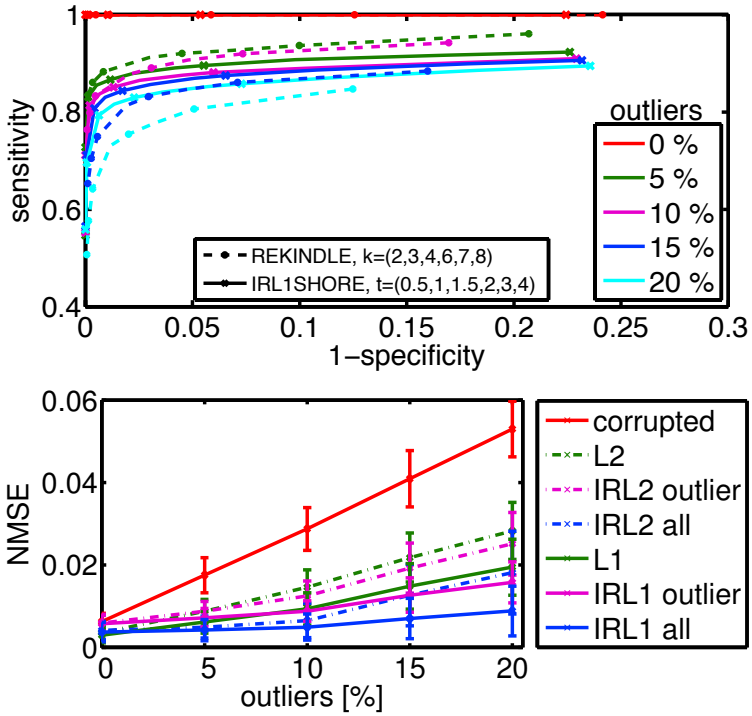

Figure 6.1: Simulations with SNR=20 and varying % of outliers: (top) sensitivity and specificity of IRL1 SHORE and REKINDLE as functions of threshold t and k, respectively; (bottom) NMSE versus % of outliers for noisy data and the correction methods using L1- or L2-norm regularizers and correcting all (IRL1/2 all) or only corrupted (IRL1/2 outlier) DWIs.

6.3 Results and discussion

6.3.1 Simulations

We investigate the performance of the proposed method using simulated data corrupted by artificial signal dropouts. In IRL1 SHORE, a critical parameter is the threshold, t, that separates outliers from good data. REKINDLE applies the corresponding threshold parameter k. We compute the sensitivity and specificity of both methods based on the applied threshold and the number of outliers in the data (Fig. 6.1, top row). For the proposed method, a threshold of $t = 2.0$ is found to provide a good balance of these two properties independently of the amount of outliers in the data. In contrast, the optimal threshold value for REKINDLE varies with the outlier percentage. IRL1 SHORE, further, provides superior outlier detection for increased percentage of outliers.

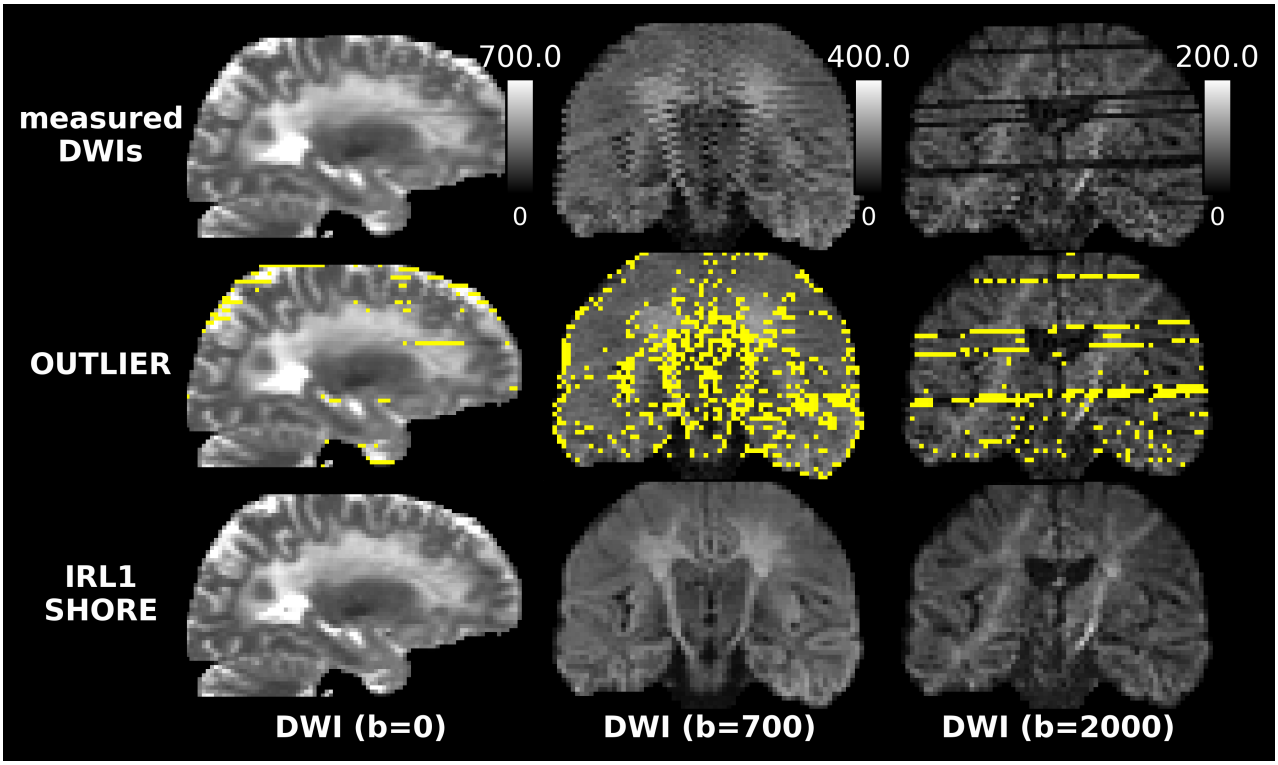

Figure 6.2: DWIs with outliers (top) that are detected (middle) and corrected (bottom) by IRL1 SHORE (b = 0, 700, 2000s/mm^2).

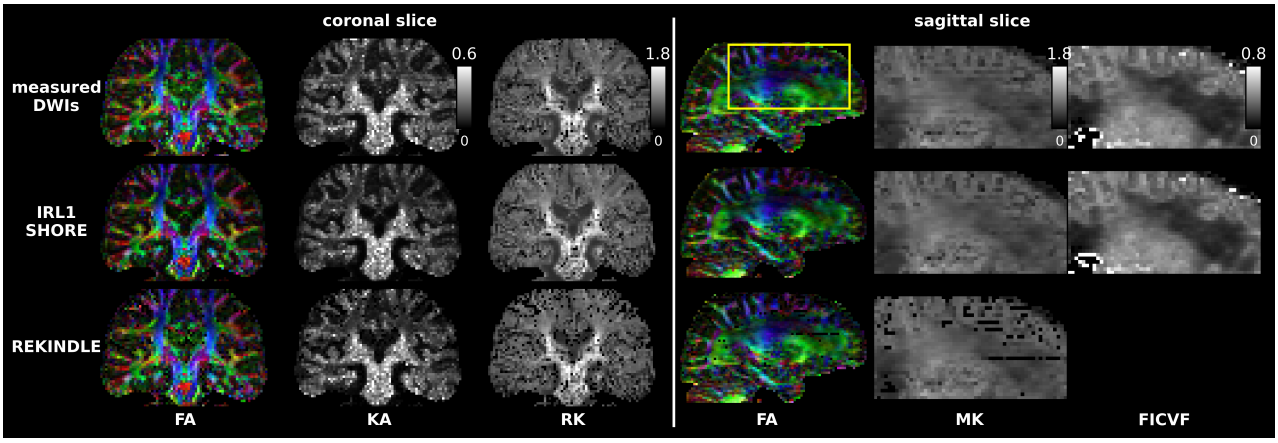

Figure 6.3: Color-encoded FA, KA, RK, MK and FICVF maps determined for the measured DWIs (top) and for the proposed IRL1 SHORE (middle) and the competing REKINDLE method (bottom).

Applying $t = 2.0$ and varying the amount of artificial outliers, we determine the NMSE between noise-free simulations and noisy simulations with and without outlier correction. REKINDLE is not considered because it only detects faulty signals but does not recover discarded DWIs. We also compare SHORE using L2-norm and L1-norm regularization as well as two different strategies for correcting the DWIs: correcting (1) only voxels detected as outliers or (2) all measurements. The results shown in figure 6.1 (bottom row) indicate that the SHORE basis already regularizes the dMRI

signal, which is known to be SNR sensitive, especially at high b-values. The detection of outliers by iteratively reweighting the model residuals and the subsequent recovery of corrupted data further reduce the NMSE. The L1-norm regularizer leads to more accurate SHORE signal estimation and therefore lower NMSE than L2 SHORE, a finding confirming recent literature (Merlet and Deriche, 2013). Modeling all DWIs rather than only the voxels detected as outliers, further improves the signal estimation and reduces the NMSE.

6.3.2 *In vivo* clinical data

In human *in vivo* images tainted by motion artifacts, we show the advantages of IRL1 SHORE. Figure 6.2 highlights that the proposed method succeeds in locating faulty signals and substantially corrects the DWIs. In contrast to state-of-the-art methods for outlier removal that discard corrupted images, IRL1 SHORE corrects and recovers all DWIs before diffusion parameter estimation. Due to this, the proposed method is potentially less susceptible to errors that might occur if diffusion measures are calculated from a reduced number of DWIs (Chen et al., 2015). As for simulations, we compare the two different strategies for correcting DWIs. Visually, no significant difference is noticeable. However, future work will investigate these strategies more thoroughly and quantitatively, also with respect to their influence on diffusion parameters. Figure 6.3 shows that IRL1 SHORE reduces the influence of artifacts in the DWIs on diffusion parameters extracted by means of different diffusion models. Compared to the DWIs (Fig. 6.2), the improvement is less pronounced. Nevertheless, the white matter structure is much better defined using IRL1 SHORE, especially in the color-encoded FA map. For DT and kurtosis measures, we also compare the proposed method to the REKINDLE method for outlier removal. On our challenging clinical data, REKINDLE appears to reduce, rather than increase the quality of kurtosis fits. Given the relatively low number of acquired DWIs, it appears that simply discarding outliers leaves a set of measurements that is insufficient to reliably fit the kurtosis model using the iteratively weighted LLS (IWLLS) approach used by REKINDLE. In contrast, our proposed method uses a sparsifying basis and an L1-regularized fit. This makes it particularly suited to restore and denoise the full set of DWIs from the sparse set of inliers. Standard methods can then be used for the final model fit. Finally, figure 6.3 depicts that IRL1 SHORE corrects for artifacts in the parameter map of the intra-cellular volume fraction, FICVF, a measure for the fiber density obtained from the NODDI model. Our results demonstrate that, in contrast to state-of-the-art methods for outlier removal, IRL1 SHORE improves diffusion features independently of the required diffusion model.

6.4 Conclusion

In this work, we propose a new method for model-independent outlier removal and robust sparse signal reconstruction that corrects dMRI data for motion artifacts, reduces the impact of defective DWIs on diffusion measures and thus improves the quality of parameter maps. Future work will apply this method to more imaging data and other diffusion models.

Acknowledgements This work was partly supported by DFG grant SCHU 3040/1-1.

7

SHORE-based detection and imputation of dropout in diffusion MRI

Based on:

Koch A, Zhukov A, Stöcker T, Groeschel S, Schultz T (2019) SHORE-based detection and imputation of dropout in diffusion MRI. Magn. Reson. Med. (under review)

Abstract

In diffusion MRI, dropout refers to a strong attenuation of the measured signal that is caused by bulk motion during the diffusion encoding. When left uncorrected, dropout will be erroneously interpreted as high diffusivity in the affected direction. We present a method to automatically detect dropout, and to replace the affected measurements with imputed values. Signal dropout is detected by deriving an outlier score from a SHORE (Simple Harmonic Oscillator Based Reconstruction and Estimation) fit of all measurements. The outlier score is defined to detect measurements that are substantially lower than predicted by SHORE in a relative sense, while being less sensitive to measurement noise in cases of weak baseline signal. A second SHORE fit is based on detected inliers only, and its predictions are used to replace outliers. Our method is shown to reliably detect and accurately impute dropout in simulated data, and to achieve plausible results in corrupted *in vivo* dMRI measurements. Computational effort is much lower than with previously proposed alternatives. Deriving a suitable outlier score from SHORE results in a fast and accurate method for detection and imputation of dropout in diffusion MRI. It requires measurements with multiple b values (such as multi-shell or DSI), but is independent from the models used for analysis (such as DKI, NODDI, deconvolution, etc.).

Keywords: diffusion MRI, multi-shell, diffusion spectrum imaging, SHORE, dropout, outliers

7.1 Introduction

For the non-invasive examination of pathological conditions of the central nervous system and for the investigation of the structural connectivity of the living human brain, diffusion magnetic resonance imaging (dMRI) is the method of choice. Based on the molecular diffusion in cerebral tissue that probes the underlying microstructure, dMRI enables the inference of diffusion measures and an accurate description of the complex white matter architecture. Despite its unique capabilities, dMRI is, however, sensitive to artifacts occurring during image acquisition. Due to great advances in dMRI acquisition techniques the occurrence of artifacts could be reduced. But additional processing of the acquired images is still required in dMRI, since remaining artifacts not corrected for potentially degrade the quality of the diffusion-weighted images (DWIs) and complicate subsequent data analysis.

State-of-the-art analysis tools for dMRI data correction account for susceptibility-induced geometric distortions, eddy-current-induced artifacts and patient motion (Andersson and Sotiropoulos, 2016; Andersson et al., 2003). The latter is the source of the frequently occurring motion artifacts. Especially in clinical applications, when data is collected from patients with disorders or children, motion artifacts cause severe image degradation. Subject motion can be classified into distinct categories: (1) slow bulk motion during the acquisition of DWIs, (2) fast motion during the collection of a single slice or between different slices and (3) physiological noise, i.e motion due to cardiac pulsation or respiration. The first describes motion leading to misalignment of collected DWIs, rather than affecting individual image quality. Registration methods to realign the acquired scans are typically used to correct for this type of motion artifact (Andersson and Sotiropoulos, 2016). In contrast, fast movements occurring during or between image slice generation can lead to signal dropout or intensity variations, respectively. The origin of these artifacts has been studied in detail (Andersson et al., 2016; Storey et al., 2007; Wedeen et al., 1994). Correcting for them is required in addition to image realignment in order to reduce the impact of the defective images on diffusion model parameters, and is the goal of our method.

Robust estimation procedures have been introduced to detect corrupted images, and to extract diffusion measures from an unaffected subset of the data. In diffusion tensor imaging (DTI), the RESTORE method (Chang et al., 2005) is widely applied for an improved estimation of model parameters through outlier rejection based on iteratively reweighted least squares (IRLS) regression. Likewise, the RANSAC paradigm has been explored for robust tensor estimation and outlier detection in DWIs (Scherrer and Warfield, 2012). In diffusion kurtosis imaging (DKI) (Jensen and Helpern, 2010) that extends DTI to provide further insights on the non-Gaussianity of water diffusion in brain tissue, the dedicated REKINDLE method (Tax et al., 2015) can be applied for outlier removal.

There is now a wide variety of diffusion and microstructural models, and it would be a tedious task to design and implement specific robust estimation procedures for each of them. Therefore, the recent approach SOLID estimates a measure of uncertainty that can be used to weight the fitting of arbitrary models (Sairanen et al., 2018). It has been pointed out that excluding DWIs due to outlier removal can effectively lead to a suboptimal sampling scheme, which adversely affects the inference of diffusion measures (Chen et al., 2015; Elhabian et al., 2014). Several approaches

have addressed this by imputing corrupted signals, so that a fully recovered data set is available for subsequent analysis.

This strategy has been followed in the `eddy` framework of Andersson et al. (2016), based on Gaussian Processes (Andersson and Sotiropoulos, 2015), as well as in our own (Tobisch et al., 2016) and a parallel work (Elhabian et al., 2016), based on sparse signal reconstruction in the SHORE (Simple Harmonic Oscillator based Reconstruction and Estimation) basis (Ozarslan et al., 2009). Another recent work has learned alternative compact basis functions for outlier detection (Christiaens et al., 2018). In the current article, we present a SHORE-based approach for dropout detection and imputation that differs significantly from our proceedings paper (Tobisch et al., 2016) in that it only performs a single weighted fit, rather than iteratively refining it. We will therefore denote the novel approach as non-iterative, to distinguish it from methods that iterate until some convergence criterion is met. Our method further employs a novel and more effective outlier score. We also present a much more extensive experimental evaluation compared to (Tobisch et al., 2016), based on simulations and *in vivo* dMRI data. In particular, we include a direct comparison between SHORE and Gaussian Processes, which indicates that a SHORE-based approach is computationally less demanding, and more accurate. For further comparison, we create a second baseline method from REKINDLE. The corresponding method has not been reported previously, even though prior work highlighted the potential of DKI-based approaches for signal reconstruction (Tax et al., 2014).

7.2 Methods

7.2.1 Detection and Imputation of Signal Dropout by Weighted L1 SHORE

Our method for detecting and imputing signal dropout proceeds in four steps: First, we perform an initial L1-regularized SHORE fit of the measurements. Second, we reduce the impact of outliers in a refined fit, by defining suitable weights based on the fitting residuals from the initial step. Third, from the residuals of the refined fit, we compute an outlier score that is used to detect measurements that are likely to be affected by signal dropout. In a final step, these are replaced by predictions from a SHORE model that is fitted to the subset of measurements that have been accepted as inliers.

7.2.1.1 Signal Modeling Using the SHORE Basis

A continuous representation of the attenuation factors measured by diffusion MRI (dMRI) can be formulated with a linear combination of the SHORE basis Φ (Ozarslan et al., 2009)

$$s(q\mathbf{u}) = \sum_{l=0,even}^{N_{max}} \sum_{n=l}^{(N_{max}+l)/2} \sum_{m=-l}^{l} c_{nlm}\Phi_{nlm}(q\mathbf{u}) \quad \text{with} \quad \Phi_{nlm}(q\mathbf{u}) = X_{nl}(q,\zeta)Y_l^m(\mathbf{u}) \tag{7.1}$$

The SHORE basis separates a radial basis X and an angular basis Y with the radial order n and, respectively, the angular order and degree l and m. q is the norm of the diffusion gradient vector $\mathbf{q}$, $\mathbf{u}$ a unit vector and c_{nlm} are the SHORE coefficients. Due to the real and symmetric diffusion signal, a real and symmetric spherical harmonic (SH) basis Y_l^m is applied. The SHORE scale factor ζ defined in units of mm^{-2} as $\zeta = 1/(8\pi^2\tau\mathrm{MD})$ is calculated based on the mean diffusivity (MD) obtained from the data (Merlet and Deriche, 2013) and the diffusion time τ. The latter can be calculated as $\tau = \Delta - (\delta/3.0)$ from the diffusion sequence parameters applied for the dMRI acquisition: the diffusion gradient separation time Δ and the gradient duration δ. In this work, we use the Dipy library (Garyfallidis et al., 2014) that implements the SHORE basis in a way that differs from the SHORE basis defined by Merlet and Deriche (2013). Due to the limited radial resolution of 2-shell dMRI investigated in this work, we select a SHORE order of 6 resulting in 50 basis functions.

We select the SHORE basis for our work, since we eventually want to make predictions based on a subset of our measurements, and SHORE was found to achieve higher accuracy than other continuous basis functions in sparse reconstruction (Merlet and Deriche, 2013). Since L1 regularization has been found to increase accuracy even when fitting to a complete set of measurements, our initial step determines the SHORE coefficients $\hat{c}_{nlm}$ corresponding to a measurement vector $\mathbf{s}$ as

$$\hat{\mathbf{c}} = \arg\min_{\mathbf{c}\in R^{n_c}} \|\mathbf{\Phi c} - \mathbf{s}\|_{l_2} + \lambda \|\mathbf{c}\|_{l_1} \tag{7.2}$$

where the entries of $\mathbf{s}$ are attenuation factors, obtained by normalizing dMRI measurements $S(q\mathbf{u})$ by the non-diffusion weighted signal $S(0)$, and the regularization parameter λ balances the data consistency term $\|\mathbf{\Phi c} - \mathbf{s}\|_{l_2}$ with the sparsity term $\|\mathbf{c}\|_{l_1}$. We set $\lambda = 10^{-6}$ based on experiments with simulation data, which used five-fold cross validation to empirically evaluate L1 SHORE performance across a range of parameter values (see Supporting Information Figure 7.9). Eq.~(7.2) defines a convex optimization problem that we solve via l_1-norm minimization, the LASSO method (Tibshirani, 1996).

7.2.1.2 Robust SHORE Fitting Using Weighted Least Squares

Since our method targets situations in which some measurements are severely corrupted by dropout, we employ a robust fitting strategy that is similar to some model-specific state-of-the-art approaches (Chang et al., 2005; Tax et al., 2015). For this, we compute model residuals $\mathbf{r} = \mathbf{s} - \hat{\mathbf{s}}$ based on the measurement vector $\mathbf{s}$ and the corresponding prediction $\hat{\mathbf{s}} := \mathbf{\Phi}\hat{\mathbf{c}}$ from the initial fit. Residuals are standardized as $\mathbf{z} = \mathbf{r}/\hat{\sigma}$ by a robust estimate $\hat{\sigma}$ of their standard deviation, which is obtained

using the median absolute deviation (MAD): $\hat{\sigma} = 1.4826 * \text{MAD}(\mathbf{r})$. Standardized residuals are then converted to sample weights using a function $w(z_i) = \frac{1}{(z_i^2+1)^2}$ that is derived from the Geman-McClure M-estimator, and which has previously been found to be suitable for robust dMRI fitting (Chang et al., 2005; Tax et al., 2015).

Eq.~(7.2) was adapted to incorporate the resulting weights during the L1-regularized fitting routine for each voxel

$$\tilde{\mathbf{c}} = \arg\min_{\mathbf{c}\in R^{n_c}} \left\|\boldsymbol{\Omega}(\boldsymbol{\Phi}\mathbf{c} - \mathbf{s})\right\|_{l_2} + \lambda \left\|\mathbf{c}\right\|_{l_1} \tag{7.3}$$

where $\boldsymbol{\Omega}$ is the diagonal weight matrix containing the weights $\sqrt{w_i}$ for each normalized measurement s_i. Quantities which result from the weighted fit are marked with a tilde, e.g., $\tilde{\mathbf{c}}$ and $\tilde{\mathbf{s}} := \boldsymbol{\Phi}\tilde{\mathbf{c}}$.

7.2.1.3 Dropout Detection

Dropout is detected when a given measurement s_i is substantially below the corresponding prediction $\tilde{s}_i$. The fact that signal dropout in diffusion MRI is commonly simulated as a multiplicative attenuation (Andersson et al., 2016; Tax et al., 2015) suggests to use a relative measure of discrepancy between s_i and $\tilde{s}_i$. Implicitly, that approach is taken in REKINDLE (Tax et al., 2015), since it assesses differences after taking the logarithm of the signal.

On the other hand, even in cases where no dropout has occurred, we have to assume that measurements are affected by noise, which is often approximated as Rician (Gudbjartsson and Patz, 1995). Therefore, small absolute deviations can reasonably be explained by the effects of measurement noise, even if they might correspond to a substantial relative error in cases where the true signal is weak. To account for this, we propose a novel outlier score $\mathbf{d}$ for detecting dropout that is in between an absolute and a relative measure of deviation. It is defined based on the standardized residuals $\tilde{\mathbf{z}}$ from the weighted fit as

$$\mathbf{d} = \frac{\tilde{\mathbf{z}}}{\tilde{\mathbf{s}}^{\alpha}} \tag{7.4}$$

where all involved quantities are vectors, so that d_i is the outlier score of measurement i, and division is performed element-wise. To avoid numerical issues when evaluating Eq.~(7.4), very small values of $\tilde{s}_i < \epsilon$ are replaced with $\epsilon := 0.001$ in the denominator. $\alpha \in [0, 1]$ can be used to determine the influence of relative and absolute errors during outlier detection: With $\alpha = 0$, $\mathbf{d}$ behaves as an absolute measure of deviations, whereas $\alpha = 1$ turns it into a relative one. Based on simulations, α was explored across $[0, 1]$ to determine the optimal level for outlier detection.

Since dropout always leads to a signal attenuation, never to an amplification, we detect it using one-sided thresholding $d_i \leq -t$; all values $d_i > -t$ are assumed to indicate a valid signal. The exact threshold value $t > 0$ balances sensitivity and specificity of detecting faulty data points in a similar

manner as REKINDLE's κ parameter (Tax et al., 2015), or the limit against which z_{gs} is compared in `eddy` (Andersson et al., 2016). Suitable thresholds t for mild to severe motion corruption in dMRI data were determined in simulation experiments. In practice, the threshold can be further adapted based on visual inspection of the resulting map of detected outliers.

Instead of detecting outliers on the voxel level, state-of-the-art outlier removal techniques propose to impute complete image slices corrupted by motion. In this work, we thus investigate slice-based outlier detection for the correction of motion corrupted *in vivo* dMRI. We compute a summary outlier score for each DWI i over all d_{isn} for voxels n of slice s

$$\bar{d}_{is} = \underset{n \in \Omega_s}{\text{median}}(d_{isn}) \tag{7.5}$$

where Ω_s is the set of brain voxels in slice s, with cardinality $|\Omega_s|$. The $\bar{d}_{is}$ are transformed to modified z-scores. In this way, the outlier threshold can be chosen based on numbers of standard deviations, as in state-of-the-art outlier correction (Andersson et al., 2016). Slices are considered to be outliers if $(\bar{d}_{is} - \text{median}(\bar{d}_{is}))/\hat{\sigma}(\bar{d}_{is}) \leq -t_s$. The threshold value $t_s > 0$ was tuned based on visual inspection of the dMRI data and based on the NMSE with respect to a reference data set without motion, if available.

7.2.1.4 Imputing Corrupted Measurements

For signal imputation of detected motion corrupted dMRI measurements, L1 SHORE is applied to the retained DWIs and rejected measurements are reconstructed. In this work, we consider outlier detection on a voxel and slice level for simulations and *in vivo* dMRI, respectively. Because the slice-based approach is not applicable for our simulations, we impute the detected outliers on the voxel level. We further investigated an alternative imputation strategy that reconstructs not only detected outliers, but all measurements. For *in vivo* dMRI, the outlier score d is determined after conventional dMRI preprocessing to correct for slow motion and distortion artifacts (Andersson et al., 2003; Andersson and Sotiropoulos, 2015). The summary outlier score per slice and DWI, however, is best computed in the original measurement space where outliers are not yet spread across different slices due to image realignment. This is due to the fact that in dMRI artifacts caused by motion during the diffusion sensitization can be expected to affect full slices because of the conventional single shot acquisition. d is therefore transformed from the coregistered space into the original measurement space to determine the map of outlier slices. This map is then transformed back into the coregistered space and used for slice-based signal imputation.

7.2.2 Simulations and *in vivo* dMRI

All procedures performed in studies involving human participants were in accordance with the ethical standards of the institutional and/or national research committee and with the 1964 Helsinki

declaration and its later amendments or comparable ethical standards.

7.2.2.1 Simulations

Using the Camino Monte-Carlo simulator (Cook et al., 2006), we generated synthetic diffusion signals to validate the proposed method. Based on a clinical dMRI protocol (see section 7.2.2.3), signals were simulated for two shells in q-space at b-values 700 and 2000 s/mm^2. Respectively, 30 and 64 diffusion-weighting directions were distributed uniformly for an optimal angular q-space coverage. Additionally, signals for two $b = 0$ scans were simulated. Other diffusion sequence parameters required for the realistic simulation of a clinical dMRI experiment were set to TE = 96 ms, Δ = 444 ms and δ = 299 ms. For signal generation a substrate for crossing microstructure was applied. Three different crossing angles were investigated: 35°, 55° and 90°. For each crossing angle, 600 instances of a crossing microstructure of well-defined, but random orientation were generated. Signal dropout due to subject motion was simulated through the reduction of signal intensities by 70% in a well-defined amount of data. Rician noise was added with SNR of 20 defined on the non-diffusion weighted data, i.e. $\text{SNR}_{\text{DWI}} < 20$.

7.2.2.2 *In vivo* research data

DMRI scans from one healthy subject (male, 34 years) were collected on a 3T Siemens MAGNETOM Skyra MRI scanner (Siemens Healthcare, Erlangen, Germany). Monopolar diffusion weighting was applied to acquire the same number of DWIs at b-values 700 and 2000 s/mm^2 as for the simulations. In addition, 5 $b = 0$ scans were collected twice with opposite phase encoding (PE) polarity. Further imaging parameters are spatial resolution of 2 x 2 x 2 mm^3, TR / TE = 9400 ms / 96 ms, Δ = 445 ms, δ = 334 ms and FOV = 208 x 208 mm^2 for 72 contiguous slices. The complete data set was acquired twice: once with and once without deliberate fast head movements to simulate fast subject motion during the collection of single or between different slices. `topup` and `eddy` (Andersson et al., 2003; Andersson and Sotiropoulos, 2015) are applied to correct for susceptibility-induced distortions, eddy-current-induced artifacts and slow motion occurring during dMRI acquisition. For a voxel-wise comparison and NMSE computation, both data sets were linearly registered to a mid-space.

7.2.2.3 *In vivo* clinical data

We investigated the impact of wL1 SHORE on *in vivo* clinical dMRI scans that are affected by strong motion artifacts. They were acquired from children suffering from metachromatic leukodystrophy, a rare neurodegenerative disease. Parents gave informed written consent for the scientific use of the data. The images were collected on a 3T Siemens MAGNETOM Prisma MRI scanner (Siemens Healthcare, Erlangen, Germany) using a twice-refocused echo planar imaging sequence. Again, 30 and 64 DWIs were acquired for two shells at b-values 700 and 2000 s/mm^2, respectively. 3 $b = 0$ scans were collected and one additional non-diffusion weighted image with opposite PE polarity.

Further, a spatial resolution of 2 x 2 x 2 mm^3, TR / TE = 9100 ms / 89 ms, and FOV = 192 x 192 mm^2 for 50 contiguous slices were applied. As for the research data set, slow motion and distortion correction was performed using `topup` and `eddy`.

7.2.3 Evaluation metrics

For simulations, we evaluated the performance of the proposed approach with respect to outlier detection, signal prediction and signal imputation. For those three categories, different evaluation metrics were considered. For wL1 SHORE outlier detection, sensitivity and specificity were determined by means of the true positive rate (TPR) and the false positive rate (FPR). From those metrics, receiver operating characteristic (ROC) curves were generated. Further quality measures for outlier detection are the F1 score, $F1 = \frac{2*P*R}{P+R}$, that incorporates precision (P) and recall (R) of the detection and the accuracy score $\mathrm{A}(\beta) = \frac{\mathrm{TP}(\beta)+\mathrm{TN}(\beta)}{\mathrm{P+N}}$ based on the detected true positives (TP) and negatives (TN) for a specific outlier detection threshold β. We selected the optimal threshold for accurate outlier detection based on $\beta = \mathrm{TPR}(\mathrm{FPR} = 0.05)$.

Besides outlier detection, we also investigated the ability of L1 SHORE to accurately predict the signal of excluded data samples. Signal prediction was evaluated for simulations with and without noise. After excluding 5%, 10%, 15% and 20% of the DWIs, the ground truth (i.e. noise free) signals were estimated from the remaining data set using L1 SHORE. The R^2 score was used to quantify signal prediction.

For the evaluation of signal imputation based on wL1 SHORE, the normalized mean square error (NMSE) at voxel location j was computed between the imputed signals $\hat{\mathbf{s}}$ and the ground truth $\mathbf{s}$ according to

$$\mathrm{NMSE}_j = \frac{\|\hat{\mathbf{s}}_j - \mathbf{s}_j\|^2}{\|\mathbf{s}_j\|^2} \tag{7.6}$$

and then averaged over all voxels. We compared two different approaches for imputation: replacing all measurements by the estimated signal or only the detected outliers.

For *in vivo* research and clinical data, we performed whole brain slice-based outlier detection and imputation. In case of the research data set, the data set without deliberate subject motion was considered a ground truth data set. A whole brain NMSE for each DWI i was calculated between the ground truth and the corresponding motion corrupted data which was corrected using wL1 SHORE. For this, we formed vectors $\mathbf{v}_i$ and $\hat{\mathbf{v}}_i$ containing the ground truth and motion corrected signals of DWI i, respectively, for all brain voxels. Equation 7.6 was then applied to these vectors.

Across all validation experiments we compared our proposed approach, wL1 SHORE, against an established state-of-the-art method for outlier detection and imputation, based on Gaussian Process modeling (Andersson et al., 2016). To obtain another point of reference, we created a second baseline method from REKINDLE. As described by Tax et al. (2015) and implemented in ExploreDTI

(Leemans et al., 2009), REKINDLE robustly estimates the diffusional kurtosis model, but does not attempt to recover the DWIs that have been discarded as outliers. We investigate how useful it is to impute discarded DWIs from the robustly fit kurtosis model. We further investigate slice-based rather than voxel-based outlier detection and signal imputation for *in vivo* dMRI, as conventionally performed by a state-of-the-art method based on Gaussian Process modeling which is implemented in FSL (Andersson et al., 2016). For research and clinical dMRI data, we compare the proposed method to this state-of-the-art method. Finally, we show that wL1 SHORE outperforms IRL1 SHORE as presented in our previous work (Tobisch et al., 2016).

7.3 Results

7.3.1 Simulations

7.3.1.1 Outlier detection

Our novel outlier score d involves a parameter α, which we explored across $[0, 1]$ based on the 2-shell simulations (Figure 7.1).

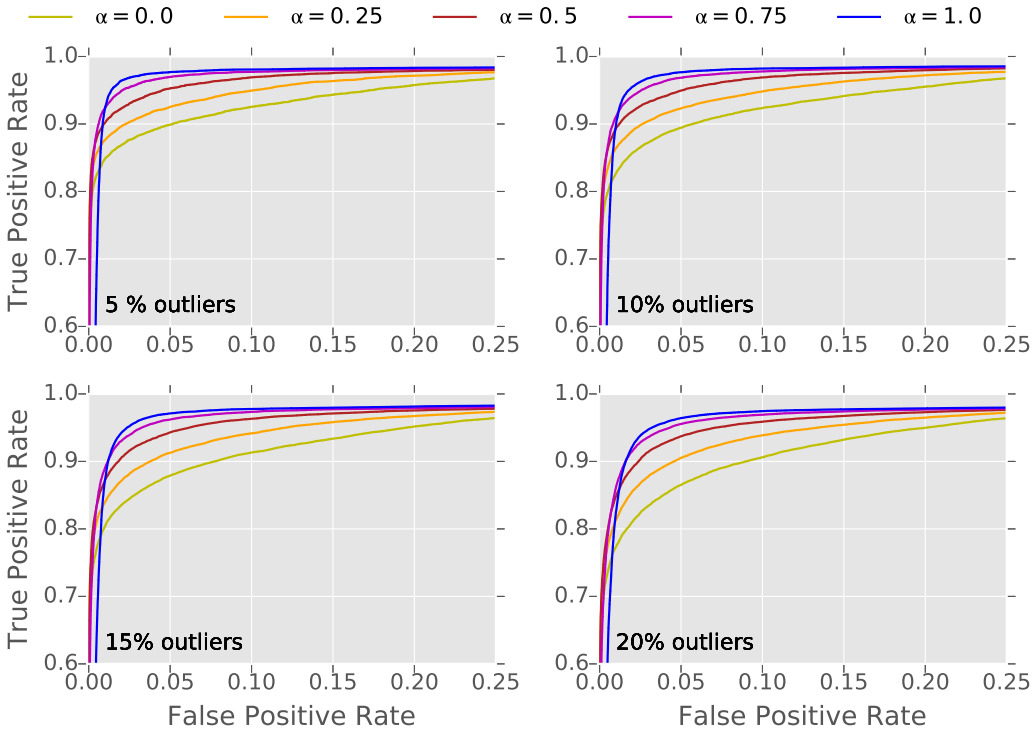

Figure 7.1: Across different levels of outliers in the simulation data (5-20%), the ROC-curves are used to quantify the performance of the outlier detection using wL1 SHORE with different values of α. Balancing sensitivity and specificity, $\alpha := 0.75$ was found optimal for outlier detection using wL1 SHORE.

Results suggest that intermediate settings achieve overall higher true positive rates than absolute differences ($\alpha = 0$). At the same time, they avoid a sharp decrease at low false positive rates, which was observed for relative differences ($\alpha = 1$). Consequently, we set $\alpha := 0.75$ in all further experiments.

Outlier detection was compared on simulations corrupted by artificial signal dropout. For wL1 SHORE, IRL1 SHORE, REKINDLE and GP, the respective thresholds t, t_{IR}, κ and g were determined based on the ROC curves depicted in Figure 7.2.

For TPR(FPR $= 0.05$), the ROC curves indicate that wL1 SHORE has higher TPR than IRL1 SHORE, REKINDLE and GP, independent of how many outliers are present in the data. REKINDLE performs better than GP for 5%, 10% and 15% of outliers. For higher numbers of outliers, GP yields better outlier detection than REKINDLE. This trend is supported by several measures extracted from the ROC curves. For each outlier detection approach, Figure 7.3 reports the TPR at TPR(FPR $= 0.05$) and the corresponding threshold β as well as the maximum F1 score and accuracy.

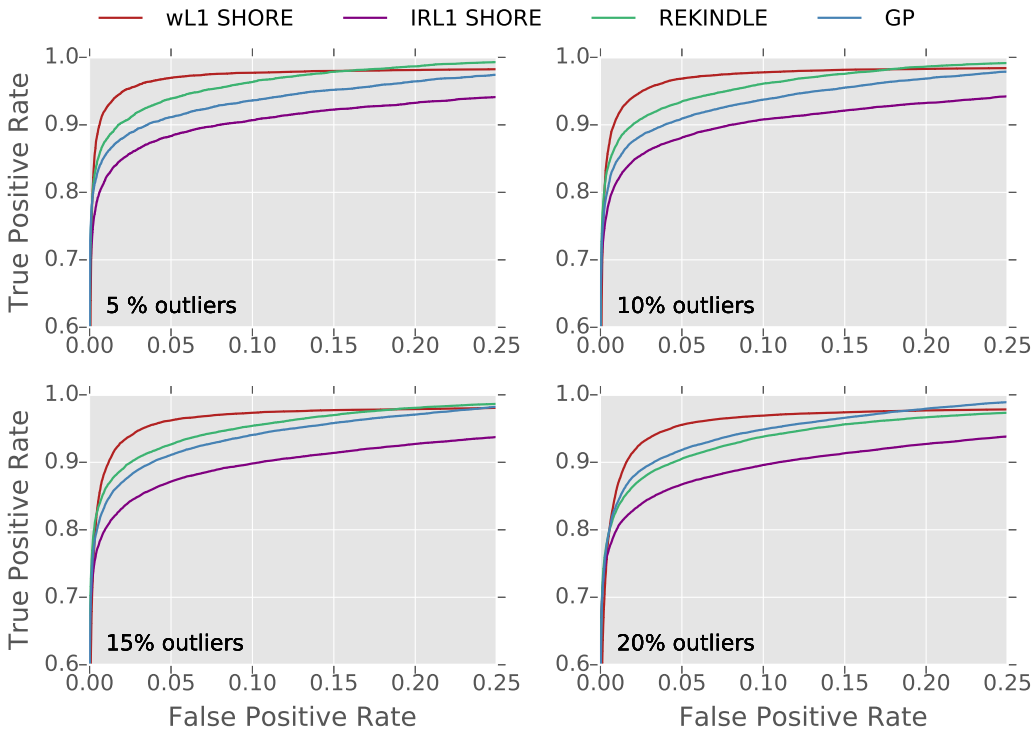

Figure 7.2: Across different levels of outliers in the simulation data (5-20%), the ROC-curves are used to quantify the performance of the outlier detection methods wL1 SHORE, IRL1 SHORE, REKINDLE and GP. Based on the true positive rate at TPR(FPR $= 0.05$) wL1 SHORE provides the best outlier detection independent of the amount of outliers in the data, followed by REKINDLE, GP and IRL1 SHORE.

wL1 SHORE outperforms IRL1 SHORE, REKINDLE and GP in terms of TPR, F1 score and accuracy, independent of the number of outliers. REKINDLE performs better than GP, except for outlier percentages as high as 20%, for which the opposite trend is observed. For low percentage of out-

liers in the data, a threshold of $t = 3.0$, $t_{IR} = 2.0$, $\kappa = 4.0$ and $g = 1.5$ is found to provide a good balance between sensitivity and specificity. For higher numbers of outliers the optimal threshold decreases. For 20% of outliers in the data, $t = 2.0$, $t_{IR} = 1.5$, $\kappa = 2.5$ and $g = 0.5$.

The results of our previously introduced outlier detection approach IRL1 SHORE are in line with those reported in (Tobisch et al., 2016). However, carefully optimizing REKINDLE's parameters and model constraints now led to a consistently better performance than with IRL1 SHORE. IRL1 SHORE is clearly outperformed by our novel wL1 SHORE method, not only for outlier detection as presented in Figure 7.2 and Figure 7.3, but for all other experiments. Combining our new outlier score with a larger number of iterations did not improve the results, it only led to longer running times. Thus, in the following, we will only report the results for wL1 SHORE, REKINDLE and GP.

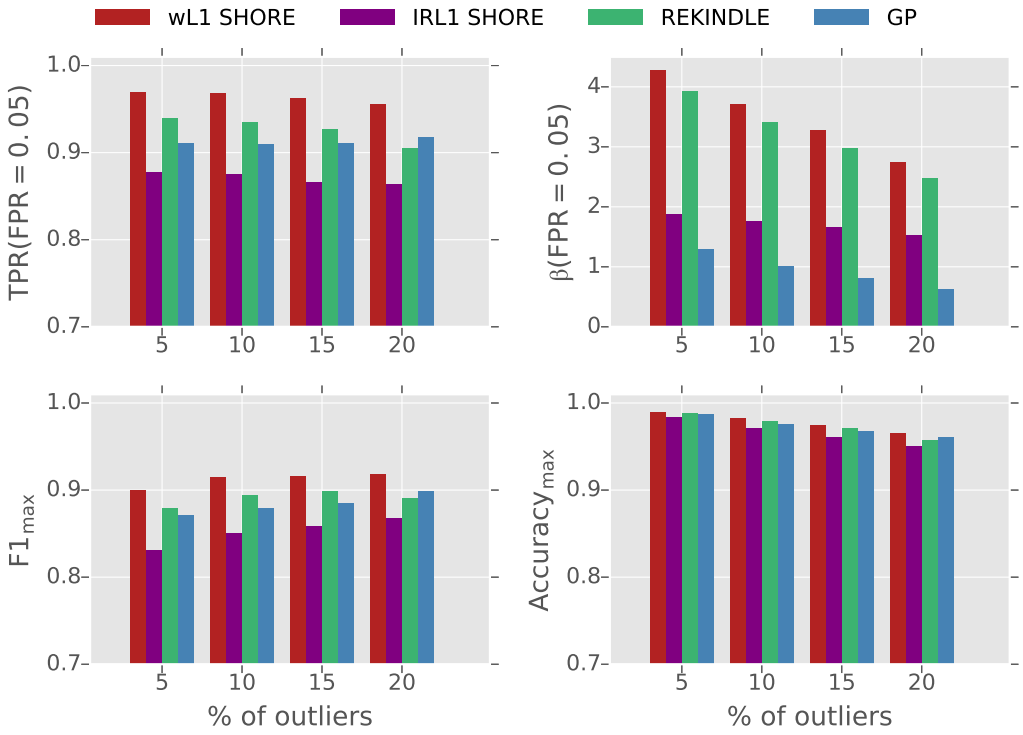

Figure 7.3: Outlier detection: For GP, REKINDLE, IRL1 SHORE and wL1 SHORE, the true positive rate (TPR) and the threshold β, both determined at TPR(FPR $= 0.05$), and the maximum F1 and accuracy are calculated from the ROC curves depicted in Figure 2. For 5-20% of outliers in the simulation data, wL1 SHORE performs the best across all metrics in detecting signal dropout.

7.3.1.2 Signal prediction

With respect to signal prediction, high R^2 scores are observed across all methods, independent of the amount of outliers. As presented in Table 7.1, wL1 SHORE and REKINDLE perform comparably, with a slight advantage for the latter. Both work better than GP.

Table 7.1: Signal prediction using GP, REKINDLE and wL1 SHORE is quantified by R^2 for different levels of outliers in the simulation data (5-20%). wL1 SHORE and REKINDLE provide comparable signal prediction, with the performance of the latter being slightly better. For GP, R^2 is lower than for both wL1 SHORE and REKINDLE.

		GP	REKINDLE	wL1 SHORE
Metric	% of outliers			
R^2	5	0.9438	0.9709	0.9608
	10	0.9599	0.9799	0.9732
	15	0.9588	0.9798	0.9733
	20	0.9548	0.9779	0.9721

7.3.1.3 Imputation

Imputation involved predicting values after discarding outliers using the thresholds reported in Figure 7.3. To assess signal imputation, we determined the NMSE between noise-free simulations and noisy simulations with and without imputation of detected outliers on the voxel level. Figure 7.4 (top row) shows the NMSE as a function of outlier percentage.

Table 7.2 compares wL1 SHORE, REKINDLE and GP used for signal imputation against no correction of the noisy data corrupted by outliers. The noise level can be estimated from the NMSE between ground truth and noisy, but uncorrupted simulations (0% outliers). The NMSE for wL1 SHORE and REKINDLE is similar to this level. When correcting all measurements, the NMSE even drops below it (see Supporting Information Figure 7.10 and Supporting Information Table 7.3). For GP, the NMSE is comparable for both correction strategies. With the chosen variant, which reconstructs only detected outliers, all methods perform similarly well, with a slight advantage of wL1 SHORE at high outlier ratios. In comparison, when correcting all measurements, the NMSE and its standard deviation is lower for wL1 SHORE and REKINDLE compared to the imputation of only detected outliers. REKINDLE and wL1 SHORE perform comparably, and both are better than GP. Lowest NMSE values are obtained by REKINDLE if less than 20% of the data is corrupted by outliers. Otherwise, wL1 SHORE performs better than REKINDLE and GP.

The middle and bottom rows of Figure~7.4 show the effect of signal imputation on diffusion and microstructural measures (FA: fractional anisotropy, MD: mean diffusivity, AK: axial kurtosis, ND: neurite density) obtained by means of state-of-the-art dMRI model fitting (Harms et al., 2017). NMSE values are shown between the ground truth and the motion corrupted data set, as well as for data corrected via wL1 SHORE, REKINDLE, and GP. All imputation methods improved accuracy when estimating dMRI measures from corrupted data. Compared to REKINDLE and GP, a slight advantage is observed for wL1 SHORE in FA, MD and AK, and in ND at high outlier ratios.

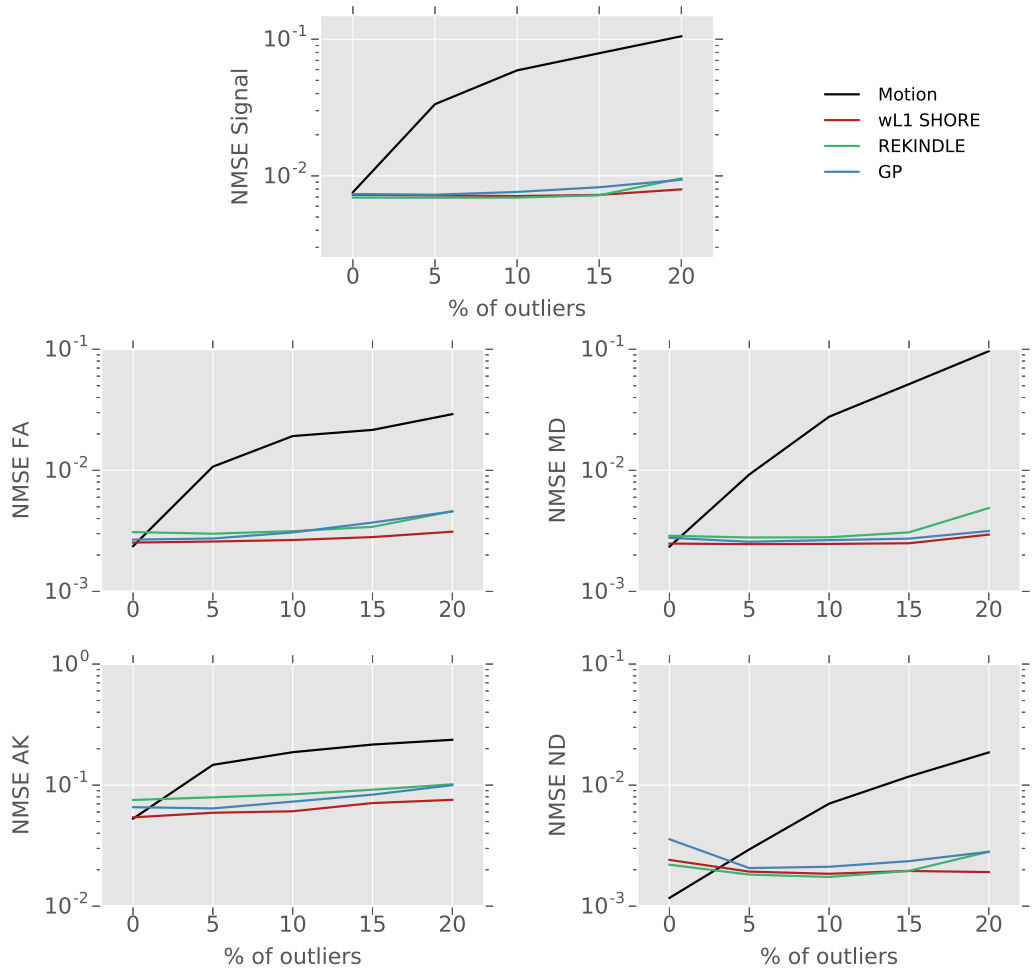

Figure 7.4: NMSE with respect to ground truth for different levels of outliers (0-20%) in simulations. The NMSE between the ground truth and the motion corrupted data is shown for reference (black line). Top row: Signal imputation using wL1 SHORE leads to NMSE comparable to REKINDLE, while GP has larger NMSE. Middle and bottom row: For FA, MD, AK and ND, NMSE is lowest using wL1 SHORE for signal imputation.

Table 7.2: Mean NMSE and standard deviation over all simulated signals. Based on the NMSE, wL1 SHORE, REKINDLE and GP used for signal imputation of the detected outliers are compared against no correction of the noisy data corrupted by outliers. Overall, all methods provide comparable NMSE. wL1 SHORE performs slightly better in case of high percentages of outliers in the data. wL1 SHORE yields lowest standard deviations, REKINDLE the highest.

		GP	**REKINDLE**	**wL1 SHORE**	**No correction**
Metric	% of outliers				
NMSE	0	0.0074±0.0013	0.0069±0.0013	0.0073±0.0012	0.0076±0.0012
	5	0.0073±0.0013	0.0069±0.0013	0.0072±0.0012	0.0335±0.0100
	10	0.0076±0.0017	0.0069±0.0020	0.0071±0.0013	0.0592±0.0136
	15	0.0083±0.0025	0.0072±0.0040	0.0073±0.0021	0.0790±0.0161
	20	0.0094±0.0031	0.0096±0.0091	0.0080±0.0041	0.1051±0.0179

Our current interest is focused on clinically feasible protocols. However, as a proof-of-concept, we also simulated a diffusion spectrum imaging (DSI) acquisition, to investigate the performance of our method at higher b-values. Specifically, we simulated 258 q-space samples on a spherically truncated Cartesian 11x11x11 grid (TE = 135.5 ms, b_{max} = 8350 s/mm^2, Δ = 65.9 ms, δ = 57.4 ms). Supporting Information Figure 7.11 depicts the results for wL1 SHORE with respect to outlier detection and imputation. An average maximum accuracy of 0.9428 and a mean R^2 of 0.9633 for signal prediction indicate accurate performance also in this scenario.

7.3.2 *In vivo* research data

The NMSE per DWI between the reference data without deliberate head movements and the measurements including subject motion is depicted in Figure 7.5.

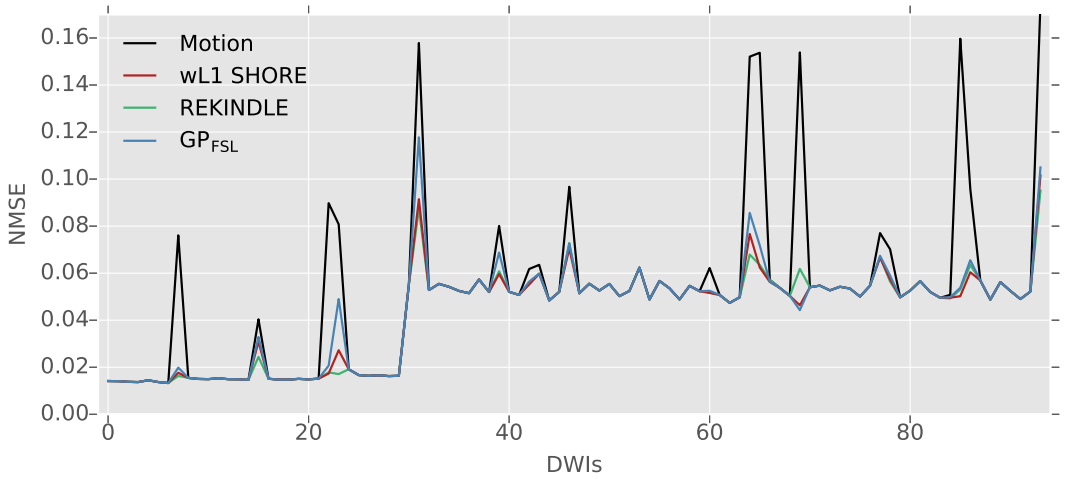

Figure 7.5: The NMSE computed per DWI between the reference and the motion corrupted *in vivo* research data is higher for DWIs with signal dropout due to deliberate fast head movements compared to DWIs not corrupted by this motion (Motion). Slice-based outlier detection and data correction is performed using wL1 SHORE, REKINDLE and GP FSL . All methods reduce the NMSE of motion corrupted DWIs, while non-corrupted DWIs are not modified. At low b-values, all methods perform comparable. At high b-values, lower NMSE values are obtained for wL1 SHORE compared to the other methods.

Distinct peaks of high NMSE are detected for DWIs corrupted by head movement compared to the other volumes (Motion). Different choices of the parameters λ and α were investigated for wL1 SHORE. The results are shown in Supporting Information Figure 7.12. They confirm that the parameters that were found to be well suited in synthetic experiments generalize well to *in-vivo* data and enable accurate outlier slice detection. Slice-based outlier detection and signal imputation using wL1 SHORE and REKINDLE was performed using outlier thresholds $t_s = 2.5$ and $\kappa_s = 3.5$. Those threshold values were found to be optimal in balancing accurate detection of true outliers and a minimum number of false positives (see Supporting Information Figure 7.13). We further compare to the outlier detection and imputation using FSL's `eddy` (GP$_{FSL}$), as a state-of-the-art method for

the correction of signal dropout. A threshold $g_{FSL} = 3$ was found to be optimal for this data (see Supporting Information Figure 7.13). Figure 7.6 compares the number of defective DWIs and corresponding outlier slices detected by the correction methods to the manual detection of defective DWIs by means of visual inspection (red stars).

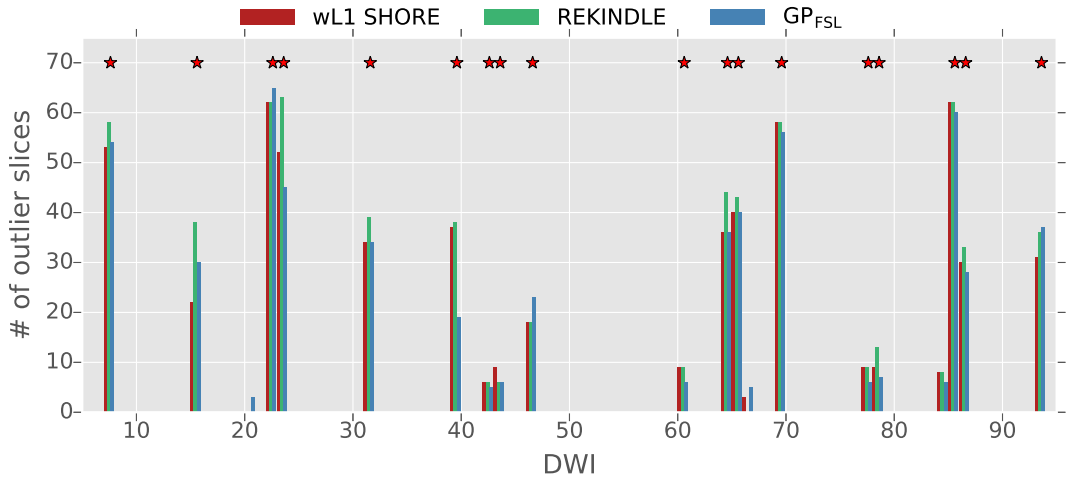

Figure 7.6: Number of outlier slices per DWI of the *in-vivo* research data detected by wL1 SHORE (top), REKINDLE (middle) and GP FSL (bottom). Applying $t_s = 2.5$, $\kappa_s = 3.5$ and $g_{FSL} = 3$ results in comparable outlier slice detection. Reds stars indicate defective volumes identified through visual inspection.

For wL1 SHORE and REKINDLE using $t_s = 2.5$ and $\kappa_s = 3.5$, respectively, an overlap in outlier slice detection of 98.9% (94.6% / 99.9%) was obtained across all DWIs (motion corrupted / uncorrupted DWIs). For wL1 SHORE and GP$_{\text{FSL}}$ applying $g_{FSL} = 3$, the overlap was 97.9% (89.5% / 99.9%). Comparing REKINDLE and GP$_{\text{FSL}}$, an overlap of 97.4% (87.2% / 99.8%) was observed.

All methods reduced the NMSE for the corrupted DWIs to an NMSE level closer to that of the non-corrupted DWIs. At $b = 700$ s/mm^2, a mean NMSE of 0.0717 $\pm$ 0.0188 is observed for DWIs with distinct motion peaks compared to a mean NMSE of 0.0151 $\pm$ 0.0012 for non-corrupted DWIs. Using wL1 SHORE, REKINDLE and GP$_{\text{FSL}}$ reduces the mean NMSE of the motion corrupted DWIs to 0.0233 $\pm$ 0.0059, 0.0189 $\pm$ 0.0032 and 0.0306 $\pm$ 0.0118, respectively. As expected, the NMSE is higher overall for $b = 2000$ s/mm^2. Here, a mean NMSE of 0.1114 $\pm$ 0.0425 for motion corrupted DWIs compares to a mean NMSE of 0.0528 $\pm$ 0.0029 for the non-corrupted DWIs. The average NMSE for DWIs with distinct motion peaks is reduced to 0.0650 $\pm$ 0.0151, 0.0655 $\pm$ 0.0120 and 0.0700 $\pm$ 0.0197 after motion correction using wL1 SHORE, REKINDLE and GP$_{\text{FSL}}$, respectively. Statistical significance of the differences in NMSE values across DWIs, as reported in Figure 7.5, was evaluated with a paired t-test. Statistically significant differences in NMSE were observed between the motion corrupted data and each of the motion correction methods ($p < 0.001$). Likewise, the NMSE for GP$_{\text{FSL}}$ differed from the one for wL1 SHORE ($p < 0.01$) or REKINDLE ($p < 0.05$). Differences between NMSE values for wL1 SHORE and REKINDLE were not statistically significant.

Figure 7.7 depicts a coronal slice of DWIs with (Motion) and without (Reference) deliberate head

movement and the slice-based correction of the former using wL1 SHORE, REKINDLE and GP_{FSL}. The corresponding maps of detected outlier slices are depicted in Supporting Information Figure 7.14 and show that all methods located faulty signals caused by subject motion. Overall, comparable quality is obtained from all correction methods, all of which substantially corrected the DWIs from severe signal dropout. wL1 SHORE, however, performed the fastest compared to the other methods. Runtime estimates were achieved on a workstation equipped with an Intel Xeon e5 24 core CPU (2.40 Ghz). The proposed method required 1.83 minutes for whole brain outlier detection and imputation. Processing times for GP_{FSL}, GP and REKINDLE were 27.85, 41.55 and 42.30 minutes, respectively. In comparison to the iterative REKINDLE and GP approaches, wL1 SHORE was much faster.

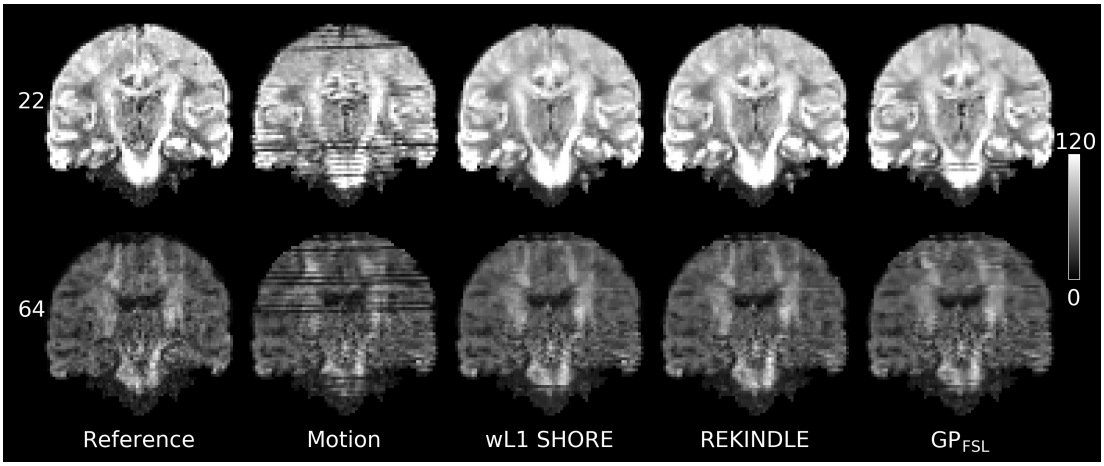

Figure 7.7: DWIs at b-values 700 s/mm^2 (top) and 2000 s/mm^2 (bottom) are depicted for the *in vivo* research data with (Motion) and without (Reference) deliberate fast head movements. The imputed motion corrected DWIs are presented for wL1 SHORE, REKINDLE and GP FSL . All methods detect severe signal dropout in the motion corrupted data and provide imputed DWIs comparable to the reference data set.

7.3.3 *In vivo* clinical data

In clinical human *in vivo* images tainted by motion artifacts, we present the advantages of wL1 SHORE. As for the research *in vivo* dMRI, slice-based outlier detection and signal imputation using wL1 SHORE, REKINDLE and GP_{FSL} was performed using outlier thresholds $t_s = 4$, $\kappa_s = 4.5$ and $g_{FSL} = 4$. We selected the optimal thresholds for whole brain outlier detection based on the results from simulation experiments and visual inspection of the data. Figure 7.8 depicts a coronal slice of acquired DWIs at b-values 700 s/mm^2 and 2000 s/mm^2 corrupted by severe signal dropout. For all methods comparable maps of detected outlier slices were obtained (see Supporting Information Figure 7.15) and used to impute the affected DWIs. The results highlight that the proposed method succeeds in locating faulty signals and substantially corrects the DWIs. While minor motion artifacts still remain present as for the research *in vivo* dMRI, all methods successfully correct severe signal dropout.

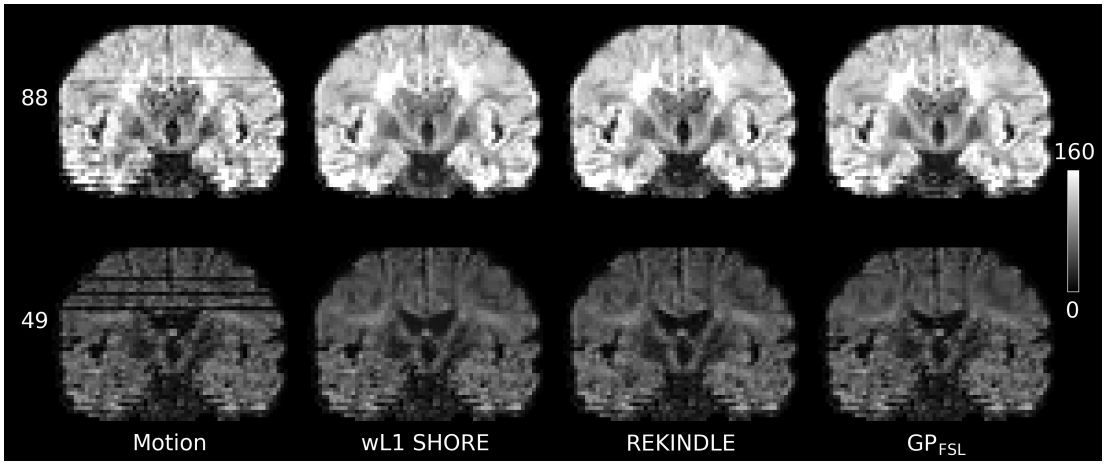

Figure 7.8: DWIs at b-values 700 s/mm^2 (top) and 2000 s/mm^2 (bottom) are depicted for the motion corrupted *in vivo* clinical data (Motion). The imputed motion corrected DWIs are presented for wL1 SHORE, REKINDLE and GP FSL . All methods perform accurate and comparable outlier detection and imputation of severe signal dropout in the data.

7.4 Discussion

We proposed a novel approach for dropout detection and imputation, wL1 SHORE. We evaluated it in terms of outlier detection, signal prediction from a subset of measurements, and signal imputation, which combined both. We compared it to our previously introduced IRL1 SHORE, to a state-of-the-art method based on Gaussian Processes and to another alternative, which we derived from REKINDLE.

Based on simulations, we found that wL1 SHORE accurately detects signal dropout, outperforming the other methods in terms of sensitivity at a fixed level of specificity. In contrast to the previously introduced iterative SHORE-based approach for dropout detection and imputation, wL1 SHORE avoids iterative reweighting which only increased processing time but did not further improve outlier detection for the proposed method. Results in Figure 7.1 indicate that this improvement can be attributed to our novel outlier score, which is in between an absolute and relative error measure, and therefore accounts for the fact that relative error is a natural indicator of dropout, while small absolute errors should still not be given excessive weight, since they might be due to measurement noise. Reported results involve diffusion weightings up to $b = 2000$ s/mm^2, but findings have been confirmed on experiments on 3-shell simulation data with b-values up to $b = 3000$ s/mm^2.

Our proposed method uses a sparsifying basis and an L1-regularized fit. We expected that this would lead to a benefit when restoring the full set of DWIs from a sparse set of inliers. Indeed, results were better than with the Gaussian Process model. However, on average, predicting the signal from a robustly fitted diffusional kurtosis (DKI) model produced even slightly lower errors. This may indicate that DKI was sufficient to capture the signals in our experiments (up to $b = 3000$ s/mm^2), for which it provides an even more parsimonious representation (6 coefficients in the diffusion tensor

plus 15 in the kurtosis tensor, compared to 50 SHORE basis functions). A proof-of-concept experiment on simulated diffusion spectrum imaging confirmed accurate performance of wL1 SHORE also for b-values that far exceed the typical range for DKI. Future work will investigate this further in *in-vivo* dMRI, and will explore the extent to which other basis functions that were found to be well suited for sparse reconstruction, such as the mean apparent propagator (MAP) basis (Fick et al., 2016; Ozarslan et al., 2009), might further improve our approach.

The ability of signal prediction is reflected in the results for signal imputation. For simulations, the NMSE was significantly reduced after detection and imputation of dropout compared to the motion corrupted data, with REKINDLE and wL1 SHORE performing the best. The fact that replacing all measurements further reduced the NMSE and its standard deviation indicates a regularizing effect on the dMRI signal. However, since it is difficult to rule out the risk of removing informative parts of the signal along with the noise, we decided to impute only detected outliers in our final method. Our simulation experiments suggest that signal imputation should be performed prior to dMRI model fitting and that outlier correction by means of wL1 SHORE provides accurate measures for the characterization of the diffusion process and the underlying tissue microstructure. Future work will further investigate the impact of motion on diffusion measures extracted from *in-vivo* dMRI.

In addition to simulations, we collected *in vivo* research dMRI acquisitions with and without head movement deliberately provoked by the participant to obtain a reference data set and one corrupted by fast motion artifacts. In this way, the performance of slice-based outlier removal and correction methods could be compared against a reference data set without motion artifacts. Overall, wL1 SHORE, REKINDLE and GP_{FSL} all substantially reduced motion related dropout. At $b = 2000$ s/mm^2, slightly lower NMSE values were obtained for our proposed method. Future work will explore this at even higher b-values. Finally, all correction methods were compared under severe uncontrolled motion in *in vivo* clinical dMRI. Visually, the proposed method gave similar results as the state-of-the-art for detection and imputation of signal dropout.

A limitation of all methods is the need to select a threshold β for outlier detection. Default values provide a reasonable balance of outliers and false positives. However, optimal results require adapting β to the degree of motion present in the data, which needs to be determined through visual inspection. Our imputation results based on the NMSE with respect to ground truth data in simulations and *in vivo* data suggest that imputing slightly more measurements than the true outliers has no adverse effect. Indeed, applying lower thresholds resulted in even lower NMSE in our investigated data sets. Nevertheless, in the *in vivo* data, we investigated suitable choices of β and chose rather conservative thresholds. As a consequence, comparing results to a manual assessment revealed nearly no false positives. Thresholds agree with typical threshold values reported for REKINDLE and GP_{FSL}. As a result, severe signal dropout was successfully detected by all methods. Minor motion artifacts still remain present in the *in vivo* data after imputing signal dropout. However, those can be related to a different type of motion artifact due to intra-volume movement for which a specifically tailored motion correction model has been proposed recently (Andersson et al., 2017).

We found that, on data with limited $b \leq 3000$ s/mm^2, wL1 SHORE and the method we derived from REKINDLE achieve similar quality. This can also be seen from the high overlap in their detection of outlier slices. An advantage of wL1 SHORE is its processing speed, due to its simplicity and non-

iterative nature. In our experiments, it performed more than twenty times faster than REKINDLE and GP. All our implementations are in Python. They use parallel processing, but have otherwise not been optimized for speed. Therefore, we expect that further speedups are possible. This is confirmed by observing that the optimized implementation in `eddy` was faster than our Python-based GP implementation (but still much slower than wL1 SHORE) despite the fact that `eddy` simultaneously performs image realignment and distortion correction.

Finally, in contrast to state-of-the-art methods for outlier removal, wL1 SHORE corrects DWIs tainted by motion artifacts independent of the applied acquisition strategy. In this work, we focused on simulation and *in vivo* dMRI data with diffusion weightings suitable for processing using REKINDLE, which can only be applied for b-values up to 3000 s/mm^2. Further, we only investigated multi-shell dMRI, since GP modeling requires q-space samples distributed on shells. Those limitations, however, do not apply to wL1 SHORE, as illustrated by our experiment on simulated DSI data (Supporting Information Figure~7.11).

7.5 Conclusion

In this work, the novel approach wL1 SHORE was proposed for the detection and imputation of signal dropout in dMRI. It corrects motion artifacts by restoring imaging data suffering from dropout, and thereby reduces the impact of defective DWIs on diffusion measures. Accurate detection of signal dropout by means of wL1 SHORE was confirmed in simulations and *in vivo* dMRI experiments for both voxel and slice-based outlier detection. An advantage of our method is computational speed: Successful signal imputation of corrupted measurements in a clinically feasible protocol was performed in about 2 minutes. At the same time, it is more flexible than existing alternatives with respect to the q-space sampling strategy and maximum diffusion weighting. On data where previous approaches can be applied, our proposed method compares to or even outperforms them in terms of outlier detection and imputation.

7.6 Supplementary material

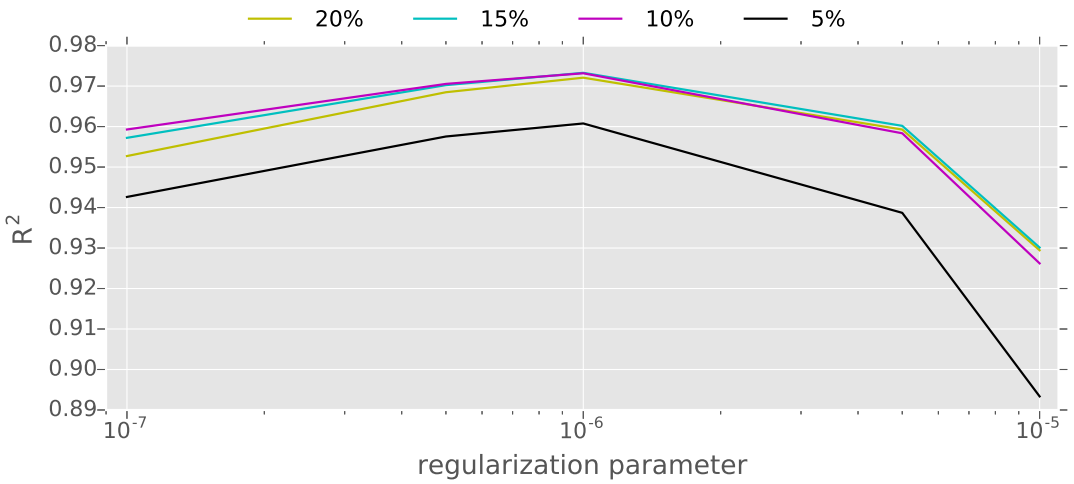

Supporting Information Figure 7.9: Signal prediction using wL1 SHORE with different values for the regularisation parameter λ is quantified by R^2 for different levels of outliers in the simulation data (5-20%). $\lambda = 10^{-6}$ is optimal for modeling the 2-shell simulation data.

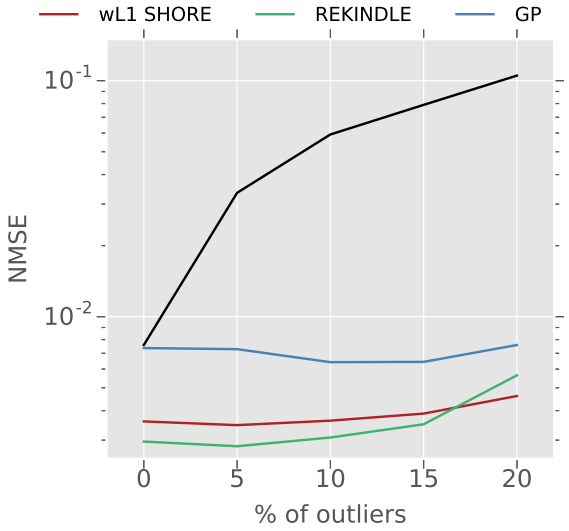

Supporting Information Figure 7.10: NMSE with respect to ground truth for different levels of outliers (0-20%) in simulations. All measurements were replaced by the estimated signals. Signal imputation using wL1 SHORE leads to NMSE comparable to REKINDLE, while GP has larger NMSE. The NMSE between the ground truth and the motion corrupted measurements is shown for reference (black line).

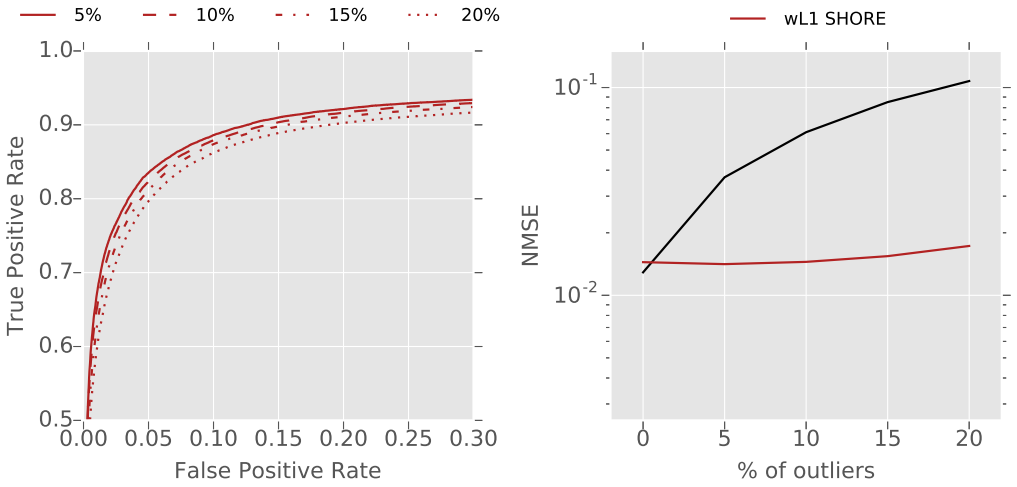

Supporting Information Figure 7.11: Left: Across different levels of outliers in the simulation data (5-20%), the ROC-curves are used to quantify the performance of the outlier detection method wL1 SHORE in DSI simulations. Right: NMSE with respect to ground truth for different levels of outliers (0-20%) in DSI simulations. Compared to the NMSE for motion corrupted measurements (black line), signal imputation using wL1 SHORE decreases the NMSE.

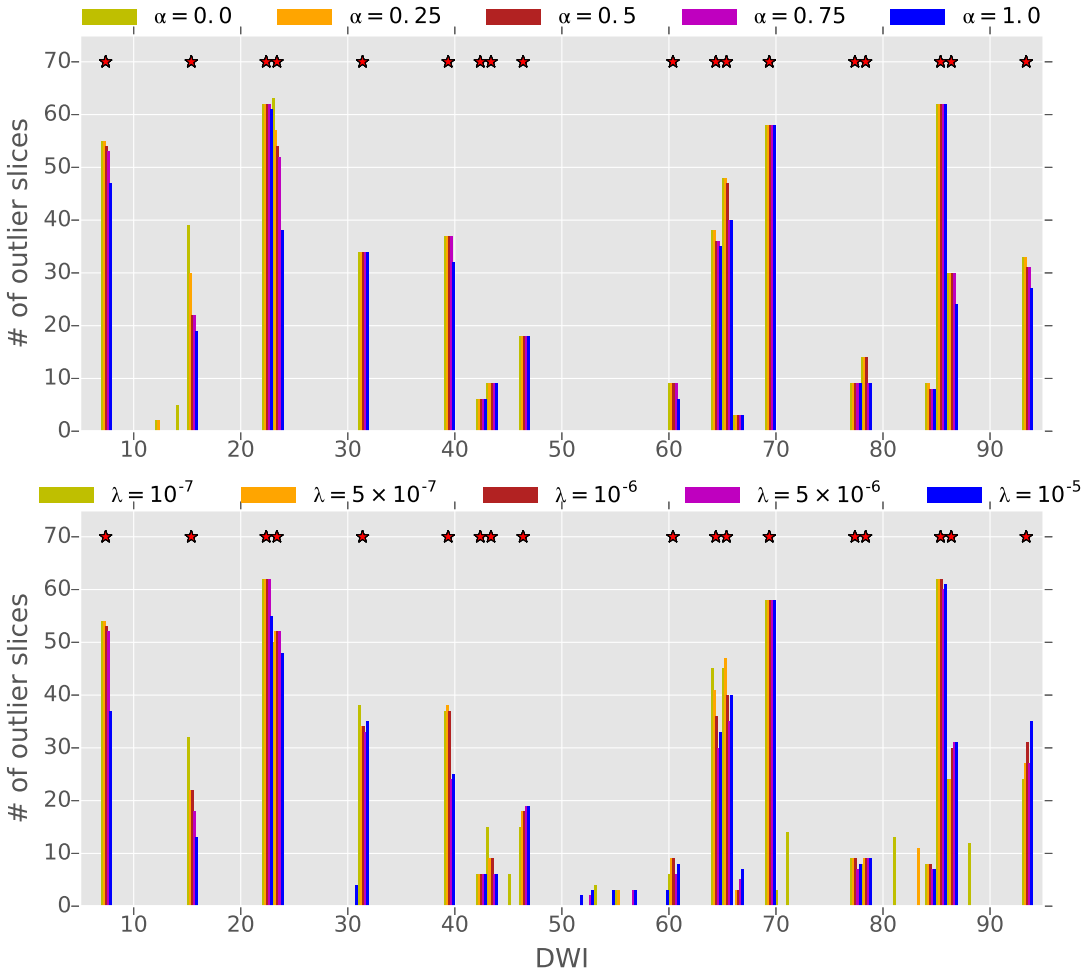

Supporting Information Figure 7.12: Number of outlier slices per DWI of the *in-vivo* research data detected by wL1 SHORE applying $t_s = 2.5$ and using different values for α (top) and λ (bottom). As for simulations, $\alpha = 0.75$ and $\lambda = 10^{-6}$ are found to be optimal for outlier slice detection. Reds stars indicate defective volumes identified through visual inspection.

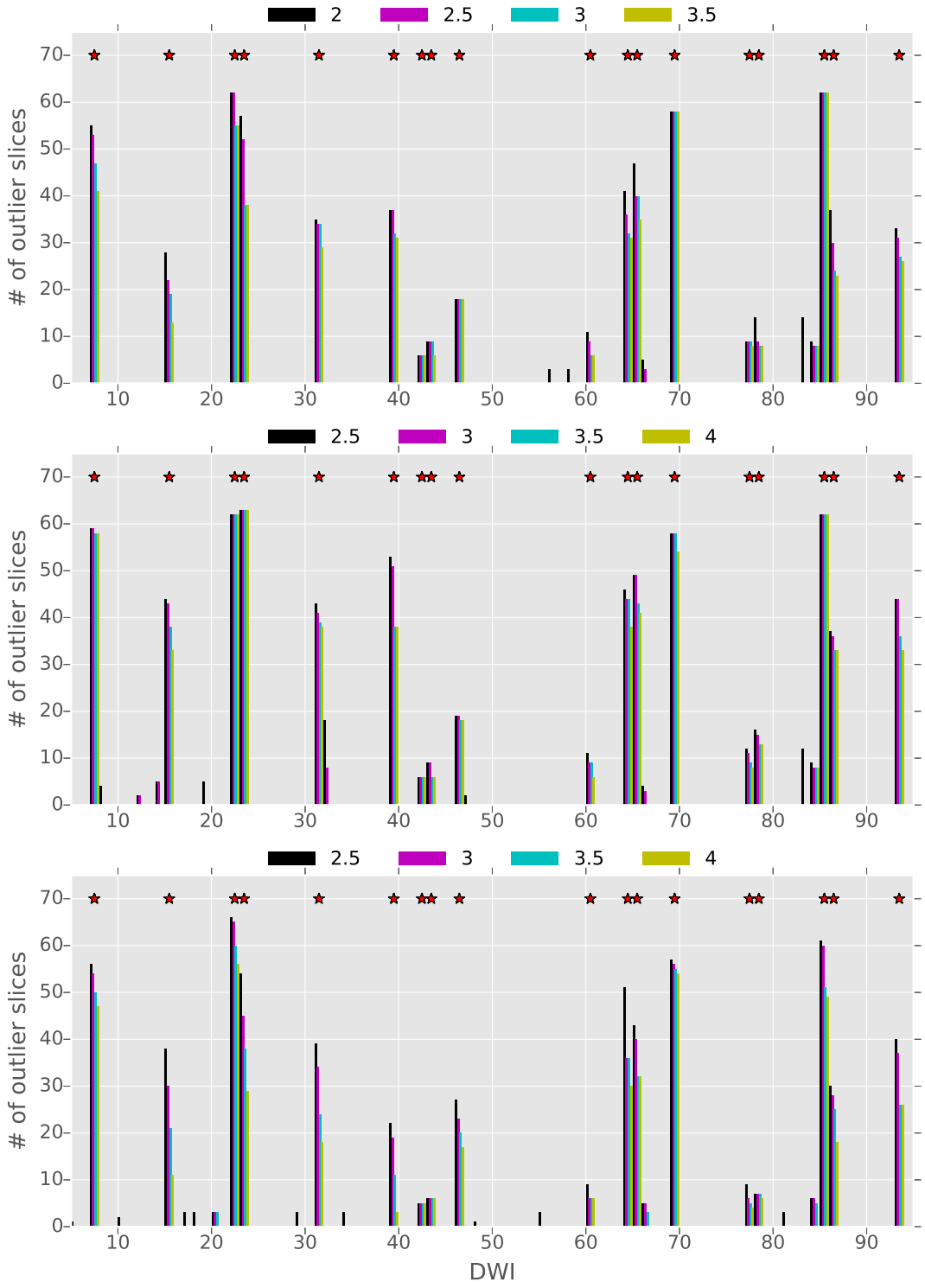

Supporting Information Figure 7.13: Number of outlier slices per DWI of the *in-vivo* research data detected by wL1 SHORE (top), REKINDLE (middle) and GP FSL (bottom) applying different values for β. $t_s = 2.5$, $\kappa_s = 3.5$ and $g_{FSL} = 3$ were found to be optimal for outlier slice detection, respectively. Reds stars indicate defective volumes identified through visual inspection.

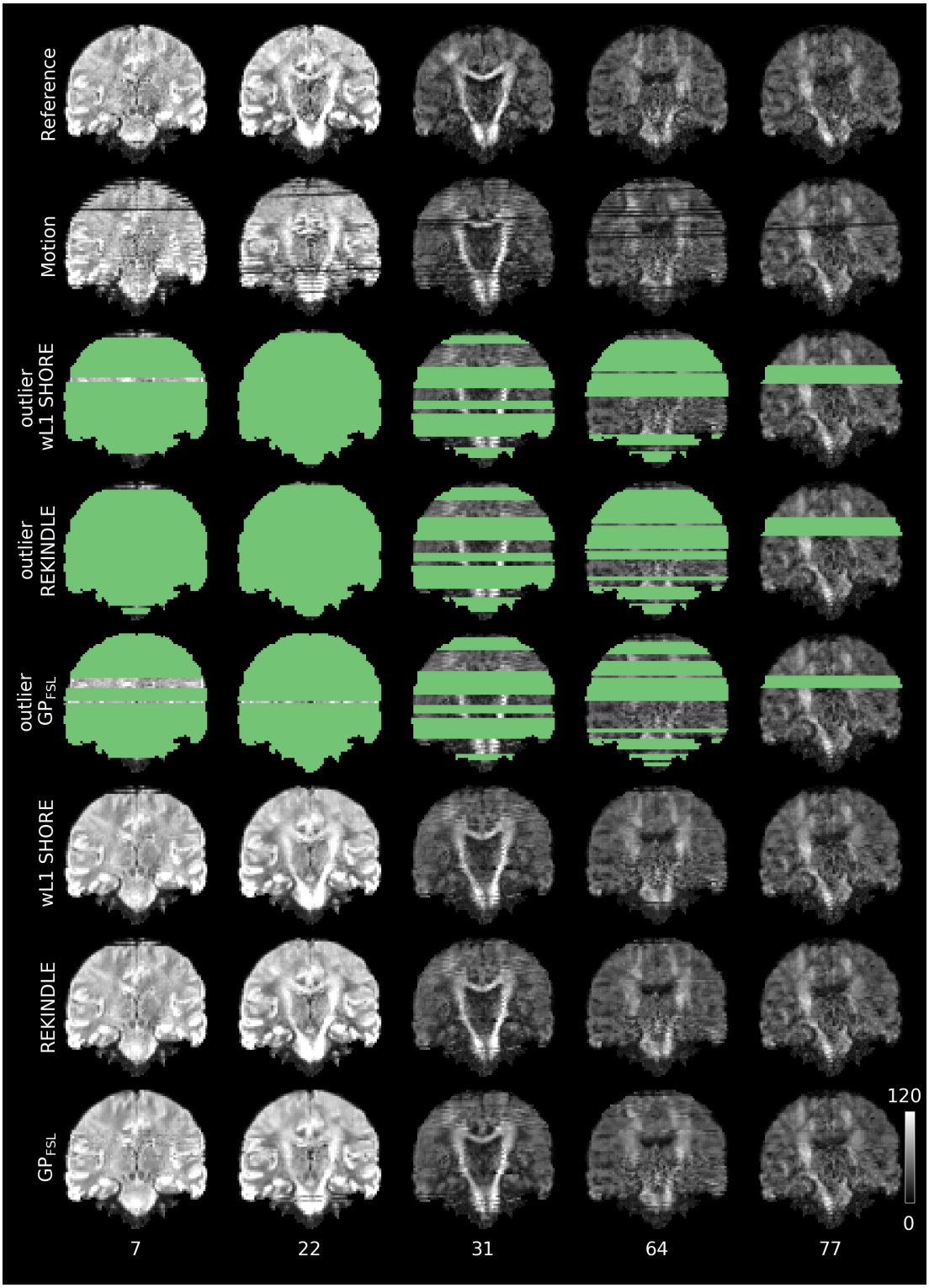

Supporting Information Figure 7.14: DWIs at b-values 700 s/mm^2 (column 1-2) and 2000 s/mm^2 (column 3-5) are depicted for the *in vivo* research data with (Motion) and without (Reference) deliberate fast head movements. Maps of outlier slices and the imputed motion corrected DWIs are presented for wL1 SHORE, REKINDLE and GP FSL . All methods detect severe signal dropout in the motion corrupted data and provide imputed DWIs comparable to the reference data set.

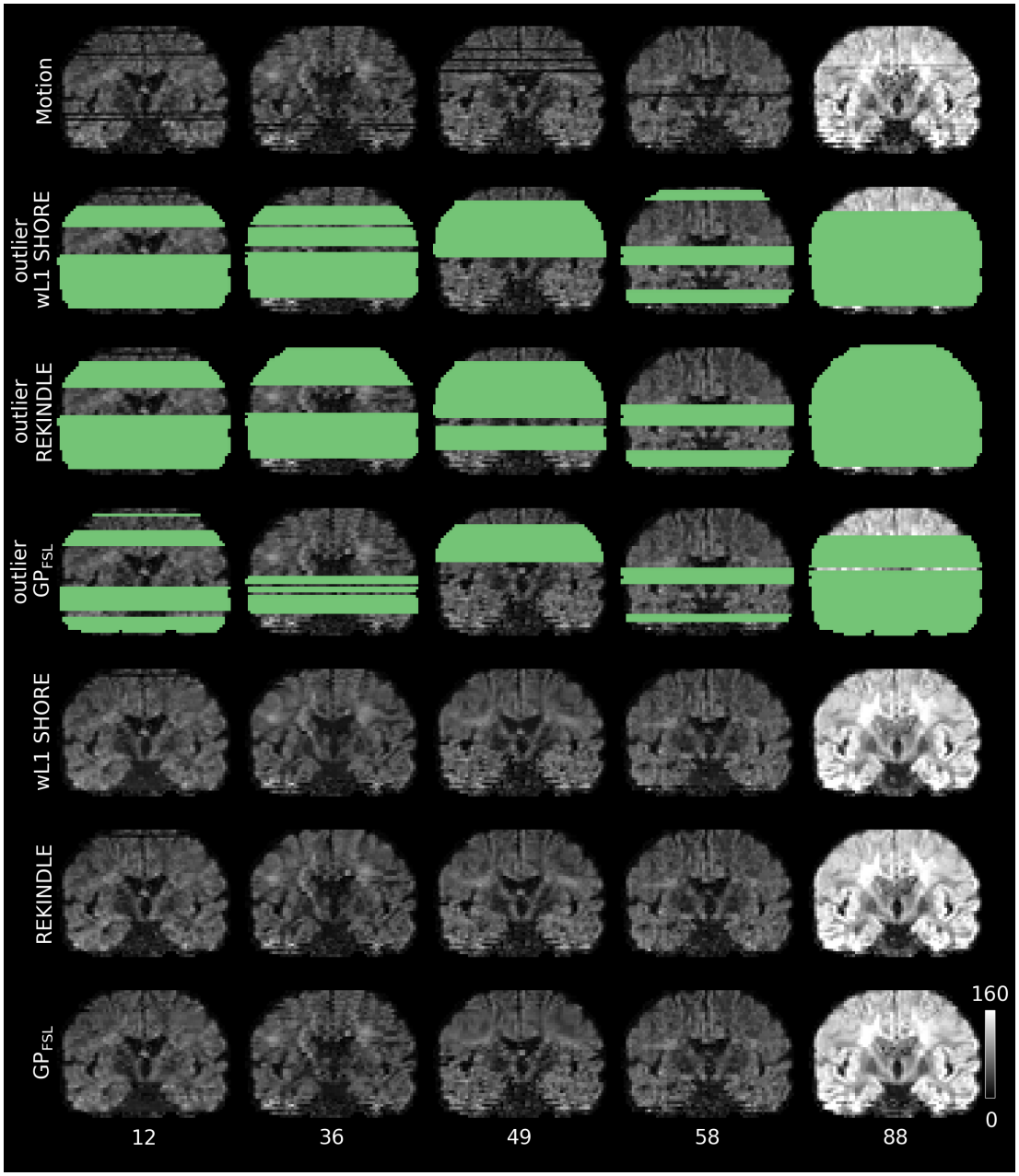

Supporting Information Figure 7.15: For DWIs at b-value 2000 s/mm^2 (column 1-4) and 700 s/mm^2 (column 5) of the *in vivo* clinical data, maps of outlier slices depict the location of signal dropout present in the measurements (Motion) detected by wL1 SHORE, REKINDLE and GP FSL . All methods perform accurate and comparable outlier detection and imputation of severe signal dropout in the data.

Supporting Information Table 7.3: Mean NMSE and standard deviation over all simulated signals. Based on the NMSE, wL1 SHORE, REKINDLE and GP used for signal imputation are compared against no correction of the noisy data corrupted by outliers. The correction strategy replaces all measurements by the estimated signal (all). wL1 SHORE and REKINDLE provide lower NMSE compared to the latter. wL1 SHORE yields lowest standard deviations, REKINDLE the highest.

		GP	**REKINDLE**	**wL1 SHORE**	**No correction**
Metric	% of outliers				
NMSE (all)	0	0.0074±0.0013	0.0030±0.0011	0.0036±0.0010	0.0076±0.0012
	5	0.0073±0.0013	0.0028±0.0010	0.0035±0.0010	0.0335±0.0100
	10	0.0064±0.0015	0.0031±0.0016	0.0036±0.0011	0.0592±0.0136
	15	0.0064±0.0023	0.0035±0.0032	0.0039±0.0016	0.0790±0.0161
	20	0.0076±0.0029	0.0056±0.0073	0.0046±0.0031	0.1051±0.0179

Part III

Closing

8

Conclusion

8.1 Thesis summary

In this thesis several contributions in the field of dMRI were presented. Our works on accelerated CS-DSI and novel techniques for fast and robust motion correction were described in chapters 4 - 7. In this concluding chapter, the thesis contributions are summarized:

1. CS theory demands the application of suitable basis functions for compressed sensing and sparse representation of the signal of interest. Chapter 4 presented multiple strategies for sparse q-space sampling and suitable basis functions for the acceleration of DSI by means of CS. 3D non-Cartesian q-space sample distributions as proposed by Knutsson and Westin (2013) were applied as CS-DSI acquisition schemes for the first time and were found to be optimal for robust CS reconstruction of orientational information even at high CS acceleration factors. Similarly, the performance of conventional Fourier-based CS-DSI was compared for the first time to CS-DSI based on SHORE signal modeling. Comprehensive evaluation experiments were implemented based on simulations, diffusion phantom data and *in vivo* dMRI. Comparable performance of both CS-DSI approaches was reported in terms of reconstructing orientational information. Better reconstruction quality of the dMRI signal and propagator features was obtained using Fourier-based CS-DSI.

2. In chapter 5, we proposed Fourier-based CS-DSI as a forward-looking dMRI acquisition strategy that allows for time efficient and versatile diffusion imaging at 3T. A pilot study was designed and conducted to fulfill the requirements of a long-term population study with limited scan time per MRI protocol. The aim was to investigate the feasibility of CS-DSI for application in a prospective cohort study, the Rhineland Study. Based on a comprehensive evaluation

framework the proposed dMRI protocol was evaluated against an alternative state-of-the-art 3-shell HARDI protocol for population imaging. In the estimation and reliability of diffusion and microstructural parameters and of orientational information, comparable performance of both dMRI imaging schemes was reported. Providing high b-value acquisitions, CS-DSI enabled analysis strategies such as CHARMED modeling and biomarkers from the diffusion propagator.

3. A pipeline for automatic analysis of dMRI acquisitions was designed and specifically tailored for CS-DSI. This pipeline facilitated and accelerated processing of CS-DSI data acquired in the extensive pilot study and will be likewise beneficial for the analysis of big data acquired in other studies, e.g. the Rhineland Study. It was implemented including both in-house developed and existing state-of-the-art processing tools, e.g. for motion and distortion correction, CS reconstruction and diffusion and microstructural feature extraction.

4. Two different methods for automatic detection of signal dropout and imputation in dMRI were developed as described in chapters 6 and 7. The latter extended and improved the initial iterative approach. A novel outlier score for the detection of dropout was introduced and evaluated in simulations as well as research and clinical *in vivo* dMRI. The final contribution was a method for fast detection of outliers based on weighted SHORE model residuals and accurate replacement of the affected measurements. Thus, the complete dMRI data set was recovered through imputed values obtained from a SHORE model fit to the sparse set of inliers. Compared to alternative approaches for outlier detection and imputation, our proposed method provides an advantage in terms of processing speed due to its simplicity and non-iterative nature and because of its ability to be applied independently of the dMRI acquisition strategy.

8.2 Future directions

The aim of the works presented in chapter 5 was to decide on a suitable dMRI protocol for time efficient versatile diffusion imaging in the Rhineland Study. A CS-DSI protocol was found optimal for application in a prospective cohort study and was therefore implemented in the Rhineland Study. Based on this finding, CS-DSI data has been collected from several thousand study participants by now. This amount of high resolution dMRI data allows on the one hand to tackle the limitations of the pilot study discussed in chapter 5 and to improve CS-DSI analysis. On the other hand, future work will focus on the interpretation of derived diffusion features and microstructural features of brain tissue. The works presented in chapter 5 thus are an important contribution to the following investigation of the aging process and the development, progression and potential prevention of brain diseases. With an automatic analysis pipeline for CS-DSI, this thesis contributed to enable fast processing of the acquired dMRI data. This pipeline will further be extended with novel and future analysis strategies.

Obtaining accurate and precise diffusion and microstructural parameters, requires robust preprocessing of the dMRI scans after data collection. As discussed in chapter 5, state-of-the-art strategies for the correction of motion artifacts in dMRI are not designed for DSI data. As a first approach

to investigate acquisition and model independent correction methods for CS-DSI, future work will thus combine the works on CS-DSI as presented in chapters 4 and 5 with the correction method proposed in chapters 6 and 7. This is of interest for both clinical applications and population imaging, especially when conducting studies with children, the elderly or patients, for which subject motion is a common source of imaging artifacts.

The methodology proposed in this thesis for accelerated dMRI is, in general, applicable to studies with limited scan time. Stringent scan time limits are imposed in population imaging, but also in most clinical studies. Strategies for rapid and robust high quality dMRI are thus of great interest for many applications. Once established in clinical studies, the contributions of this thesis can thus, firstly, benefit inter-site and -scanner harmonization of clinical and research dMRI. Secondly, they can facilitate the transition of research findings in large cohort studies to clinical applications.

References

Acosta-Cabronero J, Williams GB, Cardenas-Blanco A, Arnold RJ, Lupson V, Nestor PJ, 2013. In vivo quantitative susceptibility mapping (QSM) in Alzheimer's disease. PloS one 8, e81093.

Aganj I, Lenglet C, Sapiro G, Yacoub E, Ugurbil K, Harel N, 2010. Reconstruction of the orientation distribution function in single- and multiple-shell q-ball imaging within constant solid angle. Magnetic Resonance in Medicine 64, 554–566.

Alexander DC, Barker GJ, 2005. Optimal imaging parameters for fiber-orientation estimation in diffusion MRI. NeuroImage 27, 357–367.

Alexander DC, Dyrby TB, Nilsson M, Zhang H, 2017. Imaging brain microstructure with diffusion MRI: Practicality and applications. NMR in Biomedicine 1–26.

Anderson AW, 2005. Measurement of fiber orientation distributions using high angular resolution diffusion imaging. Magnetic Resonance in Medicine 54, 1194–1206.

Andersson JL, Graham MS, Drobnjak I, Zhang H, Filippini N, Bastiani M, 2017. Towards a comprehensive framework for movement and distortion correction of diffusion MR images: Within volume movement. NeuroImage 152, 450–466.

Andersson JL, Graham MS, Zsoldos E, Sotiropoulos SN, 2016. Incorporating outlier detection and replacement into a non-parametric framework for movement and distortion correction of diffusion MR images. NeuroImage 141, 556–572.

Andersson JL, Sotiropoulos SN, 2016. An integrated approach to correction for off-resonance effects and subject movement in diffusion MR imaging. NeuroImage 125, 1063–1078.

Andersson JLR, Skare S, Ashburner J, 2003. How to correct susceptibility distortions in spin-echo

echo-planar images: Application to diffusion tensor imaging. NeuroImage 20, 870–888.

Andersson JLR, Sotiropoulos SN, 2015. Non-parametric representation and prediction of single- and multi-shell diffusion-weighted MRI data using Gaussian processes. NeuroImage 122, 166–176.

Ankele M, Lim LH, Groeschel S, Schultz T, 2017. Versatile, robust, and efficient tractography with constrained higher-order tensor fODFs. International Journal of Computer Assisted Radiology and Surgery 12, 1257–1270.

Assaf Y, Basser PJ, 2005. Composite hindered and restricted model of diffusion (CHARMED) MR imaging of the human brain. NeuroImage 27, 48–58.

Assaf Y, Blumenfeld-Katzir T, Yovel Y, Basser PJ, 2008. Axcaliber: A method for measuring axon diameter distribution from diffusion MRI. Magnetic Resonance in Medicine 59, 1347–1354.

Assaf Y, Freidlin RZ, Rohde GK, Basser PJ, 2004. New modeling and experimental framework to characterize hindered and restricted water diffusion in brain white matter. Magnetic Resonance in Medicine 52, 965–978.

Assaf Y, Mayk A, Cohen Y, 2000. Displacement imaging of spinal cord using q-space diffusion-weighted MRI. Magnetic Resonance in Medicine 44, 713–722.

Assemlal HE, Tschumperlé D, Brun L, 2009. Efficient and robust computation of PDF features from diffusion MR signal. Medical Image Analysis 13, 715–729.

Avram AV, Sarlls JE, Barnett AS, Özarslan E, Thomas C, Irfanoglu MO, Hutchinson E, Pierpaoli C, Basser PJ, 2016. Clinical feasibility of using mean apparent propagator (MAP) MRI to characterize brain tissue microstructure. NeuroImage 127, 422–434.

Bach M, Laun FB, Leemans A, Tax CM, Biessels GJ, Stieltjes B, Maier-Hein KH, 2014. Methodological considerations on tract-based spatial statistics (TBSS). NeuroImage 100, 358–369.

Baraniuk R, Davenport M, DeVore R, Wakin M, 2008. A simple proof of the restricted isometry property for random matrices. Constructive Approximation 28, 253–263.

Barazany D, Basser PJ, Assaf Y, 2009. In vivo measurement of axon diameter distribution in the corpus callosum of rat brain. Brain 132, 1210–1220.

Bartko J, 1966. The intraclass correlation coefficient as a measure of reliability. Psychological Reports 19, 3–11.

Basser P, Mattiello J, Le Bihan D, 1994a. MR diffusion tensor spectroscopy and imaging. Biophysical Journal 66, 259–267.

Basser P, Mattiello J, Le Bihan D, 1994b. Estimation of the effective self-diffusion tensor from the NMR spin echo. Journal of Magnetic Resonance, Series B 103, 247–254.

Basser P, Pierpaoli C, 1996. Microstructural and physiological features of tissues elucidated by

quantitative-diffusion-tensor MRI. Journal of Magnetic Resonance 111, 209–219.

Beck A, Teboulle M, 2009. A Fast Iterative Shrinkage-Thresholding Algorithm for Linear Inverse Problems. SIAM Journal on Imaging Sciences 2, 183–202.

Behrens TEJ, Berg HJ, Jbabdi S, Rushworth MFS, Woolrich MW, 2007. Probabilistic diffusion tractography with multiple fibre orientations: What can we gain? NeuroImage 34, 144–155.

Behrens TEJ, Sporns O, 2012. Human connectomics. Current Opinion in Neurobiology 22, 144–153.

Behrens TEJ, Woolrich MW, Jenkinson M, Johansen-Berg H, Nunes RG, Clare S, Matthews PM, Brady JM, Smith SM, 2003. Characterization and Propagation of Uncertainty in Diffusion-Weighted MR Imaging. Magnetic Resonance in Medicine 50, 1077–1088.

Bells S, Cercignani M, Deoni S, Assaf Y, 2011. Tractometry: comprehensive multi-modal quantitative assessment of white matter along specific tracts, in: Proceedings of the 19th Scientific Meeting of the International Society for Magnetic Resonance in Medicine (Montreal, QC). p. 678.

Bilgic B, Setsompop K, Cohen-Adad J, Yendiki A, Wald LL, Adalsteinsson E, 2012. Accelerated diffusion spectrum imaging with compressed sensing using adaptive dictionaries. Magnetic Resonance in Medicine 68, 1747–1754.

Bland JM, Altman DG, 1996. Measurement error. British Medical Journal 313, 744–753.

Bloch F, 1946. Nuclear induction. Phys. Rev. 70, 460–474.

Brenner D, Stirnberg R, Pracht ED, Stöcker T, 2014. Two-dimensional accelerated MP-RAGE imaging with flexible linear reordering. Magnetic Resonance Materials in Physics, Biology and Medicine 27, 455–462.

Breteler M, Swieten JC van, Bots ML, Grobbee DE, Claus JJ, Hout JH van den, Harskamp F van, Tanghe HL, Jong PT de, Gijn J van, Hofman A, 1994. Cerebral white matter lesions, vascular risk factors, and cognitive function in a population-based study: the Rotterdam Study. Neurology 44, 1246–52.

Breuer F a, Blaimer M, Heidemann RM, Mueller MF, Griswold M a, Jakob PM, 2005. Controlled aliasing in parallel imaging results in higher acceleration (CAIPIRINHA) for multi-slice imaging. Magnetic Resonance in Medicine 53, 684–691.

Broad RJ, Gabel MC, Dowell NG, Schwartzman DJ, Seth AK, Zhang H, Alexander DC, Cercignani M, Leigh PN, 2018. Neurite orientation and dispersion density imaging (NODDI) detects cortical and corticospinal tract degeneration in ALS. Journal of Neurology, Neurosurgery and Psychiatry.

Brown R, 1866. A Brief Account on Microscopical Observations on the Particles Contained in the Pollen of Plants and on the General Existence of Active Molecules in Organic and Inorganic Bodies, in: Bennett JJ, editor.The miscellaneous botanical works of Robert Brown. R. Hardwicke,

London.

Brown RW, Cheng Y-CN, Haacke EM, Thompson MR, Venkatesan R, 2014. Magnetic Resonance Imaging: Physical Principles and Sequence Design, 2nd ed. Wiley-Blackwell.

Brusini L, Obertino S, Zucchelli M, Galazzo IB, Krueger G, Granziera C, Menegaz G, 2015. Assessment of Mean Apparent Propagator-Based Indices as Biomarkers of Axonal Remodeling after Stroke, in: Navab N, Hornegger J, Wells WM, Frangi A, editors.Med. Image Comput. Comput. Assist. Interv. (Munich, Germany), Lecture Notes in Computer Science. Springer International Publishing, Cham, pp. 199–206.

Callaghan PT, 1991. Principles of nuclear magnetic resonance microscopy. Oxford: Clarendon Press.

Callaghan PT, Eccles CD, Xia Y, 1988. NMR microscopy of dynamic displacements: K-space and q-space imaging. Journal of Physics E: Scientific Instruments 21, 820.

Candès E, Romberg J, 2007. Sparsity and incoherence in compressive sampling. Inverse Problems 23, 969–985.

Candès E, Romberg J, Tao T, 2006. Robust uncertainty principles: Exact signal reconstruction from highly incomplete frequency information. IEEE Transactions on Information Theory 52, 489–509.

Candès E, Romberg J, Tao T, 2006. Stable signal recovery from incomplete and inaccurate measurements. Communications on Pure and Applied Mathematics 59, 1207–1223.

Candès E, Wakin M, 2008. An Introduction To Compressive Sampling. IEEE Signal Processing Magazine 25, 21–30.

Caroli A, Schneider M, Friedli I, Ljimani A, De Seigneux S, Boor P, Gullapudi L, Kazmi I, Mendichovszky IA, Notohamiprodjo M, Selby NM, Thoeny HC, Grenier N, Vallée J-P, 2018. Diffusion-weighted magnetic resonance imaging to assess diffuse renal pathology: a systematic review and statement paper. Nephrology Dialysis Transplantation 33, ii29–ii40.

Carr HY, Purcell EM, 1954. Effects of diffusion on free precession in nuclear magnetic resonance experiments. Physical Review 94, 630–638.

Caruyer E, Lenglet C, Sapiro G, Deriche R, 2013. Design of multishell sampling schemes with uniform coverage in diffusion MRI. Magnetic resonance in medicine 69, 1534–40.

Cauley SF, Polimeni JR, Bhat H, Wald LL, Setsompop K, 2014. Interslice leakage artifact reduction technique for simultaneous multislice acquisitions. Magnetic Resonance in Medicine 72, 93–102.

Chang L-C, Jones DK, Pierpaoli C, 2005. RESTORE: Robust Estimation of Tensors by Outlier Rejection. Magnetic Resonance in Medicine 53, 1088–1095.

Chang YS, Owen JP, Pojman NJ, Thieu T, Bukshpun P, Wakahiro ML, Berman JI, Roberts TP, Nagarajan SS, Sherr EH, Mukherjee P, 2015. White matter changes of neurite density and fiber

orientation dispersion during human brain maturation. PLoS ONE 10.

Chen Y, Tymofiyeva O, Hess CP, Xu D, 2015. Effects of rejecting diffusion directions on tensor-derived parameters. NeuroImage 109, 160–170.

Chenevert TL, Brunberg JA, Pipe JG, 1990. Anisotropic diffusion in human white matter: demonstration with MR techniques in vivo. Radiology 177, 401–405.

Cheng J, 2012. Estimation and Processing of Ensemble Average Propagator and Its Features in Diffusion MRI (PhD thesis). University of Nice-Sophia Antipolis.

Cheng J, Jiang T, Deriche R, 2011. Theoretical Analysis and Practical Insights on EAP Estimation via a Unified HARDI Framework, in: MICCAI Workshop on Computational Diffusion MRI (Toronto, Canada).

Cheng J, Merlet S, Caruyer E, Ghosh A, Jiang T, Deriche R, 2011. Compressive Sensing Ensemble Average Propagator Estimation via L1 Spherical Polar Fourier Imaging, in: MICCAI Workshop on Computational Diffusion MRI. pp. 1–11.

Christiaens D, Cordero-Grande L, Hutter J, Price AN, Deprez M, Hajnal JV, Tournier J-D, 2018. Learning compact q-space representations for multi-shell diffusion-weighted MRI. IEEE Transactions on Medical Imaging 1–1.

Colgan N, Siow B, O'Callaghan JM, Harrison IF, Wells JA, Holmes HE, Ismail O, Richardson S, Alexander DC, Collins EC, Fisher EM, Johnson R, Schwarz AJ, Ahmed Z, O'Neill MJ, Murray TK, Zhang H, Lythgoe MF, 2016. Application of neurite orientation dispersion and density imaging (NODDI) to a tau pathology model of Alzheimer's disease. NeuroImage 125, 739–744.

Cook PA, Bai Y, Gilani NS, Seunarine KK, Hall MG, Parker GJ, Alexander DC, 2006. Camino: Open-Source Diffusion-MRI Reconstruction and Processing, in: Proceedings of the 14th Scientific Meeting of the International Society for Magnetic Resonance in Medicine. p. 2759.

Daducci A, Canales-Rodríguez EJ, Zhang H, Dyrby TB, Alexander DC, Thiran J-P, 2015. Accelerated Microstructure Imaging via Convex Optimization (AMICO) from diffusion MRI data. NeuroImage 105, 32–44.

De Groot JC, De Leeuw F-E, Oudkerk M, Van Gijn J, Hofman A, Jolles J, Breteler MMB, 2000. Cerebral white matter lesions and cognitive function: The rotterdam scan study. Annals of Neurology 47, 145–151.

De Groot M, Ikram MA, Akoudad S, Krestin GP, Hofman A, Van Der Lugt A, Niessen WJ, Vernooij MW, 2015. Tract-specific white matter degeneration in aging: The Rotterdam Study. Alzheimer's and Dementia 11, 321–330.

De Groot M, Vernooij MW, Klein S, Ikram MA, Vos FM, Smith SM, Niessen WJ, Andersson JLR, 2013. Improving alignment in Tract-based spatial statistics: Evaluation and optimization of image

registration. NeuroImage 76, 400–411.

De Santis S, Assaf Y, Evans CJ, Jones DK, 2014. Improved precision in CHARMED assessment of white matter through sampling scheme optimization and model parsimony testing. Magnetic Resonance in Medicine 71, 661–671.

De Santis S, Assaf Y, Jones D, 2012. Using the biophysical CHARMED model to elucidate the underpinnings of contrast in diffusional kurtosis analysis of diffusion-weighted MRI. Magnetic Resonance Materials in Physics, Biology and Medicine 25, 267–276.

De Santis S, Drakesmith M, Bells S, Assaf Y, Jones D, 2014. Why diffusion tensor MRI does well only some of the time: Variance and covariance of white matter tissue microstructure attributes in the living human brain. NeuroImage 89, 35–44.

Dell'Acqua F, Rizzo G, Scifo P, Clarke RA, Scotti G, Fazio F, 2007. A model-based deconvolution approach to solve fiber crossing in diffusion-weighted MR imaging. IEEE Transactions on Biomedical Engineering 54, 462–472.

Dell'Acqua F, Tournier JD, 2018. Modelling white matter with spherical deconvolution: How and why? NMR in Biomedicine 1–18.

Descoteaux M, Angelino E, Fitzgibbons S, Deriche R, 2007. Regularized, Fast, and Robust Analytical Q-Ball Imaging. Magnetic Resonance in Medicine 58, 497–510.

Descoteaux M, Deriche R, Bihan DL, Mangin J-F, Poupon C, 2011. Multiple q-shell diffusion propagator imaging. Medical Image Analysis 15, 603–621.

Donoho DL, 2006. Compressed sensing. IEEE Transactions on Information Theory 52, 1289–1306.

Edden RA, Jones DK, 2011. Spatial and orientational heterogeneity in the statistical sensitivity of skeleton-based analyses of diffusion tensor MR imaging data. Journal of Neuroscience Methods 201, 213–219.

Einstein A, 1905. On the movement of small particles suspended in stationary liquids required by the molecular-kinetic theory of heat. Annalen der Physik 17, 549–560.

Elhabian S, Gur Y, Vachet C, Piven J, Styner M, Leppert I, Pike G, Gerig G, 2014. A preliminary study on the effect of motion correction on HARDI reconstruction, in: Biomedical Imaging (Isbi), 2014 Ieee 11th International Symposium on. pp. 1055–1058.

Elhabian S, Vachet C, Piven J, Styner M, Gerig G, 2016. Compressive sensing based Q-space resampling for handling fast bulk motion in hardi acquisitions, in: 2016 Ieee 13th International Symposium on Biomedical Imaging (Isbi). IEEE, pp. 907–910.

Falangola MF, Jensen JH, Babb JS, Hu C, Castellanos FX, Di Martino A, Ferris SH, Helpern JA, 2008. Age-related non-Gaussian diffusion patterns in the prefrontal brain. Journal of Magnetic Resonance Imaging 28, 1345–1350.

Fan Q, Witzel T, Nummenmaa A, Van Dijk KRA, Van Horn JD, Drews MK, Somerville LH, Sheridan

MA, Santillana RM, Snyder J, Hedden T, Shaw EE, Hollinshead MO, Renvall V, Zanzonico R, Keil B, Cauley S, Polimeni JR, Tisdall D, Buckner RL, Wedeen VJ, Wald LL, Toga AW, Rosen BR, 2016. MGH-USC Human Connectome Project datasets with ultra-high b-value diffusion MRI. NeuroImage 124, 1108–1114.

Farrell JAD, Landman BA, Jones CK, Smith SA, Prince JL, Van Zijl PCM, Mori S, 2007. Effects of signal-to-noise ratio on the accuracy and reproducibility of diffusion tensor imaging-derived fractional anisotropy, mean diffusivity, and principal eigenvector measurements at 1.5T. Journal of Magnetic Resonance Imaging 26, 756–767.

Ferizi U, Schneider T, Panagiotaki E, Nedjati-Gilani G, Zhang H, Wheeler-Kingshott CAM, Alexander DC, 2014. A ranking of diffusion MRI compartment models with in vivo human brain data. Magnetic Resonance in Medicine 72, 1785–1792.

Fick A, 1855. Ueber Diffusion. Annalen der Physik 170, 59–86.

Fick R, Wassermann D, Sanguinetti G, Deriche R, 2014. An analytical 3d Laplacian regularized SHORE basis and its impact on EAP reconstruction and microstructure recovery, in: Mathematics and Visualization. pp. 151–165.

Fick RH, Wassermann D, Caruyer E, Deriche R, 2016. MAPL: Tissue microstructure estimation using Laplacian-regularized MAP-MRI and its application to HCP data. NeuroImage 134, 365–385.

Fieremans E, Benitez A, Jensen J, Falangola M, Tabesh A, Deardorff R, Spampinato M, Babb J, Novikov D, Ferris S, Helpern J, 2013. Novel White Matter Tract Integrity Metrics Sensitive to Alzheimer Disease Progression. American Journal of Neuroradiology 34, 2105–2112.

Fieremans E, Jensen JH, Helpern JA, 2011. White matter characterization with diffusional kurtosis imaging. NeuroImage 58, 177–188.

Fischl B, Sereno MI, 2018. Microstructural parcellation of the human brain. NeuroImage 182, 219–231.

Garyfallidis E, Brett M, Amirbekian B, Rokem A, Van Der Walt S, Descoteaux M, Nimmo-Smith I, 2014. Dipy, a library for the analysis of diffusion mri data. Frontiers in Neuroinformatics 8, 8.

Geary RC, 1930. The Frequency Distribution of the Quotient of Two Normal Variates. Journal of the Royal Statistical Society 93, 442–446.

Giezendanner S, Fisler MS, Soravia LM, Andreotti J, Walther S, Wiest R, Dierks T, Federspiel A, 2016. Microstructure and cerebral blood flow within white matter of the human brain: A TBSS analysis. PLoS ONE 11.

Gigandet X, Griffa A, Kober T, Daducci A, Gilbert G, Connelly A, Hagmann P, Meuli R, Thiran J-P, Krueger G, 2013. A Connectome-Based Comparison of Diffusion MRI Schemes. PLoS ONE 8,

e75061.

Glasser MF, Smith SM, Marcus DS, Andersson JLR, Auerbach EJ, Behrens TEJ, Coalson TS, Harms MP, Jenkinson M, Moeller S, Robinson EC, Sotiropoulos SN, Xu J, Yacoub E, Ugurbil K, Van Essen DC, 2016. The Human Connectome Project's neuroimaging approach. Nature neuroscience 19, 1175–87.

Gong P, Zhang C, Lu Z, Huang J, Ye J, 2013. A General Iterative Shrinkage and Thresholding Algorithm for Non-convex Regularized Optimization Problems, in: Proceedings of the 30th International Conference on Machine Learning (Atlanta, GA). pp. 37–45.

Gramfort a, Poupon C, Descoteaux M, 2014. Denoising and fast diffusion imaging with physically constrained sparse dictionary learning. Medical Image Analysis 18, 36–49.

Griswold MA, Jakob PM, Heidemann RM, Nittka M, Jellus V, Wang J, Kiefer B, Haase A, 2002. Generalized autocalibrating partially parallel acquisitions (GRAPPA). Magnetic Resonance in Medicine 47, 1202–1210.

Groeschel S, Hagberg GE, Schultz T, Balla DZ, Klose U, Hauser TK, Nägele T, Bieri O, Prasloski T, Mackay AL, Krägeloh-Mann I, Scheffler K, 2016. Assessing white matter microstructure in brain regions with different myelin architecture using MRI. PLoS ONE 11, 1–23.

Gudbjartsson H, Patz S, 1995. The rician distribution of noisy MRI data. Magnetic Resonance in Medicine 36, 910–914.

Haacke EM, Xu Y, Cheng Y-CN, Reichenbach JR, 2004. Susceptibility weighted imaging (SWI). Magnetic Resonance in Medicine 52, 612–618.

Hahn EL, 1950. Spin echoes. Phys. Rev. 80, 580–594.

Hall M, Alexander D, 2009. Convergence and Parameter Choice for Monte-Carlo Simulations of Diffusion MRI. IEEE Transactions on Medical Imaging 28, 1354–1364.

Hamaguchi H, Tha KK, Sugimori H, Nakanishi M, Nakagawa S, Fujiwara T, Yoshida H, Takamori S, Shirato H, 2016. Effect of respiratory and cardiac gating on the major diffusion-imaging metrics. Neuroradiology Journal 29, 254–259.

Harms R, Fritz F, Tobisch A, Goebel R, Roebroeck A, 2017. Robust and fast nonlinear optimization of diffusion MRI microstructure models. NeuroImage 155, 82–96.

Harms R, Goebel R, Roebroeck A, 2016. Diffusion microstructure in the population: variability and effect size of biophysical compartment model parameters over 100 subjects, in: Proceedings of the 24th Scientific Meeting of the International Society for Magnetic Resonance in Medicine.

Helpern JA, Falangola MF, Hu C, Tabesh A, Kwon J, Babb JS, Jensen JH, 2011. Diffusional Kurtosis Imaging in Mild Cognitive Impairment and Alzheimer's Disease, in: Proceedings of the 19th Scientific Meeting of the International Society for Magnetic Resonance in Medicine. p. 4217.

Horsfield MA, Jones DK, 2002. Applications of diffusion-weighted and diffusion tensor MRI to white

matter diseases - A review. NMR in Biomedicine 15, 570–577.

Huang SY, Nummenmaa A, Witzel T, Duval T, Cohen-Adad J, Wald LL, McNab JA, 2015. The impact of gradient strength on in vivo diffusion MRI estimates of axon diameter. NeuroImage 106, 464–472.

Hui ES, Fieremans E, Jensen JH, Tabesh A, Feng W, Bonilha L, Spampinato MV, Adams R, Helpern JA, 2012. Stroke assessment with diffusional kurtosis imaging. Stroke 43, 2968–2973.

Ikram MA, Lugt A van der, Niessen WJ, Koudstaal PJ, Krestin GP, Hofman A, Bos D, Vernooij MW, 2015. The Rotterdam Scan Study: design update 2016 and main findings. European Journal of Epidemiology 30, 1299–1315.

Jbabdi S, Sotiropoulos SN, Haber SN, Van Essen DC, Behrens TE, Essen DCV, Behrens TE, 2015. Measuring macroscopic brain connections in vivo. Nature Neuroscience 18, 1546–1555.

Jelescu IO, Veraart J, Adisetiyo V, Milla SS, Novikov DS, Fieremans E, 2015. One diffusion acquisition and different white matter models: How does microstructure change in human early development based on WMTI and NODDI? NeuroImage 107, 242–256.

Jelescu IO, Veraart J, Fieremans E, Novikov DS, 2016. Degeneracy in model parameter estimation for multi-compartmental diffusion in neuronal tissue. NMR in Biomedicine 29, 33–47.

Jensen JH, Falangola MF, Hu C, Tabesh A, Rapalino O, Lo C, Helpern JA, 2011. Preliminary observations of increased diffusional kurtosis in human brain following recent cerebral infarction. NMR in Biomedicine 24, 452–457.

Jensen JH, Helpern J a, Tabesh A, 2014. Leading non-Gaussian corrections for diffusion orientation distribution function. NMR in biomedicine 27, 202–11.

Jensen JH, Helpern JA, 2010. MRI quantification of non-Gaussian water diffusion by kurtosis analysis. NMR in Biomedicine 23, 698–710.

Jensen JH, Helpern JA, Ramani A, Lu H, Kaczynski K, 2005. Diffusional kurtosis imaging: The quantification of non-Gaussian water diffusion by means of magnetic resonance imaging. Magnetic Resonance in Medicine 53, 1432–1440.

Jeurissen B, Descoteaux M, Mori S, Leemans A, 2017. Diffusion MRI fiber tractography of the brain. NMR in Biomedicine e3785.

Jeurissen B, Leemans A, Tournier J-D, Jones DK, Sijbers J, 2013. Investigating the prevalence of complex fiber configurations in white matter tissue with diffusion magnetic resonance imaging. Human Brain Mapping 34, 2747–2766.

Jeurissen B, Tournier J-D, Dhollander T, Connelly A, Sijbers J, 2014. Multi-tissue constrained spherical deconvolution for improved analysis of multi-shell diffusion MRI data. NeuroImage 103, 411–426.

Jones DK, 2010. Challenges and limitations of quantifying brain connectivity. Imaging Med 2, 341–

355.

Jones DK, Horsfield MA, Simmons A, 1999. Optimal strategies for measuring diffusion in anisotropic systems by magnetic resonance imaging. Magnetic Resonance in Medicine 42, 515–525.

Jost W, 1960. Diffusion in Solids, Liquids and Gases. Academic Press.

Kamath A, Aganj I, Xu J, Yacoub E, Ugurbil K, 2012. Generalized Constant Solid Angle ODF and Optimal Acquisition Protocol for Fiber Orientation Mapping, in: Medical Image Computing and Computer-Assisted Intervention (Nice). pp. 67–78.

Kärger J, Heink W, 1983. The propagator representation of molecular transport in microporous crystallites. Journal of Magnetic Resonance (1969) 51, 1–7.

Khare K, Hardy CJ, King KF, Turski PA, Marinelli L, 2012. Accelerated MR imaging using compressive sensing with no free parameters. Magnetic Resonance in Medicine 68, 1450–1457.

Knutsson H, Westin CF, 2013. Tensor metrics and charged containers for 3D Q-space sample distribution, in: Med. Image Comput. Comput. Assist. Interv. (Nagoya, Japan). pp. 679–686.

Koay CG, Chang LC, Carew JD, Pierpaoli C, Basser PJ, 2006. A unifying theoretical and algorithmic framework for least squares methods of estimation in diffusion tensor imaging. Journal of Magnetic Resonance 182, 115–125.

Kober T, Gruetter R, Krueger G, 2012. Prospective and retrospective motion correction in diffusion magnetic resonance imaging of the human brain. NeuroImage 59, 389–398.

Kober T, Marques JP, Gruetter R, Krueger G, 2011. Head motion detection using FID navigators. Magnetic Resonance in Medicine 66, 135–143.

Koch A, Zhukov A, Stöcker T, Groeschel S, Schultz T, 2019. SHORE-based Detection and Imputation of Dropout in Diffusion MRI. Magnetic Resonance in Medicine (under review).

Kodiweera C, Alexander AL, Harezlak J, McAllister TW, Wu YC, 2016. Age effects and sex differences in human brain white matter of young to middle-aged adults: A DTI, NODDI, and q-space study. NeuroImage 128, 180–192.

Kuhnt D, Bauer MHA, Sommer J, Merhof D, Nimsky C, 2013. Optic Radiation Fiber Tractography in Glioma Patients Based on High Angular Resolution Diffusion Imaging with Compressed Sensing Compared with Diffusion Tensor Imaging - Initial Experience. PLoS ONE 8, e70973.

Kunz N, Zhang H, Vasung L, O'Brien KR, Assaf Y, Lazeyras F, Alexander DC, Hüppi PS, 2014. Assessing white matter microstructure of the newborn with multi-shell diffusion MRI and biophysical compartment models. NeuroImage 96, 288–299.

Kuperman V, 2000. Magnetic Resonance Imaging - Physical Principles and Applications, 1st ed. Academic Press.

Landman B, Bogovic J, Wan H, 2012. Resolution of crossing fibers with constrained compressed

sensing using diffusion tensor MRI. NeuroImage 59, 2175–2186.

Lanzafame S, Giannelli M, Garaci F, Floris R, Duggento A, Guerrisi M, Toschi N, 2016. Differences in Gaussian diffusion tensor imaging and non-Gaussian diffusion kurtosis imaging model-based estimates of diffusion tensor invariants in the human brain. Med Phys 43, 2464–2475.

Larkman DJ, Hajnal JV, Herlihy AH, Coutts GA, Young IR, Ehnholm G, 2001. Use of multicoil arrays for separation of signal from multiple slices simultaneously excited. Journal of Magnetic Resonance Imaging 13, 313–317.

Lauterbur PC, 1973. Image formation by induced local interactions. Examples employing nuclear magnetic resonance. Nature (London, United Kingdom) 242, 190–191.

Lazar M, Jensen JH, Xuan L, Helpern JA, 2008. Estimation of the orientation distribution function from diffusional kurtosis imaging. Magnetic Resonance in Medicine 60, 774–781.

Le Bihan D, Breton E, Lallemand D, Grenier P, Cabanis E, Laval-Jeantet M, 1986. MR imaging of Intravoxel Incoherent Motions: Application to Diffusion and Perfusion in Neurologic Disorders. Radiology 161, 401–407.

Lee N, Singh M, 2010. Compressed Sensing based Diffusion Spectrum Imaging. ISMRM 58, 2010.

Leemans A, Jeurissen B, Sijbers J, Jones DK, 2009. ExploreDTI: a graphical toolbox for processing, analyzing, and visualizing diffusion MR data, in: Proceedings of the 17th Scientific Meeting of the International Society for Magnetic Resonance in Medicine. p. 3537.

Lustig M, Donoho D, Pauly JM, 2007. Sparse MRI: The application of compressed sensing for rapid MR imaging. Magnetic resonance in medicine : official journal of the Society of Magnetic Resonance in Medicine / Society of Magnetic Resonance in Medicine 58, 1182–95.

Maier-Hein KH, Neher PF, Houde J-C, Côté M-A, Garyfallidis E, Zhong J, Chamberland M, Yeh F-C, Lin Y-C, Ji Q, Reddick WE, Glass JO, Chen DQ, Feng Y, Gao C, Wu Y, Ma J, Renjie H, Li Q, Westin C-F, Deslauriers-Gauthier S, González JOO, Paquette M, St-Jean S, Girard G, Rheault F, Sidhu J, Tax CMW, Guo F, Mesri HY, Dávid S, Froeling M, Heemskerk AM, Leemans A, Boré A, Pinsard B, Bedetti C, Desrosiers M, Brambati S, Doyon J, Sarica A, Vasta R, Cerasa A, Quattrone A, Yeatman J, Khan AR, Hodges W, Alexander S, Romascano D, Barakovic M, Auría A, Esteban O, Lemkaddem A, Thiran J-P, Cetingul HE, Odry BL, Mailhe B, Nadar MS, Pizzagalli F, Prasad G, Villalon-Reina JE, Galvis J, Thompson PM, Requejo FDS, Laguna PL, Lacerda LM, Barrett R, Dell'Acqua F, Catani M, Petit L, Caruyer E, Daducci A, Dyrby TB, Holland-Letz T, Hilgetag CC, Stieltjes B, Descoteaux M, 2017. The challenge of mapping the human connectome based on diffusion tractography. Nature Communications 8, 1349.

Mani M, Jacob M, Guidon A, Magnotta V, Zhong J, 2014. Acceleration of high angular and spatial resolution diffusion imaging using compressed sensing with multichannel spiral data. Magnetic Resonance in Medicine 138, 126–138.

Mansfield P, 1977. Multi-planar image formation using nmr spin echoes. Journal of Physics C: Solid

State Physics 10, 55–58.

McNab JA, Edlow BL, Witzel T, Huang SY, Bhat H, Heberlein K, Feiweier T, Liu K, Keil B, Cohen-Adad J, Tisdall MD, Folkerth RD, Kinney HC, Wald LL, 2013. The Human Connectome Project and beyond: Initial applications of 300mT/m gradients. NeuroImage 80, 234–245.

Mekkaoui C, Reese TG, Jackowski MP, Bhat H, Sosnovik DE, 2017. Diffusion MRI in the heart. NMR in Biomedicine 30, e3426.

Menzel MI, Tan ET, Khare K, Sperl JI, King KF, Tao X, Hardy CJ, Marinelli L, 2011. Accelerated diffusion spectrum imaging in the human brain using compressed sensing. Magnetic resonance in medicine : official journal of the Society of Magnetic Resonance in Medicine / Society of Magnetic Resonance in Medicine 66, 1226–33.

Merlet S, Deriche R, 2010. Compressed sensing for accelerated EAP recovery in diffusion MRI, in: MICCAI Workshop on Computational Diffusion MRI (Beijing, China). pp. 14–21.

Merlet SL, Deriche R, 2013. Continuous diffusion signal, EAP and ODF estimation via Compressive Sensing in diffusion MRI. Medical Image Analysis 17, 556–572.

Michailovich O, Rathi Y, Dolui S, 2011. Spatially Regularized Compressed Sensing for High Angular Resolution Diffusion Imaging. IEEE Transactions on Medical Imaging 30, 1100–1115.

Miller KL, Alfaro-Almagro F, Bangerter NK, Thomas DL, Yacoub E, Xu J, Bartsch AJ, Jbabdi S, Sotiropoulos SN, Andersson JLR, Griffanti L, Douaud G, Okell TW, Weale P, Dragonu I, Garratt S, Hudson S, Collins R, Jenkinson M, Matthews PM, Smith SM, 2016. Multimodal population brain imaging in the UK Biobank prospective epidemiological study. Nature neuroscience 19, 1523–1536.

Mori S, Crain BJ, Chacko VP, Van Zijl PCM, 1999. Three-dimensional tracking of axonal projections in the brain by magnetic resonance imaging. Annals of Neurology 45, 265–269.

Mori S, Oishi K, Jiang H, Jiang L, Li X, Akhter K, Hua K, Faria AV, Mahmood A, Woods R, Toga AW, Pike GB, Neto PR, Evans A, Zhang J, Huang H, Miller MI, Zijl P van, Mazziotta J, 2008. Stereotaxic white matter atlas based on diffusion tensor imaging in an ICBM template. NeuroImage 40, 570–582.

Moseley ME, Kucharczyk J, Asgari HS, Norman D, 1991. Anisotropy in diffusion-weighted MRI. Magnetic Resonance in Medicine 19, 321–326.

Moussavi-Biugui A, Stieltjes B, Fritzsche K, Semmler W, Laun FB, 2011. Novel spherical phantoms for Q-ball imaging under in vivo conditions. Magnetic Resonance in Medicine 65, 190–194.

Ning L, Laun F, Gur Y, DiBella EV, Deslauriers-Gauthier S, Megherbi T, Ghosh A, Zucchelli M, Menegaz G, Fick R, St-Jean S, Paquette M, Aranda R, Descoteaux M, Deriche R, O'Donnell L, Rathi Y, 2015. Sparse Reconstruction Challenge for diffusion MRI: Validation on a physical phantom to determine which acquisition scheme and analysis method to use? Medical Image

Analysis 26, 316–331.

Novikov DS, Fieremans E, Jespersen SN, Kiselev VG, 2018. Quantifying brain microstructure with diffusion MRI: Theory and parameter estimation. NMR in Biomedicine e3998.

Nunes RG, Hajnal JV, Golay X, Larkman DJ, 2006. Simultaneous slice excitation and reconstruction for single shot EPI . Proceedings of the 14th Scientific Meeting of the International Society for Magnetic Resonance in Medicine 293.

OpenStax College, 2013. Anatomy & physiology. OpenStax College.

Oudeman J, Nederveen AJ, Strijkers GJ, Maas M, Luijten PR, Froeling M, 2016. Techniques and applications of skeletal muscle diffusion tensor imaging: A review. Journal of Magnetic Resonance Imaging 43, 773–788.

Ozarslan E, Koay C, Shepherd TM, Blackband SJ, Basser PJ, 2009. Simple harmonic oscillator based reconstruction and estimation for three-dimensional q-space MRI, in: Proceedings of the 17th Scientific Meeting of the International Society for Magnetic Resonance in Medicine (Honolulu, HI). p. 1396.

Özarslan E, Koay CG, Shepherd TM, Komlosh ME, İrfanoğlu MO M. O.lu, Pierpaoli C, Basser PJ, 2013. Mean apparent propagator (MAP) MRI: A novel diffusion imaging method for mapping tissue microstructure. NeuroImage 78, 16–32.

Panagiotaki E, Schneider T, Siow B, Hall MG, Lythgoe MF, Alexander DC, 2012. Compartment models of the diffusion MR signal in brain white matter: A taxonomy and comparison. NeuroImage 59, 2241–2254.

Paquette M, Gilbert G, Descoteaux M, 2016. Optimal DSI reconstruction parameter recommendations: Better ODFs and better connectivity. NeuroImage 142, 1–13.

Paquette M, Merlet S, Gilbert G, Deriche R, Descoteaux M, 2015. Comparison of sampling strategies and sparsifying transforms to improve compressed sensing diffusion spectrum imaging. Magnetic Resonance in Medicine 73, 401–416.

Poot D, Dekker A den, Achten E, Verhoye M, Sijbers J, 2010. Optimal Experimental Design for Diffusion Kurtosis Imaging. IEEE Transactions on Medical Imaging 29, 819–829.

Pruessmann KP, Weiger M, Scheidegger MB, Boesiger P, 1999. SENSE: Sensitivity encoding for fast MRI. Magnetic Resonance in Medicine 42, 952–962.

Raffelt D, Tournier J-D, Salvado O, Connelly A, 2012. Mask-Based Motion and Eddy-Current Correction of High b-value Diffusion-Weighted Images. Proceedings of the 20th Scientific Meeting of the International Society for Magnetic Resonance in Medicine.

Rathi Y, Michailovich O, Laun F, Setsompop K, Grant PE, Westin CF, 2014. Multi-shell diffusion signal recovery from sparse measurements. Medical Image Analysis 18, 1143–1156.

Rathi Y, Michailovich O, Setsompop K, Bouix S, Shenton ME, Westin CF, 2011. Sparse Multi-Shell

Diffusion Imaging 2, 58–65.

Reese TG, Heid O, Weisskoff RM, Wedeen VJ, 2003. Reduction of eddy-current-induced distortion in diffusion MRI using a twice-refocused spin echo. Magnetic Resonance in Medicine 49, 177–182.

Rudin LI, Osher S, Fatemi E, 1992. Nonlinear total variation based noise removal algorithms. Physica D: Nonlinear Phenomena 60, 259–268.

Sairanen V, Leemans A, Tax C, 2018. Fast and accurate Slicewise OutLIer Detection (SOLID) with informed model estimation for diffusion MRI data. NeuroImage 181, 331–346.

Sandilya M, Nirmala SR, 2017. Compressed sensing trends in magnetic resonance imaging. Engineering Science and Technology, an International Journal 20, 1342–1352.

Scherrer B, Warfield S, 2012. Retrospective local artefacts detection in diffusion-weighted images using the Random Sample Consensus (RANSAC) paradigm, in: Biomedical Imaging (Isbi), 2012 9th Ieee International Symposium on. pp. 546–549.

Schneider T, Brownlee W, Zhang H, Ciccarelli O, Miller DH, Wheeler-Kingshott CG, 2017. Sensitivity of multi-shell NODDI to multiple sclerosis white matter changes: A pilot study. Functional Neurology 32, 97–101.

Schultz T, 2012. Learning a reliable estimate of the number of fiber directions in diffusion MRI., in: Medical Image Computing and Computer-Assisted Intervention. pp. 493–500.

Schwarz G, 1978. Estimating the dimension of a model. The Annals of Statistics 6, 61–464.

Setsompop K, Gagoski BA, Polimeni JR, Witzel T, Wedeen VJ, Wald LL, 2012. Blipped-controlled aliasing in parallel imaging for simultaneous multislice echo planar imaging with reduced g-factor penalty. Magnetic Resonance in Medicine 67, 1210–1224.

Setsompop K, Kimmlingen R, Eberlein E, Witzel T, Cohen-Adad J, McNab J a, Keil B, Tisdall MD, Hoecht P, Dietz P, Cauley SF, Tountcheva V, Matschl V, Lenz VH, Heberlein K, Potthast a, Thein H, Van Horn J, Toga a, Schmitt F, Lehne D, Rosen BR, Wedeen V, Wald LL, 2013. Pushing the limits of in vivo diffusion MRI for the Human Connectome Project. NeuroImage 80, 220–33.

Shannon C, 1949. Communication In The Presence Of Noise. Proceedings of the IRE 37, 10–21.

Shenoy-Bhangle A, Baliyan V, Kordbacheh H, Guimaraes AR, Kambadakone A, 2017. Diffusion weighted magnetic resonance imaging of liver: Principles, clinical applications and recent updates. World Journal of Hepatology 9, 1081–1091.

Shmueli K, De Zwart JA, Van Gelderen P, Li TQ, Dodd SJ, Duyn JH, 2009. Magnetic susceptibility mapping of brain tissue in vivo using MRI phase data. Magnetic Resonance in Medicine 62, 1510–1522.

Smith SM, Jenkinson M, Johansen-Berg H, Rueckert D, Nichols TE, Mackay CE, Watkins KE, Ciccarelli O, Cader MZ, Matthews PM, Behrens TEJ, 2006. Tract-based spatial statistics: Voxelwise

analysis of multi-subject diffusion data. NeuroImage 31, 1487–1505.

Sosnovik DE, Wang R, Dai G, Reese TG, Wedeen VJ, 2009. Diffusion MR tractography of the heart. Journal of Cardiovascular Magnetic Resonance 11, 1–15.

Sotiropoulos SN, Jbabdi S, Xu J, Andersson JL, Moeller S, Auerbach EJ, Glasser MF, Hernandez M, Sapiro G, Jenkinson M, Feinberg DA, Yacoub E, Lenglet C, Van Essen DC, Ugurbil K, Behrens TEJ, 2013. Advances in diffusion MRI acquisition and processing in the Human Connectome Project. NeuroImage 80, 125–143.

Sotiropoulos SN, Zalesky A, 2017. Building connectomes using diffusion MRI: Why, how and but. NMR in Biomedicine 1–23.

Sprenger T, Sperl JI, Fernandez B, Golkov V, Eidner I, Sämann PG, Czisch M, Tan ET, Hardy CJ, Marinelli L, Haase A, Menzel MI, 2016. Bias and precision analysis of diffusional kurtosis imaging for different acquisition schemes. Magnetic Resonance in Medicine 76, 1684–1696.

Stejskal EO, Tanner JE, 1965. Spin diffusion measurements: spin echoes in the presence of a time-dependent field gradient. The Journal of Chemical Physics 42, 288–292.

Stirnberg R, Brenner D, Huijbers W, Kober T, Stöcker T, 2016. PCA-aided improvements on FID-based motion tracking calibrated on resting-state EPI data without intentional motion, in: Proceedings of the 24th Scientific Meeting of the International Society for Magnetic Resonance in Medicine (Singapore). pp. 22–24.

Storey P, Frigo FJ, Hinks RS, Mock BJ, Collick BD, Baker N, Marmurek J, Graham SJ, 2007. Partialk-space reconstruction in single-shot diffusion-weighted echo-planar imaging. Magnetic Resonance in Medicine 57, 614–619.

Stöcker T, 2016. Big Data: The Rhineland Study, in: Proceedings of the 24th Scientific Meeting of the International Society for Magnetic Resonance in Medicine (Singapore).

Tabesh A, Jensen JH, Ardekani BA, Helpern JA, 2011. Estimation of tensors and tensor-derived measures in diffusional kurtosis imaging. Magnetic Resonance in Medicine 65, 823–836.

Tariq M, Schneider T, Alexander DC, Gandini Wheeler-Kingshott CA, Zhang H, 2016. Bingham-NODDI: Mapping anisotropic orientation dispersion of neurites using diffusion MRI. NeuroImage 133, 207–223.

Tax CM, Otte WM, Viergever MA, Dijkhuizen RM, Leemans A, 2015. REKINDLE: Robust Extraction of Kurtosis INDices with Linear Estimation. Magnetic Resonance in Medicine 73, 794–808.

Tax CM, Vos SB, Froeling M, Viergever MA, Leemans A, 2014. Transforming grids to shells and vice versa: An evaluation of interpolation methods in diffusion MRI q- and b-space, in: Proceedings of the 22nd Scientific Meeting of the International Society for Magnetic Resonance in Medicine. p. 4485.

Tibshirani R, 1996. Regression Selection and Shrinkage via the Lasso. Journal of the Royal Statis-

tical Society. Series B (Methodological) 58, 267–288.

Tobisch A, Schultz T, Stirnberg R, Varela G, Knutsson H, v, 2015. Comparing Fourier to SHORE Basis Functions for Sparse DSI Reconstruction, in: Proceedings of the 23rd Scientific Meeting of the International Society for Magnetic Resonance in Medicine (Toronto, ON). p. 1029.

Tobisch A, Schultz T, Stirnberg R, Varela-Mattatall G, Knutsson H, Irarrázaval P, Tony S, 2019. Comparison of basis functions and q-space sampling schemes for robust compressed sensing reconstruction accelerating diffusion spectrum imaging. NMR in Biomedicine e4055.

Tobisch A, Stirnberg R, Harms RL, Schultz T, Roebroeck A, Breteler MMB, Stöcker T, 2018. Compressed Sensing Diffusion Spectrum Imaging for Accelerated Diffusion Microstructure MRI in Long-Term Population Imaging. Frontiers in Neuroscience 12, 650.

Tobisch A, Stocker T, Groeschel S, Schultz T, 2016. Iteratively reweighted L1-fitting for model-independent outlier removal and regularization in diffusion MRI, in: 2016 Ieee 13th International Symposium on Biomedical Imaging (Isbi). IEEE, pp. 911–914.

Tobisch A, Varela G, Stirnberg R, Knutsson H, Schultz T, Irarrázaval P, Stöcker T, 2014. Sparse isotropic q-space sampling distribution for Compressed Sensing in DSI, in: Proceedings of the 22nd Scientific Meeting of the International Society for Magnetic Resonance in Medicine. p. 4451.

Torrey HC, 1956. Bloch equations with diffusion terms. Phys. Rev. 104, 563–565.

Tournier JD, Calamante F, Connelly A, 2013. Determination of the appropriate b value and number of gradient directions for high-angular-resolution diffusion-weighted imaging. NMR in Biomedicine 26, 1775–1786.

Tournier JD, Calamante F, Connelly A, 2007. Robust determination of the fibre orientation distribution in diffusion MRI: Non-negativity constrained super-resolved spherical deconvolution. NeuroImage 35, 1459–1472.

Tournier JD, Calamante F, Gadian DG, Connelly A, 2004. Direct estimation of the fiber orientation density function from diffusion-weighted MRI data using spherical deconvolution. NeuroImage 23, 1176–1185.

Tuch DS, 2004. Q-ball imaging. Magnetic Resonance in Medicine 52, 1358–1372.

Tuch DS, Reese TG, Wiegell MR, Makris N, Belliveau JW, Van Wedeen J, 2002. High angular resolution diffusion imaging reveals intravoxel white matter fiber heterogeneity. Magnetic Resonance in Medicine 48, 577–582.

Tuch DS, Reese TG, Wiegell MR, Van J. Wedeen, 2003. Diffusion MRI of Complex Neural Architecture. Neuron 40, 885–895.

Turner R, 1993. Gradient coil design: A review of methods. Magnetic Resonance Imaging 11,

903–920.

Turner R, Le Bihan D, Maier J, Vavrek R, Hedges LK, Pekar J, 1990. Echo-planar imaging of intravoxel incoherent motion. Radiology 177, 407–414.

Van Essen DC, Ugurbil K, Auerbach E, Barch D, Behrens TEJ, Bucholz R, Chang A, Chen L, Corbetta M, Curtiss SW, Della Penna S, Feinberg D, Glasser MF, Harel N, Heath AC, Larson-Prior L, Marcus D, Michalareas G, Moeller S, Oostenveld R, Petersen SE, Prior F, Schlaggar BL, Smith SM, Snyder AZ, Xu J, Yacoub E, 2012. The Human Connectome Project: A data acquisition perspective. NeuroImage 62, 2222–2231.

Varela G, Tobisch A, Stöcker T, Irarràzaval P, 2014. Curvelets, a new sparse domain for diffusion spectrum imaging, in: Proceedings of the 22nd Scientific Meeting of the International Society for Magnetic Resonance in Medicine.

Varela-Mattatall GE, Koch A, Stirnberg R, Chabert S, Uribe S, Tejos C, Stöcker T, Irarràzaval P, 2019. Comparison of q-Space Reconstruction Methods for Undersampled Diffusion Spectrum Imaging Data. Magnetic Resonance in Medical Sciences 1–11.

Veraart J, Fieremans E, Novikov DS, 2016. Universal power-law scaling of water diffusion in human brain defines what we see with MRI. arXiv:1609.09145 [physics.bio-ph].

Veraart J, Novikov DS, Christiaens D, Ades-aron B, Sijbers J, Fieremans E, 2016. Denoising of diffusion MRI using random matrix theory. NeuroImage 142, 394–406.

Veraart J, Poot DHJ, Van Hecke W, Blockx I, Van der Linden A, Verhoye M, Sijbers J, 2011. More accurate estimation of diffusion tensor parameters using diffusion kurtosis imaging. Magnetic Resonance in Medicine 65, 138–145.

Veraart J, Sijbers J, Sunaert S, Leemans A, Jeurissen B, 2013. Weighted linear least squares estimation of diffusion MRI parameters: Strengths, limitations, and pitfalls. NeuroImage 81, 335–346.

Vollmar C, O'Muircheartaigh J, Barker GJ, Symms MR, Thompson P, Kumari V, Duncan JS, Richardson MP, Koepp MJ, 2010. Identical, but not the same: Intra-site and inter-site reproducibility of fractional anisotropy measures on two 3.0T scanners. NeuroImage 51, 1384–1394.

Vovk V, Wang R, 2012. Combining p-values via averaging. arXiv:1212.4966.

Wallace TE, Afacan O, Warfield1 SK, 2018. A novel framework for head motion measurement using free induction decay navigators from multi-channel coil arrays, in: Proceedings of the 26th Scientific Meeting of the International Society for Magnetic Resonance in Medicine (Paris).

Wang R, Benner T, Sorensen AG, Wedeen V, 2007. Diffusion Toolkit: A Software Package for Diffusion Imaging Data Processing and Tractography, in: Proceedings of the 15th Scientific Meeting of the International Society for Magnetic Resonance in Medicine.

Wedeen V, Wang R, Schmahmann J, Benner T, Tseng W, Dai G, Pandya D, Hagmann P, D'Arceuil

H, Crespigny A de, 2008. Diffusion spectrum magnetic resonance imaging (DSI) tractography of crossing fibers. NeuroImage 41, 1267–1277.

Wedeen VJ, Hagmann P, Tseng WYI, Reese TG, Weisskoff RM, 2005. Mapping complex tissue architecture with diffusion spectrum magnetic resonance imaging. Magnetic Resonance in Medicine 54, 1377–1386.

Wedeen VJ, Weisskoff RM, Poncelet BP, 1994. MRI signal void due to in-plane motion is all-or-none. Magnetic Resonance in Medicine 32, 116–120.

Weiner MW, Veitch DP, Aisen PS, Beckett LA, Cairns NJ, Cedarbaum J, Green RC, Harvey D, Jack CR, Jagust W, Luthman J, Morris JC, Petersen RC, Saykin AJ, Shaw L, Shen L, Schwarz A, Toga AW, Trojanowski JQ, 2015. 2014 Update of the Alzheimer's Disease Neuroimaging Initiative: A review of papers published since its inception. Alzheimer's and Dementia 11, e1–e120.

Werring DJ, Toosy AT, Clark CA, Parker GJM, Barker GJ, Miller DH, Thompson AJ, 2000. Diffusion tensor imaging can detect and quantify corticospinal tract degeneration after stroke. Journal of Neurology Neurosurgery and Psychiatry 69, 269–272.

Willats L, Raffelt D, Smith RE, Tournier JD, Connelly A, Calamante F, 2014. Quantification of track-weighted imaging (TWI): Characterisation of within-subject reproducibility and between-subject variability. NeuroImage 87, 18–31.

Winkler AM, Ridgway GR, Webster MA, Smith SM, Nichols TE, 2014. Permutation inference for the general linear model. NeuroImage 92, 381–397.

Wu W, Miller KL, 2017. Image formation in diffusion MRI: A review of recent technical developments. Journal of Magnetic Resonance Imaging 46, 646–662.

Wu YC, Alexander AL, 2007. Hybrid diffusion imaging. NeuroImage 36, 617–629.

Wu YC, Field AS, Alexander AL, 2008. Computation of diffusion function measures in q-space using magnetic resonance hybrid diffusion imaging. IEEE Transactions on Medical Imaging 27, 858–865.

Xu J, Moeller S, Auerbach EJ, Strupp J, Smith SM, Feinberg DA, Yacoub E, Uğurbil K, 2013. Evaluation of slice accelerations using multiband echo planar imaging at 3T. NeuroImage 83, 991–1001.

Yau Y, Yeighami Y, Baker T, Larcher K, Vainik U, Dadar M, Fonov V, Hagmann P, Griffa A, Misic B, Collins D, Dagher A, 2018. Network connectivity determines cortical thinning in early Parkinsons disease progression. Nature Communications 9.

Yeh F-C, Verstynen TD, 2016. Converting Multi-Shell and Diffusion Spectrum Imaging to High Angular Resolution Diffusion Imaging. Frontiers in Neuroscience 10, 1–11.

Yeh F-C, Wedeen VJ, Tseng W-YI, 2010. Generalized q-Sampling Imaging. IEEE Transactions on Medical Imaging 29, 1626–1635.

Zerbato F, Khan S, Zucchelli M, Mendez A, Granziera C, Menegaz G, 2014. Diffusion MRI Com-

partmental Model Analysis of DSI Data, in: 2014 Ieee International Conference on Healthcare Informatics. IEEE, pp. 374–374.

Zhang H, Schneider T, Wheeler-Kingshott CA, Alexander DC, 2012. NODDI: practical in vivo neurite orientation dispersion and density imaging of the human brain. NeuroImage 61, 1000–1016.

Zhu J, Zhuo C, Qin W, Wang D, Ma X, Zhou Y, Yu C, 2015. Performances of diffusion kurtosis imaging and diffusion tensor imaging in detecting white matter abnormality in schizophrenia. NeuroImage: Clinical 7, 170–176.

Acknowledgements

Hereby I want to thank all the people who accompanied me throughout the last years with valuable support, fruitful scientific discussions and joyful distractions, and without whom this work would, therefore, not have been possible.

I am grateful for the continuous support of my supervisor Prof. Dr. Thomas Schultz, for all the scientific discussions and his valuable feedback on the works of this thesis. I also want to thank him for inviting me to participate in a Dagstuhl Seminar, where I enjoyed many great sessions and discussions with other dMRI scientists. I am further grateful for the opportunity to travel to ISBI conference to present our research and meet with scientific peers and colleagues.

I gratefully thank my supervisor Prof. Dr. Tony Stöcker who gave me the opportunity to continue with research in diffusion MRI as a doctoral student at the DZNE. I want to thank him for his continuous guidance, support and advice throughout the last years which greatly helped me during all my doctoral research projects and to further shape my research interests. I am also very grateful to him for the opportunity to work abroad at Pontificia Universidad Católica de Chile in Santiago, Chile, for several month. This was an extraordinary experience, both culturally and scientifically, resulting in continuous research collaborations. In this context, I would also like to thank Prof. Dr. Pablo Irarrázaval and Gabriel Varela-Mattatall for their hospitality in Chile and for many scientific discussions and collaborations in Germany, Chile and at international conferences.

I want to thank everyone from the MR physics group lead by Prof. Tony Stöcker for a great time in a relaxed, highly productive and joyful working atmosphere. A very big thanks goes to Dr. Rüdiger Stirnberg, who supported me throughout my doctoral studies with his great experience in (diffusion) MRI acquisition. I want to thank him for all the helpful MRI related discussion we had and last but not least for his valuable support and feedback as a co-author and reviewer. Together with him and the other members of the MR physics group I spend wonderful work-related and leisure times these last

years in Bonn, in Cologne and at retreats, ISMRM conferences and subsequent vacations. Thanks to all of you for your support. Another special thanks goes to my fellow doctoral students, Markus Boland, Jolanda Schwarz, Yannik Völzke and Suzan Akbey. Thanks also to Anke Rühling and Markus Boland for making the often times highly frustrating commuting between Bonn and Cologne much more fun.

I also want to thank all the people from the Rhineland Study and the Population Health Sciences group at the DZNE lead by Prof. Dr. Dr. Monique Breteler.

Moreover, I thank all co-authors for their support and scientific contributions to our papers and abstracts as well as their valuable feedback during writing and review processes.

I am grateful for my family's continuous support throughout the last years. I could not have achieved this goal without them. I would also like to thank my friends for their motivating discussions and joyful distractions from work. Finally, I want to thank my husband David Koch. I am so very much grateful for his continuous support and patience, especially during busy times in these last years.